

University of Alabama in Huntsville

LOUIS

Dissertations

UAH Electronic Theses and Dissertations

2020

Characterization of supercell thunderstorms exhibiting anomalous charge structures in the Southeastern United States

Sarah M. Stough

Follow this and additional works at: <https://louis.uah.edu/uah-dissertations>

Recommended Citation

Stough, Sarah M., "Characterization of supercell thunderstorms exhibiting anomalous charge structures in the Southeastern United States" (2020). *Dissertations*. 394.
<https://louis.uah.edu/uah-dissertations/394>

This Dissertation is brought to you for free and open access by the UAH Electronic Theses and Dissertations at LOUIS. It has been accepted for inclusion in Dissertations by an authorized administrator of LOUIS.

CHARACTERIZATION OF SUPERCELL THUNDERSTORMS
EXHIBITING ANOMALOUS CHARGE STRUCTURES IN THE
SOUTHEASTERN UNITED STATES

by

SARAH M. STOUGH

A DISSERTATION

Submitted in partial fulfillment of the requirements
for the degree of Doctor of Philosophy
in
The Department of Atmospheric and Earth Science
to
The School of Graduate Studies
of
The University of Alabama in Huntsville

HUNTSVILLE, ALABAMA

2020

In presenting this dissertation in partial fulfillment of the requirements for a doctoral degree from The University of Alabama in Huntsville, I agree that the Library of this University shall make it freely available for inspection. I further agree that permission for extensive copying for scholarly purposes may be granted by my advisor or, in his/her absence, by the Chair of the Department or the Dean of the School of Graduate Studies. It is also understood that due recognition shall be given to me and to The University of Alabama in Huntsville in any scholarly use which may be made of any material in this dissertation.



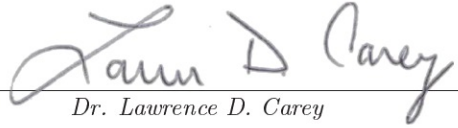
Sarah M. Stough

10/30/2020
(date)

DISSERTATION APPROVAL FORM

Submitted by Sarah M. Stough in partial fulfillment of the requirements for the degree of Doctor of Philosophy in Atmospheric Science and accepted on behalf of the Faculty of the School of Graduate Studies by the dissertation committee.


We, the undersigned members of the Graduate Faculty of The University of Alabama in Huntsville, certify that we have advised and/or supervised the candidate of the work described in this dissertation. We further certify that we have reviewed the dissertation manuscript and approve it in partial fulfillment of the requirements for the degree of Doctor of Philosophy in Atmospheric Science.



Dr. Lawrence D. Carey 10/29/2020 Committee Chair
(Date)




Dr. Daniel J. Cecil 10/29/2020
(Date)


Kevin Knupp Digitally signed by Kevin Knupp
DN: cn=Kevin Knupp, o=UAH, ou,
email=kevin.knupp@uah.edu, c=US
Date: 2020.10.29 21:13:18 -05'00'


Dr. Kevin R. Knupp 10/29/2020
(Date)



Dr. Edward R. Mansell 10/30/2020
(Date)



Dr. Udaysankar S. Nair 10/30/2020
(Date)


John R. Mecikalski Digitally signed by John R. Mecikalski
DN: cn=John R. Mecikalski, o=University of Alabama in
Huntsville, ou=Atmospheric and Earth Science
Department, email=jas-chair@uah.edu, c=US
Date: 2020.10.30 12:50:10 -05'00'

Dr. John R. Mecikalski 10/30/2020 Department Chair
(Date)



Dr. John R. Christy 11/21/2020 College Dean
(Date)

Yeqing Bao, 1/11/2021

Dr. David Berkowitz (Date) Graduate Dean

ABSTRACT

School of Graduate Studies
The University of Alabama in Huntsville

Degree Doctor of Philosophy College/Dept. Science/Atmospheric and
Earth Science

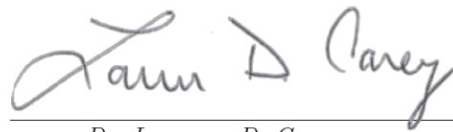
Name of Candidate Sarah M. Stough

Title Characterization of Supercell Thunderstorms Exhibiting
Anomalous Charge Structures in the Southeastern United States

This research is concerned with two supercell thunderstorms observed in the Southeastern United States that exhibited anomalous charge structures (ACSs). ACSs are characterized by an apparent reversal of dominant charge region polarity from normal charge structures (NCSs). Historically, ACSs have been rarely indicated within the Southeast and are not documented within the literature. Conceptual models of ACSs more typically observed in the Great Plains hypothesize that ACSs arise as a result of high liquid water content (LWC) in the mixed-phase region of an updraft, facilitated by conditions that increase the efficacy of the updraft in supplying LWC and reduce the efficiency of warm precipitation processes, including via increased aerosols. The lack of ACS observations in the Southeast has been attributed to regional climatic incongruence with these conditions. Total lightning observations, dual-polarization Doppler weather radar data, and environmental model analyses were used to assess the applicability of hypotheses concerning the electrical, microphysical, and kinematic structures of the supercells within which ACSs were observed (i.e., anomalous supercells) in the Southeast. Consistent with ACS conceptual models, dominant positive (negative) charge regions were observed at lower (upper) levels in precipitation ice (ice crystals). However, with the exception of decreased relative humidity, many observed environmental conditions were inconsistent with documented anomalous storms. In

a subsequent study in which the Southeastern anomalous supercells were contrasted with two comparable Southeastern supercells exhibiting NCSs, anomalous supercells had faster, deeper mixed-phase updrafts and contained more precipitation ice. Many environmental conditions associated with LWC did not substantially contrast and all storms exhibited similar metrics of warm precipitation efficiency. Observed lower relative humidity in ACS environments suggested that dry air may have been important to anomalous charging. The evolution and spatial characteristics of lightning properties were contrasted between an anomalous and normal supercell. In the anomalous supercell, both charge polarities were more closely associated with precipitation ice and lightning flashes were more frequently observed in fast updrafts. Lightning flashes were increasingly observed in the updraft of the anomalous supercell as its negative charge region became increasingly collocated with precipitation ice, suggesting a correspondence between charge region microphysics and spatial flash characteristics.

Abstract Approval: Committee Chair



Dr. Lawrence D. Carey

Department Chair



Dr. John R. Mecikalski

Graduate Dean

Yeqing Bao 1/11/2021

Dr. David Berkowitz

ACKNOWLEDGMENTS

I owe thanks to many who have provided support and shaped this research in different ways. I would first like to thank my advisor, Dr. Larry Carey, for innumerable insightful and instructive conversations that guided me through the research process. I am also especially grateful for his invaluable mentorship and time and energy invested in helping me to become a better researcher, communicator, student, instructor, and scientist. I would also like to thank my committee members, Drs. Udaysankar Nair, Kevin Knupp, Ted Mansell, and Dan Cecil for their guidance, instruction, and encouragement during the development and completion of this research as well as detailed feedback that improved the dissertation.

I am grateful to the numerous individuals and teams that collected and managed the radar and lightning data used in this research, including the National Aeronautics and Space Administration (NASA) for use of Lightning Mapping Array instrumentation and data. I thank also the entire Information Technology department at the National Space Science Technology Center and especially Denise Berendes and Ryan Driver for maintaining the necessary resources, software, and connectivity. I am also grateful to Daniela Cornelius and Michele Kennedy for the many ways that they have supported me as a student in the department and college, and especially for their friendship. I would also like to recognize financial support from NASA Severe Storms Research funding (NNH14ZDA001N), provided under contract from the NASA Marshall Space Flight Center (NNM11AA01A).

I would like to thank past and current members of the lightning and radar meteorology research group for reliably helpful research discussions and valuable teamwork. In particular, I also thank Dr. Retha Mecikalski with whom I shared an office. I am grateful

for her constant willingness to help me work through a problem or explore a new idea as well as her encouragement throughout the process. I would like to thank as well many former and current hallway neighbors for enjoyable conversations and their assistance over the years.

Finally, I am grateful for the individuals I have been fortunate to call friends and family. I thank each of my friends for enriching my life and offering support during and apart from graduate school. I would also like to acknowledge my late father who shared my childhood interest in all things weather, never missed an opportunity to engage me in my early math and science education, and through his lasting encouragement, helped guide me toward an academic career that I have thoroughly enjoyed. I thank my family as well for their ceaseless love, enthusiasm for my interests and successes, patience, and encouragement that have sustained me throughout my life and especially over these recent years.

TABLE OF CONTENTS

List of Figures	xiv
List of Tables	xxii
List of Acronyms	xxiii
Chapter	
1 Introduction	1
1.1 Hypotheses and Research Questions	4
1.2 Dissertation Organization	6
2 Observations of Anomalous Charge Structures in Supercell Thunderstorms in the Southeastern United States	8
2.1 Abstract	8
2.2 Introduction	9
2.2.1 Thunderstorm Charge Structures	11
2.2.2 Climatology of Anomalous Charge Structures in the US	13
2.2.3 Hypothesized Factors Contributing to the Development of Anomalous Charge Structures	14
2.2.4 Goals of the Present Analyses	16
2.3 Data and Methods	17
2.3.1 Lightning Data	19
2.3.1.1 Lightning Flash Clustering	20

2.3.1.2	Lightning Flash Polarity Classification	21
2.3.1.3	Charge Structure Determination	23
2.3.2	Radar Data	24
2.3.2.1	Hydrometeor Identification	25
2.3.2.2	Vertical Wind Retrieval	26
2.3.3	Environmental Data	28
2.4	Anomalous Storm Structure	28
2.4.1	10 April 2009 Anomalous Supercell	30
2.4.1.1	Characterization of All Sources	30
2.4.1.2	Characterization of Positive Sources within the Updraft . .	31
2.4.1.3	Characterization of Negative Sources within the Updraft .	33
2.4.1.4	Inferred Net Charge Structure	34
2.4.2	22 April 2017 Anomalous Supercell	35
2.4.2.1	Characterization of All Sources	35
2.4.2.2	Characterization of Positive Sources within the Updraft . .	36
2.4.2.3	Characterization of Negative Sources within the Updraft .	36
2.4.2.4	Inferred Net Charge Structure	38
2.5	Discussion	39
2.5.1	Background Environment	39
2.5.2	Charge Structure Relationships with the Updraft	44
2.5.2.1	Initial Development	45
2.5.2.2	Supercell Maturity	47
2.5.3	Charge Structure Complexities near the Updraft	47
2.5.4	Evidence of Anomalous Tripole	50

2.6	Summary and Conclusions	51
2.7	Acknowledgments and Data Availability Statement	55
3	Examining Conditions Supporting the Development of Anomalous Charge Structures in Supercell Thunderstorms in the Southeastern United States	56
3.1	Abstract	56
3.2	Introduction	57
3.2.1	Thunderstorm Electrification	60
3.2.2	Suggested Controls on Charge Structure Polarity	62
3.2.3	Motivation of the Present Study	65
3.3	Data and Methods Statement	66
3.4	Thunderstorm Properties	69
3.4.1	Charge Structure and Lightning Flashes	71
3.4.2	Kinematics	74
3.4.3	Precipitation Ice Microphysics	76
3.5	Storm Comparisons	80
3.5.1	Updraft Structure	80
3.5.1.1	Updraft Speed	81
3.5.1.2	Updraft Size	84
3.5.2	Mixed-Phase Microphysics	86
3.5.2.1	PIM in the Updraft	86
3.5.2.2	Hydrometeor Contributions	87
3.5.2.3	Updraft PIM Structure	89
3.5.3	Environmental Conditions	90
3.5.3.1	CCN Proxy	90

3.5.3.2	Instability	92
3.5.3.3	Warm Cloud Depth	93
3.5.3.4	Environmental Moisture	94
3.6	Discussion on Contributions to Anomalous Charging	95
3.6.1	Evaluation of Updraft Structure Relative to Charging Hypotheses: Low-Level Updraft	95
3.6.2	Evaluation of Updraft Structure Relative to Charging Hypotheses: Mixed-Phase Updraft	96
3.6.3	Effects of Entrainment	99
3.6.4	Summary of Potential Factors Manifesting Apparent Charge Structure	100
3.7	Conclusions	103
3.8	Acknowledgments and Data Availability Statement	106
4	Microphysical Characteristics of Supercell Thunderstorm Charge Structure and Influences on Spatial Lightning Flash Relationships with the Updraft	108
4.1	Abstract	108
4.2	Introduction	109
4.2.1	Electrification and Charge Structure	111
4.2.2	Kinematic and Microphysical Relationships between Lightning and Convective Structure	112
4.2.3	Supercell Structures	113
4.2.4	Goals of the Present Study	114
4.3	Data and Methods Statement	115
4.4	Anomalous Charge Structure Development	116
4.4.1	Initial Prominent Negative Dipole: 1718 UTC-1724 UTC	117

4.4.2	Multi-Layer Charge Structure: 1730 UTC-1737 UTC	120
4.4.3	Increasing Horizontal Charge Structure Heterogeneity: 1741 UTC-1743 UTC	125
4.5	Lightning Flash Properties Related to Kinematics and Microphysics in the Updraft	128
4.5.1	Vertical Distributions of Lightning Flash Initiations	128
4.5.2	Microphysical Characterization of Lightning Flash Propagation Locations	130
4.5.2.1	Evolution of the Negative Charge Regions	132
4.5.2.2	Elevated Positive Charge Region	135
4.5.3	Kinematic Characterizations of Lightning Flash Initiation Locations	137
4.5.3.1	Updraft Speed	138
4.5.3.2	Horizontal Gradients in Updraft Speed	141
4.6	Discussion on the Presence and Potential Impacts of Positive and Negative Graupel Charging in an ACS	142
4.6.1	Onset and Development of Possible Negative Graupel Charging	143
4.6.2	Observed Charge Structure Complexity in the Updraft	147
4.7	Conclusions	148
4.7.1	Conceptual Model	150
4.7.2	Opportunities for Future Study	153
4.8	Acknowledgments and Data Availability Statement	155
APPENDIX A: Automated Flash-by-Flash Polarity Classification		158
A.1	DBSCAN Cluster Determination	159
A.2	Source Classification	159
A.3	Limitations and Improvements	161

APPENDIX B: Storm Case Summary	164
B.1 Normal 6 February 2008 Case	164
B.2 Normal 11 April 2008 Case	165
B.3 Anomalous 10 April 2009 Case	165
B.4 Anomalous 22 April 2017 Case	166

LIST OF FIGURES

FIGURE		PAGE
2.1	Sampling domain. ARMOR and KHTX (dark blue and dark red diamonds), permanent and supplemental NALMA sensors (green circles and orange crosses) with annotations concerning special operating conditions (black dots and gold dots), the 30° beam-crossing area of the dual-Doppler domain between ARMOR and KHTX (purple rings), and storm tracks (red dashed lines) are shown.	18
2.2	Diagrams of bidirectional lightning flash propagation and detection in the VHF. (a) Bidirectional lightning flash propagation describes the development of a lightning flash which begins at the point of lightning flash initiation (yellow circle) in the strong electric field created by opposite positive and negative charge regions (red and blue ovals). Positive and negative leaders (light red and light blue arrows) first propagate vertically away from the initiation point and then horizontally throughout regions of charge which are opposite the polarity of each leader. (b) VHF source locations plotted in altitude and time as a lightning flash develops (dots colored by time, where earlier colors are cooler and later colors are warmer) show the two-layer structure of a lightning flash, identifying the altitude of each charge region. The denser sources indicate more noisy detection of negative leader propagation through positive charge (red shaded rectangle) apart from sparse sources associated with weaker detection of positive leader propagation through negative charge (blue shaded rectangle) as detected in the VHF.	22

2.3	Time-height cross-sections of lightning, kinematic, and microphysical properties of the anomalous 10 April 2009 supercell. (a) Distribution of all NALMA VHF sources detected during the full analysis period, binned in 1-km vertical and 2-min temporal increments, is shown in color fill along with the mode height at which all sources were observed (black line). Distribution of all (b) positive (c, negative) sources are shown in red (blue) color fill with mode heights of all positive (negative) sources plotted as a black line. Vertical frequency of gridded (d) positive and (e, negative) sources within updrafts $\geq 5 \text{ m s}^{-1}$ or greater are shown in red (blue) color fill along with the mode height of all positive (negative) sources as a black line. (f) The difference between the vertical relative frequency of positive and negative gridded source data is shown where net positive (negative) frequency is plotted as positive (negative) values in red (blue) color fill. (g) The 99th percentile updraft speed is plotted in grayscale with contoured 10 m s^{-1} updraft volumes in red. (h) Distribution of total PIM is shown in grayscale fill. (i) Distribution of total NPIM calculated according to the flux divergence method is shown in grayscale fill. Percentages of PIM associated with (j) hail, (k) HD graupel, and (l) LD graupel are shown in grayscale fill. In each panel, yellow and black marks along the right vertical axis represent the approximate pseudo-adiabatic parcel temperature heights of 0° C through -40° C marked in -10° C increments.	32
2.3	(continued)	33
2.4	As in Figure 2.3 for the anomalous 22 April 2017 supercell.	37
2.5	ARMOR data at 1739 UTC on 10 April 2009 along with NALMA data between 1741 UTC and 1743 UTC. Horizontal cross sections of reflectivity (a, c, e; grayscale fill) and HID (b, d, f; color fill) are shown at 5 km AGL, 11 km AGL, and 12 km AGL altitudes. Vertical cross-sections of reflectivity (g, grayscale fill) and HID (h, color fill) are shown at $y = 81 \text{ km}$ north of ARMOR, the location of which is marked as a black dashed line in the horizontal cross section panels. On each figure, vertical velocity contours in the plane are plotted at positive 5 m s^{-1} , 0 m s^{-1} , and negative 5 m s^{-1} intervals (solid blue, solid white, and dashed blue contours) as well as positive sources (red dots or gray dots), negative sources (blue or black dots), and lightning flash initiation locations (white circles if polarity was classified, green or purple circles if polarity was unclassified) within $\pm 0.5 \text{ km}$ of the plane. 41	41
2.5	(continued)	42
2.6	As in Figure 2.5 on 22 April 2017 with radar data at 2135 UTC and lightning data between 2137 UTC and 2139 UTC. (a-f) Horizontal cross sections are shown at 6 km AGL, 7 km AGL, and 10 km AGL altitudes. (g-h) Vertical cross-sections are shown at $y = 42 \text{ km}$ north of ARMOR.	43

2.7	As in Figure 2.5 on 10 April 2009 with radar data at 1733 UTC and lightning data between 1735 UTC and 1737 UTC. (a-d) Horizontal cross sections are shown at 3 km AGL and 9 km AGL altitudes. (e-f) Vertical cross-sections are shown at $y = 79$ km north of ARMOR.	46
2.8	As in Figure 2.5 on 22 April 2017 with radar data at 2114 UTC and lightning data between 2116 UTC and 2118 UTC. (a-d) Horizontal cross sections are shown at 8 km AGL and 10 km AGL altitudes. (e-f) Vertical cross-sections are shown at $x = 15$ km west of ARMOR.	49
3.1	Domain over which supercells were analyzed. ARMOR and KHTX radar sites (dark blue and dark red diamonds), permanent and supplemental NALMA sensors (green circles and orange crosses) with notes on special operating conditions pertaining to 2008 and 2017 cases (black and gold dots), the 30°C beam-crossing area of the dual-Doppler domain established between ARMOR and KHTX (purple rings), and storm centroid tracks (red and blue dashed lines) are shown. Adapted from Figure 2.1.	69
3.2	The relative difference between the vertical frequency of positive and negative sources located within updrafts of $\geq 5 \text{ m s}^{-1}$ of the (a) anomalous 10 April 2009, (b) anomalous 22 April 2017, (c) normal 11 April 2008, and (d) normal 6 February 2008 supercells. Red (blue) colors indicate that a greater vertical frequency of positive (negative) sources was located in a given layer, where altitude is plotted along the left vertical axis of each panel. Approximate mixed-phase region boundaries of 0°C and -40°C are marked (solid gray lines) with -10°C increments plotted between (dashed gray lines). The lightning flash rate time series associated with each cell (outlined yellow line) is shown as well, corresponding to lightning flash rate values along the right vertical axis of each panel.	72
3.3	Time series of (a) 5 m s^{-1} and (b) 10 m s^{-1} updraft volumes corresponding to the anomalous 10 April 2009 (light red line), anomalous 22 April 2017 (dark red line), normal 6 February 2008 (dark blue line), and normal 11 April 2008 (light blue line) supercells are shown. Composite altitudinal frequency diagrams of vertical velocity in the (c) anomalous 10 April 2009 supercell, (d) anomalous 22 April 2017 supercell, (e) normal 11 April 2008 supercell, and (f) normal 6 February 2008 supercell are shown in colorfill. Approximate mixed-phase region boundaries of 0°C and -40°C are marked (solid black lines) with -10°C increments plotted between (dashed black lines) are shown in (c-f).	77

- 3.4 Time series of (a) total PIM within updraft of $\geq 5 \text{ m s}^{-1}$ corresponding to the anomalous 10 April 2009 (light red line), anomalous 22 April 2017 (dark red line), normal 6 February 2008 (dark blue line), and normal 11 April 2008 (light blue line) supercells are shown. (b) The fractions of PIM within updraft of $\geq 5 \text{ m s}^{-1}$ at each altitude in each storm attributed to LD graupel (yellow), HD graupel (green), and hail or large drops and hail (pink) categories are shown as a stacked bar charts. Composite altitudinal frequency diagrams of PIM within updraft of $\geq 5 \text{ m s}^{-1}$ in the (c) anomalous 10 April 2009 supercell, (d) anomalous 17 April 2017 supercell, (e) normal 11 April 2008 supercell, and (f) normal 6 February 2008 supercell are shown in colorfill. Approximate mixed-phase region boundaries of 0°C and -40°C are marked (solid blue lines) with -10°C increments plotted between (dashed blue lines) are shown in (c-f). 79
- 3.5 Notched boxplots showing (a) the top 25% of maximum positive vertical velocity values observed in each layer and (b) the distribution of the altitudes of the layers in which they were observed relative to the melting level are shown for each of the four cases according to the abscissa labels. The edges of each box depict the 25th and 75th percentiles of the distribution while the center line shows the median. The whiskers are drawn to 1.5 times the interquartile range, while open circles show outliers in the data. The notches, or narrowing, around the median are used to depict its significance. Overlapping notches between boxes indicate that the medians of two distributions are not statistically significantly different. Approximate mixed-phase region boundaries of -40°C relative to the melting level are marked (dashed lines color-coded by storm case). The average 18 dBZ echo top height (closed circles) and cloud base height (open circles) associated with each storm are plotted in (b) as well. 82
- 3.6 Difference plots of the mean 5 m s^{-1} (narrow line) and 10 m s^{-1} (bold line) updraft areas relative to the melting level between the (a) anomalous 10 April 2009 and normal 11 April 2008 storms, (b) anomalous 10 April 2009 and normal 6 February 2008 storms, (c) anomalous 22 April 2017 and normal 11 April 2008 storms, and (d) anomalous 22 April 2017 and normal 6 February 2008 storms. Approximate mixed-phase temperatures of -10°C to -40°C in -10°C increments are marked (dashed lines, where red color corresponds with the anomalous case and blue color corresponds with the normal case). . . . 85
- 3.7 Total aerosol concentration profiles including dust, hydrophilic carbon species, sulphate, and sea salt aerosols thought to contribute to CCN corresponding to the (a) anomalous 22 April 2017, (b) anomalous 10 April 2009, (c) normal 11 April 2008, and (d) normal 6 February 2008 supercells. In each panel, the heights of 0°C through -40°C are marked by the blue lines in -10°C increments. The height of the LCL is marked by a horizontal green line. . . 92
- 3.8 (a) Violin plots showing the distributions of warm cloud updraft speeds in each storm. (b) Violin plots showing the distributions of WCTs in each storm, assuming a particle fall velocity of 2 m s^{-1} 97

4.1	<p>Vertical cross-sections showing supercell precipitation, kinematic, and electrical structure observed in the anomalous 10 April 2009 supercell. (a-b) Radar observations correspond to the 1716 UTC ARMOR sampling volume and lightning observations correspond to the 1718 UTC to 1720 UTC sampling period. An inset panel in (a) of a horizontal cross-section in reflectivity at $z = 2$ km AGL and between $x = 48$ and 18 km west and between $y = 50$ and 80 km north of ARMOR shows the location of vertical cross-sections in (a-b) at $y = 65$ km north of ARMOR as a dashed black line. The vertical cross-sections show (a) reflectivity and (b) HID (color fill according to the color bars along the bottom of the plot) as well as vertical motion in positive 5 m s^{-1}, 0 m s^{-1}, and negative 5 m s^{-1} intervals (solid navy, solid white, and dashed navy contours) in the cross-section plane. Storm relative motion along the plane is also shown with gray wind barbs. Positive (red or gray dots) and negative (blue or black dots) VHF sources associated with lightning flash propagation are shown within ± 0.5 km of the plane. Lightning flash initiation locations within ± 0.5 km of the plane (white circles if lightning flash polarity was classified and purple circles if lightning flash polarity was not classified) are shown on the HID vertical cross-section in panel (b). Lightning flash initiation marker sizes are scaled by flash area. Panels (c-d) are plotted as panels (a-b), showing a vertical cross-section 31 km west of ARMOR at the time of the 1720 UTC radar sample volume along with lightning activity observed between 1722 UTC and 1724 UTC. The horizontal reflectivity cross-section is shown at $z = 2$ km AGL between $x = 45$ and 15 km west and between $y = 53$ and 80 km north of ARMOR.</p>	118
4.1	(continued)	119
4.2	<p>As in Figure 4.1 for the normal 11 April 2008 supercell. Panels (a-b) show observations associated with the 1849 UTC radar sample volume and lightning properties between 1851 UTC and 1853 UTC at a cross-section located 38 km south of ARMOR. The inset shows a horizontal cross-section of the supercell at a height of $z = 2$ km AGL, between $x = 18$ km west and 15 km east of ARMOR and between $y = 48$ km and 27 km south of ARMOR. Panels (c-d) show observations associated with the 1855 UTC radar sample volume and lightning properties between 1857 UTC and 1859 UTC at a cross-section located 5 km east of ARMOR. The inset shows a horizontal cross-section of the supercell at a height of $z = 2$ km AGL, between $x = 11$ km west and 20 km east of ARMOR and between $y = 43$ and 18 km south of ARMOR.</p>	121

4.3	As in Figure 4.1 for the anomalous 10 April 2009 supercell at (a-d) 1728 UTC and (e-f) 1733 UTC. Panels (a-d) show observations associated with the 1728 UTC radar sample volume and lightning properties between 1730 UTC and 1732 UTC with vertical cross-sections located (a-b) 73 km north of ARMOR and (c-d) 19 km west of ARMOR. The inset in panels (a) and (c) show a horizontal cross-section of the supercell at a height of $z = 2$ km AGL, between $x = 35$ and 5 km west of ARMOR, and between $y = 66$ and 86 km north of ARMOR. Panels (e-f) show observations associated with the 1733 UTC radar sample volume and lightning properties between 1735 UTC and 1737 UTC with a vertical cross-section located 76 km north of ARMOR. The inset shows a horizontal cross-section of the supercell at a height of $z = 2$ km AGL, between $x = 30$ and 0 km west of ARMOR and between $y = 70$ and 90 km north of ARMOR.	123
4.3	(continued)	124
4.4	As in Figure 4.1 for the anomalous 10 April 2009 supercell at 1739 UTC. Panels (a-f) show observations associated with the 1739 UTC radar sample volume and lightning properties between 1741 UTC and 1743 UTC with vertical cross-sections located (a-b) 11 km west of ARMOR, (c-d), 80 km north of ARMOR, and (e-f) 82 km north of ARMOR. The inset in panels (a), (c), and (e) show a horizontal cross-section of the supercell at a height of $z = 2$ km AGL, between $x = 22$ km west and 5 km east of ARMOR and between $y = 71$ and 95 km north of ARMOR.	126
4.4	(continued)	127
4.5	Vertical distributions of the initiation location of lightning flashes identified in updraft regions ($w \geq 5 \text{ m s}^{-1}$) of (a) the normal 11 April 2008 supercell and the (b) anomalous 10 April 2009 supercell. Distributions are plotted as relative frequencies of observation in each 1-km vertical bin and segmented, or stacked, according to the proportion that occurred during each lightning analysis period associated with each ARMOR sample volume. The segments are colored according to the five lightning analysis time periods in each storm shown in the lower legends, where cooler (warmer) shades are indicative of earlier (later) analysis periods.	129
4.6	Distributions of lightning source locations with respect to associated hydrometeor type over time and by inferred polarity. Positive source distributions in the (a) normal 11 April 2008 supercell and (b) anomalous 10 April 2009 supercell as well as negative source distributions (c, d, respectively) are shown. Distributions are plotted as relative frequencies that are segmented, or stacked, according to the proportion that occurred during each analysis period and colored as in Figure 4.5.	131

4.7	Distributions of the locations of lightning sources observed in the $\geq 5 \text{ m s}^{-1}$ updraft by hydrometeor type and altitude. Positive and negative source location distributions in cloud ice, graupel, and hail are shown side by side in red and blue color fill, respectively. Color fill shades correspond to values of relative frequency of source distribution as indicated in the corresponding color bars on the right. The cloud ice category consists of the aggregate, ice crystal, and vertically oriented ice HID categories while the graupel category consists of both LD and HD graupel HID categories. (a) As normal 11 April 2008 source distributions did not change appreciably over the analysis period, the average distribution over the full analysis period is shown. (b-f) Distributions of sources in the 10 April 2009 anomalous storm are shown in each of the lightning analysis periods.	133
4.8	As in Figure 4.7 but for sources associated with classified lightning flashes with areas of $\leq 10 \text{ km}^2$ that initiated in vertical motions of $< 5 \text{ m s}^{-1}$ and at or above an altitude of 10 km AGL as well as sources associated with unclassified lightning flashes above 10 km AGL. (a-b) Panels represent source polarity characteristics in the latter two analysis period. As in Figure 4.7, positive and negative source distributions in cloud ice, graupel, and hail are shown side by side in red and blue color fill, respectively, as relative frequency of observation according to the corresponding color bars on the right. (c-d) Distributions of lightning source locations associated with lightning flashes that remained unclassified are plotted as relative frequency of observation in green color fill according to the corresponding color bar on the right.	138
4.9	Distributions of total updraft volume and updraft volume containing lightning initiations. The following distributions are represented as averages for the 11 April 2008 supercell (left) and time series for the 10 April 2009 supercell (right), where each time period is colored as in Figure 4.5. (a, b) Distributions of the volume of updraft characterized by a range of speeds and (c, d) distributions of those volumes in which lightning initiations occurred are shown in the top half of the plot. (e, f) Distributions of the volume of updraft characterized by a range of magnitudes of horizontal gradients in vertical motion and (g, h) distributions of those volumes in which lightning initiations occurred are shown in the bottom half of the plot.	140
4.10	Time series of distributions of (a-e) positive and (f-j) negative source locations by altitude and updraft speed associated with lightning flashes that initiated within updrafts of $\geq 5 \text{ m s}^{-1}$. Color fills represent the relative frequency of observation of positive and negative source according to the red and blue color bars, respectively.	145

4.11	Simplistic conceptual model of the evolution of charge characteristics associated with a developing thunderstorm within which variable NIC regimes in different regions influence charge structure and lightning location. Approximate thermodynamic structure is indicated along the left side of the figure. Open circles (crosses) represent precipitation ice (cloud ice) hydrometeors. Red (blue) coloring represents positive (negative) charge. The location of the 10 m s^{-1} updraft is indicated as a yellow arrow. Possible lightning flash initiation locations are shown as yellow markers, where the relative number of yellow markers is intended to convey changes in lightning flash rate. General locations where net positive and net negative charge regions might be inferred are denoted by light red and light blue boxes, respectively.	151
A.1	Representation of a single flash during DBSCAN classification process in an adapted 5-panel format. (a) Time-height plot of sources mapped in scaled coordinates as DBSCAN points, where DBSCAN-classified cluster core (purple dots), cluster edge (green dots), and noise points (black dots) are shown. Projections of sources with DBSCAN classifications are shown in the (b) vertical and west-east dimensions, (c) west-east and south-north dimensions, and (d) vertical and south-north dimensions. (e) An altitudinal histogram of sources is also provided. (f) Charge structure classification of DBSCAN results are shown, including positive sources (red dots) consistent with negative breakdown in positive charge regions, negative sources (blue dots) consistent with positive breakdown in negative charge regions, and unclassified sources (gray dots).	163
B.1	Progression of the normal 6 February 2008 supercell and its immediate surroundings as observed by ARMOR at the lowest elevation angle. Each panel shows the storm at the lowest elevation angle at the time of a dual-Doppler retrieval. Post-processed, uncorrected ARMOR reflectivity are plotted in color fill.	167
B.2	Reconstructed model sounding for the normal 6 February 2008 case, created using MetPy software (May et al., 2008 - 2020).	168
B.3	As in Figure B.2 for the normal 11 April 2008 case.	169
B.4	As in Figure B.1 for the normal 11 April 2008 supercell.	170
B.5	As in Figure B.1 for the anomalous 10 April 2009 supercell.	171
B.6	As in Figure B.2 for the anomalous 10 April 2009 case.	172
B.7	As in Figure B.2 for the anomalous 22 April 2017 case.	173
B.8	As in Figure B.1 for the anomalous 22 April 2017 supercell.	174

LIST OF TABLES

TABLE	PAGE
1.1 Documentation of the correspondence between chapter number, hypothesis number, and detailed journal manuscript reference.	7
2.1 Anomalous supercell case analysis parameters.	29
2.2 Pre-convective environmental parameters derived from a model analysis sounding in the location of each anomalous supercell an hour prior to its initial observation period. Average proximal PM2.5 data are provided as a regional proxy of estimated CCN concentration on each date.	29
3.1 Normal and anomalous supercell analysis information. Adapted from Table 2.1.	70
3.2 Environmental parameters obtained from a model sounding at the location of each normal and anomalous supercell an hour prior to its analysis period. Note that the height of the LCL and instability metrics of CAPE and NCAPE were derived from surface-based parcels. Adapted from Table 2.2.	70
3.3 Total lightning and CG lightning flash properties associated with each supercell. Total lightning properties, including IC lightning, are reported as observed by the NALMA, whereas CG properties are reported as observed by the NLDN.	75

LIST OF ACRONYMS

ACRONYM	DEFINITION
AGL	Above ground level
ACS	Anomalous charge structure
ARMOR	Advanced Radar for Meteorological and Operational Research
CAPE	Convective available potential energy
CBH	Cloud base height
CCN	Cloud condensation nuclei
CG	Cloud-to-ground
DBSCAN	Density-Based Spatial Clustering of Applications with Noise
GLM	Geostationary Lightning Mapper
HD	High density
HID	Hydrometeor identification
IC	In-cloud
IOP	Intensive observations period
LCL	Lifted condensation level
LD	Low density
LP	Low precipitation

LMA	Lightning Mapping Array
LWC	Liquid water content
ML	Melting level
NALMA	North Alabama Lightning Mapping Array
NASA	National Aeronautics and Space Administration
NCAPE	Normalized convective available potential energy
NCS	Normal charge structure
NIC	Non-inductive charging
NLDN	National Lightning Detection Network
NO _x	Nitrogen oxide
NPIM	Non-precipitation ice mass
PBL	Particle balance level
PIM	Precipitation ice mass
RAP	Rapid Refresh
RH	Relative humidity
ROI	Radius of influence
RUC	Rapid Update Cycle
VHF	Very high frequency
VORTEX-SE	Verification of the Origin of Rotation in Tornadoes EXperiment-Southeast
V _r	Doppler velocity

WCD

Warm cloud depth

WCT

Warm cloud residence time

Page intentionally left blank

CHAPTER 1

INTRODUCTION

Thunderstorm charge structures are often interpreted as storm-scale generalizations of particle-scale charging processes and macro-scale charge organization within the mixed-phase updraft, the characteristics of which are dictated by environmental controls on cloud microphysical and updraft properties. This dissertation addresses the detail in the conceptual models that describe the physical relationships between storm-scale observations, particularly with regard to the composition of and contributions to observed charge structures and spatial relationships between charge structure, the updraft, and lightning flash characteristics.

Charge structures are often described in a basic sense as “normal” or “anomalous,” terms which indicate the polarity and organization of inferred storm-scale charge regions within the mixed-phase updraft (i.e., 0°C to -40°C). Normal charge structures (NCSs) are minimally characterized by a dominant negative charge layer within the middle mixed-phase updraft beneath a positive charge layer (Williams, 1989). Anomalous charge structures (ACSs) instead minimally consist of a dominant positive charge layer in the low to middle mixed-phase updraft beneath a negative charge region (Bruning et al., 2014; Williams et al., 2005).

The dominant charge region observed in either charge structure is primarily associated with the polarity of charge carried on riming precipitation ice (i.e., mainly graupel) following particle-scale charging. In particular, ACSs are thought to occur when the dominant mode of particle-scale charging shifts throughout an extensive depth of the updraft such that riming precipitation ice hydrometeors become positively charged in the net rather than negatively charged as observed under typical conditions (Bruning et al., 2014; Saunders et al., 2006). It is thought that this reversal in particle-scale charging behavior results from an increase in mixed-phase LWC (Saunders et al., 2006; Williams et al., 2005), supported by environmental characteristics that promote a robust updraft capable of transporting more substantial quantities of cloud LWC as well as those that limit warm precipitation processes which deplete LWC before it can reach the mixed-phase region (Carey and Buffalo, 2007; Fuchs and Rutledge, 2018; Williams et al., 2005). Specifically, warm precipitation processes deplete LWC through coalescence. As drops grow, they more effectively sweep out smaller cloud droplets that could have otherwise been advected into the mixed-phase region. Drop sizes and related warm precipitation efficiency may be reduced through higher concentrations of smaller droplets, decreased moisture availability that reduces condensational growth, increased updraft speeds and reduced warm cloud depths which respectively reduce the time and depth over which drops are allowed to grow, as well as increased aerosol concentrations that increase competition for water vapor among drops (Carey and Buffalo, 2007; Rogers and Yau, 1989; Williams et al., 2002, 2005).

The development and organization of charge regions within the updraft impact spatial characteristics of lightning flashes, including where they initiate with respect to the updraft and their areal extent (Dye et al., 1986; Lhermitte and Williams, 1985). Differences in lightning flash location properties between storms exhibiting NCSs and ACSs (i.e.,

normal and anomalous storms) indicate that the polarity of charge structure may impact spatial lightning flash characteristics as well. In storms within which ACSs were observed, lightning flashes more frequently initiated at lower altitudes, in higher reflectivity regions, and nearer to the updraft (Fuchs et al., 2016; Fuchs and Rutledge, 2018). However, the specific roles of charge structure polarity and organization in influencing the location at which lightning flashes occur within the storm and with respect to the updraft are not completely understood.

Observations of ACSs are infrequent, though historically have been most commonly reported in the Great Plains region of the United States (US) (Carey et al., 2003b; Fuchs et al., 2015; Knapp, 1994; Medici et al., 2017). As such, many of the conceptual models associated with ACSs, including their particle-scale origins, the storm-scale organization of their charge regions, and the environmental characteristics that contribute to them, have been developed using observations from the Great Plains. It is thought that their relative rarity in the Eastern US and especially the Southeast is associated with environmental conditions that are more conducive to warm precipitation efficiency and therefore un-supportive of the positive charging of riming precipitation ice hydrometeors necessary for ACS development (Carey et al., 2003b; Fuchs et al., 2018, 2015; Williams et al., 2005).

The research presented herein is concerned with the atypical observations of ACSs in two supercell thunderstorms that occurred in the Southeastern US, particularly as they seemingly pose challenges to the conceptual models by which ACSs are most readily explained. Diagnosis of these charge structures and the conditions under which they developed may add detail to the existing conceptual models of ACS origins. They may also be used to advance understanding of particle-scale charging processes, storm-scale charge structure

characterization, and contributions of charge structure characteristics to the spatial development of lightning flashes with respect to the updraft.

1.1 Hypotheses and Research Questions

Chapters of the dissertation expound upon the aforementioned physical processes and connections while addressing the following hypotheses and related research questions:

1. The unusual observation of ACSs in Southeastern thunderstorms suggest that either (a) the environmental conditions in which the two observed storms formed were atypical for the Southeast but consistent with those observed in regions where anomalous storms are more common, (b) the range of environmental characteristics supportive of ACSs is broader than previously thought based on observations in the Great Plains, and/or (c) Southeastern ACSs are generally inconsistent with conceptual models of ACSs. Related research questions include:
 - (a) What are the thermodynamic and microphysical characteristics of storm-scale charge regions observed in the updrafts of the observed anomalous supercells? That is, is the positive charge region observed in the lower mixed-phase region collocated with riming precipitation ice hydrometeors (including graupel and dry hail), and the negative charge region observed above the dominant positive charge region collocated with non-riming ice hydrometeors (including ice crystals and aggregates)?
 - (b) Are kinematic and microphysical characteristics similar between Southeastern anomalous thunderstorm structures and those documented in the literature?

- (c) How do the pre-convective environmental characteristics associated with the observed Southeastern ACSs compare with those observed in other regions that are documented in the literature? Specifically, how comparable are the conditions that are expected to limit the efficiency of warm precipitation processes and promote enhanced mixed-phase LWC?
2. It is expected that environmental conditions and some aspects of storm structure would contrast between anomalous and normal supercells in the Southeast. If environmental conditions associated with ACSs in other regions were similarly influential in Southeastern anomalous storms, it is expected that the environmental conditions observed in Southeastern anomalous supercells would have favored relatively reduced warm precipitation efficiency compared with Southeastern normal supercell environments. Additionally, Southeastern anomalous storm updrafts may have been larger and stronger and their precipitation ice contents may have reflected comparative increases in riming efficiency and/or total riming consistent with increased LWC. Related research questions include:
- (a) Are environmental conditions different between normal and anomalous supercells in the Southeast? Are contrasts comparable with those typically observed to differentiate anomalous from normal storms in other regions?
 - (b) How do the sizes and speeds of updrafts compare between anomalous and normal supercells?
 - (c) How do riming precipitation ice properties, including quantity and composition, vary between anomalous and normal supercells?

3. If charge region polarity in anomalous storms were simply reversed from normal charge structures, it is expected that lightning flash initiations and charge regions would be observed in similar locations with respect to precipitation and updraft structure. Variations in lightning flash initiation location relationships with the updraft are expected to arise as a result of changes in the characteristics of dominant charge regions that may be associated with variability in particle-scale charging. Related research questions include:
 - (a) How do the spatial relationships between lightning flash initiations and the updraft compare between the anomalous and normal supercells?
 - (b) How do the microphysical characteristics of charge regions evolve during the development of an ACS?
 - (c) How do spatial relationships between lightning flash initiations and the updraft evolve? How do changes in lightning flash initiation location relationships relate to changes in anomalous charge region characteristics?

1.2 Dissertation Organization

These hypotheses and related research questions are each addressed in individual chapters, where Chapter 2 is considered foundational and each subsequent chapter (Chapters 3 and 4) follows from the prior chapter. Each of the chapters was prepared as a stand-alone manuscript intended for submission to a peer-reviewed journal. As such, each is self-contained and includes its own abstract, introduction and motivation statement, background, presentation and discussion of relevant data analyses, concluding remarks, suggestions for future work, data availability statement, and funding source acknowledgment. When converting the prepared manuscripts into dissertation chapters, minor changes

Table 1.1: Documentation of the correspondence between chapter number, hypothesis number, and detailed journal manuscript reference.

Chapter	Hypothesis	Journal Manuscript Reference
2	1	Stough, S. M., and L. D. Carey, 2020: Observations of anomalous charge structures in supercell thunderstorms in the Southeastern United States. <i>Journal of Geophysical Research: Atmospheres</i> , 125 (17), e2020JD033012, doi: 10.1029/2020JD033012.
3	2	Stough, S. M., L. D. Carey, C. J. Schultz, and D. J. Cecil, 2020a: Examining conditions supporting the development of anomalous charge structures in supercell thunderstorms in the Southeastern United States. <i>Journal of Geophysical Research: Atmospheres</i> , In preparation.
4	3	Stough, S. M., L. D. Carey, C. J. Schultz, and D. J. Cecil, 2020b: Microphysical characteristics of supercell thunderstorm charge structure and influences on spatial lightning flash relationships with the updraft. <i>Monthly Weather Review</i> , In preparation.

were made to reduce redundancies. As similar instrumentation, data, processing techniques, and analysis methods were utilized in each chapter, full descriptions are provided only once in Chapter 2. Chapters 3 and 4 each include brief documentation of any changes in or additions to the data and methods that were first presented in Chapter 2. In addition, Appendix A, following Chapter 4, details the implementation of a novel automated lightning flash-by-lightning flash polarity classification technique developed for the purposes of this study that is introduced in Chapter 2 and utilized in Chapters 2, 3 and 4. Appendix B next includes a synopsis of the background meso- α environment as well as the progression of each of the storm cases discussed. Finally, a single reference section combining references used in all chapters is provided at the end of the dissertation. Each chapter is listed in Table 1.1 along with indications of the hypotheses it addresses and detailed journal manuscript reference.

CHAPTER 2

OBSERVATIONS OF ANOMALOUS CHARGE STRUCTURES IN SUPERCCELL THUNDERSTORMS IN THE SOUTHEASTERN UNITED STATES

2.1 Abstract

Anomalous thunderstorm charge structures, characterized by a dominant layer of positive charge in the lower mixed-phase region, are uncommon and rarely reported outside of the Great Plains region of the US. The kinematics, precipitation microphysics, and charge structures of two supercell thunderstorms exhibiting ACSs that were observed in the Southeastern US are documented. Ground-based three-dimensional total lightning observations, polarimetric Doppler radar observations, and environmental model analysis of these supercells presented the opportunity to evaluate conceptual models of ACS development and characteristics in an atypical parameter space. In both anomalous storms, prominent layers of positive charge were located in lower to middle mixed-phase regions (-10°C to -30°C , corresponding to the range between approximately 5.5 km to 6.0 km and approximately 8.5 km to 9.0 km) of updrafts and were spatially associated with riming hydrometeor types. Simultaneously, negative charge regions were inferred above the primary positive charge layers in the upper mixed-phase and glaciated region of updrafts, collocated with graupel and small ice hydrometeors. While coarse inferred charge structures were consistent with

non-inductive charging-based models of anomalous storms, charge structure complexities were also observed that suggested variability in cloud microphysical conditions. Analysis of the environments in which these storms formed indicated that several parameters thought to increase mixed-phase liquid water content in favor of anomalous charging were inconsistent with those documented in the Great Plains region. However, environmental humidity metrics were most comparable. Comparisons between these and other documented anomalous storms identified similarities in kinematic structure and microphysical conditions while motivating ongoing study of the environmental parameter space supportive of ACSs.

2.2 Introduction

Though observed thunderstorm charge structures are often varied and complex, most are characterized by a dominant layer of negative charge located in the -10°C to -30°C region within the thunderstorm updraft (e.g., Stolzenburg et al., 1998). By contrast with these NCSs (Williams, 1989), ACSs are characterized by a dominant layer of positive charge thought to occur as a result of atypical particle-scale charging conditions (e.g., Bruning et al., 2014; Fierro et al., 2006; Kuhlman et al., 2006; MacGorman et al., 2005; Mansell et al., 2002; Rust et al., 2005; Williams et al., 2005). As discussed herein, ACSs are also referred to as “inverted” in the literature, terminology addressed and clarified by Bruning et al. (2014). Within the continental US, ACSs have been documented most often in the Great Plains region and are consequently attributed to a specific range of environmental conditions thought to be favored by the regional climate, including elevated cloud base heights (CBHs), increased instability, and reduced mid-level relative humidity (RH) (e.g., Carey and Buffalo, 2007; Carey et al., 2003b; Fuchs et al., 2015; Williams et al., 2005). While conditions supporting ACSs may theoretically manifest in any locale allowing deep

convection, large sample studies have repeatedly identified their relative scarcity in contrasting regions such as the Southeastern US (e.g., Carey and Buffalo, 2007; Carey et al., 2003b; Fuchs et al., 2015; Medici et al., 2017). Observations of two Southeastern supercells possessing ACSs (hereafter referred to as “anomalous supercells” or “anomalous storms”) present the opportunity to characterize the nature of these electrically exceptional storms in an atypical setting. Comparisons between these supercells and those documented in the Great Plains region allow for a more robust evaluation of the conditions presumed favorable to the development of ACSs.

Beyond advancing understanding of the physical origins of charge structure, the development of ACS characterization carries implications for remote sensing and nowcasting of thunderstorms. Lightning data are increasingly utilized for severe storm nowcasting because of intrinsic relationships between lightning, thunderstorm intensity, and production of high-impact convective phenomena (e.g., Carey et al., 2019; Deierling and Petersen, 2008; Lang and Rutledge, 2002; MacGorman et al., 1989; Reap and MacGorman, 1989; Schultz et al., 2017, 2015, 2011; Stough et al., 2017; Williams et al., 1999). Anomalous storms are often associated with increased severe weather production, including increased quantities of and/or larger severe hail (e.g., Branick and Doswell III, 1992; Carey and Rutledge, 1998; Curran and Rust, 1992; Gilmore and Wicker, 2002; Lang and Rutledge, 2002; MacGorman and Burgess, 1994; MacGorman and Nielsen, 1991; Reap and MacGorman, 1989; Seimon, 1993; Stolzenburg, 1994). However, it has been shown that lightning initiates at lower altitudes in anomalous storms, potentially impacting detectability from spaceborne optical detection platforms (Fuchs and Rutledge, 2018; Murphy and Said, 2020). Awareness of the characteristics of these storms and their detectability is vital to their correct interpretation

in the context of severe weather nowcasting, as is understanding the range of circumstances under which they may develop.

2.2.1 Thunderstorm Charge Structures

Thunderstorm charge structures arise from storm-scale separation of positive and negative charge regions following particle-scale charge separation (e.g., Williams, 1985). Ice-ice collisional non-inductive charging (NIC) is thought to be the primary mechanism of particle-scale charge separation (Jayaratne et al., 1983; Reynolds et al., 1957; Saunders et al., 2006; Takahashi, 1978), during which, rebounding collisions between riming, precipitation-sized ice and non-riming (small) ice result in the transfer of charge. The magnitude and polarity of particle-scale charge transfer have been found to be affected in part by the size and velocity of participating particles, the rate of riming and associated effective liquid water content (LWC), as well as cloud and particle temperatures (Avila and Pereyra, 2000; Emersic and Saunders, 2010; Jayaratne et al., 1983; Saunders et al., 2006; Saunders and Peck, 1998). Results from laboratory studies indicate that graupel (ice crystals) typically charge negatively (positively) during ice-ice collisional NIC (Berdeklis and List, 2001; Jayaratne et al., 1983; Saunders et al., 2006; Takahashi, 1978). However, graupel (ice crystals) instead charge positively (negatively) when LWC is increased as well as at temperatures warmer than $-10\text{ }^{\circ}\text{C}$ as a result of increased riming efficiency (Berdeklis and List, 2001; Jayaratne et al., 1983; Saunders et al., 2006; Saunders and Peck, 1998; Takahashi, 1978). Analytical models and limited results from laboratory studies have suggested that supersaturation may play an additional role in the polarity of particles charging by ice-ice collisional NIC (Emersic and Saunders, 2020; Mitzeva et al., 2005; Saunders et al., 2006; Tsenova et al., 2010). Once particle-scale charging has taken place, differential gravitational sedimentation

and advection of charged particles by kinematic processes at the storm to turbulent scales result in accumulated charged hydrometeors and net charge regions (e.g., Bruning and MacGorman, 2013; Lhermitte and Williams, 1985; Williams, 1985).

Thunderstorm charge structure classification is typically based on the primary charge layers identified near the updraft where most particle-scale charge transfer occurs and initial cloud-scale charge separation takes place (e.g., Bruning et al., 2010). In the simplified model of a normal storm, negatively charged riming ice (i.e., graupel or dry hail) separates from positively charged cloud ice particles by differential sedimentation, establishing the main negative and upper positive charge regions in the mixed-phase updraft. The lower positive charge region in the updraft in a normal tripole results from similar differential sedimentation of positively charged graupel at warm temperatures, while negatively charged cloud ice arising from these collisions is advected upward into the main negative charge region. It should be noted as well that while inductive charging, or charging in the presence of established electric fields, is not an initial primary electrification mechanism, it may also contribute to negatively charged droplets within the main negative charge region (e.g., Helsdon et al., 2002; Mansell et al., 2005).

Enhanced LWC in the mixed-phase updraft is thought to facilitate a deeper layer of more efficient riming growth. By the ice-ice collisional NIC theory, enhanced positive charging of riming ice hydrometeors extends the depth over which positive charge is observed, resulting in either a lower positive charge region that is larger than normal or a dominant mid-level positive charge layer in anomalous storms (e.g., Bruning et al., 2014; Carey and Buffalo, 2007; Fierro et al., 2006; Kuhlman et al., 2006; MacGorman and Burgess, 1994; MacGorman et al., 2005; Qie et al., 2005; Saunders et al., 2006; Tessendorf et al., 2007a,b; Wiens et al., 2005; Williams, 2001). The negative charge layer located above the dominant

positive charge region then includes small ice that charged negatively during ice-ice collisional NIC. While a lower negative charge layer is also occasionally observed in an anomalous tripole, it cannot be explained by ice-ice collisional NIC in a simple one-dimensional framework because the temperatures in this region do not support negative NIC of riming hydrometeors (Bruning et al., 2014; Saunders et al., 2006). It has been suggested that the lower negative charge region results instead from advection and sedimentation of negatively charged graupel from a region of the updraft with lower LWC, inductive charging, and/or charge deposited by lightning channels (Brothers et al., 2018; Bruning et al., 2014; Kuhlman et al., 2006; Mansell et al., 2005; Wiens et al., 2005).

2.2.2 Climatology of Anomalous Charge Structures in the US

The historical context of thunderstorm polarity and its climatology was derived from early studies utilizing cloud-to-ground (CG) lightning data in the absence of widespread availability of total lightning data including both CG and in-cloud (IC) lightning flashes. Thunderstorms with a large fraction of positive CG lightning flashes can be considered as proxies for anomalous storms. A deep positive charge layer in the lower mixed-phase region consistent with ACSs is suggested as one of the principal conditions that supports a high fraction of positive CG lightning flashes (e.g., Carey and Buffalo, 2007; MacGorman and Burgess, 1994; Rust and MacGorman, 2002; Williams et al., 2005; Williams and Stanfill, 2002), along with a minor region of lower negative charge (e.g., Mansell et al., 2002; Wiens et al., 2005).

Climatology studies have offered repeated evidence of a relative scarcity of ACSs in the Southeastern US. Early studies examining CG polarity over a large portion of the US found that tornadic storms with primarily positive CG lightning flashes were identified only

in the Midwest and Great Plains (Knapp, 1994) as well as that only 2% of severe storms with primarily positive CG lightning flashes were identified in the Eastern US compared with 48% in the Northern Plains (Carey et al., 2003b). Broader CG climatologies identified greater positive CG percentage in the Great Plains and upper Midwest compared with the Eastern US as well (e.g., Medici et al., 2017; Rudlosky and Fuelberg, 2010), with an 8.5% higher positive CG percent in the Great Plains overall compared with the South Central and Southeastern US (Medici et al., 2017). A subsequent large-scale total lightning-based study examining the climatology of ACSs identified similar results, where no anomalous storms were identified in either the North Alabama (AL) or Washington DC areas in the period of study (Fuchs et al., 2015).

2.2.3 Hypothesized Factors Contributing to the Development of Anomalous Charge Structures

Studies have examined the characteristics of and environmental settings for storms exhibiting primarily positive CG lightning flashes or explicit ACSs. These storms were often characterized in early observations as having robust updrafts (e.g., Branick and Doswell III, 1992; Curran and Rust, 1992; MacGorman and Burgess, 1994; Seimon, 1993) and/or low precipitation (LP) supercell structure (e.g., Carey et al., 2003a; Carey and Rutledge, 1998; Gilmore and Wicker, 2002; Lang and Rutledge, 2002; Smith et al., 2000). Studies of near-storm environmental conditions have been consistent with and added specificity to these structural observations, frequently identifying greater metrics of instability (Carey and Buffalo, 2007; Chmielewski et al., 2018; Fuchs et al., 2015; Gilmore and Wicker, 2002; Lang and Rutledge, 2006; Seimon, 1993), drier low- to mid-level air (Bluestein and MacGorman, 1998; Carey and Buffalo, 2007; Chmielewski et al., 2018; Seimon, 1993), decreased

melting level heights and/or increased lifted condensation levels (LCLs) resulting in more shallow warm cloud depths (WCDs) (Carey and Buffalo, 2007; Fuchs et al., 2018, 2015; Lang and Rutledge, 2006), and in some instances, increased aerosol concentrations or proximity to smoke (Fuchs et al., 2015; Lang and Rutledge, 2006; Logan, 2018; Lyons et al., 1998). Though exceptions to the aforementioned environmental relationships have been identified, including anomalous storms sometimes characterized by deeper WCDs (Chmielewski et al., 2018; Lang and Rutledge, 2011), less instability (Fuchs et al., 2018), and greater mid-level RH (Fuchs et al., 2018) compared with their normal counterparts, it has been suggested that the extent to which a complex mixture of environmental components impacts charge structure can vary such that some mechanisms may be more dominant in different circumstances (Carey and Buffalo, 2007; Carey et al., 2003b; Chmielewski et al., 2018; Fuchs et al., 2015; Williams et al., 2005).

The aforementioned environmental conditions are related to processes that promote increased mixed-phase LWC. Modeling studies and indirect observations suggest that increased mixed-phase LWC enhances riming processes and supports increased positive charging of riming hydrometeors required for the development of ACSs (e.g., Kuhlman et al., 2006; Mansell et al., 2005), though direct observations of LWC in deep convection with mature updrafts are difficult to obtain for validation. Reduction in the growth of warm rain is suggested to preserve the amount of cloud LWC available to the mixed-phase region for ice growth processes (e.g., Carey and Buffalo, 2007; Fuchs et al., 2015; Lang and Rutledge, 2011; MacGorman et al., 2008; Williams et al., 2005), as well as reduce the effects of drag of water loading on the updraft. Shallow WCDs and higher CBHs are suggested to reduce the depth over which mixing and entrainment inhibit buoyancy and limit the updraft (Carey and Buffalo, 2007; Williams et al., 2005) and warm rain processes deplete LWC (Carey and Buffalo,

2007; Fuchs et al., 2016, 2018). Large, fast updrafts are suggested to transport larger LWC quantities, limit entrainment, and shorten the time over which rain growth processes reduce cloud water (Carey and Buffalo, 2007; Fuchs et al., 2016, 2018). To similar effect, reduction in drop size through increased aerosol concentration and cloud condensation nuclei (CCN) decreases the efficiency of warm rain growth processes (Chmielewski et al., 2018; Mansell and Ziegler, 2013; Tao et al., 2012; Williams et al., 2002). Smaller cloud drops may also promote positive charging of riming hydrometeors (Avila and Pereyra, 2000).

2.2.4 Goals of the Present Analyses

At present, existing case studies of anomalous charge structures utilizing detailed observations and total lightning data have only considered storms in the Great Plains or Midwest regions (e.g., Bruning et al., 2010; Chmielewski et al., 2018; DiGangi et al., 2016; Fuchs et al., 2018; Lang et al., 2004; MacGorman et al., 2011, 2008; Rust and MacGorman, 2002; Rust et al., 2005; Tessendorf et al., 2007a,b; Wiens et al., 2005). Existing exemplary case studies have contrasted microphysical and kinematic structures and environmental characteristics in Colorado (CO) anomalous and AL normal storms (Bruning et al., 2014; Fuchs et al., 2018). However, anomalous storms in the Southeastern US have not been identified or described.

Since their existence is unexpected based on prior results and their storm and environmental properties are largely unknown, the first detailed lightning and radar observations of two anomalous supercell thunderstorms documented in the Southeastern US are introduced herein. Active charge regions, precipitation microphysics, and the kinematic structure of these storms are first analyzed, building upon and diversifying detailed diagnoses of ACSs in the literature. An automated technique used to classify charge structure

is also introduced as an alternative method to traditional manual charge structure analysis, providing the potential for more widespread future detailed charge structure diagnoses. Southeastern anomalous storms challenge existing hypotheses concerning ACS development, particularly with regard to LWC requirements. Structural and environmental characteristics of the two Southeastern anomalous supercells are compared with others documented in the literature to assess their consistency with current NIC-based conceptual models of ACS characteristics. Observations of these outlier thunderstorms in the Southeastern US and their comparisons with other anomalous storms prompt discussion of additional potential pathways to anomalous charging.

2.3 Data and Methods

The two anomalous supercells discussed herein were sampled during local research operations on 10 April 2009 and as part of the Verification of the Origins of Rotation in Supercells EXperiment - SouthEast (VORTEX-SE; Rasmussen, 2015) and the Geostationary Operational Experiment Satellite - Series R Post Launch Test (GOES-R PLT; Padula et al., 2017) Intensive Observations Periods (IOPs) on 22 April 2017 in Northern AL and Southern Tennessee (TN). In each case, total lightning data from the North Alabama Lightning Mapping Array (NALMA; Blakeslee, 2019; Carey and Blakeslee, 2020a; Koshak et al., 2004; Rison et al., 1999), the polarimetric C-band Advanced Radar for Meteorological and Operational Research (ARMOR; Carey and Blakeslee, 2020a; Carey and Knupp, 2017; Mecikalski et al., 2015), and the S-band operational Weather Surveillance Radar - 1988 Doppler (WSR-88D; Crum and Alberty, 1993; Doviak et al., 2000; NOAA National Weather Service (NWS) Radar Operations Center, 1991) KHTX were utilized. The sampling domain and instrument network configurations are mapped in Figure 2.1.

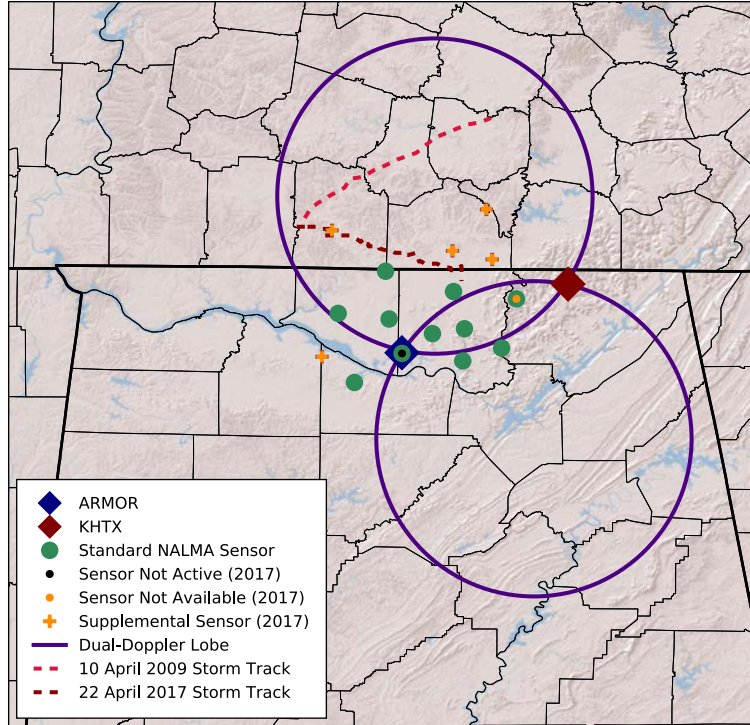


Figure 2.1: Sampling domain. ARMOR and KHTX (dark blue and dark red diamonds), permanent and supplemental NALMA sensors (green circles and orange crosses) with annotations concerning special operating conditions (black dots and gold dots), the 30° beam-crossing area of the dual-Doppler domain between ARMOR and KHTX (purple rings), and storm tracks (red dashed lines) are shown.

Supplemental environmental data were also assessed for each storm. The storms of interest were often located at considerable distances from the nearest National Weather Service Radiosonde sites and occurred over periods that did not overlap with the operational launch times. Additionally, sounding launches that occurred as part of VORTEX-SE IOPs did not overlap spatially with the 2017 storm. Hourly 13-km model analysis data from the Rapid Update Cycle (Benjamin et al., 2004) and the Rapid Refresh (Benjamin et al., 2006) were used for the 2009 case and 2017 case, respectively, to assess the pre-convective environment. The concentration of CCN constitutes an additional component of the environment that may influence the charge structure of a storm. Hourly total aerosol PM_{2.5}

data were used as a loose proxy for CCN quantities on each of the case days (Centers for Disease Control and Prevention, 2019). Concentrations of PM_{2.5} were detected using a federal reference method monitor in Morgan County, AL on 10 April 2009 and in Jefferson County, AL and Hamilton County, TN on 22 April 2017.

2.3.1 Lightning Data

Total lightning data were obtained from the NALMA. Under normal operating conditions as on 10 April 2009, the network consists of between 10 and 12 sensors distributed throughout Northern AL and Southern TN at fixed sites. During the spring of 2017, the standard array was temporarily supplemented with four additional sensors, shown in Figure 2.1. LMA sensors detect and record the time and magnitude of peak emission of very high frequency (VHF) radiation from lightning propagation in 80 μ s intervals. These VHF point detections are referred to as sources, the three-dimensional locations of which are identified using a time of arrival technique (Thomas et al., 2004). A minimum of six sensors is traditionally utilized to determine the location of sources to increase the accuracy of detection and reduce the probability that noise will be classified as lightning emission (Rison et al., 1999). To mitigate inclusion of noise associated with an increase in network sensitivity as a result of additional sensors, a seven-station minimum was instead employed with 22 April 2017 data while the typical six-station minimum was used with 10 April 2009 data.

Source location accuracy is greatest within the perimeter of the LMA sensor network with errors of 50 m or less (Koshak et al., 2004; Thomas et al., 2004). Beyond the network perimeter, location errors increase with the square of the range from the center of the network (Thomas et al., 2004). Simulations using the standard NALMA configuration have

shown that with 10-receiver source identification and no noise, horizontal (vertical) source location errors are typically less than 500 m (1000 m) within a range of 100 km of the network center (Koshak et al., 2004).

Source detection efficiency also decreases with range from the center of the LMA network and low-altitude sources at distant ranges are also not well detected because of line of sight limitations (e.g., Boccippio et al., 2001; Carey et al., 2005; Chmielewski and Bruning, 2016; Fuchs et al., 2016; Thomas et al., 2001). Source location accuracy and detection efficiency impact lightning flash detection as well, though effects are more gradual with range. For instance, while source density relaxes to half the maximum value at a range of 50 km from the network center, lightning flash density does so at a range of 125 km from the network center (Fuchs et al., 2016). Simulations with a 12-sensor LMA network configuration showed that lightning flash detection efficiency decreased from 100% at the LMA network center to 96% at a 100 km range of the network center and to 89% at a range of 150 km from the network center (Chmielewski and Bruning, 2016). If fewer stations are utilized, these reported decreases could occur at closer ranges.

Storms remained within 125 km of the network center for the duration of their analyses, wherein the reported source location accuracies and detection efficiencies are considered reasonable.

2.3.1.1 Lightning Flash Clustering

Thunderstorm charge structure analysis proceeds from aggregated sources whose polarities were classified in individual lightning flashes. Lightning flash identification therefore serves as the initial component of identifying active charge regions. The temporal and spatial information of source data were used to identify clusters considered as individ-

ual lightning flashes via the Density-Based Spatial Clustering of Applications with Noise (DBSCAN; Ester, M. et al., 1996) algorithm implemented in the lmatools Python package (Fuchs et al., 2016, 2015). Briefly, the three-dimensional locations and time of each source detection were standardized by 3.0 km and 0.3 s, scaling factors found to correspond with the spatial and temporal nature of lightning flash propagation characteristics upon examination of individual lightning flashes (Fuchs et al., 2016, 2015). These standardized spatiotemporal locations were grouped using a machine-learning approach that assessed their density (Ester, M. et al., 1996; Fuchs et al., 2016). To be considered for lightning flash clustering, each source must have had a maximum reduced chi-square value of 1.0 and have been detected by a minimum of six or seven sensors, depending on the storm case

2.3.1.2 Lightning Flash Polarity Classification

As illustrated in Figure 2.2a, positive and negative lightning flash leaders propagate bidirectionally away from the initiation location of a lightning flash, each spreading into horizontally-oriented regions of large electric potential in net charge regions of the opposite polarity (Bruning and MacGorman, 2013; Coleman et al., 2003; MacGorman et al., 1981; Mazur and Ruhnke, 1993; Thomas et al., 2001; Williams, 1985). Total lightning data from LMAs are useful for thunderstorm polarity assessment because of the nature of lightning propagation in the VHF. Negative breakdown associated with propagation of the negative leader in positive charge regions occurs more noisily and produces more power than positive breakdown associated with propagation of the positive leader in negative charge regions (Maggio et al., 2005; Rison et al., 1999; Rust et al., 2005; Shao and Krehbiel, 1996; Thomas et al., 2001). As a result, positive charge regions are more readily detected using LMA

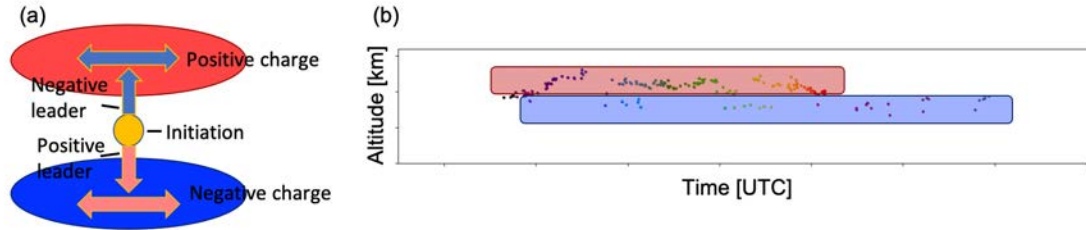


Figure 2.2: Diagrams of bidirectional lightning flash propagation and detection in the VHF. (a) Bidirectional lightning flash propagation describes the development of a lightning flash which begins at the point of lightning flash initiation (yellow circle) in the strong electric field created by opposite positive and negative charge regions (red and blue ovals). Positive and negative leaders (light red and light blue arrows) first propagate vertically away from the initiation point and then horizontally throughout regions of charge which are opposite the polarity of each leader. (b) VHF source locations plotted in altitude and time as a lightning flash develops (dots colored by time, where earlier colors are cooler and later colors are warmer) show the two-layer structure of a lightning flash, identifying the altitude of each charge region. The denser sources indicate more noisy detection of negative leader propagation through positive charge (red shaded rectangle) apart from sparse sources associated with weaker detection of positive leader propagation through negative charge (blue shaded rectangle) as detected in the VHF.

data. An example of a lightning flash detected by the NALMA and variations in detection of positive and negative breakdown are shown in Figure 2.2b.

Traditionally, thunderstorm polarity inferences have been made using vertical source distributions (e.g., Fuchs et al., 2016; Fuchs and Rutledge, 2018; Fuchs et al., 2018, 2015; Lang and Rutledge, 2011) or aggregated lightning flash-by-lightning flash source polarity analysis (e.g., Bruning et al., 2007; Chmielewski et al., 2018; Lang et al., 2004; Rust et al., 2005; Tessendorf et al., 2007a,b; Wiens et al., 2005), each method utilizing the noisier properties of lightning propagation in positive charge regions. While vertical source distributions can be used to infer gross charge structure, lightning flash-by-lightning flash methods allow more detailed examination in complex structure, including features such as shallow charge

layers and horizontal heterogeneity. It should be noted that all LMA-based methods of polarity classification only include charge regions that participate in lightning flashes and do not capture smaller or weaker regions of charge accumulation such as screening layers (Coleman et al., 2003).

Manual subjective lightning flash-by-lightning flash analysis can be time intensive, particularly over long durations and in storms with high lightning flash rates. Automated lightning flash-by-lightning flash techniques that leverage the properties of VHF lightning detection alongside the model of bidirectional lightning flash development and propagation allow for analysis of larger quantities of data (e.g., Tessendorf et al., 2007a). The clustering capabilities of the DBSCAN algorithm can be used to classify the polarity of source data in individual lightning flashes, leveraging the greater density of higher power emission of negative breakdown for identification of positive charge regions apart from weaker, more temporally sparse emissions of positive breakdown in a spatially distinct negative charge region. Density-based identification of negative breakdown is resistant to errors that may arise when the conditions of lightning flash propagation present challenges to the assumptions of lightning flash development such as in vertically slanted charge regions or when the lightning flashes themselves are erroneously identified. A new method developed to classify breakdown polarity using DBSCAN is discussed in further detail in Appendix A.

2.3.1.3 Charge Structure Determination

Classified source data were aggregated to map active net charge regions. Sources identified as associated with negative breakdown in positive charge regions are referred to as positive sources while sources identified as consistent with positive breakdown in negative charge regions are referred to as negative sources for simplicity. During each

sampling period, classified source data were gridded to match radar analysis grids. As radar volume scans occurred over an approximate four- to five-minute period, the mixed-phase region of a storm was not sampled until approximately two to three minutes after the radar volume start time. To best match lightning information with radar measurements of the mixed-phase region, lightning data from a 2-minute period beginning two minutes after the earliest volume start time of a matched radar pair used for vertical wind retrieval were used. Thunderstorm charge structure classification was determined using positive and negative sources within regions of vertical motion of $\geq 5 \text{ m s}^{-1}$. Gridded source data in these regions were recast in terms of relative vertical distribution with respect to the total positive or negative sources detected at each sampling period instead of considering raw source quantities in order to mitigate the effects of relative source detection associated with positive and negative breakdown in the VHF. Vertical distributions of positive and negative source grids were subsequently compared to assess distinct net charge layer polarity.

2.3.2 Radar Data

Data from ARMOR in RAW format were post-processed as outlined in Mecikalski et al. (2015) to correct for attenuation and differential attenuation as well as to compute specific differential phase according to the methods described by Bringi et al. (2001). All ARMOR data were manually quality controlled using the National Center for Atmospheric Research solo3 software (Oye et al., 1995) to remove artifacts such as second trip echo, three-body scatter, and ground clutter and to correct for sector shift. Additionally, ARMOR and KHTX Doppler velocity (V_r) data were dealiased using the University of Washington 4DD algorithm (James and Houze, 2001) implemented in the Python Atmospheric Radiation Measurement Radar Toolkit (Py-ART; Helmus and Collis, 2016) with subsequent manual

correction as needed using solo3 software. Additional information on radar operation, data, and data quality issues can be obtained in Rauber and Nesbitt (2018).

Prior to analysis, radar data were gridded using Py-ART to a common Cartesian coordinate system centered on the ARMOR location with three-dimensional 1-km grid spacing according to a Cressman weighting scheme. The radius of influence (ROI) used expanded by 0.025 m in the horizontal and 0.04 m in the vertical for every meter increase in horizontal and vertical distance, respectively, from the nearest radar, with a minimum ROI of 870 m.

2.3.2.1 Hydrometeor Identification

Analysis of precipitation microphysics is augmented by information from dual-polarization radar data. Dual-polarization data were only available from ARMOR in 2009. For consistency, all derived quantities dependent upon dual-polarization variables in each case were computed only using ARMOR data. For the 2017 case, comparisons of derived polarimetric products such as hydrometeor identification (HID) from KHTX and the ARMOR found no significant differences that would impact the interpretations of analyses or core results. A similar conclusion was reached by Mecikalski et al. (2015).

Regions of riming and small ice hydrometeors are of particular interest in assessing the microphysical characteristics of charge structure. The most likely hydrometeor type within each grid volume was determined from a fuzzy-logic based HID algorithm (Dolan and Rutledge, 2009; Dolan et al., 2013) implemented in the CSU RadarTools Python package (Lang et al., 2016; Mroz et al., 2017). The HID algorithm identified grid volumes dominated by one of ten hydrometeor classes based on weighted inputs of temperature, horizontal reflectivity, differential reflectivity, specific differential phase, and copolar corre-

lation coefficient. After sensitivity testing to assess relative impacts of varying emphasis of dual-polarization variables on categorized radar volumes, the selected weights applied to each data type in the fuzzy-logic expression (Dolan and Rutledge, 2009) were 1.0, 1.0, 0.45, 0.3, and 0.25, respectively. The ten hydrometeor classes diagnosed by the HID algorithm include hail, large raindrops or melting hail, high-density (HD) graupel, low-density (LD) graupel, melting snow, aggregates, ice crystals, vertically oriented ice, rain, and drizzle.

To approximate quantities of hydrometeors that were most closely associated with riming in the updraft, precipitation ice mass (PIM) in each storm was calculated from ARMOR data using reflectivity and mass relationships (Deierling et al., 2008; Heymsfield and Miller, 1988) in the regions of updraft $\geq 5 \text{ m s}^{-1}$ where large drops/melting hail, hail, HD graupel, or LD graupel categories were identified. Non-precipitation ice mass (NPIM) was calculated using reflectivity in aggregate, ice crystal, and vertically oriented ice regions according to the flux divergence method (Deierling et al., 2008). By this method, only non-precipitation-sized ice most likely participating in charging processes near the updraft was considered.

2.3.2.2 Vertical Wind Retrieval

Three-dimensional flow was obtained from dual-Doppler analysis using dealiased V_r data from KHTX and the ARMOR. Dual-Doppler analysis was accomplished using the three-dimensional variation (3DVAR) technique (Potvin et al., 2012b; Shapiro et al., 2009) implemented in the Pythonic Direct Data Assimilation (PyDDA) package (Jackson et al., 2019). The 3DVAR technique minimizes a cost function with penalty terms that compare the analysis winds with the observed V_r data from two or more radars, mass conservation of the analysis, and smoothness constraints (Potvin et al., 2012b; Shapiro et al., 2009).

The weights applied to each of the penalty terms in the cost function were determined through sensitivity testing procedures similar to those discussed in Shapiro et al. (2009). An observations weight of 1, a mass conservation weight of 1500, and a three-dimensional smoothness weight of $1e-5$ were used for each storm.

Unlike traditional techniques, the 3DVAR method does not use integration of the mass continuity equation between boundaries where vertical motion, w , is assumed to be 0 m s^{-1} . This aspect offers the important benefit of omitting the requirement that the storm top be sampled in order to retrieve vertical motion with better accuracy from the remaining parts of the storm (Potvin et al., 2012a). That is, vertical wind retrievals can be considered reliable in regions beneath levels at which upper level data were not available (Potvin et al., 2012c). It is worth noting, however, that retrievals are more susceptible to errors at upper levels, including as a result of gridding artifacts (Collis et al., 2010; Potvin et al., 2012c). Therefore, while most observed structures are physically consistent, some details could be the result of artifacts at the highest altitudes of retrievals.

The primary vertical velocity quantities analyzed consisted of the area or volume of updraft with speeds of 5 m s^{-1} or greater and 10 m s^{-1} or greater, referred to as 5 m s^{-1} or 10 m s^{-1} updraft area or volume, and maximum updraft speed, calculated as the 99th percentile of vertical velocity. A 10 dBZ reflectivity threshold was applied prior to calculation of these quantities in order to omit areas of noise associated with gridding artifacts aloft in regions of increasing vertical beam spread or lack of radar coverage (Collis et al., 2010; North et al., 2017; Potvin et al., 2012c).

2.3.3 Environmental Data

Reconstructed soundings from model analysis were examined in the nearest hour prior to each storm analysis period in its initial analyzed location to avoid convective contamination. Model sounding analysis times are listed in Table 2.1 while key environmental parameters are provided in Table 2.2. Environmental temperatures from these soundings were provided as required inputs to the HID and PyDDA algorithms. Temperature levels obtained from a virtual temperature-based pseudoadiabatic parcel were used instead of environmental temperatures as references in spatial storm analyses. Though neither a pseudoadiabatic parcel-based profile nor environmental profile accurately represents in-cloud conditions, the pseudoadiabatic profile is considered as an upper limit that may better approximate conditions within a moist updraft wherein most lightning processes are analyzed. Unless otherwise noted as environmental, temperatures in remaining discussion are based on the pseudoadiabatic parcel.

Concentrations of PM2.5 are reported as a single average value from the proximal sensor(s) from the period two hours prior to one hour after the beginning of each storm analysis period (Table 2.2). Averages were used to mitigate the effects of variability in detected concentrations, including those associated with precipitation. Though these are surface data and quantities at and above cloud base are reasonably expected to have been lower, the relative differences provide a general indication of the CCN that might have been available to each storm.

2.4 Anomalous Storm Structure

Figure 2.1 shows the path of each supercell in Southern TN through the sampling domain centered in Northern AL. As part of the process to associate lightning with its parent

Table 2.1: Anomalous supercell case analysis parameters.

Case Date	Analysis Period [UTC]	Model Analysis Sounding Time [UTC]	Min. Tracking Reflectivity [dBZ]	W., E., S., N. Expansion [km]
10 Apr 2009	1712-1825	1600	30	10, 25, 12, 10
22 Apr 2017	2056-2206	2000	20	5, 25, 10, 15

Table 2.2: Pre-convective environmental parameters derived from a model analysis sounding in the location of each anomalous supercell an hour prior to its initial observation period. Average proximal PM2.5 data are provided as a regional proxy of estimated CCN concentration on each date.

Parameter	10 April 2009	22 April 2017
CAPE [J kg^{-1}]	2123	1453
NCAPE [m s^{-2}]	0.19	0.14
0-6 km shear [m s^{-1}]	32.4	24.5
LCL height [m]	643	900
Environmental melting level (ML) [m]	3105	3617
Warm cloud depth = ML-LCL [m]	2460	2720
Surface temperature [$^{\circ}\text{C}$]	20.6	22.2
Surface dew point temperature [$^{\circ}\text{C}$]	16.6	18.2
Mean mixing ratio in the lowest 100 hPa [g kg^{-1}]	11.4	11.9
Precipitable water in the surface to 400 hPa layer [cm]	2.3	3.2
Mean RH below ML [%]	71	84
Mean RH in the 500 hPa to 700 hPa layer [%]	21	36
Average hourly PM2.5 concentrations [$\mu\text{g m}^{-3}$]	22	6

supercell, each storm was tracked using the Warning Decision Support System - Integrated Information (Lakshmanan et al., 2007) software as described in Stough et al. (2017). In summary, storm feature footprints were identified using regions of gridded reflectivity at the height of -10°C and tracked through time. These footprints were characterized by a centroid location and latitudinal and longitudinal radii that were used to construct a box within which storm data were assessed, including lightning flash initiations and associated propagation, vertical velocity metrics, and ice mass. Tracking box radii were subjectively broadened to fully capture the spatial extent of each storm while maintaining its separation

from surrounding deep convection. The tracking parameters and expansion distances used in each case are documented in Table 2.1 along with the period of time over which each storm was analyzed. The criterion determining the analysis period for each supercell was the duration over which it was sampled within the 30° beam-crossing area of the dual-Doppler domain established between the ARMOR and KHTX.

2.4.1 10 April 2009 Anomalous Supercell

The 10 April 2009 supercell was analyzed in the northern lobe of the dual-Doppler domain between 1712 UTC and 1829 UTC as it propagated from southwest to northeast through southern TN. It was first analyzed shortly after initiating, allowing observation of its maturation. Over the analysis period, it produced an average lightning flash rate of 41 min⁻¹ with a maximum lightning flash rate of 79 min⁻¹ at 1810 UTC. Several hail reports were associated with this storm with a maximum diameter of 4.44 cm.

2.4.1.1 Characterization of All Sources

As the storm intensified through the first 30 minutes of analysis, the updraft size and intensity and total PIM within the updraft increased (Figures 2.3g and 2.3h). The mode altitude of all sources detected during the analysis period similarly increased over time from between 4 km above ground level (AGL) and 5 km AGL near -10°C through 1748 UTC to between 7 km AGL and 8 km AGL near -20°C by the end of the analysis period (Figure 2.3a). The mode altitude of all classified positive sources (Figure 2.3b) was strongly correlated with that of all sources as expected given the nature of lightning propagation in the VHF. By contrast, the quantity of all classified negative sources detected

was lower and most concentrated at higher altitudes in the storm between 7 km AGL and 10 km AGL near -30°C (Figure 2.3c).

2.4.1.2 Characterization of Positive Sources within the Updraft

The distribution of positive sources located in the updraft (Figure 2.3d) was similar to that of all positive sources through 1728 UTC, most concentrated between 4 km AGL and 6 km AGL. As the updraft intensified between 1733 UTC and 1739 UTC, PIM resulting from hail (Figure 2.3j) and HD graupel (Figure 2.3k) increased in the 4 km AGL to 5 km AGL layer of the mixed-phase region. Though LD graupel continued to dominate the mixed-phase region, the largest hail fractions within the updraft were also observed during this time, consistent with reports of large hail. The height of most positive sources in the updraft increased to between 7 km AGL and 9 km AGL by 1733 UTC as the updraft developed. The mode height of all positive sources, however, lingered between 4 km AGL and 5 km AGL through 1748 UTC (Figure 2.3d). The location of most positive sources in the updraft was spatially consistent with that of the greatest increase in PIM hail fraction at that time (Figure 2.3j), indicating potential association with riming hydrometeors. The altitudinal differences observed between all positive source locations throughout the storm and those within the intensifying updraft were consistent with physical processes of lofting of charged hydrometeors by the updraft (e.g., Stolzenburg et al., 1998) as well as gravitational sedimentation of riming ice hydrometeors carrying positive charge outside of the updraft.

The increase in mode height of all positive sources at approximately 1754 UTC occurred 8 minutes after reports of large hail, concurrent with a period of intensification as the 10 m s^{-1} updraft area increased to $\geq 80\text{ km}^2$ in the upper mixed-phased region (Figure 2.3g). The mode height of all positive sources and the altitude of the greatest

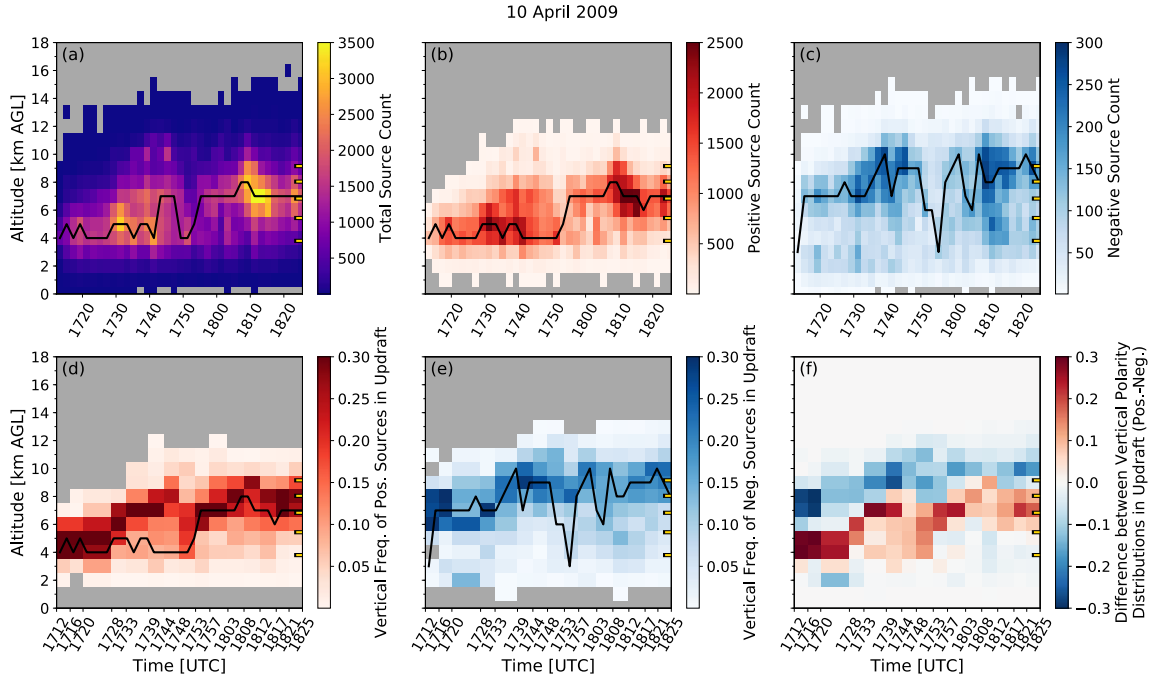


Figure 2.3: Time-height cross-sections of lightning, kinematic, and microphysical properties of the anomalous 10 April 2009 supercell. (a) Distribution of all NALMA VHF sources detected during the full analysis period, binned in 1-km vertical and 2-min temporal increments, is shown in color fill along with the mode height at which all sources were observed (black line). Distribution of all (b) positive (c, negative) sources are shown in red (blue) color fill with mode heights of all positive (negative) sources plotted as a black line. Vertical frequency of gridded (d) positive and (e, negative) sources within updrafts $\geq 5 \text{ m s}^{-1}$ or greater are shown in red (blue) color fill along with the mode height of all positive (negative) sources as a black line. (f) The difference between the vertical relative frequency of positive and negative gridded source data is shown where net positive (negative) frequency is plotted as positive (negative) values in red (blue) color fill. (g) The 99th percentile updraft speed is plotted in grayscale with contoured 10 m s^{-1} updraft volumes in red. (h) Distribution of total PIM is shown in grayscale fill. (i) Distribution of total NPIM calculated according to the flux divergence method is shown in grayscale fill. Percentages of PIM associated with (j) hail, (k) HD graupel, and (l) LD graupel are shown in grayscale fill. In each panel, yellow and black marks along the right vertical axis represent the approximate pseudo-adiabatic parcel temperature heights of 0° C through -40° C marked in -10° C increments.

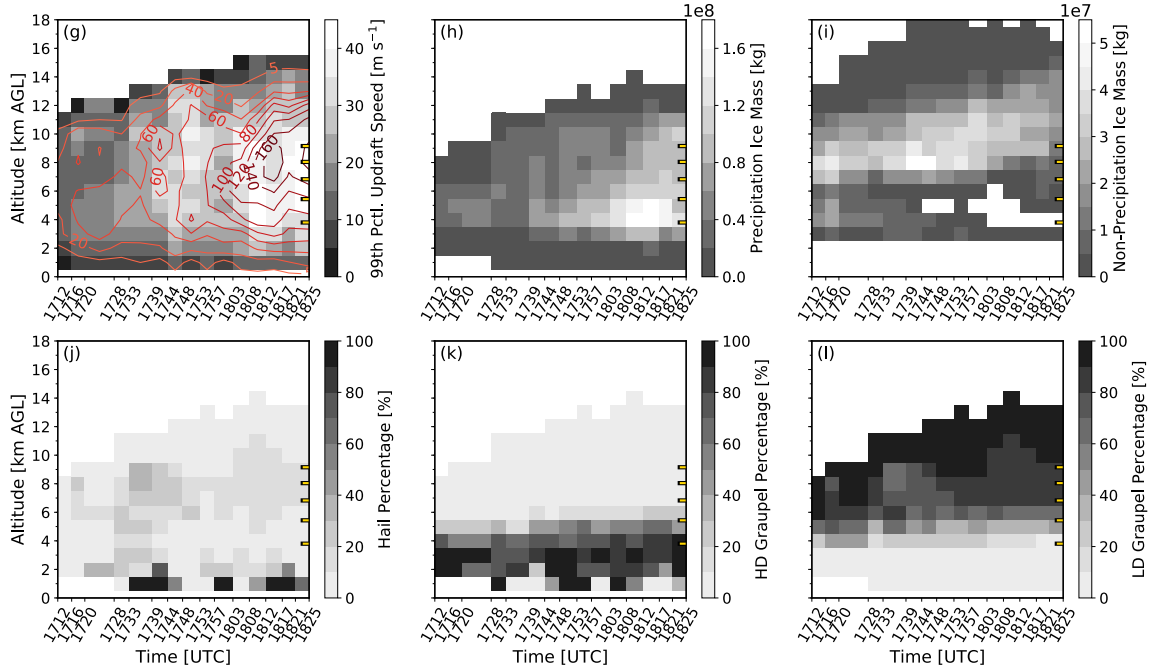


Figure 2.3: (continued)

relative frequency of those within the updraft after 1753 UTC coincided with observations of low but increasing hail fraction between 8 km AGL and 10 km AGL, suggesting that positive charge was associated with growth of riming ice in a robust, elevated updraft.

2.4.1.3 Characterization of Negative Sources within the Updraft

The relative vertical frequency of negative sources in the updraft was greatest in the 6 km AGL to 10 km AGL layer (Figure 2.3e). Relative vertical maxima in NPIM and LD graupel were observed in this region as well (Figures 2.3i and 2.3l). Between 1747 UTC and 1758 UTC as large hail was reported and total PIM gradually increased, there was a relative lull in lightning activity where a 10-minute lightning flash rate average of 57 min^{-1} decreased to an average of 35 min^{-1} (not shown). Given the relative decrease in sources associated with decreased lightning activity during this period, there was not a pronounced

negative source mode altitude and the sharp decrease observed at 1753 UTC was not a robust signal of a physical change in the location of negative sources. A subsequent rapid lightning flash rate increase to 75 min^{-1} at 1808 UTC coincided with observations of the most substantial increases in PIM and updraft size and intensity, possibly indicative of an increase in mixed-phase LWC transported by the updraft and associated invigoration of ice growth processes. As a greater number of negative sources were detected and classified with the overall increase in lightning activity, the mode height of negative sources was between 7 km AGL and 10 km AGL, overlapping with and extending above the positive layer. Increases in the altitude of the relative maximum NPIM and LD graupel fractions were observed through this layer as well as the mixed-phase updraft reached its largest observed size between 1808 UTC and 1817 UTC.

2.4.1.4 Inferred Net Charge Structure

Comparing the relative vertical positions of the positive and negative source frequencies in the updraft, a distinct negative charge region remained apparent above a dominant positive charge layer below (Figure 2.3f). As the altitudes of these distinct layers increased with intensification of the supercell, the positive charge region remained more closely associated with the larger PIM regions comprised of graupel and hail while the spatial distribution of the negative charge region was more closely associated with the location of greatest NPIM aloft. Where vertical positive and negative source frequency maxima in the updraft (Figures 2.3d and 2.3e) coincided with hail fraction maxima above 8 km AGL after 1757 UTC (Figure 2.3j), the net positive charge layer (Figure 2.3f) emerged as more consistent with vertical variations in hail, indicating a stronger association between net positive charge and lofted riming hydrometeors. Given overlap between net negative charge and LD graupel,

it is also possible that negative charge in the upper mixed-phase and glaciated regions was carried by more recently charged graupel as well as negatively charged small ice that had separated from collisions with positively charged riming hydrometeors below. That is, LD graupel could have charged negatively in the colder upper mixed-phase region if its growth had been supported by sufficient LWC in the updraft. Despite evident microphysical overlap, spatial relationships suggested that net positive charge was associated with larger rimed ice hydrometeors in the lower to middle mixed-phase region while net negative charge was primarily associated with smaller non-precipitation-sized ice advected to the top of the updraft into the glaciated region, consistent with the model of an ACS.

2.4.2 22 April 2017 Anomalous Supercell

The 22 April 2017 supercell was sampled in the northern lobe of the dual-Doppler domain in southern TN between 2056 UTC and 2206 UTC as it propagated to the east-southeast into north AL. The supercell had reached maturity before entering the domain and was already producing prolific lightning flash rates, with a minimum of 90 min^{-1} over the duration of the analysis period, an average lightning flash rate of 182 min^{-1} , and a maximum lightning flash rate of 266 min^{-1} at 2122 UTC. Numerous severe weather reports were associated with this storm during the analysis period, including damaging winds and hail with a maximum diameter of 4.44 cm.

2.4.2.1 Characterization of All Sources

The mode altitudes of all sources and positive sources were again most similar in the 22 April 2017 storm (Figures 2.4a and 2.4b), though there were smaller differences between the positive and negative source mode altitudes than observed in the 10 April 2009

storm (Figures 2.4b and 2.4c) and the relative maxima in source distributions were less concentrated than observed in the 10 April 2009 storm (Figures 2.4b to 2.4e). In general, the positive source mode altitude was located between 7 km AGL and 9 km AGL, near -20°C to -30°C (Figure 2.4b), while the negative source mode altitude remained mostly at higher altitudes between 7 km AGL and 10 km AGL near -30°C and -40°C (Figure 2.4c).

2.4.2.2 Characterization of Positive Sources within the Updraft

As in the 10 April 2009 storm, the greatest frequency of positive sources in the updraft was observed 1 km to 2 km higher than the mode height of all positive sources (Figure 2.4d), suggesting sedimentation of positively charged hydrometeors outside of the updraft. The heights at which positive sources in the updraft were most prominent were consistent with the height of the fastest updraft speeds (Figure 2.4g). Additionally, the lower boundary of the relative vertical maximum in positive sources within the updraft (Figure 2.4d) descended similarly as the updraft PIM associated with the high fractions of hail and HD graupel from 9 km AGL to 7 km AGL between 2104 UTC and 2202 UTC (Figures 2.4j and 2.4k), further indicating an association between riming hydrometeors and net positive charge.

2.4.2.3 Characterization of Negative Sources within the Updraft

A broad region of greater relative frequency of negative sources in the updraft observed between 8 km AGL and 11 km AGL (Figure 2.4e) exhibited overlap with the primary layer of positive sources in the updraft (Figure 2.4d). The depth and location of negative sources within the updraft also overlapped with the relative maximum in NPIM between 10 km AGL and 11 km AGL (Figure 2.4i).

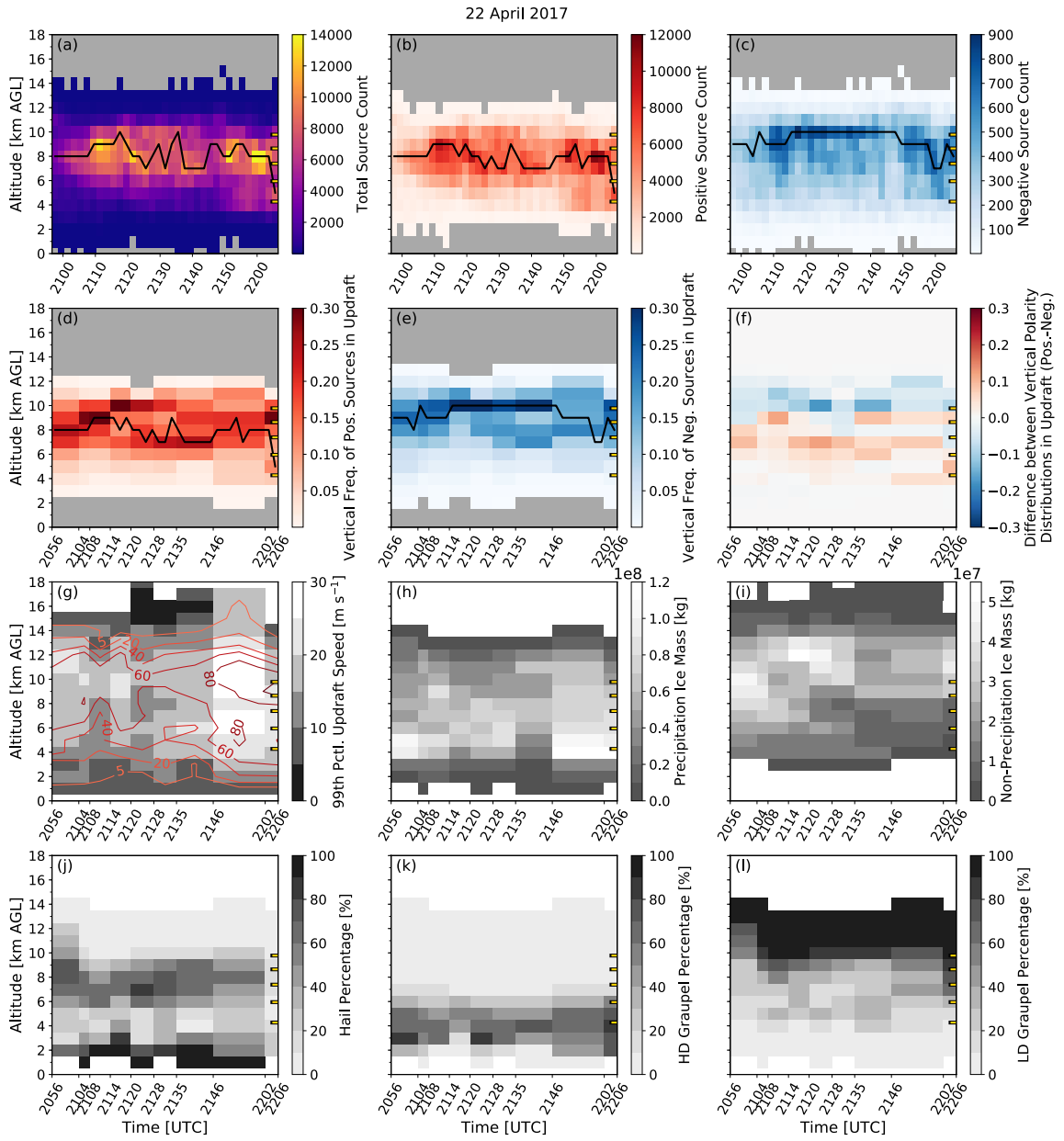


Figure 2.4: As in Figure 2.3 for the anomalous 22 April 2017 supercell.

The persistent large relative frequency of negative sources observed at 10 km AGL between 2114 UTC and 2146 UTC (Figure 2.4c) was also coincident with the lower boundary of the vertical LD graupel maximum (Figure 2.4l) and the vertical NPIM maximum (Figure 2.4i). As in the anomalous 10 April 2009 supercell, it is possible that LD graupel growing more slowly in low LWC in the upper mixed-phase region charged negatively and was lofted into the glaciated region, meaning that observed net negative charge may have been associated with both large and small ice. However, overlapping precipitation category observations in net negative charge regions could also be explained by masking of negatively charged small ice by some quantity of large ice in radar observations. For instance, overlap exhibited between the local minimum in NPIM and the region of descending hail mass between 2108 UTC and 2135 UTC (Figures 2.4i and 2.4j) suggested that small ice was present through the depth but masked by hail.

The relative vertical maximum in net negative charge observed near 10 km AGL in the updraft dissipated by 2146 UTC (Figure 2.4e) as increases in maximum updraft speeds and depth of the broadest 10 m s^{-1} updraft were observed (Figure 2.4g). After 2146 UTC, the relative vertical frequency of negative sources in the updraft between 8 km AGL and 11 km AGL also became less distinct (Figure 2.4e) and the mode height of all negative sources decreased in altitude and overlapped with that of all positive sources.

2.4.2.4 Inferred Net Charge Structure

Comparing the relative frequencies of the vertical source distributions (Figure 2.4f), a region of relatively higher positive source frequency was observed between 7 km AGL and 9 km AGL while a region of relatively higher negative source frequency was observed between 10 km AGL and 12 km AGL. The dynamic range of these regions was not as

large as observed in the 10 April 2009 supercell, even after the 10 April 2009 supercell had reached maturity for closer comparison (Figure 2.3f). It is expected that many more small lightning flashes would occur in a storm exhibiting high lightning flash rates (e.g., Bruning and MacGorman, 2013). These may result from increasing charge region complexity near a turbulent updraft (Brothers et al., 2018; Bruning and MacGorman, 2013; Calhoun et al., 2013), variability in cloud microphysical conditions adding complexity to NIC charging regimes (e.g., Bruning et al., 2010; Wiens et al., 2005), and/or contributions associated with additional charging mechanisms or charge deposition (e.g., Bruning et al., 2010; Stolzenburg et al., 1998). Any such complexity could obscure otherwise distinct net charge as observed. Further, the corresponding spatial patterns of PIM associated with hail and NPIM indicated vertical overlap between the two potentially oppositely-charged hydrometeor populations (Figures 2.4i and 2.4j), increasing the opportunity for horizontal heterogeneity in observed charge structure. Despite evidence of some degree of charge structure complexity, diffuse maxima ultimately suggested coincidence between sedimenting PIM (elevated NPIM) and positive (negative) charge patterns, consistent with ACS models.

2.5 Discussion

2.5.1 Background Environment

Instability and shear parameters in each of the supercell cases were representative of an environment supporting supercell development with convective available potential energy (CAPE) values of 2123 J kg^{-1} and 1453 J kg^{-1} , normalized CAPE (NCAPE) values of 0.19 m s^{-2} and 0.14 m s^{-2} , and 0-6 km shear of 32.4 m s^{-1} and 24.5 m s^{-1} on 10 April 2009 and 22 April 2017, respectively. General instability metrics, including CAPE, are variable among documented anomalous storm environments and do not reliably discriminate

between normal and anomalous environments (e.g., Carey and Buffalo, 2007; Chmielewski et al., 2018; Fuchs and Rutledge, 2018; Lang and Rutledge, 2011). However, NCAPE in many layers has been identified as a better discriminator, and CAPE within the mixed-phase region in particular has been documented to be statistically significantly higher in anomalous storms compared with normal storms (Carey and Buffalo, 2007). Although NCAPE values were lower than reported in some anomalous supercell storm environments (e.g., 0.22 m s^{-2} , Carey and Buffalo, 2007), each of the Southeastern anomalous supercells exhibited a robust updraft, including hallmarks of bounded weak echo regions and lightning holes (Figures 2.5a, 2.5g, 2.6a, and 2.6g), consistent with kinematic support for anomalous charging (e.g., DiGangi et al., 2016; Emersic et al., 2011; Krehbiel et al., 2000; Steiger et al., 2007; Wiens et al., 2005).

The LCL heights in the 10 April 2009 and 22 April 2017 supercells were 643 m and 900 m, while the environmental melting levels were 3105 m and 3617 m. The resultant WCDs were 2460 m and 2720 m, respectively. The values between these two storms were similar to each other, though on the order of 1000 m deeper than WCDs associated with Great Plains anomalous storm environments reported in the literature. Studies have noted that WCD inconsistently discriminates between anomalous and normal storm environments (e.g., Chmielewski et al., 2018; Lang and Rutledge, 2011), indicating that other environmental characteristics may compensate for potentially suboptimal WCDs.

Surface dew point depressions of 4°C in the Southeastern anomalous environments were lower than minimum depressions of 11°C inferred from surface data or directly reported in other anomalous storm environments (Carey and Buffalo, 2007; Chmielewski et al., 2018; Fuchs and Rutledge, 2018; Lang and Rutledge, 2011; Tessendorf et al., 2005, 2007a,b), indicating greater low-level moisture. However, precipitable water used as a metric of deeper

ARMOR: 10 April 2009 - 1739 UTC

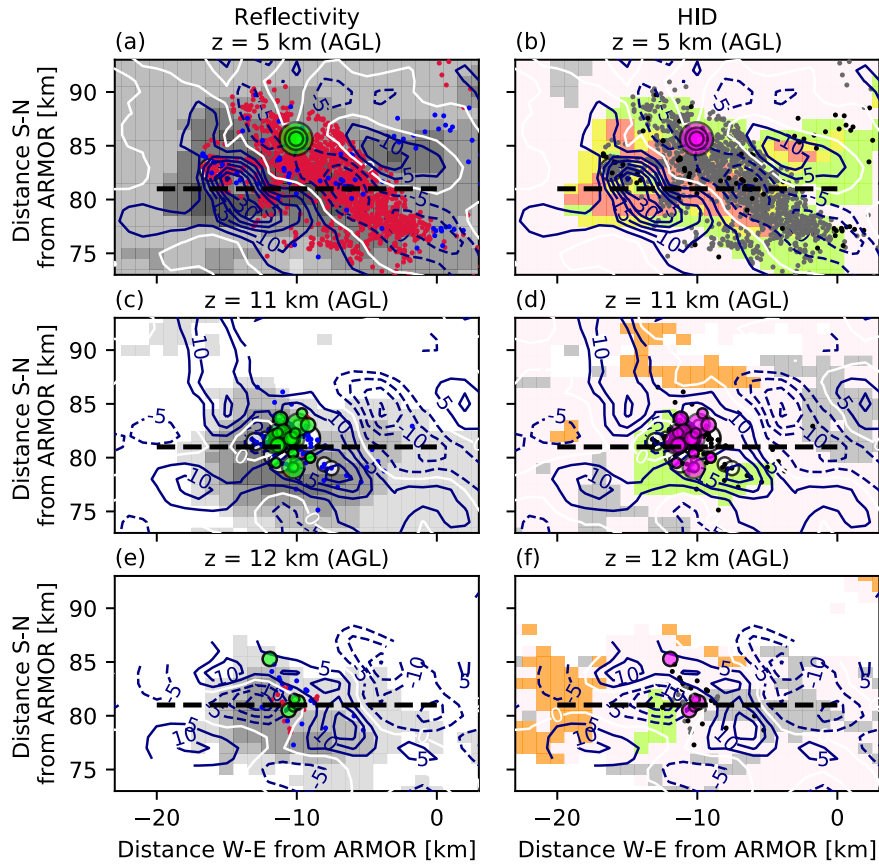


Figure 2.5: ARMOR data at 1739 UTC on 10 April 2009 along with NALMA data between 1741 UTC and 1743 UTC. Horizontal cross sections of reflectivity (a, c, e; grayscale fill) and HID (b, d, f; color fill) are shown at 5 km AGL, 11 km AGL, and 12 km AGL altitudes. Vertical cross-sections of reflectivity (g, grayscale fill) and HID (h, color fill) are shown at $y = 81$ km north of ARMOR, the location of which is marked as a black dashed line in the horizontal cross section panels. On each figure, vertical velocity contours in the plane are plotted at positive 5 m s^{-1} , 0 m s^{-1} , and negative 5 m s^{-1} intervals (solid blue, solid white, and dashed blue contours) as well as positive sources (red dots or gray dots), negative sources (blue or black dots), and lightning flash initiation locations (white circles if polarity was classified, green or purple circles if polarity was unclassified) within ± 0.5 km of the plane.

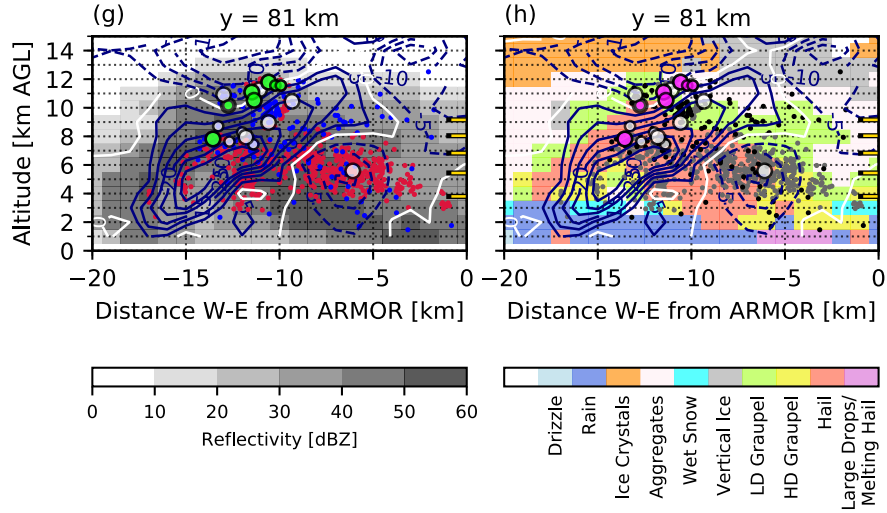


Figure 2.5: (continued)

environmental moisture was more consistent with other anomalous storm environments documented in the literature, where values in the surface to 400 hPa layer in the 10 April 2009 and 22 April 2017 storms were 2.3 cm and 3.2 cm, respectively. In other large sample studies, though not always a discriminatory parameter, measures of precipitable water associated with characteristically anomalous (normal) storm environments were reported as 2.6 cm (3.5 cm), 2.1 cm (3.1 cm), and 2.6 cm (2.5 cm) (Carey and Buffalo, 2007; Fuchs and Rutledge, 2018; Lang and Rutledge, 2011, respectively). Mean RH in the 500 hPa to 700 hPa layer, however, was 21% and 36% in the 10 April 2009 and 22 April 2017 storm environments, respectively, indicating relative dry layers near cloud base that extended into the lower mixed-phase regions. Carey and Buffalo (2007) similarly reported median RH in the 700 hPa to 500 hPa of 28% in anomalous storm environments compared with a higher median value of 45% in normal storm environments. Fuchs et al. (2018) documented conflicting results, finding that RH in the 600 hPa to 500 hPa was higher in CO anomalous

ARMOR: 22 April 2017 - 2135 UTC

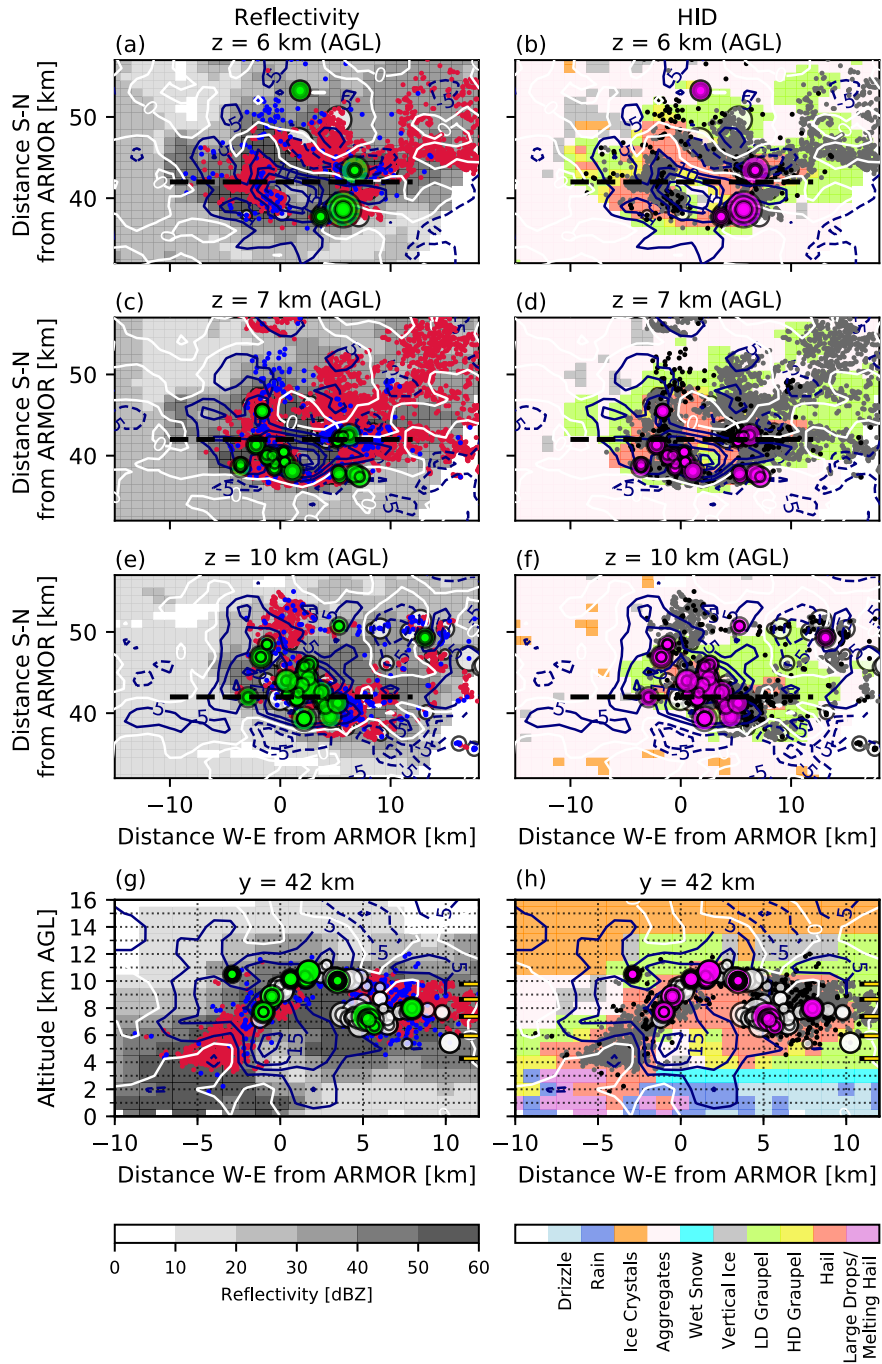


Figure 2.6: As in Figure 2.5 on 22 April 2017 with radar data at 2135 UTC and lightning data between 2137 UTC and 2139 UTC. (a-f) Horizontal cross sections are shown at 6 km AGL, 7 km AGL, and 10 km AGL altitudes. (g-h) Vertical cross-sections are shown at $y = 42$ km north of ARMOR.

storms than in AL normal storms with median values of 40.1% and 31.4%. They suggested that updrafts in normal storms were likely more susceptible to entrainment of and dilution by the observed drier air, reducing kinematic support of anomalous charging. Chmielewski et al. (2018) identified dry layers in the 700 hPa to 600 hPa layer closer to cloud base as an outstanding factor differentiating anomalous from normal storms, hypothesizing that dry air entrainment specifically near cloud base could decrease the size of cloud droplets, and reducing warm precipitation efficiency in favor of anomalous charging. However, effects of dry air may compete with other elements that promote anomalous charging such as updraft strength. Additionally, pathways preserving sufficient LWC from evaporation associated with dry air entrainment for extensive positive charging of riming hydrometeors are as of yet unclear.

Concentrations of PM_{2.5} used as a proxy for relative CCN concentrations were disparate between the 10 April 2009 and 22 April 2017 environments at $22 \mu\text{g m}^{-3}$ and $6 \mu\text{g m}^{-3}$, respectively. It is difficult to directly apply this range of values to CCN concentrations, though the higher values observed on 10 April 2009 suggest that CCN concentration may have been elevated in favor of anomalous charging.

2.5.2 Charge Structure Relationships with the Updraft

Various relationships were observed between charge structure and kinematic and microphysical properties of the updraft during the development (10 April 2009) and mature stages (10 April 2009 and 22 April 2017) of the supercells. The following discussion synthesizes these relationships and discusses any consistencies exhibited with anomalous supercells documented in the literature in the Great Plains.

2.5.2.1 Initial Development

Storm development and intensification was observed only in the 10 April 2009 super-cell. During the first 15 minutes of analysis, maximum vertical velocities in the mixed-phase region were less than 15 m s^{-1} within a relatively narrow 10 m s^{-1} updraft of $\leq 20 \text{ km}^2$ (Figure 2.3g). Less than $1.5 \times 10^8 \text{ kg}$ of precipitation ice (Figure 2.3h), primarily composed of LD graupel (Figure 2.3l), was observed at any altitude. Most of the positive sources within the updraft were identified between 4 km AGL and 5 km AGL in the warmer mixed-phase region of $> -20^\circ\text{C}$ (Figure 2.3d) with a dominant negative charge layer aloft between 6 km AGL and 8 km AGL in the mid- to upper mixed-phase region between approximately -20°C and -30°C (Figure 2.3e). These observations indicate that ACS characteristics did not evolve from an NCS with an initial dominant negative (upper positive) charge layer associated with graupel (small ice). Similar early charge structure characteristics were observed in the development of an anomalous supercell in Kansas documented by Wiens et al. (2005) where initial lightning flashes were located between a low positive charge region and mid-level negative charge.

As the updraft intensified, an increase in lightning flashes was observed near 9 km AGL at 1733 UTC (Figures 2.7c and 2.7d). A vertical cross section along the northern edge of the updraft shows that negative sources associated with these lightning flashes were located at the edge of 30 dBZ reflectivity and the upper extent of a region of LD graupel (Figures 2.7e and 2.7f), consistent with those of Rust et al. (2005) who discussed observations of negative charge near the top of an anomalous storm's precipitation core.

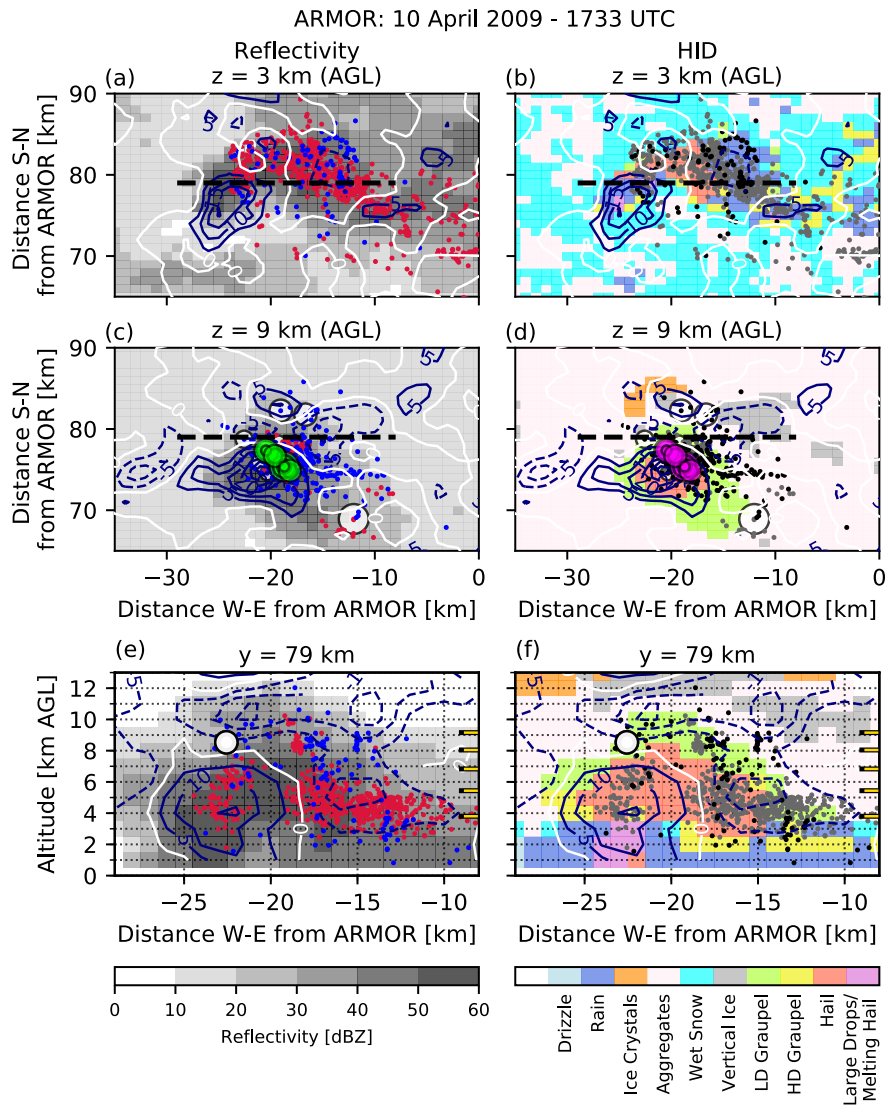


Figure 2.7: As in Figure 2.5 on 10 April 2009 with radar data at 1733 UTC and lightning data between 1735 UTC and 1737 UTC. (a-d) Horizontal cross sections are shown at 3 km AGL and 9 km AGL altitudes. (e-f) Vertical cross-sections are shown at $y = 79$ km north of ARMOR.

2.5.2.2 Supercell Maturity

Updraft intensification was observed in the 10 April 2009 storm beginning at 1728 UTC, attendant with an increase in the altitude of the primary charge layers and an increase in PIM attributed to an increase in hail in the upper mixed-phase region. Increasing updraft sizes and speeds may have invigorated efficient riming through an increased LWC supply while also further elevating graupel and small hail along with primary charge layers associated with these microphysical fields. Wiens et al. (2005) similarly documented a graupel volume response to updraft pulses along with spatial correlations between vertical shifts in graupel volume and VHF source maxima associated with predominantly positive charge. Although the primary positive charge region exhibited somewhat more bimodal behavior in the 22 April 2017 supercell after 2114 UTC, characteristics of both main charge regions in the updraft also varied in vertical space alongside ice fields. The lower maximum in positive source frequency was spatially associated with vertical variations in the location of PIM maximum and its relative hail fraction maximum while the relative negative source maximum trended similarly in the vertical with the lower boundary of the NPIM maximum. In both storms, the primary positive charge locations within the updraft were most closely associated with PIM maxima, and particularly with vertical hail distributions, indicating that positive charge in the updraft existed in regions of efficient riming in accordance with ACS conceptual models.

2.5.3 Charge Structure Complexities near the Updraft

A particularly active period of lightning propagation was observed near 10 km AGL between 2114 UTC and 2146 UTC in the 22 April 2017 supercell (Figures 2.4a and 2.4e). These lightning flashes were typically smaller and primarily occurred between positive

charge proximal to the updraft core near -20°C (Figures 2.8c and 2.8e) and negative sources near the top of the reflectivity maximum in decreasing updraft speeds (Figures 2.8c and 2.8e). Similar charge structure complexity including a large number of small, unclassified lightning flashes was observed near the top of the updraft in the 20 April 2009 supercell as well (Figure 2.5c). Small lightning flashes near 10 km AGL in each supercell were located in a compact region over which the dominant precipitation type between approximately 10 km AGL and 13 km AGL transitioned between hail, LD graupel, and aggregates or ice crystals (Figures 2.5h, 2.6h, and 2.8f).

Unclassified lightning flashes, representative of smaller discharges that are not uncommon in supercell updrafts (e.g., Bruning et al., 2010; Calhoun et al., 2013; Wiens et al., 2005), were consistent with inherent kinematic texture in the gradient region of vertical velocity and horizontal flows at the top of a supercell updraft (Brothers et al., 2018; Bruning and MacGorman, 2013). Given the variability in the microphysical landscape near the top of the anomalous storm, it is possible that changes in charging regimes in and around the updraft may have contributed to observed complexity alongside kinematic texture. It is worth noting that the smaller resolved charge regions and majority of unclassified lightning flashes in each storm were identified above the level of homogeneous freezing near approximately 9 km to 10 km where ice-ice collisional NIC is inactive in the absence of LWC (though it is possible that other non-inductive methods could be active, e.g., Mitzeva et al., 2006). However, vertical updraft gradients may have supported lofting and continued differential sedimentation of previously charged hydrometeors to and within the glaciated region. The hydrometeor populations could have included some mixture of positive rimed hydrometeors lofted by the strongest updraft core from mid-levels, negatively-charging rimed hydrometeors that grew more slowly in reduced LWC at cooler temperatures in the upper mixed-phase

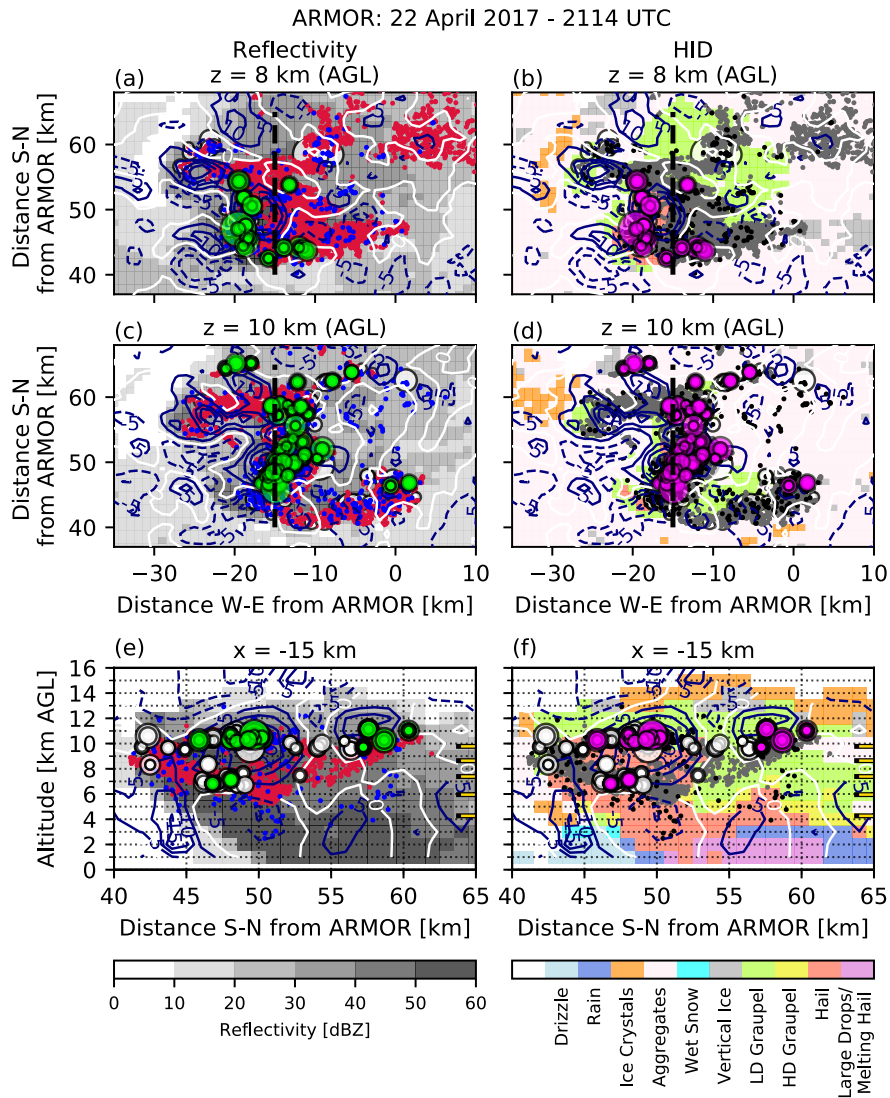


Figure 2.8: As in Figure 2.5 on 22 April 2017 with radar data at 2114 UTC and lightning data between 2116 UTC and 2118 UTC. (a-d) Horizontal cross sections are shown at 8 km AGL and 10 km AGL altitudes. (e-f) Vertical cross-sections are shown at $x = 15$ km west of ARMOR.

region, and small ice hydrometeors of both polarities separating from rebounding collisions and lofted furthest by the broadest range of updraft velocities. Similarly, variations in charge polarity over horizontal gradients of hydrometeor type and vertical motion were observed, where three-dimensional variations in charging across the mixed-phase updraft may have contributed to observed horizontal complexities in charge structure (Figures 2.6a, 2.6c, and 2.8a). Differentiation of microphysical and kinematic contributions to observed charge structure complexity is relevant to understanding the origins of charge structure as well as implications for lightning flash relationships with the updraft. However, further related analyses and discussion are necessarily left to future, more thorough treatment.

2.5.4 Evidence of Anomalous Tripole

Gross charge structures inferred in each storm periodically indicated the presence of a lower negative charge region (Figures 2.3f and 2.4f). Shallow regions of negative charge were observed below the level of 0°C , beneath the updraft core and in weak vertical motions outside of the primary updraft region in the 10 April 2009 supercell (Figures 2.5g and 2.7e) and beneath the updraft core near -10°C in the 22 April 2017 supercell (Figure 2.8e). These negative charge regions were associated with mixtures of hail, HD graupel, and melting hail hydrometeor categories (Figures 2.5f, 2.7f, and 2.8f), consistent with indications that lower negative charge resulted from rearrangement of charged particles outside of the updraft core, though specific origins are not clear. Interestingly, a band of negative charge was also inferred in the eastern gradient of the updraft in the 10 April 2009 storm (Figure 2.5g), consistent with hypothesized roles of three-dimensional variations in charging, kinematics, and differential sedimentation in establishing additional charge regions observed in an anomalous tripole (e.g., Bruning et al., 2014; Wiens et al., 2005).

2.6 Summary and Conclusions

Observations of two anomalous supercells in the Southeastern US that occurred on 10 April 2009 and 22 April 2017 were documented in this Chapter. The first study to address anomalous charge structure and its relationships with kinematic and microphysical properties in supercells in the US outside of the High Plains and Midwest, it facilitated an evaluation of fundamental aspects of traditional NIC-based conceptual models of ACS characteristics. These observations also provided a novel opportunity to test hypotheses concerning the conditions thought to be favorable for ACS development based on results from studies of ACSs in the Great Plains. Key observations and main results include:

1. The supercell charge structures were characterized by distinct regions of high positive source density in and near the -20°C to -30°C isotherm within the updraft where a negative charge region would usually be identified in normal charge structures. Net negative charge layers were instead identified above the primary positive charge layer in the upper mixed-phase and glaciated regions of these storms.
2. Gross positive charge regions in the updraft of storms were primarily associated with regions of riming precipitation-sized ice. Vertical variations in positive charge region locations with time were closely associated with vertical variations in precipitation ice fields in response to updraft trends.
3. The greatest density of negative sources near the top of the updraft was spatially collocated with non-precipitation sized ice mass maxima as well as LD graupel in the colder mixed-phase and glaciated regions. Though the net negative charge region may have primarily been composed of negatively charged small ice masked in radar observations by some amount of positively charged or neutral large ice, these observations

are consistent with charging theory indicating that riming ice in an anomalous storm may also charge negatively in the colder mixed-phase region and contribute to net negative charge aloft.

4. Charge structure complexity was embedded within coarse storm-scale charge structure characterization. Common regions exhibiting charge structure complexity included the top of updrafts as well as within horizontal gradients of vertical velocity and dominant hydrometeor type across the updraft. Alongside mechanisms such as secondary inductive charging or charge deposition, these gradients may have also contributed to periodic lower minor negative charge layers consistent with anomalous tripole structures. These observations suggest that local variations in microphysical conditions influenced local normal charging, though dominant charging conditions were conducive to more widespread net charge regions consistent with ACSs.
5. Numerous lightning flashes were observed within regions of complex charge structure at the top and within horizontal gradients of the updraft, many of which were small and remained unclassified. Zhang and Cummins (2020) found that detection efficiency of lightning flashes by the Geostationary Lightning Mapper (GLM), a spaceborne optical lightning detection instrument, was reduced to 20% to 40% for small or short-duration lightning flashes compared with 95% detection efficiency of large or long-duration lightning flashes. The presence of numerous small lightning flashes may contribute to reduced detection of lightning flashes by optical detection platforms in anomalous storms alongside conditions such as preferred lightning flash initiation at lower altitudes (e.g., Fuchs and Rutledge, 2018; Murphy and Said, 2020).

6. Compared with anomalous storm structure documented in the Great Plains in the literature, Southeastern anomalous supercells include in common the presence of large hail; negative charge regions associated with precipitation-sized ice lofted to the top of the updraft (e.g., Rust et al., 2005); elevated positive charge regions associated with a robust mid-level updraft (as in high-instability anomalous storm environments in Oklahoma, e.g., Fuchs et al., 2015); and, specific to the anomalous 22 April 2017 case, high total lightning flash rates (e.g., Tessendorf et al., 2005).
7. Of environmental parameters indicative of reduced warm precipitation efficiency, a reduction in moisture was most evident in Southeastern anomalous supercells and most consistent with observations in other regions. Midlevel RH values of 21% and 36% in 10 April 2009 and 22 April 2017 anomalous environments were similar to observations of 28% (Carey and Buffalo, 2007) and 41% (Fuchs and Rutledge, 2018) in mid-levels in anomalous storm environments in the Great Plains. Observed dry layers were also consistent with generally dry mid-levels and LP supercell structures observed in anomalous storm environments (e.g., Branick and Doswell III, 1992; Curran and Rust, 1992; Lang et al., 2004; MacGorman and Burgess, 1994; Seimon, 1993; Tessendorf et al., 2007b) and indications that dry layers near cloud base differentiate anomalous environments (Chmielewski et al., 2018). Other environmental parameters thought to be influential to precipitation efficiency and mixed-phase LWC were not consistent with observations in Great Plains and Midwest anomalous storm environments, including lower surface dew point depressions, lower NCAPE than observed in other anomalous supercells, and lower LCLs and deeper WCDs.

The Southeastern ACS storm structures and characteristics demonstrated consistencies with ACS models derived from observations in the Great Plains. However, inconsisten-

cies in several key environmental parameters thought to favor anomalous charging challenge the suggested role of warm precipitation inefficiency in promoting the development of ACSs in these storms. It is not clear that the dry layers in Southeastern anomalous supercells were alone sufficient to counter the deleterious effects of deep WCDs and other seemingly modest environmental parameters associated with warm precipitation efficiency. As such, determinations of the roles of environmental contributions and their relationship with LWC implications for collisional NIC in Southeastern anomalous supercells were inconclusive.

While leading hypotheses favor the modification of LWC in ACS development, environmental conditions may support anomalous NIC in other ways. In particular, the effects of dry air on supersaturation with respect to ice and its theorized impact on the relative growth and associated charging of riming and non-riming hydrometeors should be considered (e.g., Lang and Rutledge, 2002). Results from limited laboratory studies and theoretical analyses have found that the degree of environmental supersaturation may play a role in the polarity of graupel charging in addition to cloud LWC (Berdeklis and List, 2001; Emersic and Saunders, 2020; Mitzeva et al., 2005; Saunders et al., 2006; Tsenova et al., 2010). If cloud supersaturation is an additional factor in the observed polarity of charging hydrometeors and resultant net charge regions, it may explain some variation observed in environmental parameters between interregional ACSs in addition to ACS development despite competing environmental influences on mixed-phase LWC. It may also contribute to variability in small charge structures observed in and near the three-dimensional updraft.

A more rigorous test of conditions favorable for anomalous charge structures would result from direct comparisons of anomalous and normal storm structures and environments outside of the Great Plains, particularly where updraft observations are available. A detailed comparison between anomalous and normal supercell storms in the Southeastern US is

the subject of ongoing work to better highlight their structural differences and assess the relative roles of the environment that are hypothesized to impact NIC and charge structure, including those parameters affecting LWC and supersaturation.

2.7 Acknowledgments and Data Availability Statement

The authors acknowledge support from National Aeronautics and Space Administration (NASA) Severe Storms Research funding (NNH14ZDA001N), provided under contract from the NASA Marshall Space Flight Center (NNM11AA01A). Data collected from the ARMOR and NALMA on 10 April 2009 can be accessed at <https://zenodo.org/record/3738553> (license: Creative Commons Attribution 4.0 International, Carey and Blakeslee, 2020a). Data collected from the ARMOR on 22 April 2017 are available through the VORTEX-SE 2017 data catalog at the UCAR/NCAR Earth Observing Laboratory data archive (<http://catalog.eol.ucar.edu/vortex-se-2017>, Carey and Knupp, 2017) and NALMA data are available through the NASA Global Hydrology Resource Center Distributed Active Archive Center (<https://earthdata.nasa.gov/eosdis/daacs/ghrc>, Blakeslee, 2019). KHTX data are publicly available from <https://www.ncdc.noaa.gov/data-access/radar-data/nexrad>. Environmental analysis data from the RUC and RAP models are publicly available from <https://www.ncdc.noaa.gov/data-access/model-data/model-datasets/rapid-refresh-rap>. Pre-generated hourly PM_{2.5} data are publicly available from the US Environmental Protection Agency at <https://www.epa.gov/air-data>.

CHAPTER 3

EXAMINING CONDITIONS SUPPORTING THE DEVELOPMENT OF ANOMALOUS CHARGE STRUCTURES IN SUPERCELL THUNDERSTORMS IN THE SOUTHEASTERN UNITED STATES

3.1 Abstract

Conditions hypothesized to favor anomalous charging have primarily resulted from studies within the Great Plains region of the United States, where conditions that decrease the efficiency of warm precipitation processes are thought to be of fundamental importance in anomalous charging. Rare observations of anomalous charge structures in the Southeastern region challenge existing conceptual models used to explain anomalous charging. As a more rigorous test of conditions that support anomalous charge structures, two normal and two anomalous supercell thunderstorms observed in the Southeast were compared. Within the anomalous storms, greater quantities of precipitation ice were identified at higher altitudes, indicative of a greater depth of riming growth and increased vertical transport of rimed hydrometeors. Deeper anomalous supercell updrafts were also larger and stronger in the upper mixed-phase and glaciated regions of the anomalous supercells. Trends in environmental parameters traditionally thought to promote enhanced mixed-phase liquid water content in favor of anomalous charging were observed, including shallower warm cloud depth in anomalous storms. However, contrasts were not as large as observed in

other studies comparing normal and anomalous thunderstorm environments. Further, normal supercells were characterized by more robust low-level updrafts, resulting in comparable warm cloud residence time that suggested warm precipitation efficiency was not necessarily lower in anomalous storms. However, anomalous storm environments were characterized by lower RH in the 700 mb to 500 mb layer between approximately 3.1 km AGL and 5.7 km AGL. Evidence of impacts from dry air in anomalous storm structures suggested that water vapor content may have affected particle-scale charge transfer in support of anomalous charge structure development.

3.2 Introduction

Understanding of the catalysts leading to the development of ACSs over NCSs in thunderstorms remains incomplete. A dominant layer of positive (negative) charge in the lower to middle mixed-phase region characterizes ACSs (NCSs), where the mixed-phase region is considered as the layer between 0°C to -40°C (e.g., Bruning et al., 2014; Fuchs et al., 2015; Kuhlman et al., 2006; MacGorman et al., 2005; Rust et al., 2005; Stolzenburg et al., 1998; Wiens et al., 2005; Williams, 1989; Williams et al., 2005). Results of studies addressing the structural and environmental relationships between dominant charge structure polarities are often varied. The consensus is that a combination of competing factors likely plays a role, where emergent factors are those thought to favor increased LWC in the mixed-phase updraft of anomalous storms (Carey and Buffalo, 2007; Carey et al., 2003b; Chmielewski et al., 2018; Fuchs et al., 2018, 2015; Lang and Rutledge, 2011; Williams et al., 2005). The prominent role of LWC in anomalous charging is related to its importance to thunderstorm electrification, where increased LWC supports the enhanced positive charging of precipitation ice hydrometeors that comprise the dominant charge layer in the lower to

middle mixed-phase region (Jayaratne et al., 1983; Reynolds et al., 1957; Saunders et al., 2006; Takahashi, 1978). The conditions thought to primarily support enhanced mixed-phase LWC include a robust updraft and/or environmental factors that limit warm precipitation process efficiency (e.g., Bruning et al., 2014; Carey and Buffalo, 2007; Chmielewski et al., 2018; Fuchs et al., 2018, 2015; MacGorman et al., 2005; Tessororf et al., 2007a,b; Wiens et al., 2005; Williams, 2001; Williams et al., 2005).

However, questions remain concerning the causative roles of environmental conditions and thunderstorm structures in supporting ACS development, including the sensitivity of ACSs to and the relative importance of specific conditions. Understanding of these relationships carries implications in a number of different applications. For instance, it has been observed that in some ACSs, lightning flashes occur at lower altitudes than in their normal counterparts (Fuchs et al., 2016; Fuchs and Rutledge, 2018), influencing how and where nitrogen oxide (NO_x) is produced and may affect ozone concentration (e.g., Chmielewski et al., 2018; Davis et al., 2019) as well as the optical detection of lightning in deep convection from space (e.g., Fuchs et al., 2016; Fuchs and Rutledge, 2018; Murphy and Said, 2020). Further, anomalous storms have been shown to exhibit later development and more limited quantities of CG compared with IC lightning flashes (e.g., Carey and Rutledge, 1998; Lang and Rutledge, 2002; MacGorman et al., 2011; Tessororf et al., 2007a; Wiens et al., 2005), implying variations in risk relationships associated with CG lightning flashes in normal versus anomalous storms (Chmielewski et al., 2018). Proposed relationships between ACSs and thunderstorm microphysics also carry implications for other storm processes driven by specific microphysical relationships, including hail production (Fuchs et al., 2018). Therefore, ACS relationships need to be well understood in order to draw appropriate inferences about detection of lightning and other storm characteristics.

Most anomalous thunderstorms have been documented in the Great Plains and Midwest regions of the US (e.g., Bluestein and MacGorman, 1998; Branick and Doswell III, 1992; Carey and Buffalo, 2007; Carey et al., 2003b; Chmielewski et al., 2018; Curran and Rust, 1992; Fuchs et al., 2018, 2015; Gilmore and Wicker, 2002; Lang and Rutledge, 2002, 2006, 2011; Logan, 2018; Lyons et al., 1998; MacGorman and Burgess, 1994; MacGorman and Nielsen, 1991; Reap and MacGorman, 1989; Seimon, 1993; Smith et al., 2000; Williams et al., 2005), and therefore, most relationships between ACSs, thunderstorm structures, and environmental conditions have been derived from observations from those regions. Several studies examining contrasts between anomalous and normal thunderstorm structures and environments have compared anomalous thunderstorm data in the Great Plains with the normal thunderstorms in Eastern Atlantic and Southeastern US (Fuchs et al., 2016; Fuchs and Rutledge, 2018) and tropics (Lang and Rutledge, 2002). However, contrasts arising from differences between interregional climates are difficult to separate from controls on anomalous versus normal charge structures. Similar issues in interpretation could arise in the convolution of storm morphology in comparisons. Addressing aspects of these problems, Chmielewski et al. (2018) compared normal and anomalous charge structures observed in ordinary convection in West Texas over a 3-hour period, identifying likely complex relationships in controlling environmental parameters as well as consistent differences associated with environmental moisture parameters. However, the variability between charge structures inferred from total lightning data and related conditions in intense deep convection in a limited region have not been similarly addressed.

The first documented cases of ACSs and associated supercell thunderstorm structures in the Southeastern US were discussed in Chapter 2, wherein departures in environmental parameters typically associated with ACSs were noted. Comparisons between rare

anomalous and more typical normal supercells within the Southeast allow the opportunity to evaluate hypotheses concerning the kinematic and microphysical characteristics of and environmental support for ACSs in an atypical parameter space. Additionally, restrictions of the comparison to supercells within the same region reduces complex effects of interregional climate differences and differences in intensity between storm modes that may have affected interpretation of comparisons between storm structures and environmental characteristics in previous studies.

3.2.1 Thunderstorm Electrification

Thunderstorm electrification requires first the transfer of charge between hydrometers and then the organization of these particles into net charge regions. The greatest magnitudes of particle-scale charge transfer are thought to result from rebounding collisions between non-precipitation-sized (small) and riming (large) ice in the presence of supercooled cloud water droplets, referred to as the ice-ice collisional NIC mechanism (Jayaratne et al., 1983; Reynolds et al., 1957; Saunders et al., 2006; Takahashi, 1978). Current understanding of charge transfer suggests that the particle undergoing more rapid depositional growth is characterized by a greater thickness of what is referred to as a semi-liquid layer, resulting in a greater number of hydroxide (OH^-) ions over its surface (Baker and Dash, 1994). More negative ions are thought to transfer from the particle experiencing faster depositional growth during rebounding collisions, leaving the faster-growing particle with positive charge and imparting the slower-growing particle with negative charge (Baker et al., 1987; Baker and Dash, 1989, 1994). Under normal conditions at cooler temperatures and lower LWC, non-riming small ice particles (i.e., ice crystals or aggregates) become positively charged during rebounding collisions as a result of their faster depositional growth over smaller sur-

face areas while riming ice (i.e., graupel or dry hail) particles become negatively charged as a result of slower or less efficient growth (Baker et al., 1987; Baker and Dash, 1994).

Laboratory studies have shown that the magnitude and polarity of charge transfer are controlled by the velocity of the particle collisions, riming rate associated with effective LWC, ice crystal and cloud water size spectra, and cloud and particle temperatures (Avila and Pereyra, 2000; Emersic and Saunders, 2010; Jayaratne et al., 1983; Saunders et al., 2006; Saunders and Peck, 1998), pointing to the importance of riming efficiency in enhancing the depositional growth rate and positive charging of graupel (e.g., Baker et al., 1987; Mitzeva et al., 2005; Saunders et al., 2006). Limited laboratory studies have also suggested that some of the discrepancies in LWC and the reversal temperature at which positive charging rather than negative charging was observed may have resulted from variations in supersaturation that were unaccounted for (e.g., Berdeklis and List, 2001; Emersic and Saunders, 2020, 2010; Saunders et al., 2006). Theoretical models also indicate that the saturation ratio influences the growth of small ice relative to graupel such that graupel charges positively at lower values of effective LWC in the presence of reduced supersaturation (Mitzeva et al., 2005; Saunders et al., 2001; Tsenova et al., 2010).

The simplified tripole model of a normal charge structure only accounts for gravitational sedimentation of recently charged hydrometeors into collective regions of like charge. Neglecting effects of three-dimensional flows and factors such as charge deposition by lightning channels, such simplified charge structure explanations are most applicable near a storm's updraft (e.g., Bruning et al., 2010; Stolzenburg et al., 1998). At temperatures warmer than the charge reversal temperature in the lower mixed-phase region of a storm's updraft, sedimenting positively charged graupel comprises the smaller lower positive charge region of the tripole. At temperatures cooler than the charge reversal temperature,

negatively charged graupel combines with advected negatively charged small ice resulting from rebounding collisions with positively charged graupel below. Positively-charged non-precipitation-sized ice resulting from rebounding collisions with the negatively charged graupel is advected in the updraft and forms the larger upper positive charge region. Whereas NCSs are thought to arise under standard conditions in which LWC is limited below temperatures of approximately -10°C to -15°C (e.g., Saunders et al., 2006; Takahashi, 1978), ACSs are suggested to develop when the LWC in the mixed-phase region of the storm increases to sufficiently lower the charge reversal temperature, deepening the layer over which a dominant positive charge region is observed and seemingly replacing the dominant negative charge region (e.g., Bruning et al., 2014). In this way, charge structures can be more appropriately considered as a continuum of NIC-based structural relationships more than as an inversion from one another (Bruning et al., 2014). While anomalous tripole structures are occasionally observed as a result of emergent lower negative charge regions, these charge regions cannot be explained simply by one-dimensional NIC-based conceptual models since they are observed where all sedimenting, riming ice would charge positively. However, variations in LWC in the updraft and advection have been suggested to contribute to the appearance of a lower negative charge region in the updraft of anomalous storms in addition to negatively charged cloud water resulting from inductive charging following the establishment of sufficient electric fields (Bruning et al., 2014; Kuhlman et al., 2006; Mansell et al., 2005; Wiens et al., 2005).

3.2.2 Suggested Controls on Charge Structure Polarity

Pathways providing for a deeper region of high LWC in the mixed-phase updraft in support of increased high-LWC riming and positive charging have been suggested as

those which limit depletion of cloud water through warm rain processes, including shallow WCDs, robust updrafts, and high concentrations of CCN (e.g., Carey and Buffalo, 2007; Fuchs et al., 2018, 2015; Kuhlman et al., 2006; Lang and Rutledge, 2011; Lang et al., 2016; MacGorman et al., 2005; Mansell and Ziegler, 2013; Tessendorf et al., 2007b; Wiens et al., 2005; Williams et al., 2002; Williams, 2001; Williams et al., 2005; Williams and Stanfill, 2002). Shallow WCDs are thought to reduce the depth over which warm rain can grow and deplete cloud water (e.g., Carey and Buffalo, 2007; Fuchs and Rutledge, 2018; Williams et al., 2005). Similarly, fast updrafts not only transport LWC deeper into the mixed-phase region, they also reduce the time over which cloud LWC can be depleted by warm precipitation growth (e.g., Carey and Buffalo, 2007; Fuchs et al., 2018). Large updrafts supported by high cloud base heights also limit entrainment, maintaining a more robust updraft capable of transporting increased LWC, and may limit precipitation recirculation in the mixed-phase region that would increase competition for LWC (e.g., Fuchs et al., 2018; MacGorman et al., 2011, 2005). High instability metrics, particularly near cloud base and in the lower mixed-phase region, are thought to support these updraft characteristics conducive to ACS development. Other environmental characteristics thought to support ACS development by reducing warm rain efficiency include increased CCN and dry layers near cloud base and in the warm cloud region, each suggested to create competition among growing drops for water vapor in a way that reduces the efficiency of warm rain growth and promotes the availability of LWC in the mixed-phase region (e.g., Chmielewski et al., 2018; Fuchs et al., 2018; Lang and Rutledge, 2002). The size of cloud droplet populations have also been suggested to affect the sign of graupel charging, where it has been observed that smaller droplets favor positive charging of graupel (Avila and Pereyra, 2000). Not all of these environmental conditions were observed in documented anomalous storms or

consistently differentiate anomalous and normal storm environments and it is thought that only some combination and degree of these conditions may be required to result in ACS development (e.g., Carey and Buffalo, 2007; Chmielewski et al., 2018; Fuchs et al., 2018; Lang and Rutledge, 2011).

These microphysical and kinematic effects thought to promote high LWC riming in the mixed-phase region have an assortment of environmental roots that have been explored in detail (e.g., Carey and Buffalo, 2007; Fuchs et al., 2018, 2015; Lang and Rutledge, 2011). Some large-sample studies have identified that anomalous storms often occur in environments with greater CAPE in the mixed-phase region than their normal counterparts, or given greater CAPE observed within specific layers (normalized CAPE, or NCAPE) (Carey and Buffalo, 2007). Environmental measures such as the LCL are used to derive the CBH and the WCD through which warm precipitation growth occurs. Environments in which anomalous storms form have been characterized by higher LCLs and CBHs associated with shallower WCDs and broader updrafts (Carey and Buffalo, 2007; Williams et al., 2005).

Additionally, the combination of environmental contributions to ACSs may be varied and complex, potentially competing with other environmental factors. For instance, it has also been suggested that dry air near cloud base may contribute to entrainment which limits condensational growth of cloud droplets, inhibits growth of warm rain, and effectively increases the availability of small cloud droplets for enhanced ice growth processes, despite also reducing instability and suppressing the updraft (Chmielewski et al., 2018). Owing to these overlaps and complexities, no single parameter may be used as a discriminatory factor in all situations supporting anomalous storms. However, combinations of parameters may be more informative, as Fuchs et al. (2018) have shown that a calculation of warm cloud residence time (WCT) which combines WCD with warm-cloud updraft velocities and

representative particle fall speeds may more effectively identify conditions conducive to enhanced mixed-phase LWC leading to increased positive charging of riming hydrometeors.

3.2.3 Motivation of the Present Study

Kinematic and microphysical relationships with charge structures are compared between a sample of two normal and two anomalous supercells observed in the Southeastern US. The environmental characteristics associated with each are also contrasted in the context of the observations to examine the conditions that supported the unusual development of the ACSs. It is hypothesized that conditions favoring the requisite mixed-phase microphysical state in an anomalous storm may manifest as discernible differences from normal storms in kinematic and microphysical structure. If consistent with conceptual models of anomalous charging based on LWC aspects of NIC theory, elements differentiating Southeastern ACSs in environmental data are expected to include those that promote robust updrafts, limit warm rain efficiency, and support the microphysical parameter space in favor of positive charging of riming hydrometeors. However, environmental distinctions between normal and anomalous charge structures may be more subtle and may not be observed at similar magnitudes as Great Plains anomalous environments. Additionally, the relative infrequency of observed Southeastern ACSs suggests that influential environmental factors are likely uncommon to the Southeast. Departures from relationships gleaned from Great Plains observations may also raise questions concerning additional factors that may promote anomalous charging, including water vapor considerations in particle-scale charging (e.g., Berdeklis and List, 2001; Mitzeva et al., 2005; Tsenova et al., 2010). Observations of Southeastern anomalous supercells and comparisons against their normal counterparts are expected to contribute to understanding of the relative emphases of environmental

contributions to and requirements of NIC-based ACS development as well as fundamental understanding of cloud electrification. Results specific to regional variability may also benefit applications in which lightning flash characteristics related to ACSs may impact optical detection of lightning, accuracy in NO_x modeling, and risk relationships associated with the timing of the onset of CG lightning flashes.

3.3 Data and Methods Statement

Two normal supercell thunderstorms were observed on 6 February 2008 and 11 April 2008 in North AL and two anomalous thunderstorms were observed on 10 April 2009 and 22 April 2017 in South Central TN. The anomalous supercells were documented in Chapter 2. Similar instrumentation, datasets, processing methods, and analysis techniques as described in Section 2.3 were utilized for analysis of the normal supercells introduced herein. These normal supercells in particular were selected for comparison because they were well-observed over periods of similar duration within the sampling domain as the documented anomalous supercells. As supercells, their storm modes were sufficiently matched to the documented anomalous supercells and they also exhibited similar metrics of intensity, including robust updrafts, and in one case, the production of large hail.

Adapted from Figure 2.1, Figure 3.1 documents the path of each of the four supercells through the radar and lightning sampling domain. Tracking information used for each supercell case and the LMA sensor thresholds applied for lightning flash clustering are documented in Table 3.1. The progression of these storms over their respective analysis periods is provided in Appendix B.

While total lightning and radar data remained similar between the two sets of storms, two datasets were added by which the storms were compared and additional lightning metrics were utilized.

First, CG data from the US National Lightning Detection Network (NLDN, Cummins and Murphy, 2009) were incorporated to compare lightning properties between the storms in more detail. Although the NLDN was upgraded to include detection of IC lightning flashes in 2006, it has historically provided information on the detection of CG lightning flashes over the continental US. Data include information about the timing, location, number of strokes, polarity, and peak current of detected lightning flashes, with reported CG lightning flash detection efficiency of $\geq 90\%$ within the continental US within the period of data considered in this study (Biagi et al., 2007; Cummins and Murphy, 2009). While NLDN data discriminate between IC and CG lightning flashes, studies have shown that IC lightning flashes are occasionally misclassified as CGs, where errors are most often found in lightning flashes labeled as CGs with positive peak current magnitudes of < 15 kA and negative peak current magnitudes of > 10 kA (Biagi et al., 2007; Fleenor et al., 2009; Zhu et al., 2016). As a result, NLDN CG data used in this study were filtered to remove lightning flashes with peak currents of between > -10 kA and < 15 kA. In addition to the use of total lightning data detected by the NALMA as described in Section 2.3, total lightning flash rate data were calculated over the analysis period of each supercell by taking the one-minute average lightning flash count in two-minute periods (e.g., Schultz et al., 2009). The storm total IC:CG lightning flash ratio was calculated as well as the total percentage of CGs that were positive. With the exception of these two quantities and where otherwise noted, all other lightning properties, including total lightning flash rate, were determined exclusively using NALMA observations. Additionally, “lightning” or “lightning flash rate”

will be used to refer to further discussion of “total lightning” or “total lightning flash rate” for simplicity.

The second dataset introduced in this study includes aerosol data obtained from the Modern-Era Retrospective analysis for Research and Applications, Version 2 (MERRA-2, Gelaro et al., 2017). This reanalysis dataset was used in place of PM_{2.5} concentrations similar to what was reported in Chapter 2 to more specifically assess the concentration of aerosols that may have contributed as CCN. MERRA data are available every three hours over a domain with $5/8^\circ$ longitude and $1/2^\circ$ latitude spacing. Vertical profiles of aerosol mixing ratio data corresponding to dust with particle radii of between $0.1 \mu\text{m}$ and $1.8 \mu\text{m}$, hydrophilic black carbon with particle radius of $0.35 \mu\text{m}$, hydrophilic organic carbon with particle radius of $0.35 \mu\text{m}$, sulphate with particle radius of $0.35 \mu\text{m}$, and sea salt with particle radii of between $0.1 \mu\text{m}$ and $1.5 \mu\text{m}$ were selected from the analysis period prior to the time each storm was first sampled. These data were converted to mass concentration, summed in the vertical, and averaged over 12 data points associated with the northern extent of the sampling domain for the anomalous storms or the southern extent of the sampling domain for the normal storms. The final profiles used are representative of analysis locations bounded within the longitudinal range of -87.5° west and -85.625° west and the latitudinal range between 35.0° north and 36.0° north for the anomalous cases to the north or the latitudinal range of 33.5° north to 35.4° north for the normal cases to the south.

Finally, environmental data differed somewhat for the normal supercell cases compared with the dataset reported in Section 2.3. As in the anomalous 10 April 2009 case, model analysis from the RUC was utilized for each of the 2008 cases, though the analysis grid spacing was 20 km instead of 13 km. Summary descriptions of the synoptic to meso- α

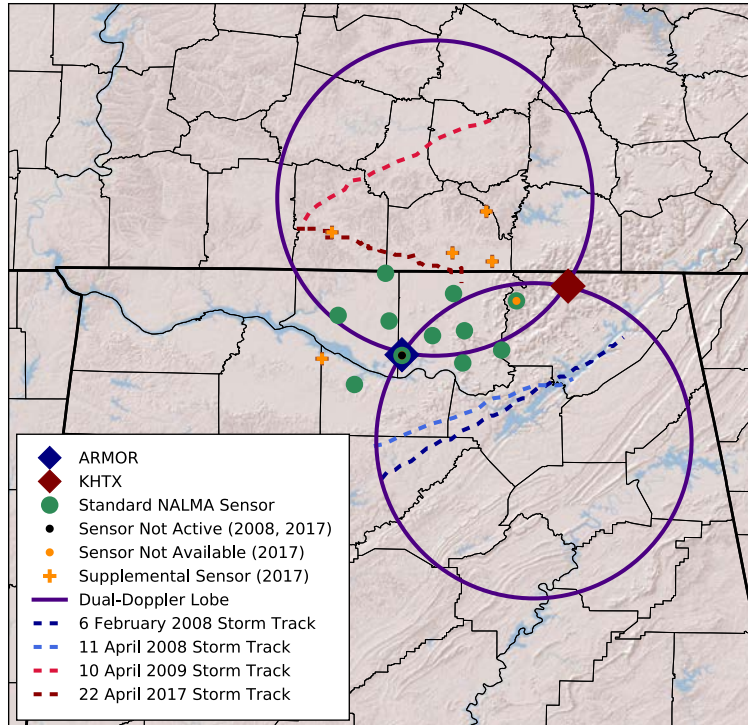


Figure 3.1: Domain over which supercells were analyzed. ARMOR and KHTX radar sites (dark blue and dark red diamonds), permanent and supplemental NALMA sensors (green circles and orange crosses) with notes on special operating conditions pertaining to 2008 and 2017 cases (black and gold dots), the 30°C beam-crossing area of the dual-Doppler domain established between ARMOR and KHTX (purple rings), and storm centroid tracks (red and blue dashed lines) are shown. Adapted from Figure 2.1.

background in which each storm developed and model sounding profiles are provided in Appendix B. Environmental data pertaining to each case are provided in Table 3.2.

3.4 Thunderstorm Properties

Charge structure and updraft kinematics and microphysics are intrinsically related through the development of thunderstorm electrification. The following section discusses how these properties related in the four supercells before comparing the differences observed between normal and anomalous supercells.

Table 3.1: Normal and anomalous supercell analysis information. Adapted from Table 2.1.

Case Date	Analysis Period [UTC]	Min. Stations Required for lightning flash Clustering	Min. Tracking Reflectivity [dBZ]	W., E., S., N. Expansion [km]
6 Feb 2008	1002-1123	6	20	10, 35, 20, 25
11 Apr 2008	1844-1956	6	30	10, 20, 5, 15
10 Apr 2009	1712-1825	6	30	10, 25, 12, 10
22 Apr 2017	2056-2206	7	20	5, 25, 10, 15

Table 3.2: Environmental parameters obtained from a model sounding at the location of each normal and anomalous supercell an hour prior to its analysis period. Note that the height of the LCL and instability metrics of CAPE and NCAPE were derived from surface-based parcels. Adapted from Table 2.2.

	6 Feb 2008	11 Apr 2008	10 Apr 2009	22 Apr 2017
Model analysis sounding time	0900 UTC	1800 UTC	1600 UTC	2000 UTC
Surface temperature [°C]	19.5	24.9	20.6	22.2
Surface dew point temperature [°C]	17.8	18.9	16.6	18.2
Height of env. 0°C (ML) [m]	3860	4365	3105	3617
Height of env. -40°C [m]	9640	9810	8177	9449
Wet bulb zero height [m]	3403	3619	2336	3192
PW in sfc. to 400 hPa layer [cm]	3.5	3.8	2.3	3.2
Mean mixing ratio in lowest 100 hPa [g kg ⁻¹]	11	13	11	12
Midlevel RH (700 hPa - 500 hPa layer) [%]	55	41	21	36
Mean RH through full depth [%]	68	54	41	54
LCL height [m]	585	1022	643	900
WCD = ML - LCL [m]	3280	3340	2460	2720
CAPE [J kg ⁻¹]	447	1214	2123	1453
NCAPE [m s ⁻²]	0.06	0.11	0.19	0.14
0-6 km AGL shear [m s ⁻¹]	29	25	32	24

3.4.1 Charge Structure and Lightning Flashes

The difference between the relative vertical frequencies of positive and negative sources observed in each storm highlights two primary charge layers near the updraft in each case. In the anomalous supercells (Figures 3.2a and 3.2b), the lower dominant charge region in the lower to middle mixed-phase region was inferred as positive with a primary negative charge layer inferred aloft in the colder mixed-phase and glaciated regions. This trend was reversed as expected in the normal storms (Figures 3.2c and 3.2d) in which the lower dominant charge layer in the lower to middle mixed-phase region was negative with a positive charge layer aloft, in the upper mixed-phase and glaciated regions.

In general, charge layers within the updraft were better defined in the anomalous 10 April 2009 (Figure 3.2a) and normal supercells (Figures 3.2c and 3.2d), while relative differences in positive and negative charge layers were more diffuse in the anomalous 22 April 2017 supercell (Figure 3.2b). As discussed in Section 2.5.3, the anomalous 22 April 2017 supercell exhibited charge structure complexity throughout the three-dimensional updraft, potentially associated with microphysical variability in horizontally-adjacent regions. The maximum lightning flash rates in the 22 April 2017 supercell were two to three times as large as observed in the other storms, further indication that many small lightning flashes were occurring. As Zhang and Cummins (2020) discussed, small lightning flashes may reduce the GLM detection efficiency, potentially contributing to reduced detection efficiency in anomalous storms by spaceborne optical lightning detection instrumentation (Fuchs and Rutledge, 2018; Murphy and Said, 2020). Numerous small lightning flashes in the anomalous 22 April 2017 supercell were associated with complex arrangement of small charge pockets. This complexity contributed to overlap in charge regions in each layer, though in the net, positive charge was more dominant in the lower mixed-phase region while negative charge

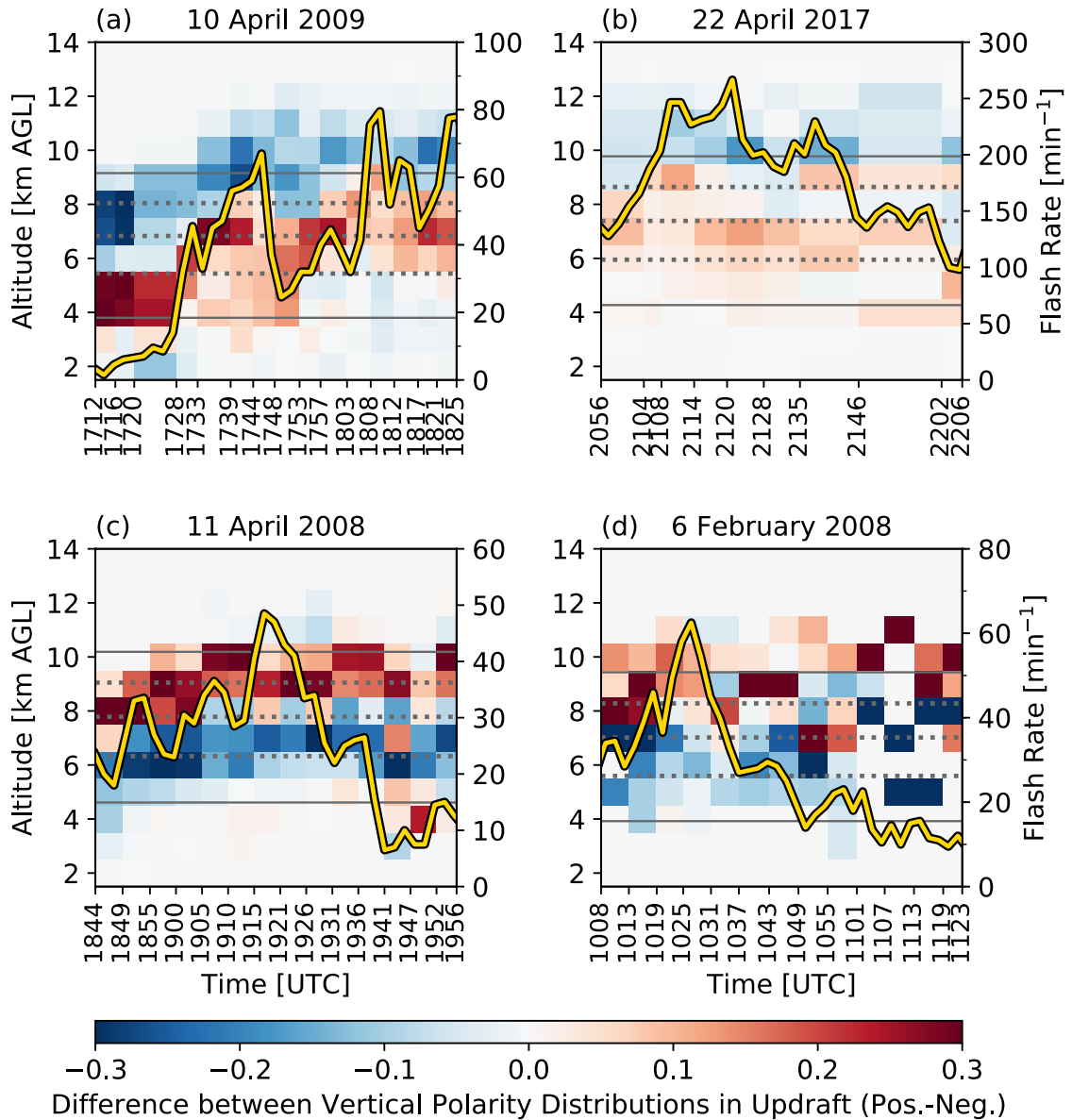


Figure 3.2: The relative difference between the vertical frequency of positive and negative sources located within updrafts of $\geq 5 \text{ m s}^{-1}$ of the (a) anomalous 10 April 2009, (b) anomalous 22 April 2017, (c) normal 11 April 2008, and (d) normal 6 February 2008 supercells. Red (blue) colors indicate that a greater vertical frequency of positive (negative) sources was located in a given layer, where altitude is plotted along the left vertical axis of each panel. Approximate mixed-phase region boundaries of 0°C and -40°C are marked (solid gray lines) with -10°C increments plotted between (dashed gray lines). The lightning flash rate time series associated with each cell (outlined yellow line) is shown as well, corresponding to lightning flash rate values along the right vertical axis of each panel.

was more dominant in the upper mixed-phase and glaciated regions, consistent with an ACS.

The charge layers in the anomalous 10 April 2009 supercell exhibited more vertical variation than those in the other storms. Development was captured during the analysis period of the 10 April 2009 storm whereas all other storms were analyzed after they had already reached maturity (Chapter 2). As the updraft developed in the 10 April 2009 supercell, lightning flash rates both steadily increased and the net charge layers associated with charged hydrometeor populations were lofted to higher altitudes within the storm (Figure 3.2a). Charge layers remained relatively distinct in the anomalous supercells as they retained robust updrafts through the end of their analysis periods, evidenced by increasing or high lightning flash rates. However, initial decaying phases were captured in the analysis periods of each of the normal supercells as reflected by steadily declining lightning flash rates. As these storms weakened, fewer lightning flashes were observed from which to derive charge structure. As a result, the charge polarity in a given layer became more poorly defined after 1941 UTC in the 11 April 2008 supercell and after 1037 UTC in the 6 February 2008 supercell (Figures 3.2c and 3.2d). After 1107 UTC in the 6 February 2008 case, very few lightning flashes occurred and were mostly located outside of the updraft (not shown), resulting in sparse, strong polarity signals (Figure 3.2d).

In addition to charge structure differences, the four storms exhibited differences in lightning flash properties (Table 3.3). It has been documented that the onset of CG lightning flashes in anomalous storms may be delayed owing to the later development of the lower negative charge region needed to facilitate ground lightning flashes compared with the development of the lower positive charge region in a normal storm (e.g., Carey and Rutledge, 1998; MacGorman et al., 2011; Tessendorf et al., 2007b; Wiens et al., 2005), as well as that

relatively fewer CGs may occur at all given either a weak or absent lower negative charge region (Lang and Rutledge, 2002; Tessendorf et al., 2007b). These conditions are thought to contribute to the higher ratios of IC to CG lightning flashes (IC:CG ratio) typically observed in Great Plains anomalous storms (e.g., Boccippio et al., 2001; Carey and Rutledge, 1998; MacGorman et al., 1989). In addition, it has been observed that compared with normal storms, anomalous storms tend to exhibit higher fractions of positive CG versus negative CG lightning flashes (e.g., Carey and Buffalo, 2007; Carey et al., 2003b; Lang and Rutledge, 2002; Williams et al., 1999). In the two anomalous supercells documented herein, not only were the maximum total lightning flash rates higher, the IC:CG ratios were considerably greater at 60.5 and 139.6 compared with 7.0 and 15.2 observed in the normal supercells. These values are consistent with IC:CG ratios observed in Great Plains storms documented in the literature in which lightning flash rates and IC:CG rates were high (e.g., Boccippio et al., 2001). Further, the percentage of positive CGs observed in the anomalous storms were 20% and 60% compared with 5% and 6% positive CG lightning flashes observed in the normal storms. While the percentage of positive CGs observed in the anomalous 10 April 2009 supercell was lower than observed in the anomalous 22 April 2017 supercell, it was still greater than the typical maximum value of 10% positive CGs within a normal storm (e.g., Carey et al., 2003b) and generally consistent with Great Plains anomalous storm characteristics.

3.4.2 Kinematics

The sizes of the updrafts in each of the four storms represented as updraft volume (Figures 3.3a and 3.3b) reflected changes in intensity that could be inferred from the time series of vertical charge structures (Figure 3.2). Of the four storms, the anomalous 10 April

Table 3.3: Total lightning and CG lightning flash properties associated with each supercell. Total lightning properties, including IC lightning, are reported as observed by the NALMA, whereas CG properties are reported as observed by the NLDN.

	Normal 6 Feb 2008	Normal 11 Apr 2008	Anomalous 10 Apr 2009	Anomalous 22 Apr 2017
Peak total lightning lightning flash rate [min^{-1}]	62	48	79	266
IC:CG ratio	7.0	15.2	60.5	139.6
Percent positive CG [%]	6	5	20	60

2009 supercell updraft volume, and particularly its 10 m s^{-1} updraft volume, exhibited the most change over the course of the storm analysis period (Figures 3.3a and 3.3b) as its development and maturation were observed. At 1757 UTC, approximately 45 minutes into the analysis period, its charge structure became more steady (Figure 3.2a). Up to this time, both measures of updraft volume in the anomalous 10 April 2009 supercell were comparable to the anomalous 22 April 2017 and normal 6 February 2008 supercells. However, as it continued to intensify, its 5 m s^{-1} (10 m s^{-1}) updraft volume reached a relative maximum that was at least 497 km^3 (522 km^3) greater than that of the other storms (Figures 3.3a and 3.3b). The updraft volumes of the normal 11 April 2008 supercell were noticeably lower than the other storms over most of the course of its analysis period. The updraft was largest in the normal 11 April 2008 supercell at 1905 UTC, approximately 20 minutes after its analysis period began, after which time it began to decrease steadily. Its lightning flash rate decreased after 1915 UTC (Figure 3.2c), approximately 45 minutes into the analysis period as the 10 m s^{-1} fell below 50 km^3 . The overall charge structure then began to exhibit more variability after 1941 UTC (Figure 3.2c), approximately 55 minutes into the analysis period as the 10 m s^{-1} updraft volume decreased to 3 km^3 (Figure 3.3b). Whereas decreasing kinematic support was evident in the normal 11 April 2008 supercell, the low

lightning flash rates and obscured gross charge structure observed in the normal 6 February 2008 supercell (Figure 3.2d) coincided with 5 m s^{-1} updraft volumes comparable to those observed in the anomalous 22 April 2017 supercell (Figure 3.3a) and decreasing 10 m s^{-1} updraft volume that reached a minimum of 249 km^3 , approximately 153 km^3 smaller than observed in the anomalous 22 April 2017 supercell (Figure 3.3b). Although it exhibited similar gross kinematic properties as observed in the normal 6 February 2008 supercell, the anomalous 22 April 2017 supercell exhibited a minimum lightning flash rate of 90 min^{-1} compared with the 10 min^{-1} minimum observed in the normal 6 February 2008 supercell.

The altitudinal frequency of vertical velocity in each storm in Figures 3.3c to 3.3f was related to a range of velocity structures observed between the four supercells. The greatest updraft velocities were observed in the anomalous 10 April 2009 supercell near 50 m s^{-1} (Figure 3.3c), while the weakest maximum updraft velocities were observed in the normal 11 April 2008 supercell with maxima near 25 m s^{-1} (Figure 3.3e). These extrema are consistent with the trends in total updraft size observed in each storm. Just as updraft sizes were generally most similar in the anomalous 22 April 2017 and normal 6 February 2008 supercells (Figures 3.3a and 3.3b), velocities in each exhibited similar extrema with maximum values near 30 m s^{-1} (Figures 3.3d and 3.3f).

3.4.3 Precipitation Ice Microphysics

The total PIM associated with the updraft (Figure 3.4a) trended similarly with changes in updraft intensity as observed through updraft properties and inferred from charge structure observations (Figures 3.2 and 3.3). The anomalous 22 April 2017 supercell had a consistently greater PIM with a value exceeding $4.5 \times 10^8 \text{ kg}$ throughout the duration of its analysis period. The total PIM observed in the anomalous 10 April 2009 supercell

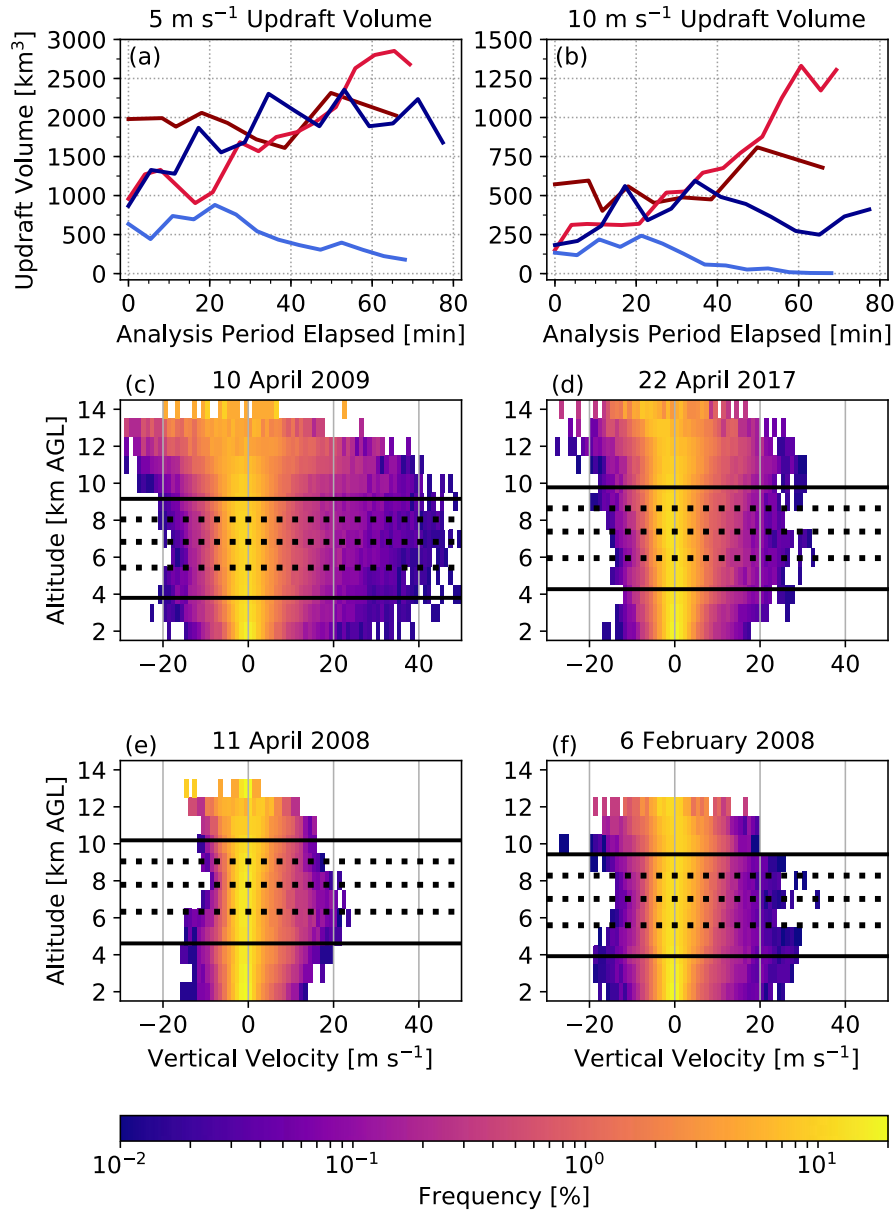


Figure 3.3: Time series of (a) 5 m s⁻¹ and (b) 10 m s⁻¹ updraft volumes corresponding to the anomalous 10 April 2009 (light red line), anomalous 22 April 2017 (dark red line), normal 6 February 2008 (dark blue line), and normal 11 April 2008 (light blue line) supercells are shown. Composite altitudinal frequency diagrams of vertical velocity in the (c) anomalous 10 April 2009 supercell, (d) anomalous 22 April 2017 supercell, (e) normal 11 April 2008 supercell, and (f) normal 6 February 2008 supercell are shown in colorfill. Approximate mixed-phase region boundaries of 0°C and -40°C are marked (solid black lines) with -10°C increments plotted between (dashed black lines) are shown in (c-f).

increased with the intensity of the updraft, with total PIM comparable to that observed in the anomalous 22 April 2017 supercell by approximately 35 minutes into the analysis period at 1748 UTC, and exceeding the anomalous 22 April 2017 total PIM 20 minutes later at 1808 UTC. Despite similar kinematic trends over time, more PIM was observed in the anomalous 22 April 2017 supercell updraft than in the normal 6 February 2008 updraft (Figures 3.3a, 3.3b, and 3.4a). This is attributed to the greater average hail contributions to total PIM observed in the anomalous 22 April 2017 supercell of 29% compared with the 2% observed in the normal 6 February 2008 supercell (Figure 3.4b). Consistent with the observed hydrometeor type means, the normal 6 February 2008 supercell was the only one of the four from which large hail was not reported, while reports of up to 4.44 cm in diameter were associated with each of the other three storms. Although the normal 11 April 2008 supercell was composed of a relatively large fraction of hail, particularly in the lower mixed-phase region (Figure 3.4b), it was characterized by the lowest total updraft PIM of the four supercells for most of its analysis period (Figure 3.4a).

The altitudinal frequency of PIM per storm grid volume reflects observed hydrometeor fractions (Figures 3.4c to 3.4f). The anomalous 22 April 2017 storm exhibited greater frequencies of higher PIM throughout the mixed-phase region and particularly above -10°C (Figure 3.4d), consistent with a high total updraft PIM (Figure 3.4a) and relatively higher average hail fraction (Figure 3.4b). Between the two normal storms which had comparatively lower total PIM values than the anomalous storms (Figure 3.4a), the normal 11 April 2008 supercell had greater frequencies of higher PIM values above the level of -10°C as well (Figure 3.4e), associated with a comparatively higher hail fraction than observed in the normal 6 February 2008 supercell (Figure 3.4b). Although the average hail fraction in the anomalous 10 April 2009 supercell was relatively low at 7% (Figure 3.4b), it exhibited high

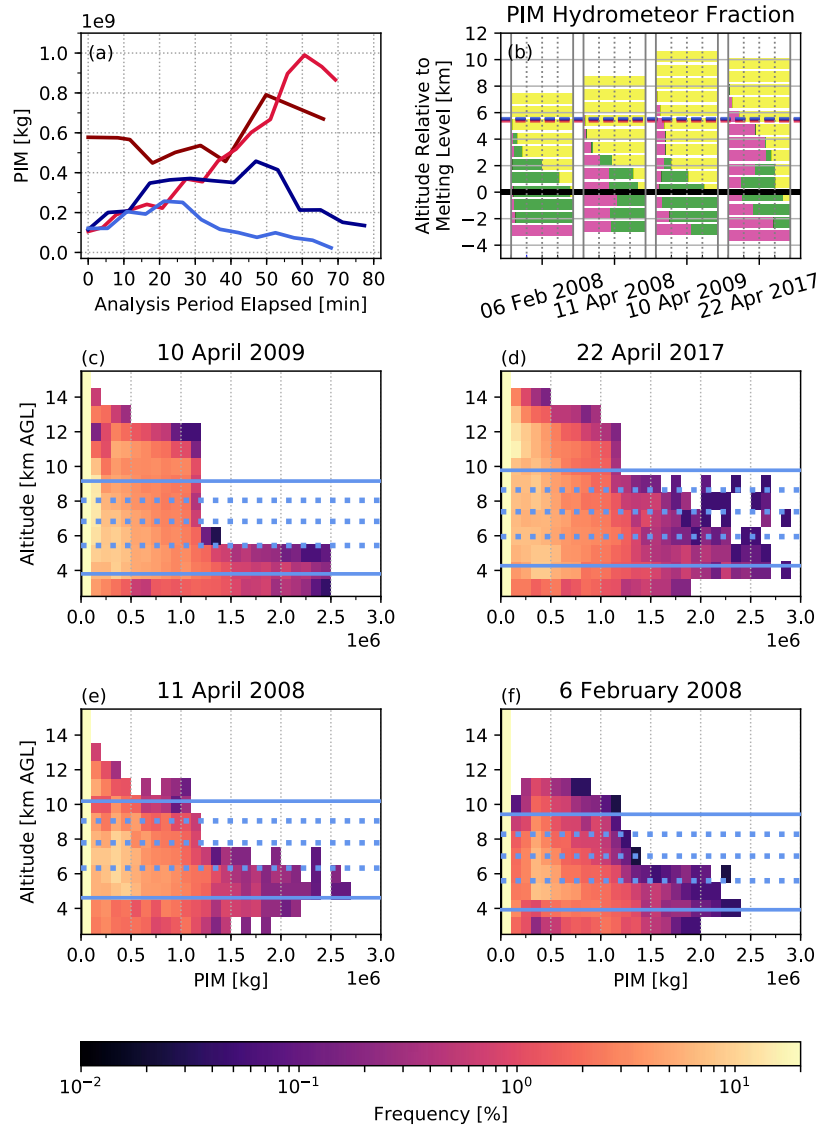


Figure 3.4: Time series of (a) total PIM within updraft of $\geq 5 \text{ m s}^{-1}$ corresponding to the anomalous 10 April 2009 (light red line), anomalous 22 April 2017 (dark red line), normal 6 February 2008 (dark blue line), and normal 11 April 2008 (light blue line) supercells are shown. (b) The fractions of PIM within updraft of $\geq 5 \text{ m s}^{-1}$ at each altitude in each storm attributed to LD graupel (yellow), HD graupel (green), and hail or large drops and hail (pink) categories are shown as a stacked bar charts. Composite altitudinal frequency diagrams of PIM within updraft of $\geq 5 \text{ m s}^{-1}$ in the (c) anomalous 10 April 2009 supercell, (d) anomalous 17 April 2017 supercell, (e) normal 11 April 2008 supercell, and (f) normal 6 February 2008 supercell are shown in colorfill. Approximate mixed-phase region boundaries of 0°C and -40°C are marked (solid blue lines) with -10°C increments plotted between (dashed blue lines) are shown in (c-f).

total updraft PIM after approximately 35 minutes, comparable to and eventually exceeding total PIM observed in the anomalous 22 April 2017 supercell (Figure 3.4a). Given the relative lack of hail, the total PIM was attributed to increased graupel quantities within the storm, especially LD graupel. Generally, PIM within the glaciated region extending above the height of -40°C was associated with LD graupel or some small fraction of hail as a result of the microphysical properties of each hydrometeor type represented in the HID algorithm. The two anomalous supercells were observed to have greater PIM quantities above the mixed-phase region (Figures 3.4c and 3.4d, consistent with higher mean LD graupel fractions observed in each (Figure 3.4b). However, the anomalous 10 April 2009 supercell was observed to have the greatest frequencies of higher PIM in the glaciated region (Figure 3.4c), even compared with the other anomalous supercell (Figure 3.4d), indicating that it contained more LD graupel per storm volume than the other supercells, particularly in the mixed-phase and glaciated regions.

3.5 Storm Comparisons

The following section discusses comparisons of the supercells' kinematic and microphysical structures. These comparisons are first used to identify common features in Southeastern anomalous storms that differentiate them from normal storms. Combined with information from environmental analyses, structural observations are used to explore support for the microphysical processes thought to be required for the development of ACSs.

3.5.1 Updraft Structure

The following discussion considers details of and comparisons between the updraft characteristics indicated from observations in Figure 3.3.

3.5.1.1 Updraft Speed

Vertical velocity distributions (Figures 3.3c to 3.3f) indicated discrepancies in updraft speeds and vertical structure of the updrafts between storms. Despite the range in extrema exhibited between the four cases, including differences between the anomalous storms, the velocity distributions of the anomalous supercells each exhibited higher frequencies of greater updraft speeds above 9 km than those of the normal storms. Part of these structural differences can be attributed to storm depth, where the normal storms were observed to be relatively less deep than the anomalous supercells with differences in 18 dBZ echo top heights ranging from 1.2 km to 2.7 km (Figure 3.5b). However, analysis of the peak vertical winds indicates that the depths over which relative maxima were experienced were not deeper in anomalous storms, though their locations within the storms was offset from that of the normal storms (Figure 3.5b).

Notched box plots shown in Figure 3.5 were used to examine the top 25% of the maximum vertical motion observed in each layer (layer-maximum updraft speeds) and the altitudes at which the top 25% of layer-maximum updraft speeds occurred. Notched box plots illustrate the confidence around the median of a distribution and can be used to identify whether distributions are similar based on the comparative notch location and shape within each box. Considering first the relative distributions of peak updraft speeds in Figure 3.5a, trends were consistent with updraft speed distributions observed in Figure 3.3. The peak updraft speeds in the anomalous 10 April 2009 supercell were comparatively higher than observed in the other storms with a minimum difference of 15.4 m s^{-1} in the median. Although the notches in the normal 6 February 2008 supercell and the anomalous 22 April 2017 supercell were least offset, none of the notches overlapped, indicating the medians of peak layer-maximum updraft speeds were each significantly different from each other even

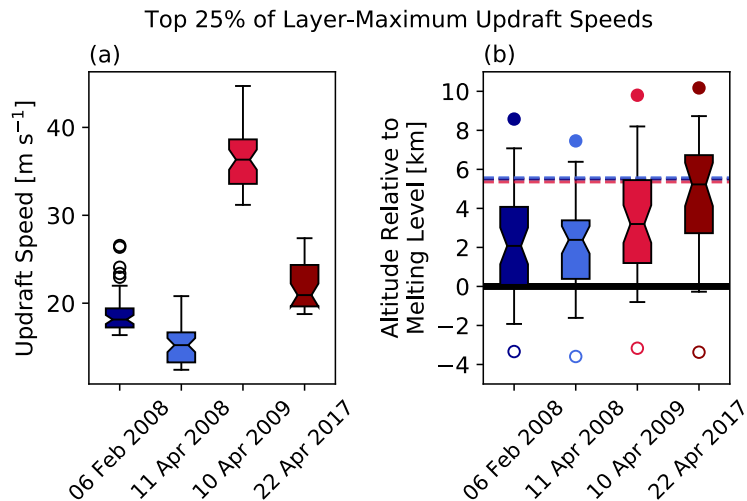


Figure 3.5: Notched boxplots showing (a) the top 25% of maximum positive vertical velocity values observed in each layer and (b) the distribution of the altitudes of the layers in which they were observed relative to the melting level are shown for each of the four cases according to the abscissa labels. The edges of each box depict the 25th and 75th percentiles of the distribution while the center line shows the median. The whiskers are drawn to 1.5 times the interquartile range, while open circles show outliers in the data. The notches, or narrowing, around the median are used to depict its significance. Overlapping notches between boxes indicate that the medians of two distributions are not statistically significantly different. Approximate mixed-phase region boundaries of -40°C relative to the melting level are marked (dashed lines color-coded by storm case). The average 18 dBZ echo top height (closed circles) and cloud base height (open circles) associated with each storm are plotted in (b) as well.

as some distributions overlapped. The anomalous 10 April 2009 distribution in particular exhibited no overlap with that of the other storms, consistent with inferences drawn from the vertical velocity distributions shown in Figure 3.3 that it represented the relative maximum in updraft speeds in the dataset.

Higher updraft speeds were observed above the mixed-phase region in the anomalous supercells (Figures 3.3c and 3.3d) compared with the normal supercells (Figures 3.3e and 3.3f), likely associated in part with differences in storm depth. Figure 3.5b shows the

distributions of the altitudes of the peak layer-maximum updraft speeds relative to the melting level observed in each case, facilitating a more direct comparison of the spatial distribution of updraft speeds within the mixed-phase region. Vertical distributions of the peak layer-maximum updraft speeds exhibited more overlap than was observed in the distributions of the speeds themselves, with most notable differences observed in the location of peak layer-maximum updraft speeds relative to the mixed-phase region between the two subsets. The majority of each of the normal storm's peak layer-maximum updraft speeds were confined to the mixed-phase region with less than 10% located at heights above -40°C , while over 25% of peak layer-maximum updraft speeds in the anomalous supercells were observed at heights above -40°C . Further, less than 5% of each of the anomalous storm's peak layer-maximum updraft speeds were observed within the warm cloud region. By contrast, at least 15% of the normal storms' peak layer-maximum updraft speeds were located within the warm cloud region.

It is evident that the anomalous 10 April 2009 supercell was characterized by a comparatively stronger updraft in a deeper storm. However, bulk updraft characteristics were most comparable between the normal 6 February 2008 supercell and the anomalous 22 April 2017 supercell with regard to the range and depth of observed velocities (Figure 3.3), though the anomalous supercell exhibited faster peak velocities (Figure 3.5a). The distinct separation in the notches between anomalous and normal box plots in Figure 3.5b informs that the medians of the vertical distributions of their peak updraft speeds were significantly different at the 95th% confidence level, indicating the contrast in structure of these two individual updrafts and two sets of storms. While this could be attributed to differences in storm size, the difference between the 75th percentile value of altitudes and the 18 dBZ ET height was 1.1 km lower in the anomalous 22 April 2017 supercell than that of the

normal 6 February 2008 supercell. A difference in 18 dBZ ET of 1.6 km indicated that peak level-maximum updraft speeds were shifted higher in the 22 April 2017 supercell relative to storm top and were not only higher because of a higher storm top.

3.5.1.2 Updraft Size

With the exception of the normal 11 April 2008 supercell, it is evident from Figures 3.3a and 3.3b that total updraft sizes were comparable between three of the supercells for a substantial portion of their analysis periods, particularly considering their 5 m s^{-1} updrafts. However, differences in updraft area with height were observed in addition to differences in distributions of updraft speed when average vertical profiles of updraft areas were compared (Figure 3.6).

Each anomalous supercell was characterized by both a larger average 5 m s^{-1} area and average 10 m s^{-1} area through the full depth of each storm compared with the normal 11 April 2008 supercell (Figures 3.6a and 3.6c). However, the relationships were more variable when the anomalous storms were compared with the normal 6 February 2008 supercell, in which the 5 m s^{-1} updraft area was larger throughout most of the middle mixed-phase region, approximately between -5°C and -25°C , than observed in the anomalous supercells. However, the 10 m s^{-1} updraft area, considered as a demarcation of the updraft core, was greater in the anomalous storms in the mixed-phase region than in the normal storm, particularly in the upper mixed phase and glaciated regions, above the height of -20°C .

Comparing the differences in the vertical distributions of anomalous and normal storm updraft areas in Figures 3.6a to 3.6d, it is evident that the area of the updraft core was larger at higher altitudes in the anomalous storms than in the normal storms. Combined with information from Figure 3.3, these comparisons indicate that the updraft core was not

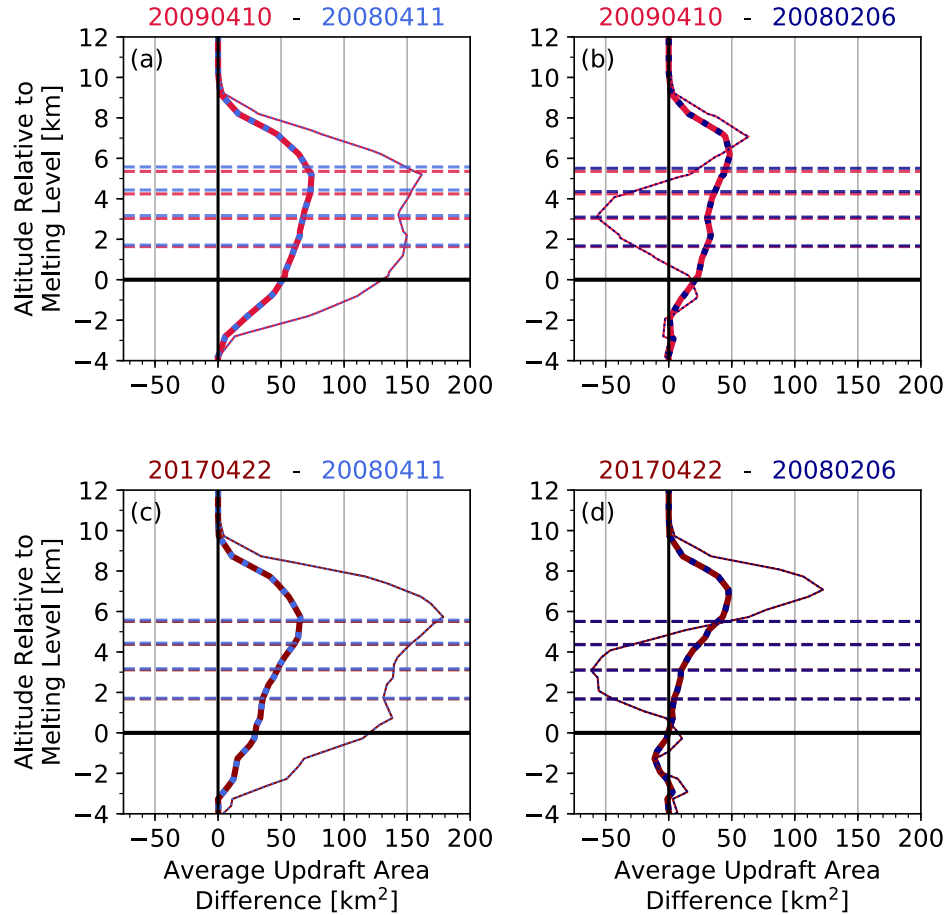


Figure 3.6: Difference plots of the mean 5 m s^{-1} (narrow line) and 10 m s^{-1} (bold line) updraft areas relative to the melting level between the (a) anomalous 10 April 2009 and normal 11 April 2008 storms, (b) anomalous 10 April 2009 and normal 6 February 2008 storms, (c) anomalous 22 April 2017 and normal 11 April 2008 storms, and (d) anomalous 22 April 2017 and normal 6 February 2008 storms. Approximate mixed-phase temperatures of -10°C to -40°C in -10°C increments are marked (dashed lines, where red color corresponds with the anomalous case and blue color corresponds with the normal case).

only stronger in the upper mixed-phase region of anomalous storms but was also larger than in normal storms.

3.5.2 Mixed-Phase Microphysics

The quantity and vertical distribution of PIM in Figure 3.4 was used for comparison between cases particularly because of its relationship with the dominant layer of the overall charge structure and implications related to ice-ice collisional NIC. Specifically, dominant regions of positive (negative) charge are expected to be associated with regions of riming hydrometeors, or greater precipitation ice mass in anomalous (normal) storms. In anomalous storms in particular, it is expected that more efficient riming of graupel particles takes place in higher liquid water content to promote positive charging of the riming hydrometeors. Therefore, understanding differences in large ice quantities and distributions between normal and anomalous storms may provide insight as to how anomalous storm development differed.

3.5.2.1 PIM in the Updraft

The anomalous 22 April 2017 supercell contained the most PIM within the updraft through the majority of the elapsed analysis period compared with the normal storms, where only the maximum values of updraft PIM in the normal 6 February 2008 briefly approached the anomalous 22 April 2017 updraft PIM minima (Figure 3.4). During the first 20 minutes of its development, the anomalous 10 April 2009 updraft PIM was similar to that of both normal storms, with magnitudes remaining comparable to those of the normal 6 February normal supercell over the first 40 minutes in total. As the anomalous 10 April 2009 supercell continued to strengthen, its updraft PIM magnitudes surpassed the relatively high updraft

PIM magnitudes maintained by the anomalous 22 April 2017 supercell. As expected, these trends generally correspond with trends and variations in updraft size exhibited in each of the four supercells (Figures 3.3a and 3.3b).

3.5.2.2 Hydrometeor Contributions

While hail, HD graupel, and LD graupel are all rimed ice categories, hail and HD graupel in particular represent the larger, denser, and more efficient riming hydrometeors. Appreciable hail fractions were observed in all but the normal 6 February 2008 supercell (Figure 3.4b), consistent with generally lower frequencies of higher PIM values at all levels in the normal 6 February 2008 supercell when comparing vertical PIM distributions in all storms (Figures 3.4c to 3.4f). These HID analyses were consistent with a lack of hail reports associated with the normal 6 February 2008 supercell, indicative of less efficient riming processes therein resulting from some possible combination of reduced mixed-phase LWC or a kinematic environment that did not favor sufficient residence time of riming particles for hail growth.

Hail contributed the most to PIM within the updraft in the anomalous 22 April 2017 supercell with fractions of approximately 50% or greater in the upper mixed-phase region (Figure 3.4b), consistent with its generally higher updraft PIM quantity over the analysis period (Figure 3.4a) and reflected by high values of PIM observed throughout the mixed-phase region (Figure 3.4d). Coupled with multiple reports of large hail of up to 4.44 cm in diameter, these metrics indicated that efficient riming processes within the supercell may have been supported by sufficient mixed-phase LWC or conducive kinematic structure and likely extended throughout a substantial depth of the mixed-phase region.

The smaller normal 11 April 2008 supercell was characterized by a relatively smaller, weaker updraft as well as the least PIM compared with the other storms (Figure 3.4a). However, its precipitation ice composition was similar to that of the anomalous 22 April 2017 supercell in the lower mixed-phase region with between 25% to 50% hail composition in multiple layers. Comparing the normal supercells, higher frequencies of greater PIM values at any depth in the mixed phase region in the normal 11 April 2008 supercell was consistent with comparatively higher riming efficiency than indicated in observations of the normal 6 February 2008 supercell. PIM frequencies within the lower mixed-phase region (below the level of -20°C) of the normal 6 February 2008 and anomalous 22 April 2017 supercells (Figures 3.4d and 3.4e) exhibited the strongest similarities, indicating similar ice precipitation efficiency at warmer mixed-phase temperatures.

Despite observations of large hail associated with the anomalous 10 April 2009 supercell, LD graupel was the primary contributor to PIM. This difference resulted in the generally higher frequencies of lower PIM values observed throughout the mixed-phase region (Figure 3.4c) compared with lower frequencies of higher PIM values observed in the anomalous 22 April 2017 supercell (Figure 3.4d). Compared with all other supercells, the anomalous 10 April 2009 supercell was characterized by lower fractions of the larger, denser, more efficient riming hydrometeors in the lower mixed-phase region and by comparison with the anomalous 22 April 2017 supercell, exhibited lower fractions of larger riming hydrometeors in the upper mixed-phase region as well (Figure 3.4b). Even so, on average, the anomalous 10 April 2009 supercell had $\geq 1.9\text{e}7$ kg more PIM associated with hail and HD graupel in the lowest 3 km of the mixed-phase region of the updraft compared with the same region in the normal supercells (not shown). However, it also had $2.9\text{e}7$ kg ($5.9\text{e}7$ kg) less PIM associated with hail and HD graupel on average in the lowest 3 km of the mixed-

phase region of the updraft (combined upper 2 km of the mixed-phase region and glaciated region of the updraft) compared with the anomalous 22 April 2017 supercell (not shown). These values indicate that although its relative distribution of larger precipitation ice was lower than in the normal storms, the anomalous 10 April 2009 supercell still contained more large precipitation ice in the form of hail and HD graupel. However, it did not contain as much large precipitation ice as observed in the anomalous 22 April 2017 supercell. The temporal increase in updraft PIM observed in the 10 April 2009 supercell that represented the eventual maximum of the dataset could be attributed to the greater capability of its large updraft (Figures 3.3a and 3.3b) in supporting a larger quantity of smaller, less dense graupel. In addition, its lightning flash rates were generally comparable to the normal supercells prior to their weakening phases and significantly lower than the other anomalous supercell, indicating from multiple metrics that large riming ice growth processes in the anomalous 10 April 2009 supercell may have been relatively inefficient by comparison.

3.5.2.3 Updraft PIM Structure

Vertical profiles of hydrometeor fractions alluded to structural differences in PIM observed between the four supercells. For instance, despite relatively lower hail fractions observed in the anomalous 10 April 2009 supercell, both anomalous storms exhibited minor hail fractions in the upper mixed-phase region that extended into the glaciated region, whereas the normal storms did not. The greater depth to which LD graupel was observed and the presence of hail contributed to PIM at higher altitudes, as well as higher frequencies of larger PIM within the glaciated region in the anomalous storms (Figures 3.4c and 3.4d). While differences in the depths of PIM observed can partially be attributed to differences in the storm depths, the anomalous storms were characterized by higher frequencies of larger

PIM values closer to their respective storm tops than were the normal storms, indicating riming hydrometeors were more vertically extensive therein. This may have been the result of greater depths over which riming growth was supported in anomalous storms or the ability of anomalous storms to loft rimed hydrometeors to higher altitudes given stronger updraft profiles aloft (Figures 3.3c and 3.3d).

3.5.3 Environmental Conditions

Coarse environmental data can be considered within the context of the observed kinematic and microphysical structure of each supercell to further understand the differences in gross charge structure. Each of the four storms shared some commonalities in the environmental parameter spaces in which they formed (Table 3.2). There were no obvious trends differentiating anomalous and normal storm environments in the surface temperature and dew point temperature, mean mixing ratio in the lowest 100 hPa, depth of the free convective layer, or 0-6 km shear. However, parameters exhibiting differences included metrics of environmental moisture, warm cloud depth, and instability. It should be noted that while some studies have identified some of these parameters as discriminators between anomalous and normal supercell storm environments (e.g., Carey and Buffalo, 2007; Fuchs et al., 2018), differences in parameters identified in the comparisons discussed herein are not always observed between normal and anomalous storm environments (e.g, Chmielewski et al., 2018; Fuchs et al., 2018; Lang and Rutledge, 2011).

3.5.3.1 CCN Proxy

Aerosol concentration profiles derived from MERRA reanalysis are shown in Figure 3.7, from which estimates of CCN concentrations were inferred. Estimated CCN pro-

vides an indication of the nature of the cloud and precipitation particle size distributions in each of the storms. The aerosol profiles corresponding to the anomalous storm environments and the normal 11 April 2008 supercell were most similar, particularly below the height of approximately -10°C . However, the relatively low aerosol concentration in the normal 6 February 2008 profile is consistent with the idea that fewer CCN may have prevented competition for water vapor and did not comparatively reduce warm precipitation efficiency. By contrast, the anomalous 10 April 2009 supercell aerosol profile indicates that more aerosols were present within the warm cloud region with an absolute maximum just above the height of the LCL, with relatively higher concentrations that persisted into the mixed-phase region. The normal 11 April 2008 supercell, however, also possessed relatively greater aerosol concentrations throughout the mixed-phase region, though did not exhibit a similar relative maximum near the inferred cloud base height. These profiles are consistent with the idea that more CCN were available to the anomalous supercells, potentially shifting the particle size distribution toward smaller particles and effectively reducing the efficiency of warm rain processes. As PIM distributions and lightning flash rates indicated in the anomalous 10 April 2009 supercell in particular, it is possible that increased CCN contributed not only to a possible reduction in warm precipitation efficiency but to reduced precipitation efficiency in general throughout the storm. Precipitation inefficiency may have impacted ice growth processes as indicated by discrepancies between quantities of large precipitation ice between anomalous supercells (Figure 3.4), particularly given the robust updraft in the 10 April 2009 supercell that seemingly could have supported high-LWC riming (Figure 3.3d).

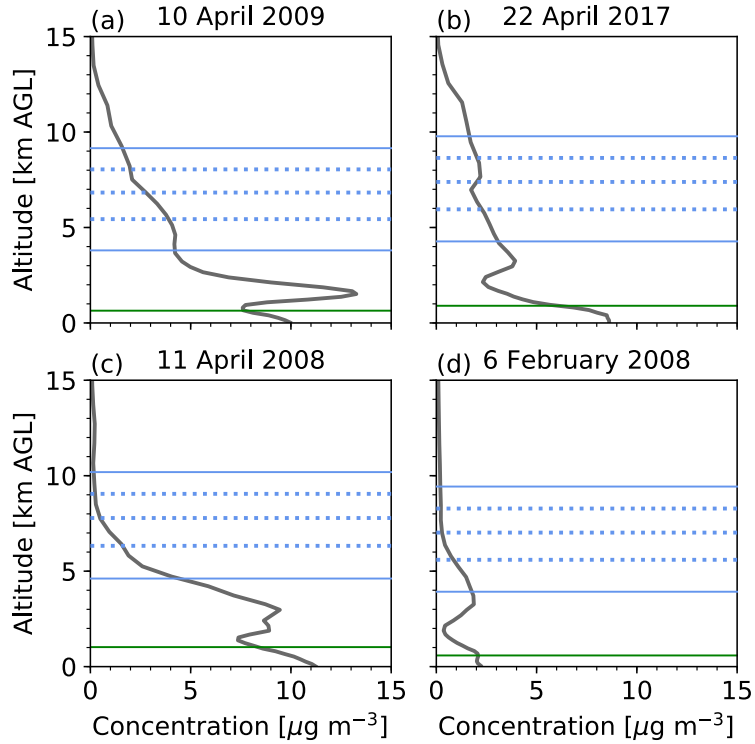


Figure 3.7: Total aerosol concentration profiles including dust, hydrophilic carbon species, sulphate, and sea salt aerosols thought to contribute to CCN corresponding to the (a) anomalous 22 April 2017, (b) anomalous 10 April 2009, (c) normal 11 April 2008, and (d) normal 6 February 2008 supercells. In each panel, the heights of 0°C through -40°C are marked by the blue lines in -10°C increments. The height of the LCL is marked by a horizontal green line.

3.5.3.2 Instability

Similar to WCD, results concerning the relationship between instability and ACS development have been varied. Generally, higher NCAPE has consistently discriminated anomalous from normal storms, while CAPE within the mixed-phase region has been shown to be higher in anomalous storms compared with normal storm environments (Carey and Buffalo, 2007). CAPE values associated with the Southeastern supercells of interest ranged from 447 J kg^{-1} to 2123 J kg^{-1} , with NCAPE varying between 0.06 m s^{-1} and 0.19 m s^{-2} (Table 3.2). For each metric, the greater (lesser) values corresponded with the anomalous

(normal) supercells, with minimum differences of 239 J kg^{-1} and 0.03 m s^{-2} . Generally, trends toward higher NCAPE in anomalous storm environments were consistent with their more robust updrafts.

3.5.3.3 Warm Cloud Depth

The shallowest environmental WCD of approximately 2460 m was associated with the anomalous 10 April 2009 supercell environment, given an LCL height of 643 m and an environmental melting level of 2105 m. The second most shallow WCD of approximately 2720 m was associated with the anomalous 22 April 2017 supercell environment, associated with a comparatively high 900 m LCL and an environmental melting level height of 3617 m. By contrast, the lowest environmental LCL of 585 m associated with the normal 6 February 2008 supercell environment combined with a similar environmental melting level of 3860 m resulted in the second deepest WCD of the sample of approximately 3280 m. Despite having the highest LCL of 1280 m, the comparatively high environmental melting level height of 4365 m resulted in the deepest WCD of approximately 3340 m associated with the normal 11 April 2008 supercell.

These general trends agree with findings in the literature that anomalous supercells sometimes have a more shallow WCD than their normal counterparts, where a shallower WCD likely reduces the depth over which warm precipitation may grow and deplete cloud LWC. However, the anomalous WCDs in these Southeastern supercells were deeper by approximately 1000 m than values reported in the literature associated with anomalous supercells (e.g., Carey and Buffalo, 2007; Chmielewski et al., 2018; Fuchs et al., 2018). However, the minimum 820 m difference between the shallowest anomalous and the deepest normal WCDs was similar to that observed by Fuchs et al. (2018), with a difference of

892 m between storm environments in different regions. While shallower WCD has been linked as a discriminator separating anomalous from normal storm environments, others have identified the opposite when examining storms in the same region on the same day (Chmielewski et al., 2018) and storms in the same region on different days (Lang and Rutledge, 2011). Observations of these four Southeastern supercell environments support findings that while a shallower WCD may promote conditions favoring the development of ACSs, they also suggest that the determination of a sufficiently shallow WCD likely varies related to other environmental conditions affecting precipitation efficiency, cloud LWC, and ice growth processes.

3.5.3.4 Environmental Moisture

Relationships between the storms based on metrics of environmental moisture varied according to the layers considered. Mixing ratios in the lowest 100 hPa were not substantially different between subsets of storms, varying between 11 g kg^{-1} and 13 g kg^{-1} . However, RH in the 700 hPa to 500 hPa layer trended lower in anomalous storms with values of 21% and 36% compared with values of 41% and 55% in normal storms.

Metrics that encompassed more of the full storm depths also tended toward lower moisture in anomalous storm environments. Precipitable water between the surface and 400 hPa was lower in anomalous storms at 2.3 cm and 3.2 cm compared with 3.5 cm and 3.8 cm in normal storms. RH in the full depth, meanwhile, was 41% and 54% in anomalous storms and 54% and 68% in normal storms. RH through any depth considered was consistently lowest in the anomalous 10 April 2009 supercell, which may have also contributed to its inferred relative precipitation inefficiency. The normal 11 April 2008 and anomalous 22

April 2017 environmental RH values were most comparable in the middle of the observed range, while the highest RH was observed in the normal 6 February 2008 environment.

3.6 Discussion on Contributions to Anomalous Charging

The following section discusses contrasts in the structural and environmental aspects associated with each of the supercells through which conditions favoring the development of anomalous charge structure may be interpreted.

3.6.1 Evaluation of Updraft Structure Relative to Charging Hypotheses: Low-Level Updraft

More robust updrafts in lower levels are thought to support ACS development by reducing warm precipitation efficiency such that cloud LWC remains available to reach the mixed-phase region for more efficient riming growth in favor of increased positive charging of riming hydrometeors. In addition to the benefit of fast updrafts to reduce cloud water residence time in the warm cloud, wide updrafts as well are thought to be less susceptible to entrainment, ultimately preserving LWC and maintaining fast updraft speeds. Generally, higher CBHs are thought to favor broader updrafts (e.g., Carey and Buffalo, 2007; Williams et al., 2005). Therefore, anomalous storms are thought to be associated with elevated cloud structure as well as broad, fast updrafts in the warm cloud region that contribute to initial reduction of LWC loss to warm precipitation growth. Although the maximum updrafts were located at the top of the mixed-phase region in the anomalous storms, the anomalous 10 April 2009 storm was characterized by higher updraft speeds below the melting level than observed in the other three storms (Figure 3.3c), seemingly supporting the hypothesis related to low-level updraft support.

The anomalous 22 April 2017 supercell also exhibited a faster, broader updraft in the warm cloud region when compared with the normal 11 April 2008 supercell. However, when compared with the normal 6 February 2008 supercell with which the anomalous 22 April 2017 supercell shared similar bulk updraft properties, the normal supercell exhibited both faster updraft speeds and a larger updraft core below the melting level (Figures 3.3d, 3.3f, and 3.6d). If a large, fast updraft, particularly in the warm cloud region, were the primary requirement supporting conditions favorable to anomalous charging, the 6 February 2008 supercell would have been expected to be anomalous rather than the 22 April 2017 supercell. However, a weaker updraft that comparatively facilitates warm precipitation efficiency may also be compensated by other environmental factors that adequately reduce warm precipitation efficiency. The idea of WCT (Fuchs et al., 2018) addresses this idea. However, it was observed that the distribution of WCTs based on updraft speed percentiles and a representative hydrometeor fall speed of 2 m s^{-1} exhibited substantial overlap in the Southeastern anomalous and normal supercells (Figure 3.8). Moreover, while the tails of the two anomalous WCT distributions were generally lower than the normal storms on the order of 5 mins to 8 mins, the anomalous storms WCTs were not comparable to those observed in anomalous storms in CO by Fuchs et al. (2018) and all more closely resembled the distributions observed in normal storms in AL analyzed by Fuchs et al. (2018). These data indicate that additional environmental factors likely contributed to the observed ACSs.

3.6.2 Evaluation of Updraft Structure Relative to Charging Hypotheses: Mixed-Phase Updraft

Within the mixed-phase region, similar arguments apply as were discussed with respect to low-level updrafts. Large, fast updrafts are more resistant to entrainment of dry

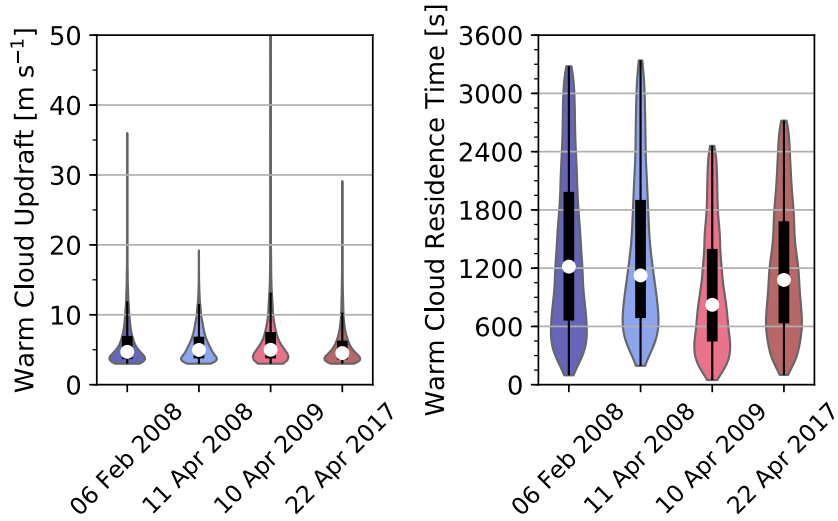


Figure 3.8: (a) Violin plots showing the distributions of warm cloud updraft speeds in each storm. (b) Violin plots showing the distributions of WCTs in each storm, assuming a particle fall velocity of 2 m s^{-1} .

air and may be less favorable for particle recirculation which can increase competition for LWC and reduce riming efficiency.

The mixed-phase updraft structures in anomalous storms were larger and faster in the middle to upper mixed-phase region compared with the larger, faster updrafts observed in the lower to middle mixed-phase regions of the normal storms. Fast updrafts at higher levels in anomalous storms may have been supported in part by the additional latent heat release associated with their apparent greater depths of riming (e.g., Fuchs and Rutledge, 2018). However, the relative *differences* in updraft structure between the observed Southeastern anomalous and normal supercells were collocated with observed dry layers, indicating that dry air entrainment may have impacted updraft strength in the low- to mid-levels of anomalous storms, altering their profiles. Specifically, it is possible that

maximum updrafts were identified at higher altitudes in the anomalous storms because the mid-level updrafts were comparatively reduced by negative buoyancy associated with dry air entrainment. The “top-heavy” updraft profiles of anomalous storms were comparable to updraft profiles in supercell simulations conducted by Grant and van den Heever (2014) in which dry layers were imposed. Compared with control simulations in their study, those that included dry layers centered at 3.5 km AGL (near 650 mb) were able to maintain strong maximum updrafts aloft though low-level velocities were diminished locally where affected by injection of dry air (Grant and van den Heever, 2014). Additionally, results from simulations by Nowotarski et al. (2020) suggest that as much as 30% of the air within the updraft core may originate above the effective inflow layer that is typically observed within the lowest 3 km, further suggesting the possibility of entrainment within the mid-levels that could have introduced dry air to the updraft.

In the anomalous supercells, maximum updraft speeds were either aligned with or located above the dominant positive charge region and extended into the glaciated region where collisional NIC involving riming hydrometeors would have been inactive as a result of homogeneous freezing (although studies have shown that some amount of charging may occur in the absence of LWC, e.g., Dye and Bansemer, 2019; Emersic and Saunders, 2020; Mitzeva et al., 2006). Therefore, the most likely region of positive charging of riming hydrometeors did not strictly coincide with storm maximum updraft speeds. Chmielewski et al. (2020) similarly observed that maximum updraft speeds and anomalous charging did not necessarily coincide in their study. However, observations of comparably drier layers in the Southeastern anomalous storms are also consistent with others reported in the literature (e.g., Carey and Buffalo, 2007; Carey et al., 2003b; Chmielewski et al., 2018; Knapp, 1994) and numerous observations of anomalous charge structure in LP supercells (e.g. Branick

and Doswell III, 1992; Curran and Rust, 1992; Lang et al., 2004; MacGorman and Burgess, 1994; Seimon, 1993; Tessorf et al., 2007b).

3.6.3 Effects of Entrainment

Environmental indicators of water vapor content suggested that the anomalous storm environments were drier, particularly just below the melting level and into the lower mixed-phase region. The structure of their updrafts, wherein peak updraft speeds were located at higher altitudes with weaker updrafts in the mid- to low-level mixed-phase region, indicated that they may have been affected by dry air entrainment associated with lower metrics of RH.

The role of dry air entrainment is often considered from an LWC perspective in the context of ice-ice collisional NIC. As it pertains to precipitation efficiency, several effects of entrainment have been suggested. As discussed in Chmielewski et al. (2018), dry air in lower levels of storms may decrease droplet sizes, reducing precipitation efficiency. However, the possible limiting effects of dry air entrainment to LWC include evaporation of cloud liquid water needed for riming (e.g., Hoffmann, 2020) and erosion of buoyant parcels that would both increase the residence time of LWC, promoting precipitation efficiency, and reduces the updraft's ability to transport larger LWC (e.g., Chmielewski et al., 2018; Fuchs et al., 2018)

The effects of dry air entrainment on the relative diffusional growth of ice particles and its impact to particle-scale charging have not been considered as deeply in the literature on storm-scale electrification. However, it has been shown in theoretical models and from limited laboratory studies that reduced supersaturation with respect to ice relatively increases the magnitude of positive charging of riming precipitation ice for a given LWC

over a range of mixed-phase temperatures (Berdeklis and List, 2001; Mitzeva et al., 2005; Saunders et al., 2006; Tsenova et al., 2010).

While factors such as a shallow WCD and fast low-level updraft (in the case of the 10 April 2009 supercell) may have promoted mixed-phase LWC, the differences in WCT in normal storms were not substantial enough to explain the resultant drastic difference in charge structure. It is suggested that entrainment of dry air may have contributed to anomalous charging in these storms dually by (a) reducing the warm rain efficiency and facilitating the availability of LWC in the mixed-phase region as well as (b) reducing supersaturation with respect to ice in the charging region and thereby altering relative growth rate relationships and decreasing the LWC required for positive graupel charging. This is not to say that the impacts of dry air are more significant than or preclude the requirement of LWC for anomalous charging. Rather, it is suggested that dry air entrainment and its impact on saturation ratios can augment and increase the effects of requisite available LWC.

It is unclear how often the Southeastern environment includes mid-level dry air, though it is expected to be somewhat infrequent given the availability of deep moisture owing to the proximity of the Gulf of Mexico. The contrast offers a physically consistent explanation for the relatively low frequency of anomalous storm observations in the Southeast compared with the Great Plains where environmental dry layers are more prevalent as a result of elevated mixed layers and/or the proximal dryline (e.g., Chmielewski et al., 2018; Grant and van den Heever, 2014).

3.6.4 Summary of Potential Factors Manifesting Apparent Charge Structure

In many ways, the anomalous 10 April 2009 supercell was superlative, demonstrating a robust updraft and observed within a favorable environment for anomalous charging

by standards established in the Great Plains. While conditions were seemingly favorable for the availability of LWC in the mixed-phase updraft, it is possible that dry air entrainment contributed to anomalous charging as well. Having formed in a dry pre-convective environment characterized by relatively high warm cloud aerosol concentrations, the anomalous 10 April 2009 storm was apparently not particularly precipitation-efficient in the warm cloud or mixed-phase regions, given its relatively low lightning flash rate, low hail fraction, and low total PIM compared with the anomalous 22 April 2017 storm. Its shallow WCD and particularly broad, fast updraft may have compensated sufficiently to provide mixed-phase cloud LWC for riming growth despite deleterious effects of environmental dry air. The effects of dry air entrainment exhibited through low- to mid-level updraft structure may have also inhibited ice crystal depositional growth relative to riming growth, shifting the LWC requirement for positive graupel charging and lowered the threshold to achieve an ACS consisting of deep, positive charging of riming hydrometeors.

The anomalous 22 April 2017 supercell exhibited less definition in charge structure, indicating relatively increased charge structure complexity. This complexity could have been attributed to three-dimensional variability in kinematics as well as cloud microphysical properties. That is, conditions within the updraft may have been variably favorable for both anomalous and normal charging, with predominantly anomalous charging occurring in the net. The structural similarities between the anomalous 22 April 2017 storm and the normal storms support this possibility, as do indications of some environmental overlap. It is possible that different factors contributed to comparative net anomalous structure in the 22 April 2017 storm than contributed to the 10 April 2009 ACS.

The gross updraft structures were most similar between the normal 6 February 2008 storm and the anomalous 22 April 2017 supercell. The primary differences between the

storms included a faster low-level updraft in the normal supercell and a shallower WCD, increased warm cloud aerosol concentrations, and drier environmental conditions in the anomalous supercell. While WCTs were comparable between the two storms, indicating similar support for mixed-phase liquid water content from the contrast between WCD and low-level updraft characteristics, the normal 6 February 2008 supercell was characterized by substantially less PIM in its structure and produced negligible hail fractions within the updraft. While prolific hail production is not necessary for an anomalous storm (e.g., Tessendorf et al., 2007b), its absence suggests low mixed-phase cloud LWC or limited ice precipitation efficiency. These are indications of relatively increased warm precipitation efficiency in the normal 6 February 2008 supercell, possibly due to decreased competition for droplet growth in the warm cloud region as a result of relatively fewer aerosols and comparatively increased low-level moisture. The relatively drier air in the lower and mid-levels of the 22 April 2017 supercell, by contrast, may have contributed both to reduced warm precipitation efficiency and benefits to relative growth rate of ice crystals and graupel in the mixed-phase region supportive of greater net anomalous charging.

Metrics of environmental humidity were most similar between the normal 11 April 2008 supercell and the anomalous 22 April 2017 supercell of the four storms, as were the precipitation ice characteristics. However, the WCD was the deepest, the wet bulb zero height was the highest, and the precipitable water was greatest in the normal 11 April 2008 supercell environment, indicating moist low levels and efficient warm rain production despite an aerosol profile depicting relatively large concentrations in the warm cloud region. Even though conditions suggested that LWC may have been reduced in the mixed-phase region, relatively high hail fractions in the lower mixed-phase region were observed, indicating that conditions were favorable in some part of the storm for hail growth via riming. However,

the observed charge structure suggests that weak kinematic support and factors favoring warm precipitation efficiency precluded sufficient LWC for positive charging of riming hydrometeors through a substantial depth of the storm despite favorable humidity values and evident riming efficiency. Had adequate kinematic support provided sufficient LWC to the mixed-phase region, it is possible that the dry environment similar to or increased warm cloud aerosol concentrations greater than that observed in the anomalous 22 April 2017 supercell may have favored a similar ACS in the otherwise normal 11 April 2008 supercell.

3.7 Conclusions

The kinematic structure, precipitation microphysics, lightning properties in, and environmental characteristics surrounding four supercell thunderstorms exhibiting normal and anomalous charge structures in the Southeastern US were examined and compared. The kinematic and microphysical conditions associated with and the environmental support for dominant negative charge regions in normal storms and dominant positive charge regions in anomalous storms were evaluated. Primary characteristics differentiating the anomalous supercell thunderstorms were identified as follows:

1. The anomalous supercells were deeper storms with larger, stronger updrafts in the upper mixed-phase regions that extended into the glaciated region. By contrast, the most robust portions of updrafts in normal supercells were confined to the warm cloud and lower to middle mixed-phase regions.
2. The anomalous supercells had larger quantities of precipitation-sized ice in the upper mixed-phase region and within the glaciated region than normal supercells. These observations indicated more efficient riming growth through a deeper extent and/or

greater kinematic support lofting rimed hydrometeors to higher altitudes than occurred in normal supercells.

3. Trends in environmental conditions that favored microphysical processes associated with anomalous charging included shallower WCDs, greater instability, increased warm cloud aerosol concentrations, and reduced measures of moisture in the lower to middle mixed-phase regions. However, the values observed and the differences between anomalous and normal storms were not necessarily consistent with Great Plains storm environments. While environmental data were coarse in nature, general magnitudes of these environmental parameters and their differences reinforce the idea that the extent to which each is necessary relies on the combined influence of all factors that affect the mixed-phase microphysical parameter space.
4. Despite increased instability metrics, anomalous storm updrafts were not necessarily comparatively stronger than normal storm updrafts in the warm cloud region, leading to comparable WCTs. Warm cloud conditions were seemingly alone insufficient to account for anomalous charging. In addition to considering combined and competing influences of multiple environmental parameters, results suggest that mixed-phase considerations for anomalous charging may extend beyond LWC considerations to include effects of variable water vapor content on relative ice growth rates and associated charging of riming and non-riming ice.

These results further highlight the complexity concerning the requirements and relative sufficiency of specific environmental conditions for anomalous charging. They also motivate several areas for future study that may improve upon the clarity of results presented herein. For instance, the limited number of storms addressed by these analyses was

the byproduct of a relatively rare phenomenon in Southeastern anomalous supercell development as well as limited quality observations of comparable storm mode, intensity, and duration. Not only would a larger sample of both anomalous and normal supercells be desirable, but future analyses of similar thunderstorm observations should also seek to broaden the pool of high-intensity normal storms for closer comparison with the robust anomalous storms herein. Similarly, an environmental analysis study may improve understanding of how often the conditions thought to be associated with Southeastern anomalous storms are present, providing further insight to understanding of their frequency. To complement and advance understanding from observational results, future modeling studies should also continue to assess the sensitivity of ACS development to microphysical parameters. In particular, various environmental impacts to mixed-phase LWC such as instability, CCN and ice nuclei concentrations, RH, and the thermal profile should be addressed. Similarly, it would be of interest to further evaluate the impacts of environmental conditions such as CCN and RH on updraft structure and intensity as well.

The results also raise questions concerning the multi-phase aspect of ice precipitation growth processes in the context of particle-scale charging, among which is whether the effects of dry air and supersaturation on relative ice crystal and graupel growth rates may sometimes be just as important as LWC to ice-ice collisional NIC processes?

The potential role of supersaturation in gross charge structures in particular requires further consideration, though tools by which to address this topic are limited as of yet. For instance, laboratory charging studies have not yet tested the effects of water vapor on relative ice particle growth rates over a sufficient range of supersaturation ratio nor has the complete three-dimensional parameter space of temperature, LWC, and supersaturation been addressed in a laboratory setting. These empirical data are necessary to inform de-

velopment of an appropriate parameterization for numerical simulations that may be used to test hypotheses for which observations are limited. From the observational perspective, current studies are limited by the lack of LWC or water vapor observations in deep convection and difficulty of direct measurement. In their absence, data and techniques that improve current estimates of properties such as CCN are of potential benefit. Surface-based instruments such as ceilometers, sun photometers, and Light Detection and Ranging (LiDAR) may provide observations of aerosol optical depth from which CCN concentrations could be derived in limited-area studies. Techniques utilizing satellite data to estimate CCN in convection may be more widely useful as well (e.g., Rosenfeld et al., 2014; Yue et al., 2019). Storm penetrating aircraft and similar efforts exist among the few avenues by which necessary direct measurements of CCN, LWC, and water vapor in convection may be acquired in the future. However, as current techniques are insufficient to explore LWC and supersaturation in thunderstorms at the required scales, laboratory and subsequent modeling studies hold the most immediate promise toward further clarity on their roles in charge structure polarity.

3.8 Acknowledgments and Data Availability Statement

Funding for this study was provided by NASA Severe Storms Research (NNH14ZDA0-01N), under contract from the NASA Marshall Space Flight Center (NNM11AA01A) for UAH authors. The authors thank Drs. Kevin Knupp, Ted Mansell, and Udaysankar Nair for discussions that improved the clarity and quality of the manuscript. Data from the ARMOR and NALMA corresponding to the 2008 cases and the 10 April 2009 case can be accessed via Carey and Blakeslee (<https://zenodo.org/record/3783694>, license: Creative Commons Attribution 4.0 International, 2020b) and Carey and Blakeslee (<https://zenodo.org/record/3783694>, license: Creative Commons Attribution 4.0 International, 2020b).

[//zenodo.org/record/3738553](https://zenodo.org/record/3738553), license: Creative Commons Attribution 4.0 International, 2020a), respectively. Data from the ARMOR used for the 22 April 2017 case analysis can be accessed through the VORTEX-SE 2017 data catalog at the UCAR/NCAR Earth Observing Laboratory data archive (http://catalog.eol.ucar.edu/vortex-se_2017, Carey and Knupp, 2017). Data from the NALMA used for the 22 April 2017 case are available from the NASA Global Hydrology Resource Center Distributed Active Archive Center (<https://earthdata.nasa.gov/eosdis/daacs/ghrc>, Blakeslee, 2019). Other data sources, including KHTX level-2 data (<https://www.ncdc.noaa.gov/data-access/radar-data/nexrad>), RUC and RAP model analysis data (<https://www.ncdc.noaa.gov/data-access/model-data/model-datasets/rapid-refresh-rap>), and MERRA-2 data (<https://gmao.gsfc.nasa.gov/reanalysis/MERRA-2/data.access/>), are publicly accessible.

CHAPTER 4

MICROPHYSICAL CHARACTERISTICS OF SUPERCELL THUNDERSTORM CHARGE STRUCTURE AND INFLUENCES ON SPATIAL LIGHTNING FLASH RELATIONSHIPS WITH THE UPDRAFT

4.1 Abstract

Relationships between active charge structure, lightning location, and kinematic and microphysical updraft characteristics during the development of an anomalous supercell observed in the Southeastern United States are addressed. The initial charge structure was characterized as an anomalous dipole in which positive (negative) charge was most closely associated with regions of precipitation (cloud) ice. The dominant anomalous charge structure evolved to include additional minor layers as well as evidence of horizontal charge structure complexity. While positive charge was primarily observed in precipitation ice regions, negative charge was increasingly observed in precipitation ice regions in addition to cloud ice regions. As charge structure characteristics evolved, spatial lightning flash relationships with the updraft also changed, where lightning flash initiations were increasingly observed in regions of faster updrafts and stronger horizontal gradients in updraft speed. These observations were contrasted with those of a comparable supercell with a normal charge structure (i.e., normal supercell), within which it was identified that sources were more typically closely associated with hydrometeor regions characteristic of normal particle-scale

charging with positive (negative) charge observed in predominantly cloud (precipitation) ice regions, while lightning flash initiations remained within slower updraft speeds and weaker updraft gradients. It is suggested that the evolution of spatial relationships between lightning and the updraft structure observed in the anomalous storm, as well as deviations from characteristics observed in the normal supercell, were associated with storm-scale variability in particle-scale charging behavior.

4.2 Introduction

Anomalous charge structures are thought to result from the response in charging behavior to extensive atypical cloud microphysical conditions (e.g., Bruning et al., 2014; MacGorman et al., 2005; Rust et al., 2005). Anomalous charge structure organization is often discussed in a similar one-dimensional framework as normal charge structures (e.g., Bruning et al., 2014). Differences between charge structures are understood through ice-ice collisional NIC theory, where inferred vertical variations in temperature and cloud LWC are thought to influence the polarity of charge being carried by precipitation and cloud ice hydrometeors (Reynolds et al., 1957; Saunders et al., 2006; Takahashi, 1978). In reality, three-dimensional variations in cloud microphysical conditions within a thunderstorm updraft may also contribute to horizontal inhomogeneity and increased complexity in charge structure (Kuhlman et al., 2006; Wiens et al., 2005). As observed relationships between lightning flash trends and convective intensity have a physical basis in the microphysical and kinematic conditions of electrification, it is expected that cloud microphysical variations affect how lightning relates to the updraft.

Recent studies have identified differences in general relationships between lightning flash initiation and propagation in storms with inferred normal versus anomalous charge

structures (Fuchs and Rutledge, 2018; Fuchs et al., 2018). Within a large sample of storms, it was noted that lightning flashes in normal storms (i.e., storms with a normal charge structure) tend to occur at higher altitudes and in lower reflectivity regions than observed in anomalous storms (i.e., storms with an anomalous charge structure), indicating microphysical differences in anomalous charge structures (Fuchs and Rutledge, 2018). Within a smaller subset of storms, a larger fraction of propagation in anomalous storms was observed in regions of stronger updraft gradient regions and somewhat faster updraft speeds, thought to indicate that lightning flashes in anomalous storms occurred closer to the updraft (Fuchs et al., 2018). However, few studies have addressed the influence of inferred variations in particle-scale charging conditions on the microphysical composition of charge structures or how the microphysical characteristics of charge structure impact spatial relationships between lightning flashes and the updraft. Identification of these relationships may add specificity to current understanding of how lightning properties relate to convective metrics that are used to interpret intensity (e.g., Carey et al., 2019; Schultz et al., 2017).

Observations of the development and early evolution of charge structure and lightning flash properties within an anomalous supercell documented in the Southeastern US are presented. Special consideration is given to inferred microphysical characteristics of charge regions, changes in charge structure, and the location of lightning flash initiation with respect to the updraft. Comparisons with a normal supercell observed in the region for which similar observations are available are used to contrast charge structure characteristics as well as spatial lightning flash relationships with updraft properties.

4.2.1 Electrification and Charge Structure

Although there are several probable processes through which thunderstorm electrification arises, the primary method is thought to be ice-ice collisional NIC. Ice-ice collisional NIC theory describes the transfer of charge during rebounding collisions between precipitation and cloud ice particles growing in the presence of supercooled liquid cloud water. Results from laboratory studies indicate that the polarity of charge associated with each hydrometeor type is thought to result from cloud microphysical conditions including LWC, temperature, and supersaturation (e.g., Berdeklis and List, 2001; Jayaratne et al., 1983; Saunders et al., 2006; Takahashi, 1978). Typical conditions within the mixed-phase region of a thunderstorm provide for the normal charging regime associated with cooler temperatures and lower LWC in which precipitation ice becomes negatively charged. By contrast, the anomalous charging regime is characterized as positive (negative) charging of precipitation (cloud) ice at warmer temperatures, in the presence of higher cloud LWC, and possibly at lower environmental supersaturation (e.g., Berdeklis and List, 2001; Mitzeva et al., 2005; Saunders et al., 2006). Vertical variations in the aforementioned thermodynamic and cloud microphysical properties along with gravitational sedimentation of oppositely charged cloud and precipitation ice hydrometeors comprise the simplified dipole and tripole conceptual models of charge structure (e.g., Williams, 1989, 2001). In reality, charging behaviors are more complex. Within varying kinematic and cloud microphysical conditions in a three-dimensional updraft, multiple charging regimes may be present even as net charge regions reflect the dominant behavior (e.g., Chmielewski et al., 2020). Additionally, other non-inductive and inductive charging mechanisms may affect charging behavior while three-dimensional flows at storm to turbulent scales, differential sedimentation, and charge deposition by lightning flashes contribute observed charge structures (e.g., Brothers et al.,

2018; Bruning and MacGorman, 2013; Bruning et al., 2010; Lhermitte and Williams, 1985; Stolzenburg et al., 1998).

4.2.2 Kinematic and Microphysical Relationships between Lightning and Convective Structure

Various foundational studies have examined fundamental relationships between microphysics, kinematics, and lightning behavior, addressing the precipitation characteristics of electrified regions as well as roles and relationships between lightning initiation and hydrometeor advection and sedimentation. Early investigations identified consistencies between observations and NIC theory, including the presence of negative charge in the region where LWC and riming growth of graupel were assumed to be greatest (e.g., Dye et al., 1986; Krehbiel et al., 1979; Proctor, 1983) and evidence of the vertical advection of particles carrying positive charge (e.g., Dye et al., 1986; Lhermitte and Williams, 1985). Dye et al. (1986) also discussed the relative roles of hydrometeor distributions and their fall speeds with respect to an updraft greater than 10 m s^{-1} to 15 m s^{-1} in the arrangement of charge transfer processes and charged particles with respect to an updraft. Together with a study documenting precipitation development in a nascent updraft (Dye et al., 1974), these observations constituted the framework for primary conceptual models addressing the interface between the updraft and downdraft as a favorable location for (a) the development of precipitation given the proximal supply of supercooled cloud water via the updraft, (b) interactions between precipitation and non-precipitation ice between upward and downward vertical motions, (c) the pooling of charge associated with precipitation ice in weaker positive vertical motion, and (d) initial lightning flash initiation locations between advecting cloud ice in the updraft and sedimenting precipitation ice in the negative

and weaker positive vertical motions (Dye et al., 1986). In a similar study, Lhermitte and Williams (1985) identified evidence for and suggested the role of particle balance levels in tying lightning flashes to the updraft, where a particle balance level (PBL) is the height at which the fall speed of a sedimenting population of hydrometeors is equal to the positive vertical motion of the updraft. In their analysis, Lhermitte and Williams (1985) observed a negative charge center less than 1 km above the identified PBL, as well as a positive charge center located approximately 6 km above the PBL that was thought to be associated with small ice hydrometeors that advected through the PBL in the updraft.

4.2.3 Supercell Structures

Increasingly challenging charge structure interpretations proceed as dynamic processes and convective intensity increase beyond single-cell, ordinary convection used to establish understanding of fundamental relationships between electrification, precipitation, and kinematics. Results from various studies of supercell structures have documented the transience and complexity of charge structures with respect to the microphysical and kinematic characterization of the updraft region wherein the effects of NIC are thought to be most immediate (e.g., Bruning and MacGorman, 2013; Bruning et al., 2010; Calhoun et al., 2013; Carey and Rutledge, 1998; Chmielewski et al., 2020; DiGangi et al., 2016; Emersic et al., 2011; MacGorman et al., 2005; Stolzenburg et al., 1998; Tessendorf et al., 2007b; Wiens et al., 2005). Results from case studies of anomalous storms in particular have suggested as well that variations in charging regime may occur across an updraft, contributing to aspects such as the lower negative charge layer in an anomalous structure (e.g., MacGorman et al., 2005; Wiens et al., 2005). Analysis of sub-regions within the broader charge structure in an anomalous supercell updraft have also shown that broader net charge

structures in active lightning regions may result from recent, local hydrometeor charging or arise following the advection of previously charged hydrometeors. Further, charging within different regions of the updraft were observed to vary as a result of three-dimensional variations of LWC (Chmielewski et al., 2020). These studies have resulted in key observations of microphysical characteristics of charge structures, providing evidence for and advancing the understanding of the prevalence of NIC in storm-scale charge generation, including in anomalous supercells.

4.2.4 Goals of the Present Study

While charge structures have been of primary interest for the purposes of understanding electrification processes, few studies have approached the development of anomalous charge structure from the perspective of addressing the impacts of microphysical characteristics of charge regions to evolving spatial relationships between lightning and updraft structure.

Dual-Doppler radar-inferred vertical wind retrievals and dual-polarization radar analyses of a single anomalous supercell thunderstorm observed on 10 April 2009 in the Southeastern US are used to provide further insight as to how primary charge structure develops alongside kinematic and microphysical fields and how spatial lightning flash relationships with updraft structure evolve. Although the anomalous 22 April 2017 supercell discussed in Chapters 2 and 3 was also anomalous, it was observed during maturity when its flash rates were much higher and its charge structure more complex, lending difficulty to interpretation. Because lightning flash rates remained relatively low during the development of the anomalous 10 April 2009 supercell analyzed herein, spatial characteristics of its charge structure were more visible and more readily contrasted with kinematic and microphysical

properties compared with other analyses of more mature, robust anomalous supercells (e.g., Bruning et al., 2010; DiGangi et al., 2016; Emersic et al., 2011), including later periods of the 10 April 2009 supercell after it had reached maturity and the Southeastern anomalous 22 April 2017 supercell. Data from a comparable single, established normal supercell that was observed in the Southeast on 11 April 2008 were contrasted with observations from the anomalous 10 April 2009 supercell, providing context to observed variations of charge structure characteristics and differences in relationships between lightning and the updraft.

Results are presented first in a detailed discussion of the development of charge structure followed by summary analyses of lightning properties with respect to kinematic and microphysical characteristics of the updraft. Subsequent discussion addresses charge structure variability and potential roles of normal and anomalous charging regimes on spatial lightning flash relationships with the updraft.

4.3 Data and Methods Statement

Summary environmental, electrical, kinematic, and microphysical properties associated with the anomalous 10 April 2009 and normal 11 April 2008 supercells were discussed in Chapters 2 and 3. The present analyses are concerned with the three-dimensional spatial and temporal evolution of those corresponding properties, including a new emphasis on lightning flash relationships. Discussions in the following sections focus upon aspects of the development of the anomalous 10 April 2009 storm between 1718 UTC and 1743 UTC. For comparison with properties observed during the development period in the anomalous supercell, analysis of the mature normal 11 April 2008 supercell over a period of similar length between 1851 UTC and 1914 UTC is also discussed. Data and processing techniques

are described fully in Section 2.3 with specific updates pertaining to the 11 April 2008 data provided in Section 3.3.

While datasets used in the following analyses and discussions remained the same, storm-relative flow fields were newly added. Incorporation of storm-relative flow allowed for consideration of the local effects of three-dimensional kinematics, including advection, on the arrangement of inferred charge regions. The horizontal U and V components of storm-relative flow fields were calculated for each of the storms by taking the difference between the horizontal wind fields retrieved from dual-Doppler analysis and an estimate of the mean storm motion.

The following discussions focus heavily on spatial relationships between lightning flash initiation and propagation and supercell structure. As a result, selected lightning data periods were chosen to capture a narrow temporal region of activity for clarity of analysis as well as to provide for closest correspondence with the time during which a radar would have sampled the mixed-phase region where most charging processes occur. Following these considerations, only two-minute periods of lightning data were analyzed, beginning two minutes after each ARMOR volume start time used in a dual-Doppler analysis pair.

4.4 Anomalous Charge Structure Development

The charge structure observed during the development of the anomalous storm was consistently characterized as anomalous. However, it underwent a series of transformations in which additional charge regions and increasing charge region complexity was observed. The evolution of anomalous charge structure is described, beginning from the radar analysis volume when mapped charge structure was first most apparent. Though lightning flashes were observed as early as 1702 UTC, lightning flash rates had remained $\leq 3.5 \text{ min}^{-1}$ prior to

1714 UTC, preventing a well-defined perspective of the three-dimensional charge structure until after this time.

4.4.1 Initial Prominent Negative Dipole: 1718 UTC-1724 UTC

Ten lightning flashes were observed during the 1718 UTC to 1720 UTC lightning analysis, providing a clear three-dimensional picture of the charge regions associated with the 1716 UTC radar analysis volume. A positive charge layer was inferred across the top of the 5 m s^{-1} updraft core from 4 km AGL to 6 km AGL, overlapping regions characterized as HD graupel and hail in the updraft core and LD graupel to the east of the updraft (Figures 4.1a and 4.1b). Most negative sources were located to the east of the updraft between 6 km AGL and 9 km AGL, extending through the upper mixed phase regions in weak vertical motions with magnitudes $\leq 5 \text{ m s}^{-1}$ above the height of -10°C . Though portions of the volume in which negative sources were identified were characterized as LD graupel, more of the negative sources were associated with aggregate regions (Figure 4.1b). Together, these charge regions mapped an initial primary negative dipole charge structure (i.e., lower positive and upper negative charge regions) that was consistently observed over the full duration of storm analysis. Two lightning flash initiations were observed with $\pm 0.5 \text{ km}$ of the cross-section, located between the observed dipole charge pair in regions of weak vertical motion at the edge of the 5 m s^{-1} updraft and near the interface between the updraft and downdraft regions (Figure 4.1b).

The next dual-Doppler analysis began at 1720 UTC. Between 1722 UTC and 1724 UTC, 20 lightning flashes were observed within the storm volume and their propagation continued to map a prominent negative dipole charge structure (Figures 4.1c and 4.1d). Positive sources were primarily associated with LD graupel and hail regions, though extended

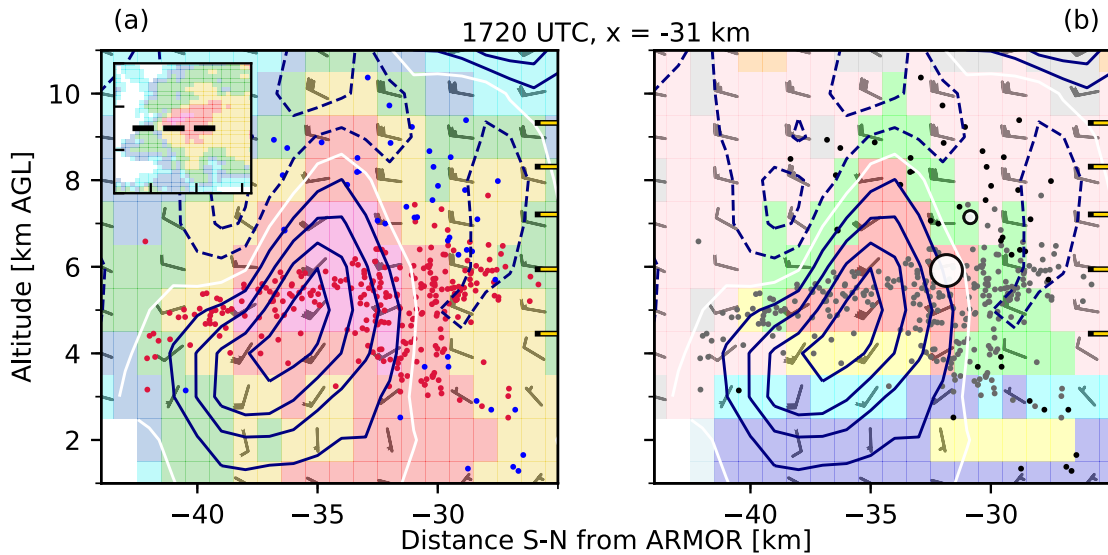


Figure 4.1: Vertical cross-sections showing supercell precipitation, kinematic, and electrical structure observed in the anomalous 10 April 2009 supercell. (a-b) Radar observations correspond to the 1716 UTC ARMOR sampling volume and lightning observations correspond to the 1718 UTC to 1720 UTC sampling period. An inset panel in (a) of a horizontal cross-section in reflectivity at $z = 2$ km AGL and between $x = 48$ and 18 km west and between $y = 50$ and 80 km north of ARMOR shows the location of vertical cross-sections in (a-b) at $y = 65$ km north of ARMOR as a dashed black line. The vertical cross-sections show (a) reflectivity and (b) HID (color fill according to the color bars along the bottom of the plot) as well as vertical motion in positive 5 m s^{-1} , 0 m s^{-1} , and negative 5 m s^{-1} intervals (solid navy, solid white, and dashed navy contours) in the cross-section plane. Storm relative motion along the plane is also shown with gray wind barbs. Positive (red or gray dots) and negative (blue or black dots) VHF sources associated with lightning flash propagation are shown within ± 0.5 km of the plane. Lightning flash initiation locations within ± 0.5 km of the plane (white circles if lightning flash polarity was classified and purple circles if lightning flash polarity was not classified) are shown on the HID vertical cross-section in panel (b). Lightning flash initiation marker sizes are scaled by flash area. Panels (c-d) are plotted as panels (a-b), showing a vertical cross-section 31 km west of ARMOR at the time of the 1720 UTC radar sample volume along with lightning activity observed between 1722 UTC and 1724 UTC. The horizontal reflectivity cross-section is shown at $z = 2$ km AGL between $x = 45$ and 15 km west and between $y = 53$ and 80 km north of ARMOR.

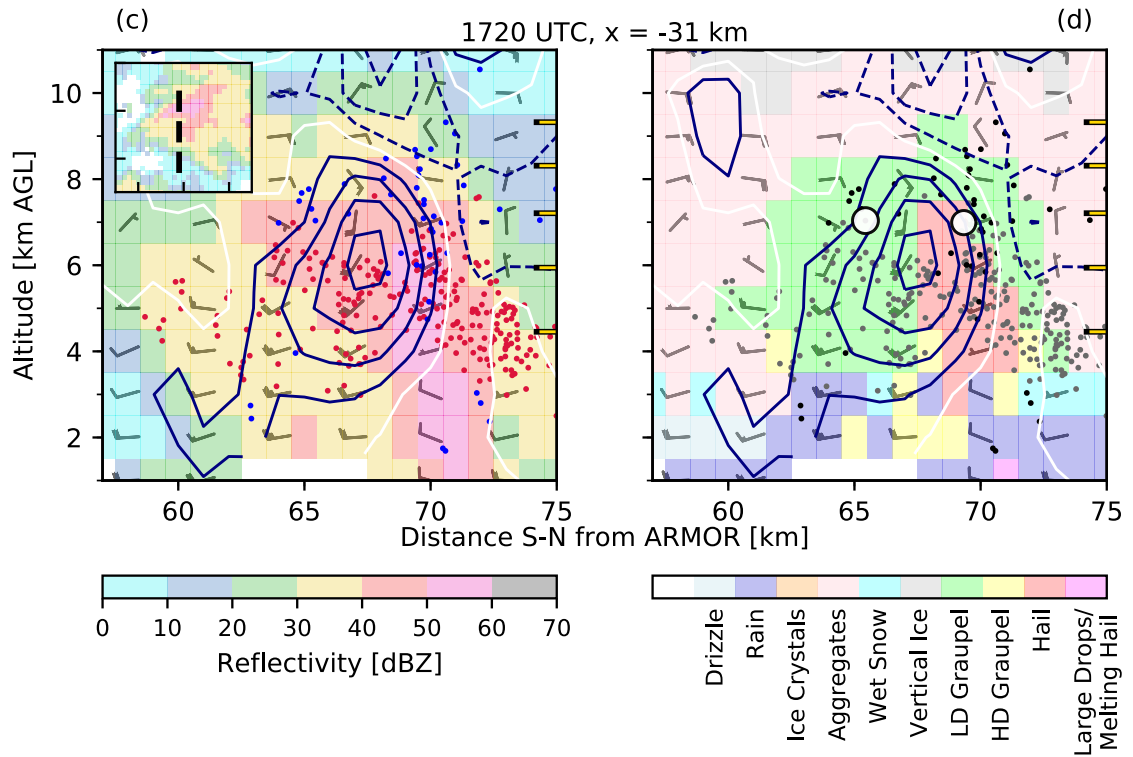


Figure 4.1: (continued)

through the lower half of the updraft instead of the upper portion as previously observed (Figure 4.1d). Two lightning flashes were again observed within ± 0.5 km of the cross-section and were similarly located within the dipole, though initiated in faster updraft speeds along the boundary of the 10 m s^{-1} updraft (Figure 4.1d). Negative sources during this period were collocated with LD graupel regions, distributed over and around the 10 m s^{-1} updraft contour (Figure 4.1d).

Selected periods in the normal 11 April 2008 supercell were considered for comparison with the early stages of the anomalous storm structure (Figure 4.2). The mid-level negative charge inferred in the normal tripole structure of the normal 11 April 2008 supercell was primarily associated with hail and graupel regions while positive charge was pooled

over and around the 10 m s^{-1} updraft in LD graupel and aggregate regions (Figures 4.2a and 4.2b). Although the polarity of the main dipole was reversed, these spatial relationships between charge regions, updraft structure, and hydrometeor regions were similar to those observed in the anomalous supercell between 1718 UTC and 1720 UTC. Lightning flash initiations within the upper positive dipole (i.e., main negative beneath the upper positive charge region) in the normal supercell were located closer to the upper half and top of the updraft, most similar to lightning flashes during the earlier period of observations in the anomalous supercell (Figure 4.1b). The dipole in the anomalous supercell shifted downward in height relative to the altitude of the updraft maximum and the upper charge layer became collocated with precipitation ice regions between 1722 UTC and 1724 UTC. As the location of the dipole changed with respect to the updraft structure, the charge region interface and focus for lightning flash initiations in the anomalous storm also shifted closer to the level of the updraft core, exhibiting fewer consistencies with spatial relationships observed in the normal supercell (Figure 4.1d).

4.4.2 Multi-Layer Charge Structure: 1730 UTC-1737 UTC

Lightning flash rates in the anomalous supercell increased from 32 min^{-1} at 1730 UTC to a relative maximum of 67 min^{-1} within the following 15-minute period, indicating increasing charging rates during charge structure development. Between 1730 UTC and 1732 UTC, the original mid-level positive charge layer between 0°C and -20°C and the negative charge region extending to -40°C associated with the main negative dipole remained prominent (Figures 4.3a and 4.3b). An additional lower negative charge region observed in the updraft between 0°C and -5°C and outside of the updraft was also more apparent. Examination of the lightning flashes associated with these negative sources indicates that the sources were

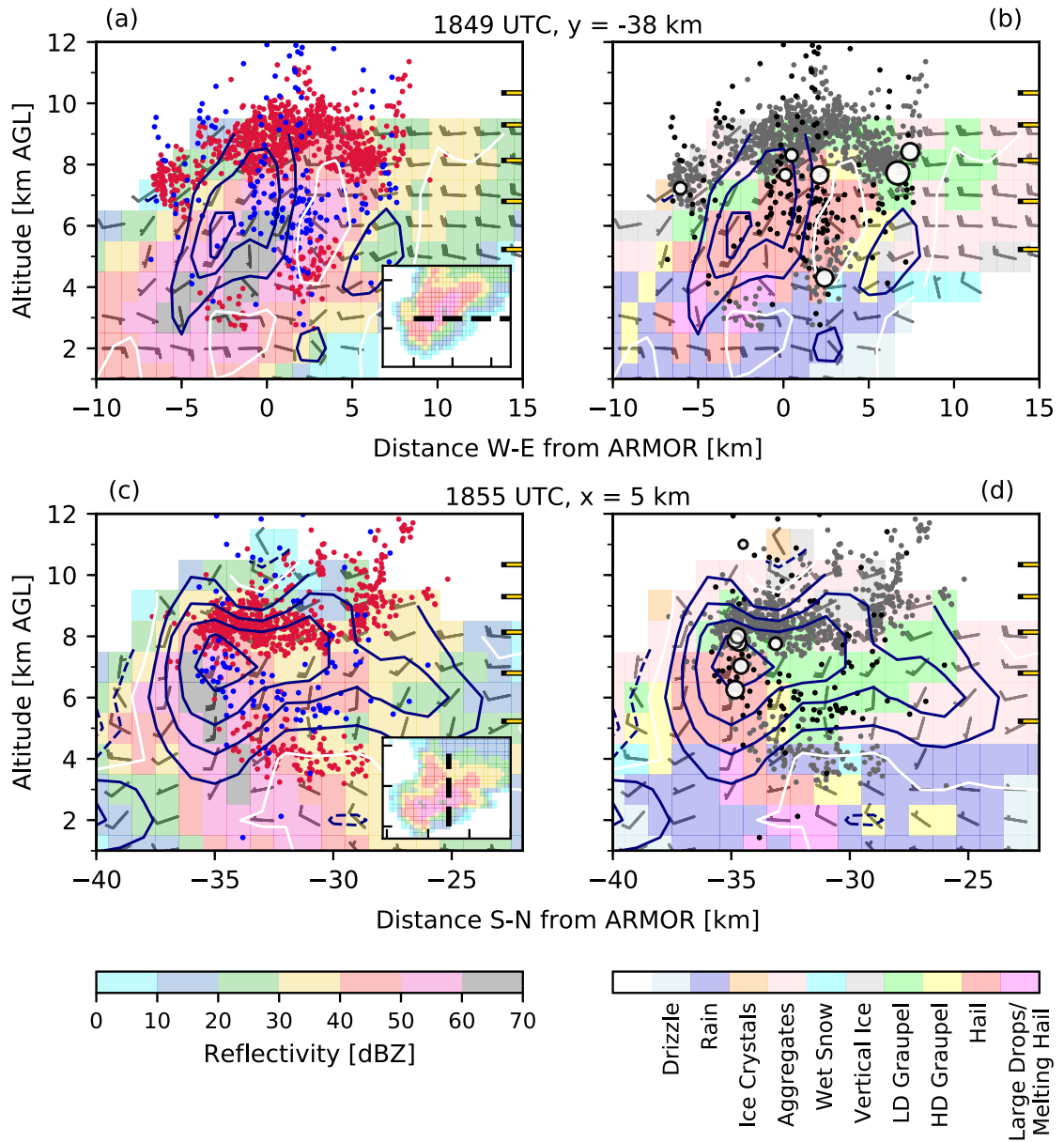


Figure 4.2: As in Figure 4.1 for the normal 11 April 2008 supercell. Panels (a-b) show observations associated with the 1849 UTC radar sample volume and lightning properties between 1851 UTC and 1853 UTC at a cross-section located 38 km south of ARMOR. The inset shows a horizontal cross-section of the supercell at a height of $z = 2$ km AGL, between $x = 18$ km west and 15 km east of ARMOR and between $y = 48$ km and 27 km south of ARMOR. Panels (c-d) show observations associated with the 1855 UTC radar sample volume and lightning properties between 1857 UTC and 1859 UTC at a cross-section located 5 km east of ARMOR. The inset shows a horizontal cross-section of the supercell at a height of $z = 2$ km AGL, between $x = 11$ km west and 20 km east of ARMOR and between $y = 43$ and 18 km south of ARMOR.

physically consistent with a lower negative charge region and were not an artifact of charge classification.

A group of lightning flash initiations was first observed during this period near 9 km AGL to 10 km AGL above the negative charge region of the main negative dipole. The higher of the lightning flashes near 10 km AGL were small and remained unclassified (Figure 4.3b). However, the lightning flashes identified at 9 km AGL were associated with a portion of a sloping positive charge region to the east of the updraft that extended from a height of 8 km AGL south of the updraft to a height of 3 km AGL north of the updraft, indicating the three-dimensional nature of the charge structure (Figure 4.3d). The positive sources observed near the top of the sloping region in particular were located in northerly storm-relative flow, downstream of observed negative sources (Figures 4.3c and 4.3d). Charge structure between 6 km AGL and 8 km AGL was somewhat more complex than observed earlier, with evidence of negative and positive sources occupying the same horizontal region adjacent to the updraft (Figures 4.3c and 4.3d).

Between 1735 UTC and 1737 UTC, many more lightning flashes were observed near 10 km AGL (Figure 4.3f). While several lightning flashes were unclassified, the classified lightning flashes mapped a small positive charge region above -40°C located over the negative charge region associated with the dominant negative dipole below. The smaller region of positive sources aloft and most proximal negative sources were typically observed outside of the tilted 15 m s^{-1} updraft in regions classified as hail, LD graupel, or aggregates (Figure 4.3f). Negative sources through the -20°C to -40°C region, however, were identified throughout the updraft gradient as well as within the hail region and updraft where speeds exceeded 25 m s^{-1} . Although the positive sources above the updraft constituted a comparatively small charge region, associated lightning flash initiation locations and charge

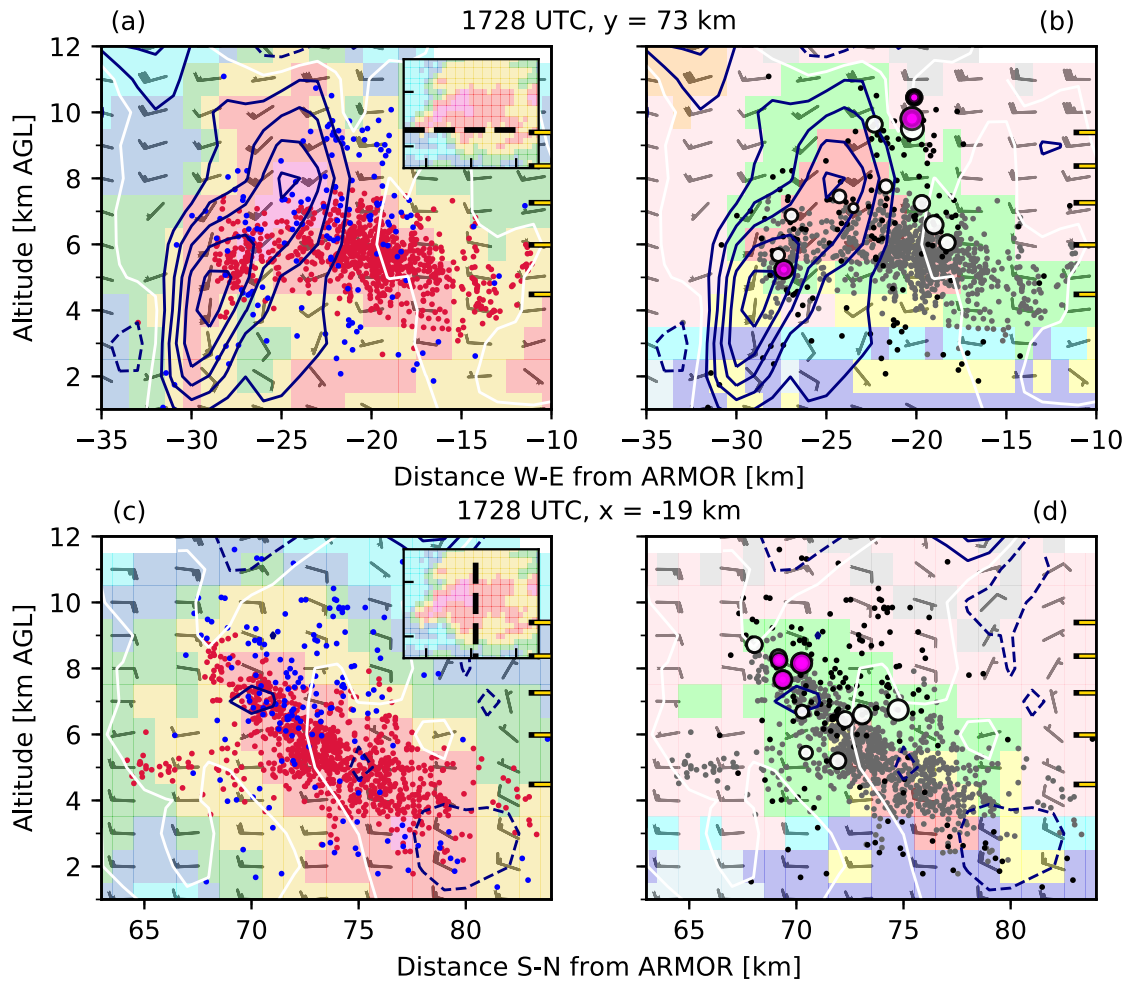


Figure 4.3: As in Figure 4.1 for the anomalous 10 April 2009 supercell at (a-d) 1728 UTC and (e-f) 1733 UTC. Panels (a-d) show observations associated with the 1728 UTC radar sample volume and lightning properties between 1730 UTC and 1732 UTC with vertical cross-sections located (a-b) 73 km north of ARMOR and (c-d) 19 km west of ARMOR. The inset in panels (a) and (c) show a horizontal cross-section of the supercell at a height of $z = 2$ km AGL, between $x = 35$ and 5 km west of ARMOR, and between $y = 66$ and 86 km north of ARMOR. Panels (e-f) show observations associated with the 1733 UTC radar sample volume and lightning properties between 1735 UTC and 1737 UTC with a vertical cross-section located 76 km north of ARMOR. The inset shows a horizontal cross-section of the supercell at a height of $z = 2$ km AGL, between $x = 30$ and 0 km west of ARMOR and between $y = 70$ and 90 km north of ARMOR.

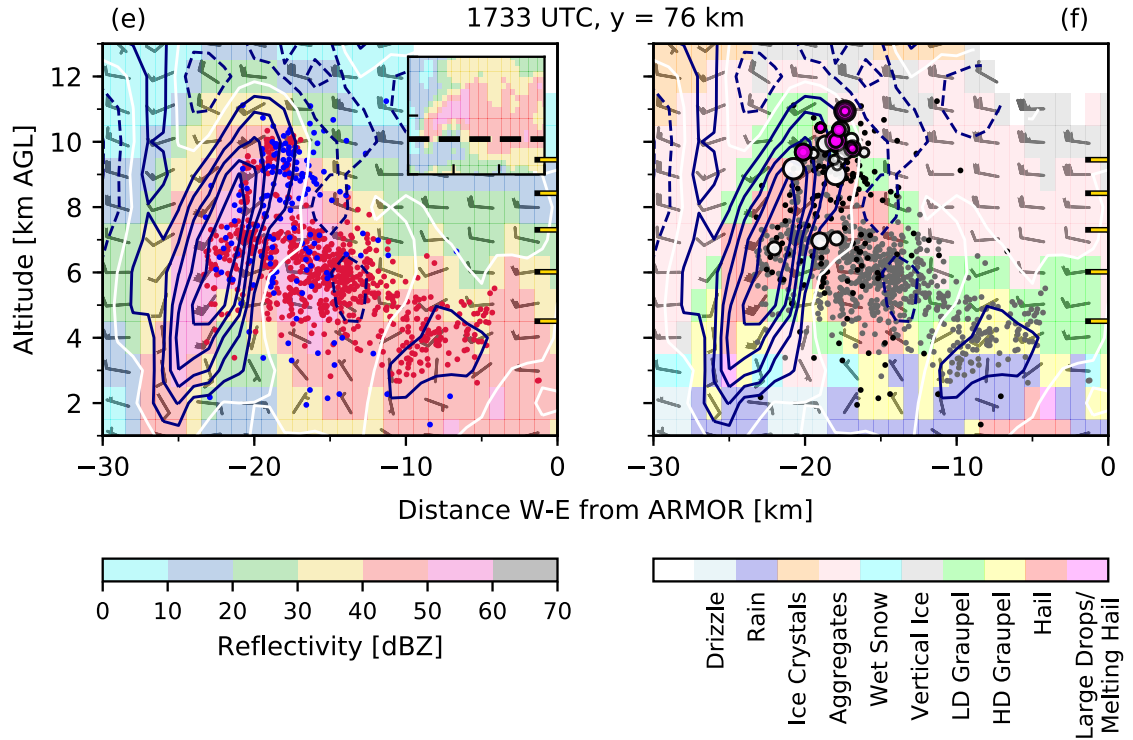


Figure 4.3: (continued)

layer characteristics shared more similarities with observations of the upper dipole in the normal storm (Figures 4.2c and 4.2d) than with the primary anomalous dipole observed between 1718 UTC and 1724 UTC (Figures 4.1c and 4.1d). Specifically, positive and adjacent negative sources mapped similar sloping patterns over and around the $\leq 15 \text{ m s}^{-1}$ updraft volume as observed in the positive dipole in the updraft of the normal supercell (Figures 4.2c, 4.2d, 4.3e, and 4.3f).

While the broader dominant negative dipole charge structure remained present, a mixture of source polarities was observed near 7 km AGL where lightning flashes continued to initiate (Figures 4.3e and 4.3f). This local charge structure obscurity between -10°C and

-20°C was similar to that observed adjacent to the updraft in the previous analysis period (Figures 4.3c and 4.3d).

4.4.3 Increasing Horizontal Charge Structure Heterogeneity: 1741 UTC-1743 UTC

Two distinct lightning flash initiation clusters were observed between 1741 UTC and 1743 UTC amid the consistent negative dipole and a third less extensive positive charge region aloft. As in the previous observation period, the number of small lightning flashes observed at the top of the updraft continued to increase near 10 km AGL (Figures 4.4b, 4.4d, and 4.4f).

Above the updraft core, a relatively dense region of negative sources was observed in the glaciated region within the updraft gradient and outside of the updraft to the north (Figures 4.4a and 4.4b). Meridional flow was weak where most negative sources were located but became more northerly over top and to the south of the updraft, downstream of which most positive sources were located (Figures 4.4a and 4.4b). Multiple lightning flash initiation locations were identified between these positive and negative regions aloft (Figure 4.4b), many of which were not classified.

The charge regions associated with the main negative dipole shown in a zonal cross-section along the tilted updraft core (Figures 4.4c and 4.4d) were generally distinct, though charge mixtures were also apparent near 7 km AGL as observed in the previous analysis volume (Figures 4.3c and 4.3e). Additional indications of complexities were observed in cross-sections through regions around the updraft core. In a meridional cross-section bisecting the tilted updraft, positive and negative sources were observed adjacent to each other in gradients of vertical motion to the north of the updraft core as well as within the

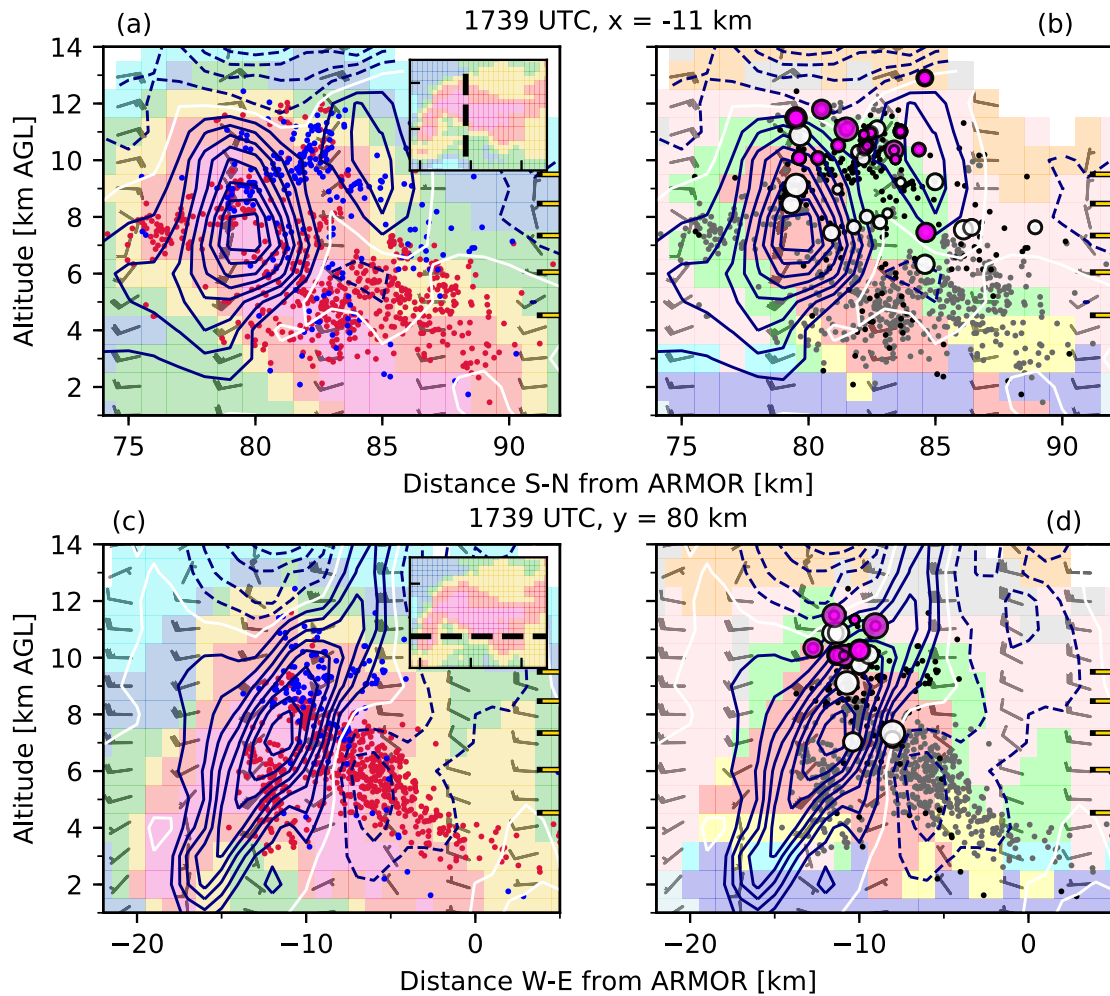


Figure 4.4: As in Figure 4.1 for the anomalous 10 April 2009 supercell at 1739 UTC. Panels (a-f) show observations associated with the 1739 UTC radar sample volume and lightning properties between 1741 UTC and 1743 UTC with vertical cross-sections located (a-b) 11 km west of ARMOR, (c-d), 80 km north of ARMOR, and (e-f) 82 km north of ARMOR. The inset in panels (a), (c), and (e) show a horizontal cross-section of the supercell at a height of $z = 2$ km AGL, between $x = 22$ km west and 5 km east of ARMOR and between $y = 71$ and 95 km north of ARMOR.

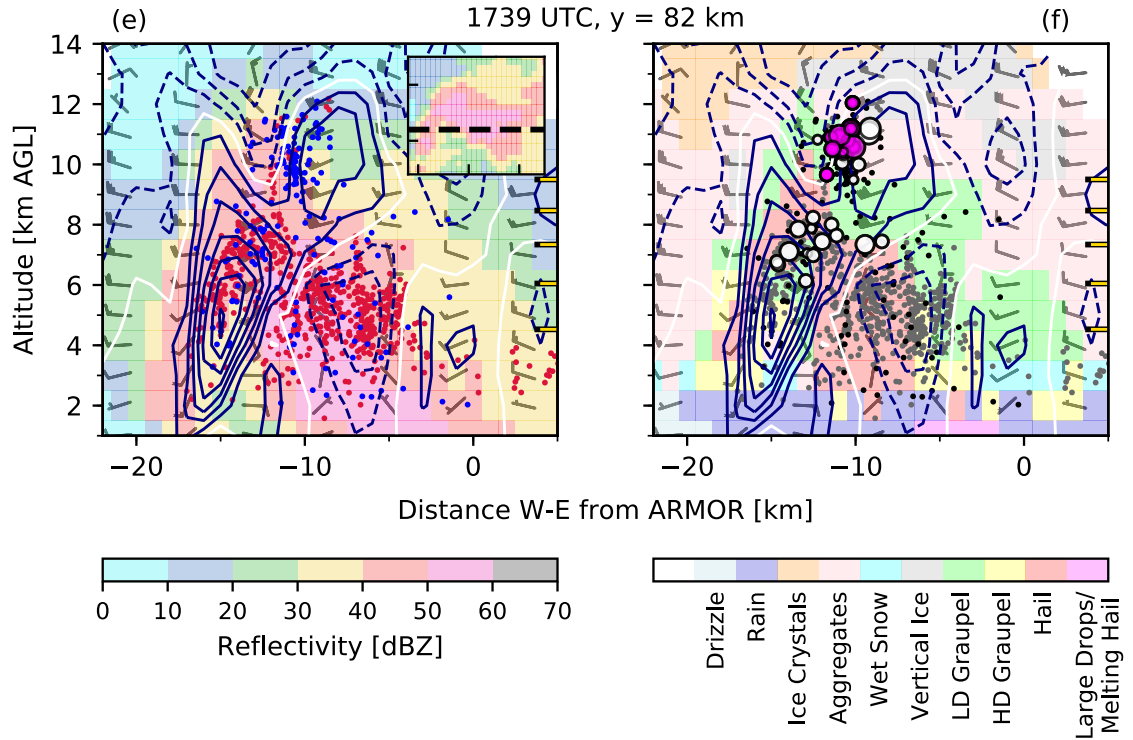


Figure 4.4: (continued)

hail cascade extending to the north out of the updraft (Figures 4.4a and 4.4b). An additional zonal cross-section to the north of the updraft core shows narrow vertical bands of negative sources within the gradient of the updraft above approximately -10° (Figures 4.4e and 4.4f), providing another view of the apparent mixture of sources observed in the meridional cross-section (Figures 4.4a and 4.4b). A persistent group of lightning flash initiations was observed near 7 km AGL and 8 km AGL as before (Figures 4.3a and 4.3f) in the gradient of the updraft amid these varied charge regions (Figures 4.4b and 4.4f).

4.5 Lightning Flash Properties Related to Kinematics and Microphysics in the Updraft

While all lightning flash initiations and associated classified sources, thought of as lightning flash propagation, were discussed in the previous section, the following analyses exclusively discuss lightning flashes that initiated within the 5 m s^{-1} updraft. Propagation associated with these lightning flash initiations may have extended outside of the updraft.

4.5.1 Vertical Distributions of Lightning Flash Initiations

The mode altitude of lightning flash initiation locations in the developing anomalous supercell was also more variable with time than observed in the normal supercell (Figures 4.5a and 4.5b). Between 1718 UTC and 1720 UTC, one lightning flash initiated in the updraft near 8 km AGL, though observations of select lightning flashes in the cross-section at that time showed initiations in weaker vertical velocities and outside the updraft near 6 km AGL and 7 km AGL as well (Figure 4.1b). Between 1722 UTC and 1724 UTC, however, more lightning flash initiations were observed in the updraft in the 5 km AGL to 7 km AGL range (Figure 4.5b). The distributions are consistent with observations of the apparent downward shift of select lightning flash initiations observed within and near the updraft in the cross-section at that time (Figure 4.1d). The primary negative dipole in the developing anomalous supercell resulted in lightning flashes that initiated both at lower altitudes and adjacent to the updraft (Figure 4.1d). This was the first clear indication that the charge structure in the anomalous supercell was not merely inverted from the primary positive dipole of the mature normal supercell in which lightning flashes initiated instead near the top of the updraft in the vertical reflectivity gradient (Figures 4.2b and 4.2d).

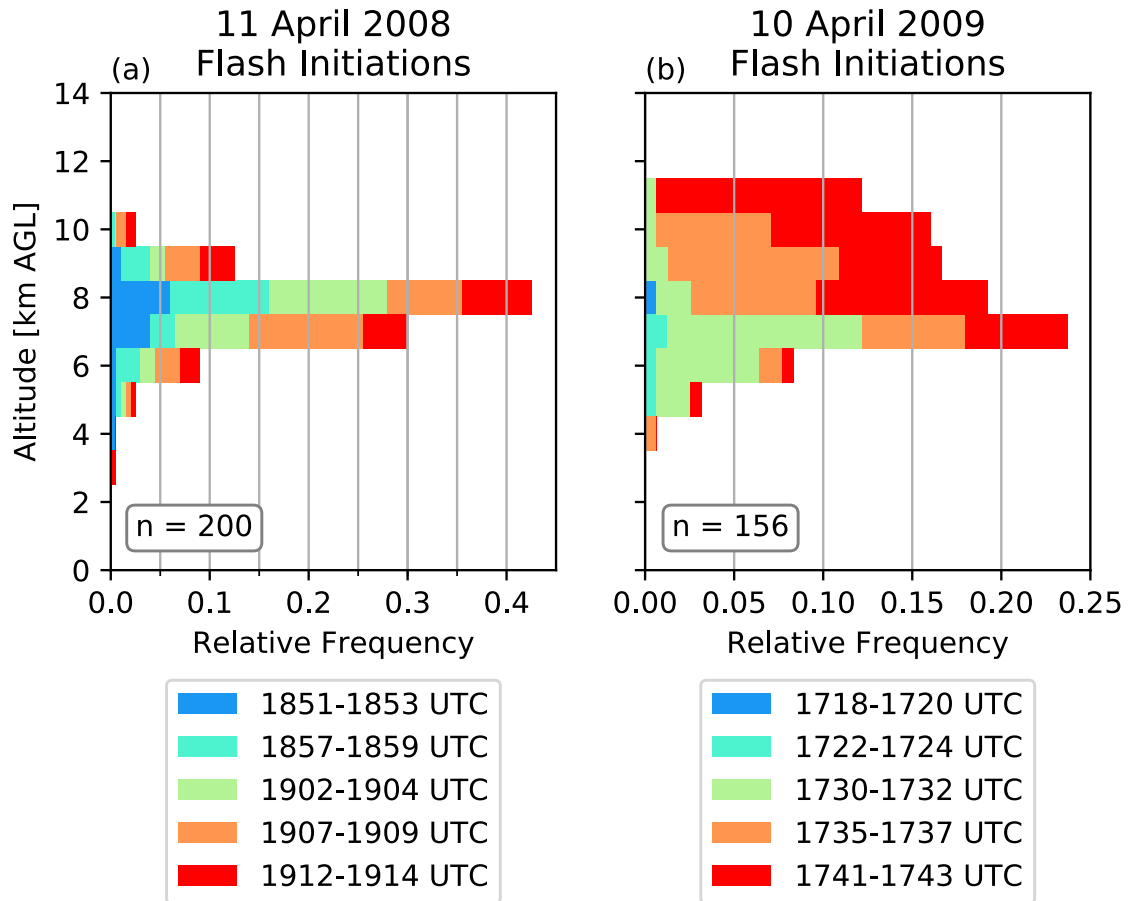


Figure 4.5: Vertical distributions of the initiation location of lightning flashes identified in updraft regions ($w \geq 5 \text{ m s}^{-1}$) of (a) the normal 11 April 2008 supercell and the (b) anomalous 10 April 2009 supercell. Distributions are plotted as relative frequencies of observation in each 1-km vertical bin and segmented, or stacked, according to the proportion that occurred during each lightning analysis period associated with each ARMOR sample volume. The segments are colored according to the five lightning analysis time periods in each storm shown in the lower legends, where cooler (warmer) shades are indicative of earlier (later) analysis periods.

While the number of lightning flashes in the anomalous supercell had increased by 1728 UTC, the mode altitude of lightning flash initiation locations remained in the 6 km AGL to 7 km AGL region, similar to that observed minutes prior. However, lightning flash initiations were also first observed in the updraft between 9 km AGL and 11 km AGL (Figure 4.5b). As the number of lightning flashes continued to increase between 1735 UTC and 1743 UTC, the mode altitude of initiations shifted upward. From 1735 UTC to 1737 UTC, the mode was located near 9 km AGL and from 1741 UTC to 1743 UTC, near 11 km AGL (Figure 4.5b). During these latter periods, the distribution of lightning flash initiations was generally more broad between 7 km AGL and 10 km AGL than observed prior to 1735 UTC.

4.5.2 Microphysical Characterization of Lightning Flash Propagation Locations

As expected from simple conceptual models of normal charge structure based on the ice-ice collisional NIC method, cloud ice categories were the dominant hydrometeor types associated with most negative breakdown of lightning flashes that initiated in the updraft in the normal supercell, representing over 50% of positive sources analyzed, while precipitation ice categories were primarily associated with most positive breakdown of lightning flashes, representing over 75% of negative sources analyzed (Figures 4.6a and 4.6c). These observations are also consistent with spatial coherency between groups of sources and HID characterization observed in selected cross-sections (Figure 4.2), including a non-trivial overlap between positive sources at the top of the updraft and the upper region of the lofted LD graupel volume. Over the full analysis period, 35% of positive sources were ultimately identified in LD graupel regions (Figure 4.6a).

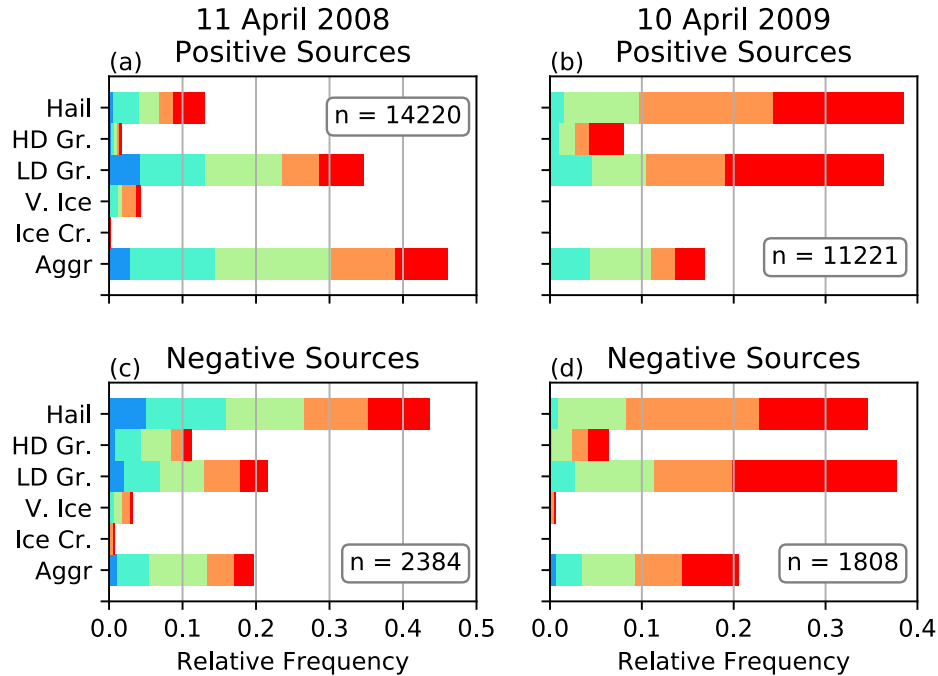


Figure 4.6: Distributions of lightning source locations with respect to associated hydrometeor type over time and by inferred polarity. Positive source distributions in the (a) normal 11 April 2008 supercell and (b) anomalous 10 April 2009 supercell as well as negative source distributions (c, d, respectively) are shown. Distributions are plotted as relative frequencies that are segmented, or stacked, according to the proportion that occurred during each analysis period and colored as in Figure 4.5.

The distributions of positive and negative sources associated with lightning flashes that initiated in the updraft in the anomalous supercell were not as distinct between precipitation and cloud ice categories. A basic description of the conceptual model of an inverted or anomalous charge structure based on NIC theory would suggest that positive (negative) charge would be more closely associated with precipitation ice (cloud ice). While 82% of positive sources were associated with precipitation ice categories, only 21% of negative sources were associated with cloud ice categories (Figures 4.6b and 4.6d). The relative frequencies of negative sources observed in precipitation ice regions also became larger with

time, while the relative frequency of positive sources located in precipitation ice regions generally remained relatively constant (Figures 4.6b and 4.6d). These characteristics are consistent with a transition in NIC polarity near the top of the mixed-phase updraft.

4.5.2.1 Evolution of the Negative Charge Regions

The following discussions concern sources, or lightning flash propagation, that were observed within the 5 m s^{-1} updraft, regardless of the location of lightning flash initiation. This restricts analysis to electrification characteristics associated with most recent NIC (e.g., Bruning et al., 2010; Stolzenburg et al., 1998). Given the relative steadiness of charge structure characteristics observed in the normal 11 April 2008 supercell (not shown), a summary figure of the average distributions of positive and negative source locations by altitude and hydrometeor type over the 1851 UTC to 1914 UTC period (Figure 4.7a) is used for comparison with the evolution of distributions observed in the anomalous supercell (Figures 4.7b to 4.7f). Consistent with expectations based on the conceptual model of a normal charge structure, positive sources in the updraft were most frequently located at higher altitudes in cloud ice and graupel regions compared with negative sources that were mostly observed at lower altitudes in precipitation ice regions (Figure 4.7a). Consistent with previous observations, the relative maximum in positive sources associated with graupel regions was located at 8 km AGL to 9 km AGL, slightly offset from the maximum in cloud ice regions between 9 km AGL and 10 km AGL.

During the first analysis period in the anomalous supercell, positive sources were associated with both precipitation and cloud ice regions between 4 km AGL and 6 km AGL (Figure 4.7b). The negative sources, meanwhile, were primarily associated with cloud ice

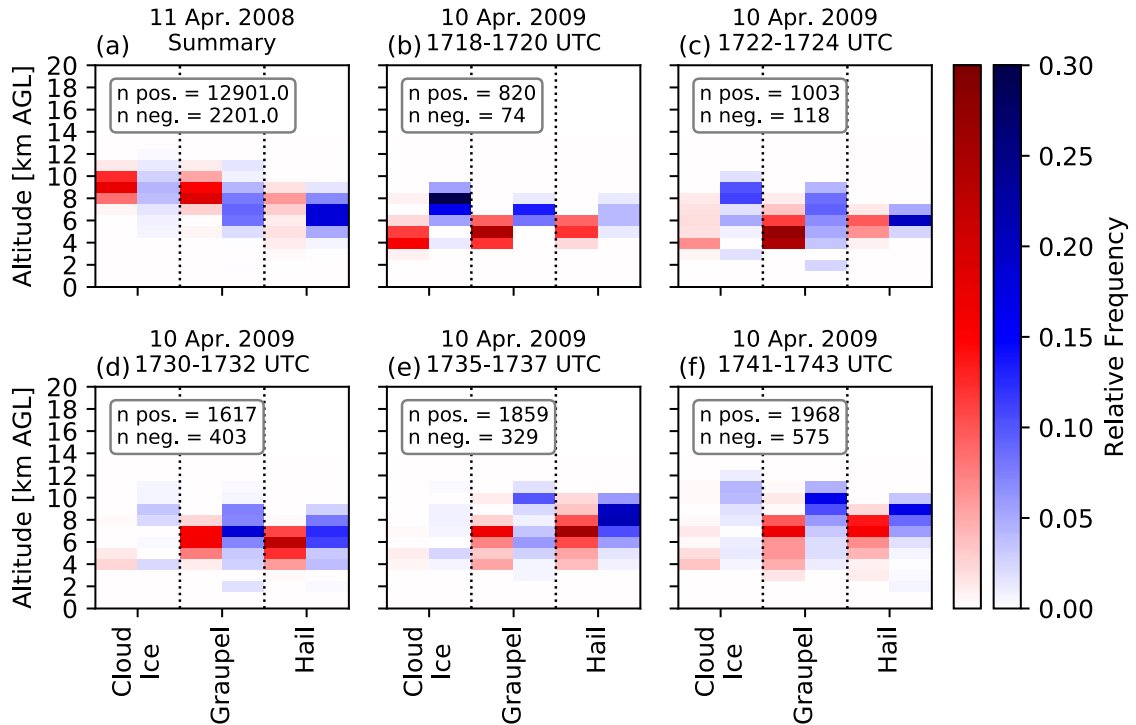


Figure 4.7: Distributions of the locations of lightning sources observed in the $\geq 5 \text{ m s}^{-1}$ up-draft by hydrometeor type and altitude. Positive and negative source location distributions in cloud ice, graupel, and hail are shown side by side in red and blue color fill, respectively. Color fill shades correspond to values of relative frequency of source distribution as indicated in the corresponding color bars on the right. The cloud ice category consists of the aggregate, ice crystal, and vertically oriented ice HID categories while the graupel category consists of both LD and HD graupel HID categories. (a) As normal 11 April 2008 source distributions did not change appreciably over the analysis period, the average distribution over the full analysis period is shown. (b-f) Distributions of sources in the 10 April 2009 anomalous storm are shown in each of the lightning analysis periods.

between 7 km AGL and 8 km AGL. However, similar to the positive source distributions in the normal storm, there was a secondary maximum in graupel near 7 km AGL as well.

During the following analysis period between 1722 UTC and 1724 UTC (Figure 4.7c), negative sources were distributed at higher altitudes near 8 km AGL to 9 km AGL in cloud ice regions but were observed through a greater depth in graupel with a relative maximum at 7 km AGL to 8 km AGL. Negative sources were also more frequently observed in hail re-

gions at 6 km AGL. Positive sources at this time were primarily observed in graupel regions between 5 km AGL and 6 km AGL.

Between 1730 UTC and 1732 UTC, negative sources were more frequently distributed within graupel and hail regions between 6 km AGL and 9 km AGL and were observed less frequently in cloud ice regions aloft (Figure 4.7d). Positive sources were also more uniformly distributed in graupel and hail regions between 4 km AGL and 7 km AGL, overlapping with negative source distributions. Elements of these distributions at this time were consistent with anomalous charging characteristics and the anomalous negative dipole, with lower positive charge mostly associated with precipitation ice and some fraction of negative charge aloft associated with cloud ice. However, aspects of the negative charge distribution between hydrometeor categories shared similarities with the negative charge distributions in the normal supercell as well, particularly with respect to the relative distributions of negative sources observed in precipitation ice regions between 6 km AGL and 8 km AGL. If the primary dipoles and charging behaviors in the normal and anomalous supercells had been purely reversed, the negative charge in the anomalous supercell should have shared more similarities with the positive charge distributions in the normal supercell. That is, relatively few negative sources should have been identified within hail regions in the anomalous storm as relatively few positive sources were located in hail regions in the normal supercell. The negative source regions in the anomalous supercell shared microphysical characteristics expected of both anomalous and normal charging even though the dominant charge structure was an anomalous negative dipole.

Between 1735 UTC and 1737 UTC, both positive and negative sources were most frequently distributed in hail regions though their relative maxima were offset at 6 km AGL to 8 km AGL and 7 km AGL to 8 km AGL, respectively (Figure 4.7e). Secondary relative

maxima in positive and negative sources were also observed in graupel regions at similar altitudes and relatively few sources of either polarity were observed in cloud ice regions in the updraft (Figure 4.7e). More than earlier, positive and negative source distributions were occupying more of the same vertical depths as well as relatively similar hydrometeor regions in similar proportions. This change was observed as lightning flashes were both increasingly observed near 10 km and vertical lightning flash distributions became more broad between 7 km AGL and 10 km AGL (Figure 4.5b). Between 1741 UTC and 1743 UTC, there was less general vertical overlap between maxima in positive and negative source distributions in graupel and hail hydrometeor regions as the negative source region in particular became more vertically compact (Figure 4.7f). Though relatively few negative sources were observed aloft in cloud ice regions compared with precipitation ice regions, negative sources were observed in cloud ice regions with greater frequency than in the previous period, located between 10 km AGL and 11 km AGL. As negative charge within cloud ice as well as graupel was observed with greater frequency at higher altitudes, lightning flash initiation locations also increased to 11 km AGL (Figure 4.5b).

4.5.2.2 Elevated Positive Charge Region

Distributions of negative charge in precipitation ice regions suggested the increasing presence of negative charging of graupel. By NIC theory, collisions resulting in negatively charged graupel should also result in positively charged cloud ice. While distributions indicated prominence of negative charge within graupel regions in the updraft in Figures 4.7c to 4.7f, a relative dearth of positive sources in cloud ice regions within the upper mixed-phase and glaciated regions was notable. By considering only sources within the $\geq 5 \text{ m s}^{-1}$ updraft, lightning flash propagation above the updraft was not considered. The fraction of

unclassified lightning flashes such as those observed at and above 10 km also resulted in the omission of information about associated charge regions (Figures 4.3 and 4.4).

Vertical and HID distributions of sources associated with classified lightning flashes that initiated at 10 km AGL or higher and were outside of the 5 m s^{-1} updraft as well as sources associated with unclassified lightning flashes observed at 10 km AGL or higher are shown in Figure 4.8. Additionally, only sources associated with classified lightning flashes with lightning flash areas of less than 10 km^2 are shown because a few larger lightning flashes were found to propagate through the extensive lower positive charge regions, skewing relative frequencies away from the area of interest at higher altitudes. Note that all unclassified lightning flashes that initiated at or above 10 km AGL were characterized by small lightning flash areas of $\leq 7 \text{ km}^2$, consistent with known classification challenges presented by compact lightning flashes. From 1735 UTC to 1737 UTC and from 1741 UTC to 1743 UTC, classified lightning flashes exhibited breakdown that was primarily observed between 8 km AGL and 12 km AGL (Figures 4.8a and 4.8b). From these analyses, positive charge regions were identified in cloud ice between 10 km AGL and 12 km AGL. With regard to unclassified sources, it is expected that a large fraction were associated with positive charge regions since most breakdown observed in the VHF tends to be negative (e.g., Maggio et al., 2005; Rison et al., 1999; Rust et al., 2005; Shao and Krehbiel, 1996; Thomas et al., 2001). At these altitudes, however, it is not likely that sources observed in graupel regions were associated with recent positive graupel charging. Negative graupel charging is more likely at temperatures below -30°C absent local availability of very high LWC such as in an updraft core (Bruning et al., 2014; Saunders et al., 2006). It is more likely that smaller previously charged positive graupel had been advected to the 10 km AGL to 12 km AGL region from lower altitudes. Alternatively, positive charge may have been primarily carried on

small ice hydrometeors that were masked within radar data by the presence of a few larger neutral or weakly charged precipitation ice hydrometeors since hydrometeor size rather than concentration dominates the radar return signal as a result of sixth power weighting of particle diameter in radar reflectivity. Observations of possible masking of positively charged cloud ice by graupel were noted at 1730 UTC to 1732 UTC and 1741 UTC to 1743 UTC in cross-section analyses (Figures 4.3c and 4.4b). During these periods, positive sources observed near 8 km AGL were displaced downstream from negative sources in storm-relative flow, consistent with separation following normal NIC via differential advection. Though the observed positive sources may have been carried with cloud ice, they were observed at the edge of the volume identified as graupel (Figures 4.3b and 4.4b).

4.5.3 Kinematic Characterizations of Lightning Flash Initiation Locations

The evolution of lightning characteristics within the anomalous supercell suggested that more lightning flashes occurred within the updraft core and around the sides of the updraft (Figures 4.1, 4.3, and 4.4) compared with the normal storm (Figure 4.2). The following analyses discuss the spatial distributions of lightning flash initiations within the updraft in terms of the updraft volume in which lightning flash initiations were observed. That is, rather than consider the number of lightning flashes observed in a given updraft volume, the total number of 1 km^3 grid pixels in which at least one lightning flash initiation was observed is discussed. This perspective provides a better sense of the spatial extent of the updraft through which lightning flash initiations were distributed, whereas the observation of numerous lightning flash initiations in fast updraft regions could result from either an extensive spatial distribution of lightning flash initiations within the updraft region or from a high density of lightning flash initiations in a localized area. Consideration of the spatial

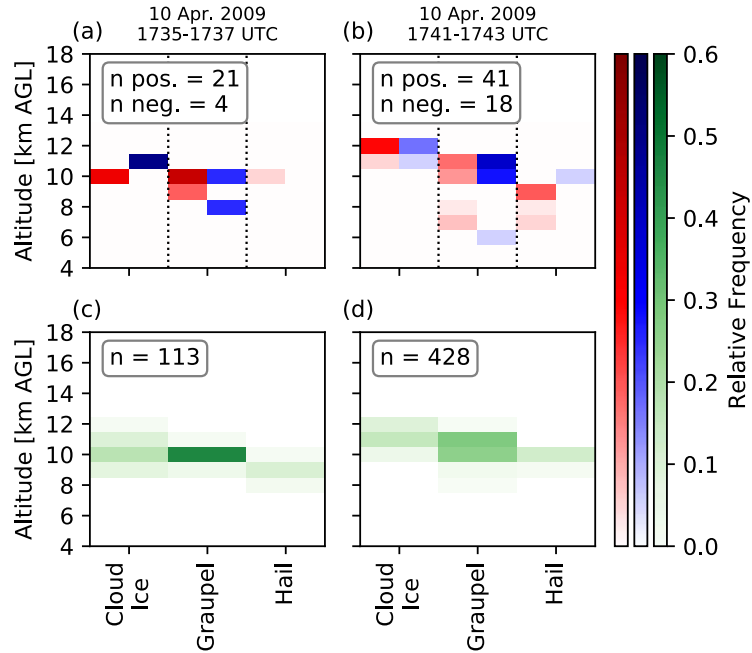


Figure 4.8: As in Figure 4.7 but for sources associated with classified lightning flashes with areas of $<10 \text{ km}^2$ that initiated in vertical motions of $<5 \text{ m s}^{-1}$ and at or above an altitude of 10 km AGL as well as sources associated with unclassified lightning flashes above 10 km AGL. (a-b) Panels represent source polarity characteristics in the latter two analysis period. As in Figure 4.7, positive and negative source distributions in cloud ice, graupel, and hail are shown side by side in red and blue color fill, respectively, as relative frequency of observation according to the corresponding color bars on the right. (c-d) Distributions of lightning source locations associated with lightning flashes that remained unclassified are plotted as relative frequency of observation in green color fill according to the corresponding color bar on the right.

distribution of lightning flash initiations allows for interpretation of the spatial extent of the strong electric fields within the updraft that resulted from proximal charge regions.

4.5.3.1 Updraft Speed

While lightning flash rates were low in the anomalous supercell between 1718 UTC and 1720 UTC, only one lightning flash initiated in the updraft and therefore only 1 km^3 of the $\geq 5 \text{ m s}^{-1}$ updraft contained any lightning flash initiations. This lightning flash as well

as all the others that initiated during this period occurred in relatively low updraft speeds of $\leq 10 \text{ m s}^{-1}$ even though over 200 km^3 of the updraft volume exhibited faster speeds between 10 m s^{-1} and 25 m s^{-1} (Figure 4.9b). Between 1722 UTC and 1724 UTC, several more lightning flashes initiated in the updraft (Figure 4.9d), though still only within updraft speeds of $\leq 15 \text{ m s}^{-1}$ despite the presence of a similarly large volume of faster updraft speeds (Figure 4.9b).

Once updraft speeds reached at least 25 m s^{-1} by the 1728 UTC analysis volume, lightning flash rates observed between 1730 UTC and 1732 UTC had also increased and more of the weak updraft as well as faster updraft speeds contained lightning flash initiations. The updraft volume distributions of the two supercells were most comparable during this period of observation of the anomalous supercell, especially considering the volume of updraft with speeds greater than 10 m s^{-1} (Figures 4.9a and 4.9b). However, although the anomalous storm's updraft volume in the 5 m s^{-1} to 10 m s^{-1} range over the course of the full analysis period was nearly double the average observed in the normal storm, the 5 m s^{-1} to 10 m s^{-1} volume within which lightning flash initiations were distributed was not proportionally larger at any time. Further, while the 10 m s^{-1} to 15 m s^{-1} updraft volumes were comparable in each storm between 1730 UTC and 1732 UTC (Figures 4.9a and 4.9b), lightning flash initiations were distributed throughout only a third as much of the 10 m s^{-1} to 15 m s^{-1} updraft volume compared with the normal storm (Figures 4.9c and 4.9d). Rather, lightning flash initiations were distributed throughout more of the faster updraft in the anomalous storm.

Increasing volumes of faster updrafts were observed during the 1735 UTC to 1737 UTC and 1742 UTC to 1743 UTC analysis periods in the anomalous supercell. Whereas no lightning flashes initiated within the limited volume of the fastest updraft with speeds between

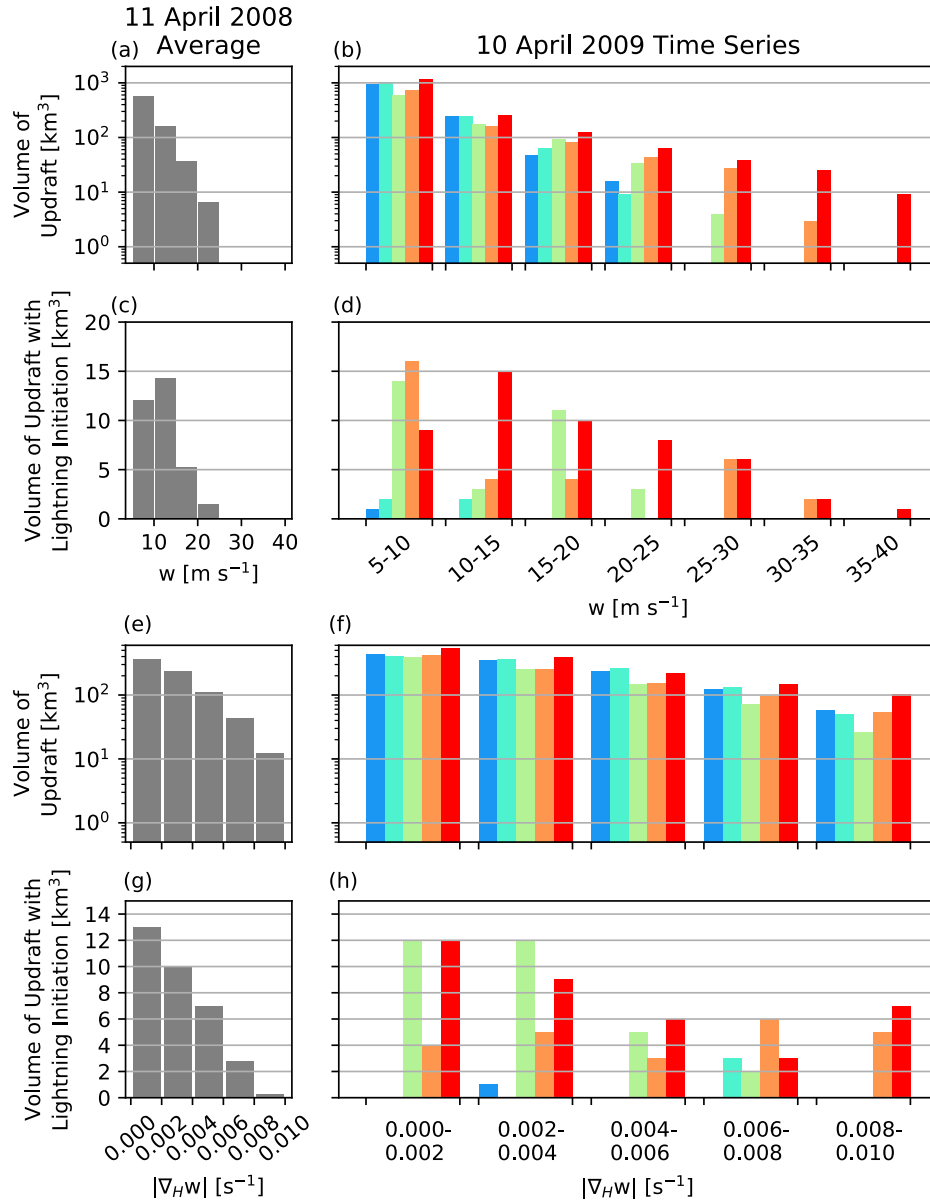


Figure 4.9: Distributions of total updraft volume and updraft volume containing lightning initiations. The following distributions are represented as averages for the 11 April 2008 supercell (left) and time series for the 10 April 2009 supercell (right), where each time period is colored as in Figure 4.5. (a, b) Distributions of the volume of updraft characterized by a range of speeds and (c, d) distributions of those volumes in which lightning initiations occurred are shown in the top half of the plot. (e, f) Distributions of the volume of updraft characterized by a range of magnitudes of horizontal gradients in vertical motion and (g, h) distributions of those volumes in which lightning initiations occurred are shown in the bottom half of the plot.

25 m s⁻¹ and 30 m s⁻¹ during the 1730 UTC and 1732 UTC analysis period (Figure 4.9d), lightning flash initiations were observed in some portion of the similarly sized fastest updraft volume with speeds between 30 m s⁻¹ to 35 m s⁻¹ in the subsequent 1735 UTC to 1737 UTC period. Additionally, lightning flash initiations were observed within the increasing volume of faster updraft speeds between 35 m s⁻¹ and 40 m s⁻¹ during the 1741 UTC to 1743 UTC period (Figures 4.9b and 4.9d).

4.5.3.2 Horizontal Gradients in Updraft Speed

In the later periods of observations in the anomalous supercell, lightning flash initiations near 7 km AGL to 8 km AGL were increasingly observed in gradient regions of the updraft alongside increasing horizontal heterogeneity in charge structure (Figures 4.3f, 4.4b, 4.4d, and 4.4f). The following discussion considers the volumes of varying horizontal gradients of vertical velocity, or updraft gradients, in which lightning flash initiations were observed.

Generally, there were larger volumes of stronger updraft gradients ≥ 0.006 s⁻¹ in the anomalous storm than in the normal storm (Figures 4.9d and 4.9f). Relatively few lightning flashes were observed in the updraft of the anomalous supercell prior to 1730 UTC, though these were distributed in stronger updraft gradient regions (Figure 4.9h), as suggested by the observed locations of select lightning flashes between 1722 UTC and 1724 UTC (Figures 4.1c and 4.1d). The relative distribution of lightning flash initiations within gradient regions became more comparable between the normal supercell and the 1730 UTC and 1732 UTC period in the anomalous supercell as its lightning flash rate increased (Figures 4.9g and 4.9h). Between 1735 UTC and 1743 UTC, however, the distributions became

increasingly dissimilar as lightning flash initiations were distributed throughout more of the stronger gradients compared with volumes of weaker gradients (Figure 4.9h).

4.6 Discussion on the Presence and Potential Impacts of Positive and Negative Graupel Charging in an ACS

Observations of the development of storm structure and summary statistics suggested that while gross charge structure was consistent with that of an anomalous storm, both negative and positive sources were observed in precipitation ice regions in the 10 April 2009 supercell, counter to expectations of a strict anomalous NIC regime. Bruning et al. (2014) discuss the possibility of both normal and anomalous NIC regimes in their presentation of the conceptual model of ACSs as a continuum of charging behavior. However, it is not clear that the conceptual model accounts for an extensive lower positive region associated with graupel along with a deep middle mixed-phase region of negative graupel charging, or that these characteristics have been observed in an anomalous supercell updraft core (Bruning et al., 2014, their Figure 4). In the absence of LWC or cloud microphysical data to support specific assertions of graupel charging, it is necessary to consider that these observations may be related to a variety of physical processes ranging from (a) predominant positive (negative) charging of precipitation (cloud) ice in an anomalous charging regime and subsequent masking of negative cloud ice by some quantity of neutral or weakly charged precipitation ice to (b) some non-trivial amount of negative (positive) charging of precipitation (cloud) ice hydrometeors corresponding to a normal charging regime adjacent to regions characterized by an anomalous charging regime (Bruning et al., 2014). The following discussion will consider information from the previous documentation of charge structure

development and spatial lightning flash initiation and propagation analyses to address the possible charging regimes under which the anomalous charge structure developed.

4.6.1 Onset and Development of Possible Negative Graupel Charging

The earliest indications that negative charging of precipitation ice may have begun contributing to observed lightning flash characteristics occurred between 1722 UTC and 1724 UTC as the updraft core increased in vertical extent and potentially became more capable of supplying LWC to colder regions in support of extended riming growth. Lightning flash initiations representative of the location of the interface between charge regions began to shift downward with respect to the updraft during this period and into increasing vertical velocities even as net charge regions ultimately increased in altitude with updraft growth. This increase in lightning flash initiations at lower altitudes (Figure 4.5b) occurred as the upper negative charge region became more closely associated with graupel regions (Figure 4.7c). This is consistent with a microphysical shift in negative charge carriers from advecting cloud ice toward sedimenting precipitation ice in the region. However, between 1722 UTC and 1724 UTC, negative charge was not yet distributed with higher frequency in faster vertical motion (Figure 4.10g) and other explanations for these observations at this stage of charge structure development exist. For instance, the appearance of negative charge in a graupel region may have been attributed to radar masking of negatively charged cloud ice by the presence of some quantity of neutral or positively charged graupel, as even a few larger hydrometeors in a region primarily composed of smaller hydrometeors would dominant the radar return signal. It should be noted that the presence of neutral graupel would indicate lack of active charging while the presence of positive graupel would suggest that some part of the negative charge region would have been neutralized, resulting in a

dissipative electrical process. However, increasing lightning flash rates through this period were indicative of increasing charging rates. Alternate explanations for the observed change in vertical characteristics of lightning flash initiations during this stage of development exist as well, including the charge masking and unmasking hypothesis (Bruning et al., 2007) by which series of charge deposition processes, charge neutralization, and sedimentation associated with sequential lightning flashes may cause an apparent downward shift of lightning flashes. Specifically, as lightning flash propagation occurs, charge of the same polarity of propagating lightning leaders is thought to primarily attach to cloud ice within the vicinity, either neutralizing it or possibly increasing its charge depending on its pre-existing charge magnitude and polarity. In the case of a negative dipole consistent with anomalous NIC, charge deposition associated with propagation of oppositely charged lightning leaders could neutralize the region associated with negatively charged cloud ice aloft through positive charge deposition as well as enhance any charge on the negative polarity cloud ice located in the positive charge region below through negative charge deposition. Positively charged graupel not neutralized during the lightning flash would be masked by the enhanced deposition of negative charge on coincident cloud ice until it could sediment and contribute to a distinct lower positive charge region. The downward displacement of the lower charge region associated with the masking and unmasking of sedimenting graupel over the course of several lightning flashes would shift the interface between opposite charge regions and location of lightning flash initiations to lower altitudes as well. The charge masking hypothesis becomes less supported as an explanation for the apparent downward shift in lightning activity near 5 km AGL to 7 km AGL after 1724 UTC as it requires proximal regions of both oppositely charged cloud and precipitation ice, such as are supported near the top of the updraft via PBLs and differential advection (Dye et al., 1986; Lhermitte and Williams,

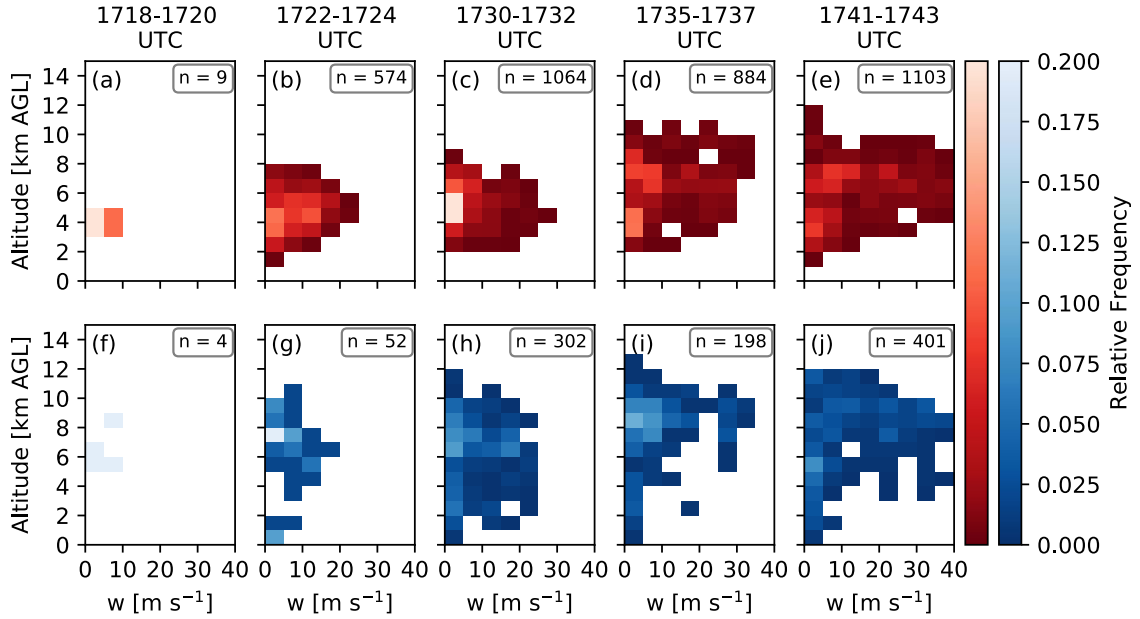


Figure 4.10: Time series of distributions of (a-e) positive and (f-j) negative source locations by altitude and updraft speed associated with lightning flashes that initiated within updrafts of $\geq 5 \text{ m s}^{-1}$. Color fills represent the relative frequency of observation of positive and negative source according to the red and blue color bars, respectively.

1985). However, after 1724 UTC, large quantities of cloud ice would not have been able to reside near 7 km AGL where lightning flashes continued to be observed even as the updraft deepened.

As the updraft continued to intensify between 1730 UTC and 1732 UTC, lightning flashes continued to initiate in the lower 5 km AGL to 7 km AGL region while lightning initiations also began to occur between 9 km AGL and 11 km AGL (Figures 4.3 and 4.5b). Simultaneously, negative sources were observed more frequently in precipitation ice (Figure 4.6b) particularly in the 6 km AGL to 9 km AGL region (Figure 4.7d). Lightning flash initiations at lower altitudes near 7 km AGL were increasingly observed in updraft regions with vertical velocities reaching into the 20 m s^{-1} range (Figure 4.3a) and became

more distributed through the fastest updraft volumes (Figure 4.9d). During earlier observations between 1718 UTC and 1724 UTC, positive sources associated with lightning flashes that initiated in the updraft were identified in maximum updraft regions (Figures 4.10a and 4.10b) while negative sources were primarily restricted to regions with updraft speeds of $\leq 10 \text{ m s}^{-1}$ (Figures 4.10f and 4.10g). However, beginning during the 1730 UTC to 1732 UTC analysis period, negative sources were increasingly identified in regions of faster updraft speeds (Figures 4.10h to 4.10j). While the negative charge region at this time may have been composed of cloud ice from collisions with positively charged precipitation ice, increasing proportions of negative charge identified in stronger updraft speeds and in regions primarily characterized as precipitation ice were together consistent with precipitation ice acting as an additional prominent carrier of negative charge. Additionally, the second region of lightning flash initiations located at higher altitudes is consistent with the idea of a second PBL established by negatively charged graupel near the top of the updraft.

The number of lightning flash initiations observed near 10 km AGL increased substantially beginning at 1735 UTC (Figure 4.5d). The majority of unclassified lightning flashes in this region propagated through both cloud ice and graupel regions (Figures 4.8c and 4.8d), while the few available classified lightning flashes provided evidence that cloud ice carried positive charge within the region (Figures 4.8a and 4.8b). Evidence of horizontally-adjacent areas of positive and negative charge was also inferred near 8 km AGL, with positive charge displaced downstream from negative charge regions identified closer to the updraft (Figures 4.3c and 4.3e). While this positive charge was identified within regions characterized as graupel, the horizontal separation is consistent with differential advection of cloud and small precipitation ice suspended in the weaker updraft aloft. These observations are physically consistent with normal ice-ice collisional NIC in the mid to upper mixed-phase

region near the updraft that would have contributed some volume of negatively charged precipitation ice as well as positively charged cloud ice.

4.6.2 Observed Charge Structure Complexity in the Updraft

By 1735 UTC, increasing fractions of positive and negative sources were observed within precipitation ice regions through the 10 km AGL layer (Figure 4.7e) and within regions of increasing updraft speeds (Figures 4.10d, 4.10e, 4.10i, and 4.10j). Positive and negative sources associated with the fastest vertical velocities were most frequently observed between approximately between 7 km AGL and 8 km AGL (Figures 4.10e and 4.10j), where temperatures were between approximately -20°C and -25°C . Temperatures in this region could have supported transitions in dominant ice-ice collisional NIC regimes, particularly given any variability in cloud microphysical properties including LWC and saturation ratio. Horizontal complexity in charge polarity was also observed in this region, seemingly forming a favorable location for lightning flash initiation as lightning flashes were increasingly observed in updraft gradients (Figures 4.4b and 4.9h) and over a deeper vertical depth (Figure 4.5b). However, the origins of the observed horizontal charge structure complexity supporting lightning flash initiation in the gradients of the updraft in the anomalous storm are unclear. It is possible that horizontal charge variability within the updraft could result from adjacent organization of oppositely charged precipitation ice sedimenting from different regions and charging regimes. Adjacent, horizontally varying charging regimes within and outside of the LWC-rich updraft core could have served as another possible origin. Assuming negative graupel charging was not prevalent, charge complexities could have resulted as well from turbulent mixing and three-dimensional differential advection of positively charged graupel and negatively charged cloud ice.

4.7 Conclusions

This study documented the evolution of electrical, kinematic, and microphysical structure within a developing anomalous supercell located in the Southeastern US. The microphysical characterization of lightning flash propagation and lightning flash initiation locations with respect to updraft structure were specifically discussed, particularly as they varied from relationships observed in a normal supercell from the same region. Key observations and results include:

1. Development of anomalous charge structure within the updraft proceeded from a primarily two-layer to a multi-layer model, elements of which exhibited consistency with NIC theory. Specifically, the original two-layer prominent charge structure was physically consistent with the differential sedimentation and advection of positively charged precipitation ice and negatively charged cloud ice hydrometeors. Additional layers were observed as the storm developed, including a shallow lower negative charge region and a small upper positive charge region, forming a quadrupole charge structure within which the original dominant anomalous dipole was nested. During development, lightning flash initiations within the $\geq 5 \text{ m s}^{-1}$ updraft were primarily observed between the central anomalous dipole and upper positive charge region.
2. The anomalous NIC regime was defined as positive charging of riming precipitation ice and negative charging of non-riming ice associated with warmer temperatures, increasing LWC, and/or decreasing saturation ratio. By contrast, the normal NIC regime was defined as the negative charging of riming precipitation ice and positive charging of non-riming ice associated with cooler temperatures and/or lower LWC. In the anomalous supercell, negative charge was increasingly observed within precipitation

ice regions and in increasing updraft speeds over time. Although the negative charge region in the anomalous supercell was at first most consistent with the anomalous NIC regime (i.e., associated with non-riming ice at cooler temperatures), aspects of the vertical distributions and hydrometeor characteristics of negative charge evolved to share similarities with the negative charge region associated with the normal NIC regime (i.e., associated with riming ice at cooler temperatures).

3. The negative charge inferred in the precipitation ice region in the anomalous supercell could have been explained as the result of the masking of negatively charged cloud ice in radar observations by some quantity of neutral or weakly positively charged precipitation ice. However, the presence of negatively charged precipitation ice within the mixed-phase updraft was supported by observations of positively-charged cloud ice within the glaciated region. Additionally, positive charge regions were observed adjacent to negative charge regions where the spatial arrangement of each region with respect to storm-relative flow was consistent with the action of differential advection of positively charged cloud ice and negatively charged precipitation ice. These observations were indicative of the presence of the normal NIC regime within some part of the mixed-phase updraft of an otherwise anomalous supercell.
4. Horizontal charge structure complexity within the updraft region of the thunderstorm included horizontally adjacent, discrete regions of negative charge within layers predominantly associated with positively charged precipitation ice. Lightning flash initiations were often observed in these regions, associated as well with fast updraft speeds and large horizontal gradients in vertical motion. Given the coarse temporal

and spatial resolution of the available data, the origins of these local charge structures were not discernible.

5. Differences in lightning flash locations with respect to updraft structure were observed between the anomalous and normal supercells. Specifically, lightning flash initiation locations were distributed throughout faster updraft regions and in stronger updraft gradients in the anomalous supercell. These observations suggest that established electric fields associated with proximal charge regions were located in or near faster updrafts in the anomalous supercell to support lightning flash initiations within stronger updraft regions compared with the normal supercell. If this was the case, larger hydrometeors of opposite polarity could have maintained PBLs in faster vertical velocities, shifting the charge region interface at which lightning flash initiate into faster updraft regions. As such, observed lightning flash locations are consistent with the presence of a non-trivial component of negatively charged precipitation ice within the negative charge region in addition to the characteristic positively charged precipitation ice region in the anomalous charge structure.

4.7.1 Conceptual Model

The following conceptual model integrates aspects of the spatial observations presented herein as well as results extrapolated from prior studies, summarizing hypotheses concerning complexities that could not be addressed with the resolution of existing data or lack of cloud microphysical information (Figure 4.11). It also presents a framework by which the evolution of storm structure and lightning characteristics may be considered in the context of multiple NIC regimes in future studies. It should be noted as well that aspects of charge structure evolution and spatial lightning flash relationships with the updraft

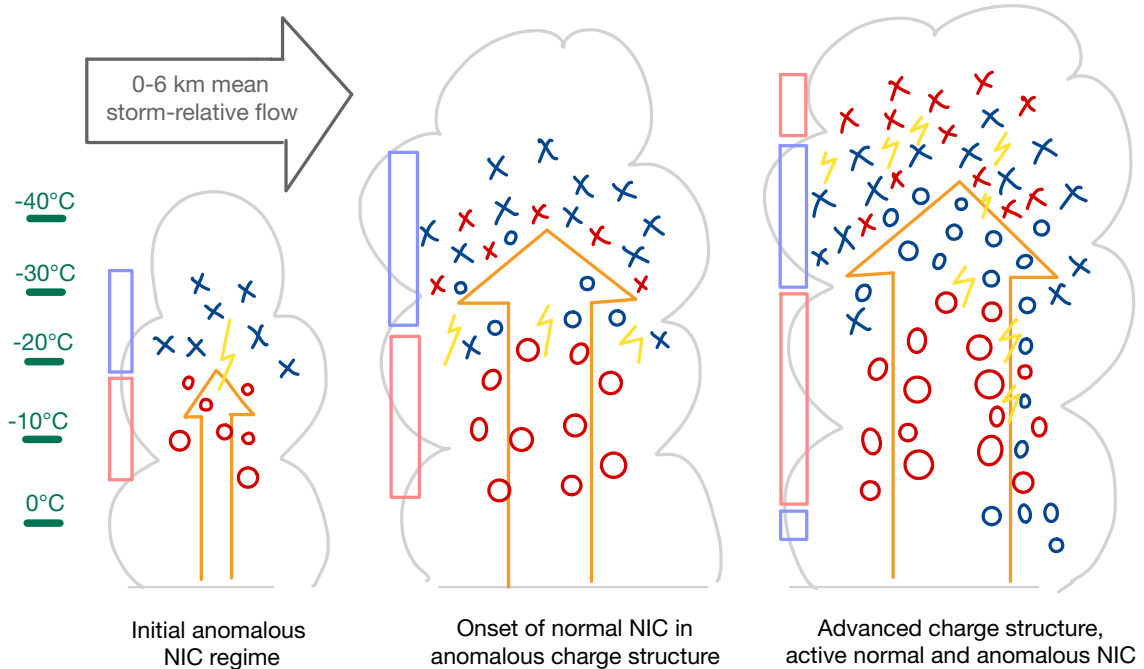


Figure 4.11: Simplistic conceptual model of the evolution of charge characteristics associated with a developing thunderstorm within which variable NIC regimes in different regions influence charge structure and lightning location. Approximate thermodynamic structure is indicated along the left side of the figure. Open circles (crosses) represent precipitation ice (cloud ice) hydrometeors. Red (blue) coloring represents positive (negative) charge. The location of the 10 m s^{-1} updraft is indicated as a yellow arrow. Possible lightning flash initiation locations are shown as yellow markers, where the relative number of yellow markers is intended to convey changes in lightning flash rate. General locations where net positive and net negative charge regions might be inferred are denoted by light red and light blue boxes, respectively.

that are highlighted within the conceptual model were not specifically unique to the single anomalous storm of study in Chapter 4, but were anecdotally observed in an anomalous supercell storm that occurred on 22 April 2017 in the Southeastern US as well. Though not detailed as carefully, some elements were discussed in Chapters 2 and 3.

It is suggested that in a storm within which the initial charge structure is anomalous, the initial NIC regime would also be anomalous as the developing updraft confines adequate LWC supply to the warmer mixed-phase region in support of the growth and positive

charging of precipitation ice. Lightning flashes would be expected to initiate near the top of the updraft, between advected negatively charged cloud ice and the PBL of positively charged graupel near the top of the updraft.

As the updraft deepens and supplies LWC to the colder middle mixed-phase region, precipitation ice growth becomes supported at higher altitudes in cooler temperatures and so growing precipitation ice charges negatively in rebounding collisions as cloud ice charges positively. Depending on graupel growth rates in the cooler mixed-phase region, negatively charged precipitation ice may remain smaller than precipitation ice growing in the warmer mixed phase region and may reach a PBL at slower updraft speeds near the top of the updraft. If positively charged cloud ice does not advect out of the main negative charge region, it may neutralize in the net some portion of the upper negative charge region primarily composed of cloud ice. Combined with relative sedimentation of negatively charged precipitation ice versus the advection of cloud ice, the negative charge center may shift downward. As oppositely charged precipitation ice of different sizes maintain PBLs at different regions within the updraft and the interface between positive and negative charge regions shifts lower with respect to the updraft structure and into faster updraft speeds, lightning flash initiations may be observed at lower relative altitudes in or around the middle of the updraft rather than at the top of the updraft. They may also be observed within faster updraft speeds. As graupel content contributes to charge generation participating in active lightning through two charging regimes, lightning flash rates relative to the volume of graupel could also increase as charge structure heterogeneity increases.

As the updraft continues to develop and precipitation ice growth is supported through greater depths of the storm, it is suggested that some quantity of positively charged cloud ice may collect relative to the negative charge region and support lightning flash initi-

ations between the smaller positive charge region aloft and more expansive negative charge region. The organization of pooled charge pockets associated with cloud ice of opposite polarity resulting from local charging in different NIC regimes may also contribute to frequent small lightning flashes, supporting a continued increase in lightning flash rate relative to observed updraft and graupel volumes as more of the charging processes result in increases in the electric field. Additionally, while larger quantities of negatively charged graupel may accumulate within the storm as the updraft extends through more of the colder mixed-phase region, it is expected that it would still grow more slowly and remain smaller in the colder mixed-phase region as a result of reduced LWC. It is expected that smaller negatively charged precipitation ice would sediment with respect to the slower vertical motions at the edge of the updraft. These particles may contribute to horizontal heterogeneity in charge structure in gradient regions of the updraft as they sediment adjacent to larger positively charged precipitation ice balanced within faster vertical motions nearer to the updraft core. Through sedimentation and advection, graupel from normal NIC regimes may also contribute to a minor lower negative charge layer occasionally observed in the mixed-phase region at temperatures warmer than -10°C (e.g., Bruning et al., 2014; Kuhlman et al., 2006; Mansell et al., 2005; Wiens et al., 2005). It is possible as well that a combination of three-dimensional flows and gradients in cloud microphysical conditions within the updraft would support horizontal variations in charging regime that further contribute to charge structure heterogeneity and increased charging.

4.7.2 Opportunities for Future Study

Increased lightning flash rates in anomalous storms have a physical basis in an increase in charging rate associated with the support of a robust updraft. Studies have

suggested that kinematic texture contributes to an increase in the number of lightning flashes by organizing smaller charge regions between which more numerous, smaller lightning flashes initiate (e.g., Brothers et al., 2018; Bruning and MacGorman, 2013). However, the extent to which charge structure complexity associated with three-dimensional variability in ice-ice collisional NIC regimes contributes to extraordinary lightning flash rates remains unaccounted for. It is suggested that three-dimensional cloud microphysical variations may contribute to charge structure complexity beyond small-scale reorganization of charged hydrometeors associated with kinematic variations, contributing to numerous smaller charge regions that present more opportunities for lightning flash initiations. Subsequent factors such as additional secondary charging mechanisms as well as charge deposition by many active lightning channels may then further increase the complexity of charge and lightning flash relationships in anomalous storms.

Increased charge structure complexity in anomalous storms accompanied by increases in the number of flashes, particularly those of small extent or short duration, may pose additional challenges to GLM detection efficiency beyond those suggested by a tendency toward lower flash initiation altitudes in anomalous storms (e.g., Fuchs and Rutledge, 2018; Murphy and Said, 2020). Zhang and Cummins (2020) found that small or short-lived flashes, regardless of their vertical location, reduce GLM detection efficiency, providing another pathway by which detection efficiency may be markedly reduced in anomalous storms in particular. To better understand potential challenges of interpretation of GLM measurements in anomalous storms and the frequency with which they may arise, future studies may wish to investigate the consistency of relationships observed herein between evolution of charge structure heterogeneity and associated changes to lightning flash size distribution as well as the locations in which lightning flashes initiate. These relationships may

be used to better predict reduction in GLM detection efficiency associated with anomalous storm characteristics that may be incorrectly interpreted as reduction in lightning activity, even as kinematics, microphysics, and ground-based detection of lightning flash properties otherwise indicate intensification.

Additionally, addressing the interaction and relative impacts of microphysical and kinematic properties on charging processes, resultant organization of charge structure, and lightning flash properties may resolve sources of variability observed in lightning flash rates and convective parameters such as updraft speed or volume. Refining understanding of these relationships may also add specificity to the success of metrics such as lightning flash rate relationships based on graupel volume (e.g., Carey et al., 2019). Alongside rich observational data and numerical modeling studies, further evaluation of spatial relationships between charge structure, lightning, and properties of the convective updraft may contribute specificity to the lightning flash-based conceptual models by which convective intensity is interpreted.

4.8 Acknowledgments and Data Availability Statement

This study was funded by NASA Severe Storms Research (NNH14ZDA001N), provided under contract to the UAH authors from the NASA Marshall Space Flight Center (NNM11AA01A). The authors thank Drs. Kevin Knupp, Ted Mansell, and Udaysankar Nair for helpful discussions from which the manuscript benefitted. Data from ARMOR and NALMA corresponding to the 10 April 2009 supercell can be accessed at <https://zenodo.org/record/3738553> (license: Creative Commons Attribution 4.0 International, Carey and Blakeslee, 2020a). ARMOR and NALMA data corresponding to the 11 April 2008 case can be accessed at <https://zenodo.org/record/3783694> (license: Creative Commons At-

tribution 4.0 International, Carey and Blakeslee, 2020b). Data from KHTX and RUC and RAP model analysis data are available from <https://www.ncdc.noaa.gov/data-access/radar-data/nexrad> and <https://www.ncdc.noaa.gov/data-access/model-data/model-datasets/rapid-refresh-rap>, respectively.

APPENDICES

APPENDIX A

AUTOMATED FLASH-BY-FLASH POLARITY CLASSIFICATION

The DBSCAN algorithm (Ester, M. et al., 1996) within the scikit-learn Python package (Pedregosa et al., 2011) is applied to flash-by-flash polarity classification because of its ability to identify regions of dense data points apart from sparse data. It is well adapted to the problem of identifying temporally dense, noisy negative breakdown in positive charge regions apart from spatially separate, temporally sparse positive breakdown in negative charge regions as detected in the VHF. This is a second, separate application of DBSCAN following its initial use to identify flashes from total VHF source data.

Though sources from multiple flashes are aggregated to infer net charge structure, the algorithm operates on source data provided from individual flashes. Leveraging the roles of temporal and vertical properties of VHF flash detection and bidirectional flash propagation, the time and altitude data of each source in a flash are supplied to the DBSCAN algorithm as the criteria by which to identify clusters. These data are first standardized using the standard scaler in the scikit-learn Python package which subtracts the mean from each value before dividing by the standard deviation (Pedregosa et al., 2011). Standardization of source data on a per-flash basis rather than applying the same scaling criteria to all flashes allows the spatial properties of each flash to be considered individually, reducing the spatial and temporal implications of size differences between compact and extensive flashes.

Individual treatment of flashes also mitigates impacts from source detection efficiency differences with range from the LMA network center.

A.1 DBSCAN Cluster Determination

Clusters of dense data points are identified by DBSCAN using an n-dimensional neighborhood-defining Euclidean distance and a minimum count threshold. Selections of the distance and count threshold were accomplished subjectively. From visual inspection of numerous flashes, it was determined that a Euclidean standardized distance of 0.5 performed most uniformly over a range of flash characteristics, most often appropriately grouping regions of sources indicative of negative breakdown. The minimum number of sources required to identify a cluster in a flash was 5 percent of the total number of sources in a flash, rounded up to the nearest integer, with a threshold floor of 3 sources. The threshold floor of 3 sources was selected in order to retain the classification of single isolated sources as DBSCAN noise in flashes with few sources as well as to increase the likelihood that clusters could be large enough, even in small or poorly detected flashes, to be identified as representative of the expected behavior of negative breakdown.

A.2 Source Classification

Points within a DBSCAN cluster are either classified as cluster core or cluster edge points, while points not included in a cluster are termed noise points. Cluster core points are located within the neighborhooddefining distance of at least the threshold minimum specified number of other points whereas cluster edge points are not. Figure A.1a illustrates the implementation of the cluster identification criteria and point definitions within the DBSCAN algorithm using LMA sources in a flash as scaled data points. Following

the determination of noise, cluster core, and cluster edge sources, each type is assessed and provided a label corresponding to charge structure classification. Sources identified as DBSCAN noise are interpreted as sparse sources detected during positive breakdown in the negative charge region, and so are labeled “negative sources.” Cluster edge sources remain unclassified and are not used to identify charge regions. These are located around cluster core sources and inherently between charge regions, also often representing the region of initial flash development that typically remains unclassified in manual analysis (Rust et al., 2005). Cluster core sources, those that occur in the regions of highest density of sources, are used to identify sources that occurred during negative breakdown in the positive charge region. If the number of core sources in each cluster is greater than 20 percent of the total sources, these points are labeled “positive sources.” Otherwise, they remain unclassified in order to limit ambiguity associated with small clusters of sources separate from classified charge regions as well as to avoid misclassification of recoil leaders as a positive charge region within an original negative charge region (e.g., Bruning et al., 2010; MacGorman et al., 2005; Mazur and Ruhnke, 1993; Mazur et al., 2013; Shao and Krehbiel, 1996). Once core sources in all clusters have been labeled, positive and negative sources remain classified if the total number of positive sources is greater than 50 percent of the total number of sources in the flash, reflecting that most sources detected in a flash result from negative breakdown. Otherwise, the flash is deemed unclassified and its sources are not used to identify charge regions.

Each of the applied thresholds were identified through subjective testing to be most consistent with traditional subjective flash-by-flash classification for a variety of flashes. Sensitivity testing of thresholds should similarly be evaluated prior to implementing this technique with other applications and networks, including assessment of the effectiveness of

station and source criteria used for flash clustering to control for non-lightning noise sources that may result in classification errors.

A.3 Limitations and Improvements

As with other classification methods, there are limitations. Primarily, flashes with few sources often remain unclassified since regions of appreciable density present classification challenges. Cluster edge points are also excluded from classification, limiting the spatial extents to which charge regions are resolved. Detection of unusually noisy propagation of positive breakdown facilitated by a particularly sensitive LMA presents other classification concerns. From examination of flashes that were detected using the NALMA configuration on 22 April 2017, it was found that in the rare flashes in which positive propagation was detected with an unusually high density of sources, the density of negative propagation remained dominant. As a result, clusters associated with unusually dense positive breakdown did not meet required size criteria and were labeled as unclassified. In these instances, true positive breakdown was not classified as negative charge and the negative charge regions were not mapped as completely. However, as identification of the location of positive charge regions is sufficient for storm-scale charge structure identification, this method meets the minimum requirement. A related concern is the possible false identification of positive charge regions when recoil leaders occur. Recoil leaders include a negative leader component that radiates strongly as it propagates through the original channels from the original net negative charge region (Bruning et al., 2010; MacGorman et al., 2005; Mazur and Ruhnke, 1993; Shao and Krehbiel, 1996). While the present method limits classification of sources occurring in recoil leaders, these as well as particularly well resolved positive breakdown

may still present challenges in particularly well resolved flashes near the center of sensitive LMAs.

Automation of flash-by-flash classification reduces the time required of manual flash identification, particularly for large datasets. The density-based aspect of the DBSCAN method is also resistant to poor flash clustering performance, correctly identifying charge regions based on VHF properties when multiple flashes in close spatial and temporal proximity may be falsely combined and assumptions associated with bilevel flash structure are challenged. Similarly, density-based clustering allows correct classification of charge regions in large, sloping flashes that can pose challenges to other altitude-based automated methods (e.g., the “bifurcation” method, Tessendorf et al., 2007a). While this method improves on existing classification methods, future refinements and adaptations are possible. For instance, classifications may be more resistant to errors as integration of additional information afforded from other breakdown properties, such as propagation speed (van der Velde and Montanyà, 2013), are considered.

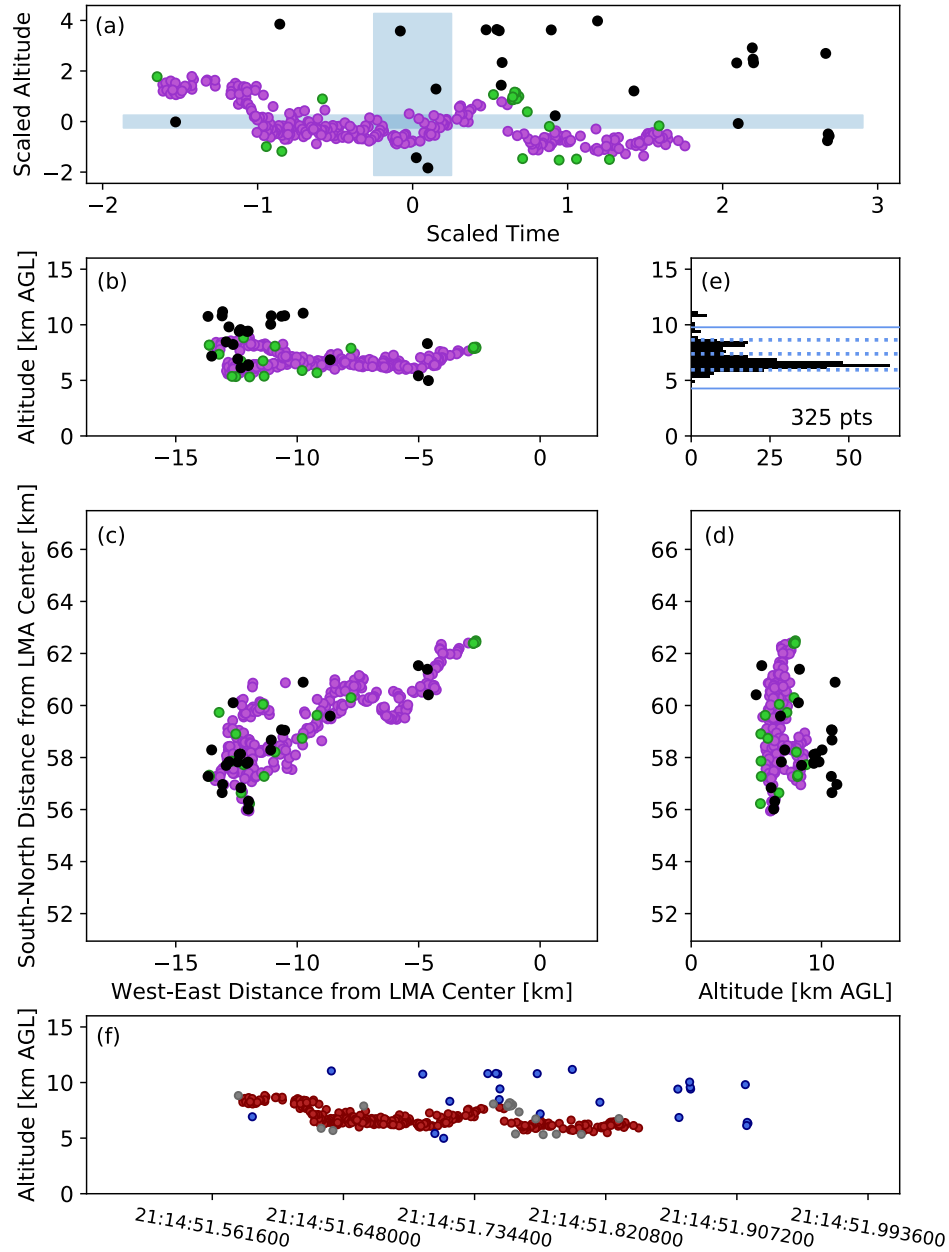


Figure A.1: Representation of a single flash during DBSCAN classification process in an adapted 5-panel format. (a) Time-height plot of sources mapped in scaled coordinates as DBSCAN points, where DBSCAN-classified cluster core (purple dots), cluster edge (green dots), and noise points (black dots) are shown. Projections of sources with DBSCAN classifications are shown in the (b) vertical and west-east dimensions, (c) west-east and south-north dimensions, and (d) vertical and south-north dimensions. (e) An altitudinal histogram of sources is also provided. (f) Charge structure classification of DBSCAN results are shown, including positive sources (red dots) consistent with negative breakdown in positive charge regions, negative sources (blue dots) consistent with positive breakdown in negative charge regions, and unclassified sources (gray dots).

APPENDIX B

STORM CASE SUMMARY

The synoptic to meso- α conditions under which each storm developed are described, providing further context to the observed pre-convective environmental parameters. The sounding profiles used for pre-convective environmental analyses accompany these descriptions. The progression of each storm within the broader domain over the full analysis period is also shown.

B.1 Normal 6 February 2008 Case

A broad upper level trough in the middle Mississippi Valley region was connected with a surface low and associated cold front that forced deep convection in the early morning hours of 6 February 2008. An extensive area of low-level moisture with dew point temperatures $>12^{\circ}\text{C}$ was present over the Tennessee Valley region and together with a weak cap, many storms were able to develop and merge to form linear convective modes, visible around the supercell of interest during its progression (Figure B.1). Additionally, a strong mid-level jet with wind speeds in excess of 55 m s^{-1} at 500 mb supported both speed and directional shear, resulting in bulk shear of 30 m s^{-1} that favored the development of supercell structures in isolated convection. The model analysis sounding representative of the pre-convective environment is shown in Figure B.2.

B.2 Normal 11 April 2008 Case

An extensive area of deep convection from the Ohio River Valley into the Southeast was supported by a large, deep upper-level low located in the upper Mississippi River Valley. As most of the synoptic forcing and associated favorable conditions for deep convection were located nearer to the Northwestern Ohio River Valley region, instability remained comparatively low in the Tennessee Valley during this event (Table 3.2). Low-level southwesterly flow associated with the trough resulted in an expansive supply of low-level moisture with dew point temperatures of $>12^{\circ}\text{C}$ extending into the Ohio River Valley. However, deeper low-level moisture associated with 700 mb dew point temperatures of $>0^{\circ}\text{C}$ was restricted mostly to Mississippi and the Western Tennessee Valley region. Despite more modest support for deep convection in the Southern Tennessee Valley where the storm of interest was observed, strong speed shear in the region supplemented unidirectional wind profiles in favor of the development of supercell structures. The pre-convective model analysis sounding profile associated with these conditions is shown in Figure B.3. The progression of the supercell of interest is shown in Figure B.4.

B.3 Anomalous 10 April 2009 Case

Conditions associated with a deep upper-level low pressure region in the middle Mississippi Valley favored the development of deep convection in the Tennessee Valley along and to the east of an attendant cold front. A southwesterly low-level jet with maximum wind speeds of 20 m s^{-1} resulted in the greatest low-level moisture supply extending into northern Mississippi and the southwestern Tennessee Valley region. This jet and associated moisture supply promoting destabilization in the warm sector. The development of a quasi-linear convective system (QLCS) in West-Central Tennessee observed prior to and

during the analysis period (Figure B.5) was associated with unidirectional flow near the advancing cold front. Simultaneously, veering wind profiles further to the east supported the development of isolated supercells in northern Alabama and South Central Tennessee ahead of the QLCS. The reconstructed sounding from model analysis associated with the pre-convective environment during this case is shown in Figure B.6.

B.4 Anomalous 22 April 2017 Case

Deep convection in the local evening hours was associated with a positively tilted upper level trough over the middle Mississippi and Ohio Valleys and a stronger surface low and associated cold front in Northern Mississippi and Alabama. During the daytime hours prior, clearing conditions over South Central Tennessee and North Alabama supported diabatic heating and destabilization ahead of the advancing cold front. Bulk shear of up to 20 m s^{-1} supported supercell development, while southeasterly storm motion facilitated propagation into increasing low-level moisture associated with a small region of dew point temperatures of $>12^\circ\text{C}$ in Northeastern Alabama. The reconstructed model analysis sounding representative of the pre-convective environment is shown in Figure B.7 while the progression of the supercell during the analysis period is shown in Figure B.8.

Normal 6 February 2008 Supercell

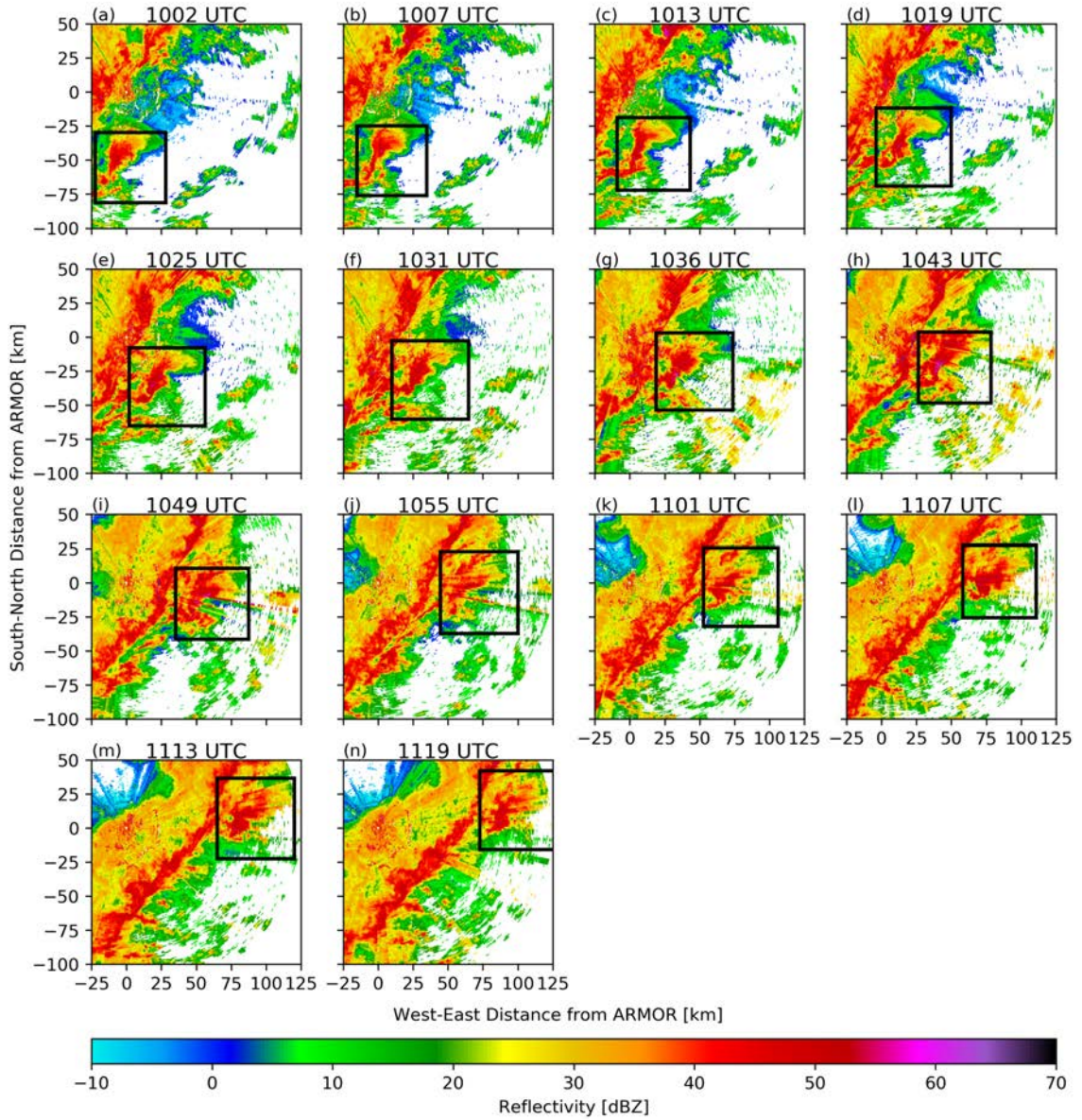


Figure B.1: Progression of the normal 6 February 2008 supercell and its immediate surroundings as observed by ARMOR at the lowest elevation angle. Each panel shows the storm at the lowest elevation angle at the time of a dual-Doppler retrieval. Post-processed, uncorrected ARMOR reflectivity are plotted in color fill.

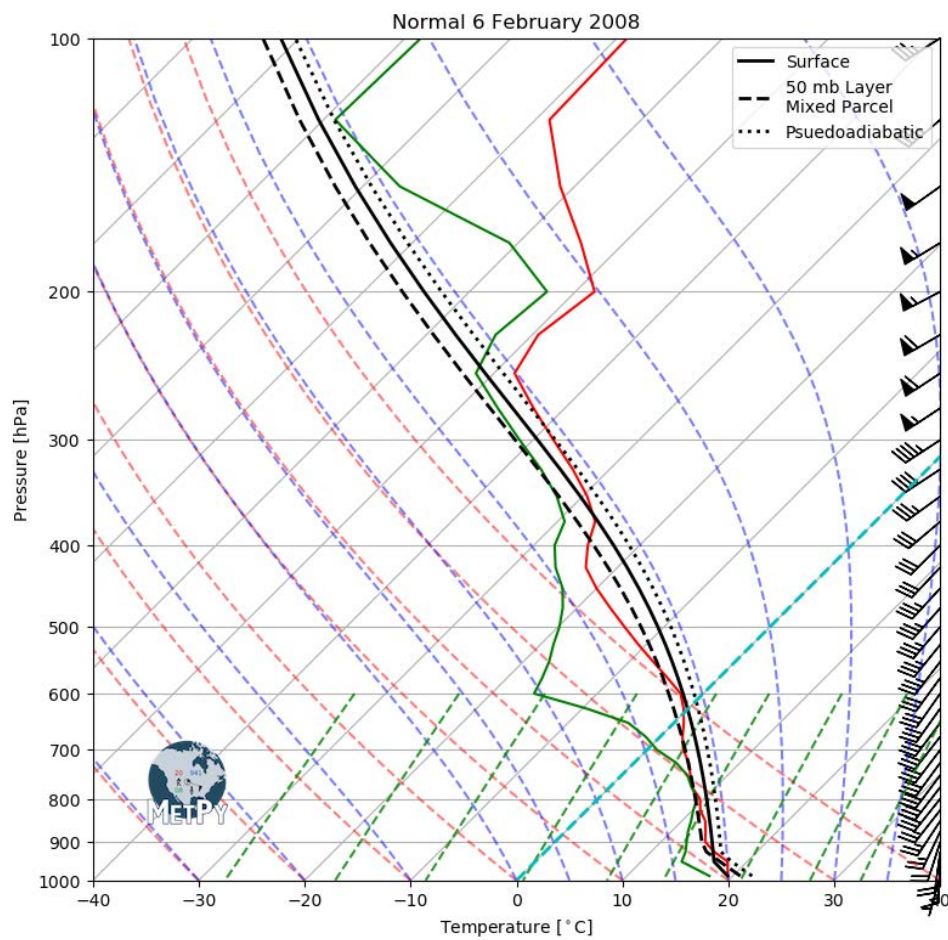


Figure B.2: Reconstructed model sounding for the normal 6 February 2008 case, created using MetPy software (May et al., 2008 - 2020).

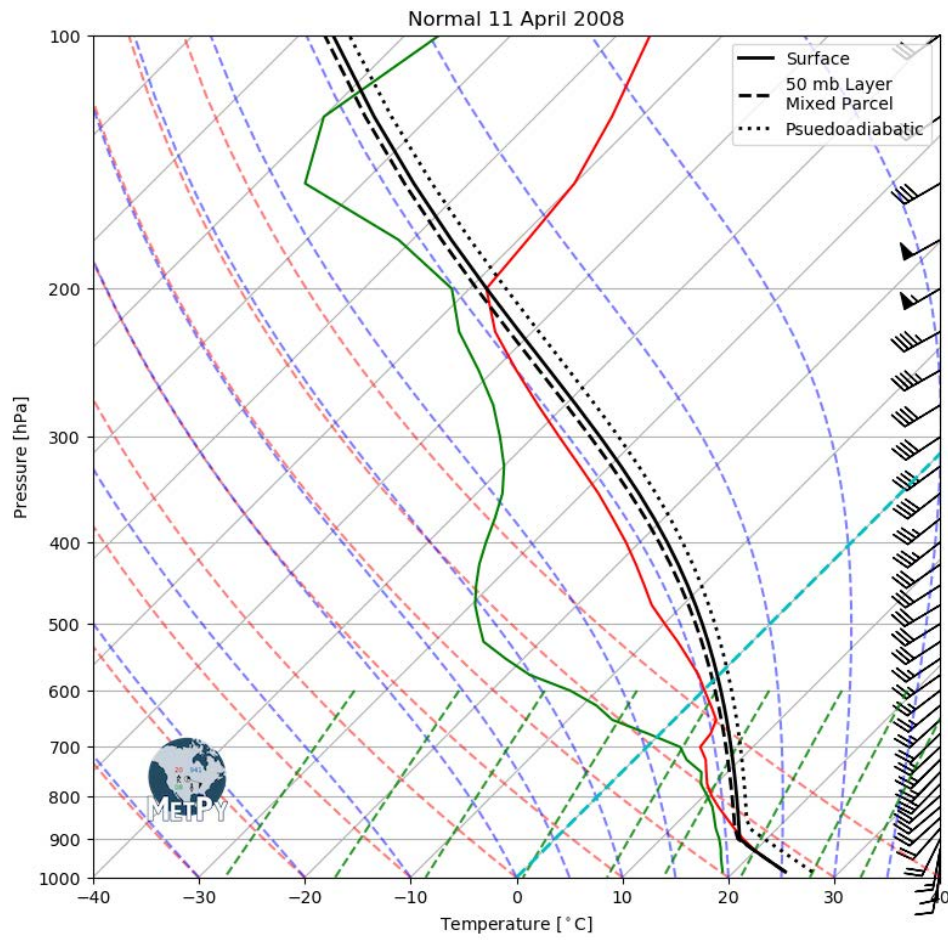


Figure B.3: As in Figure B.2 for the normal 11 April 2008 case.

Normal 11 April 2008 Supercell

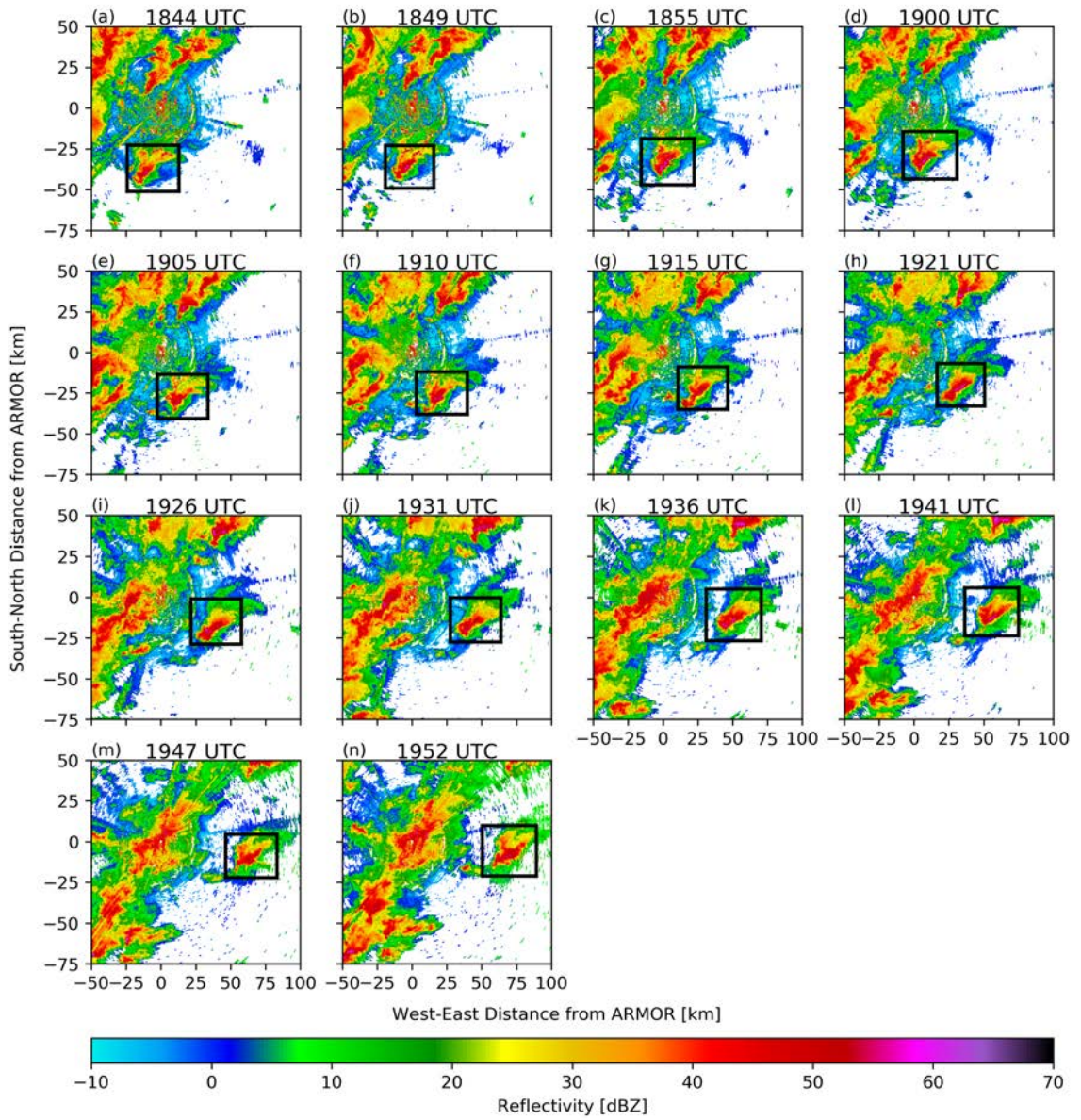


Figure B.4: As in Figure B.1 for the normal 11 April 2008 supercell.

Anomalous 10 April 2009 Supercell

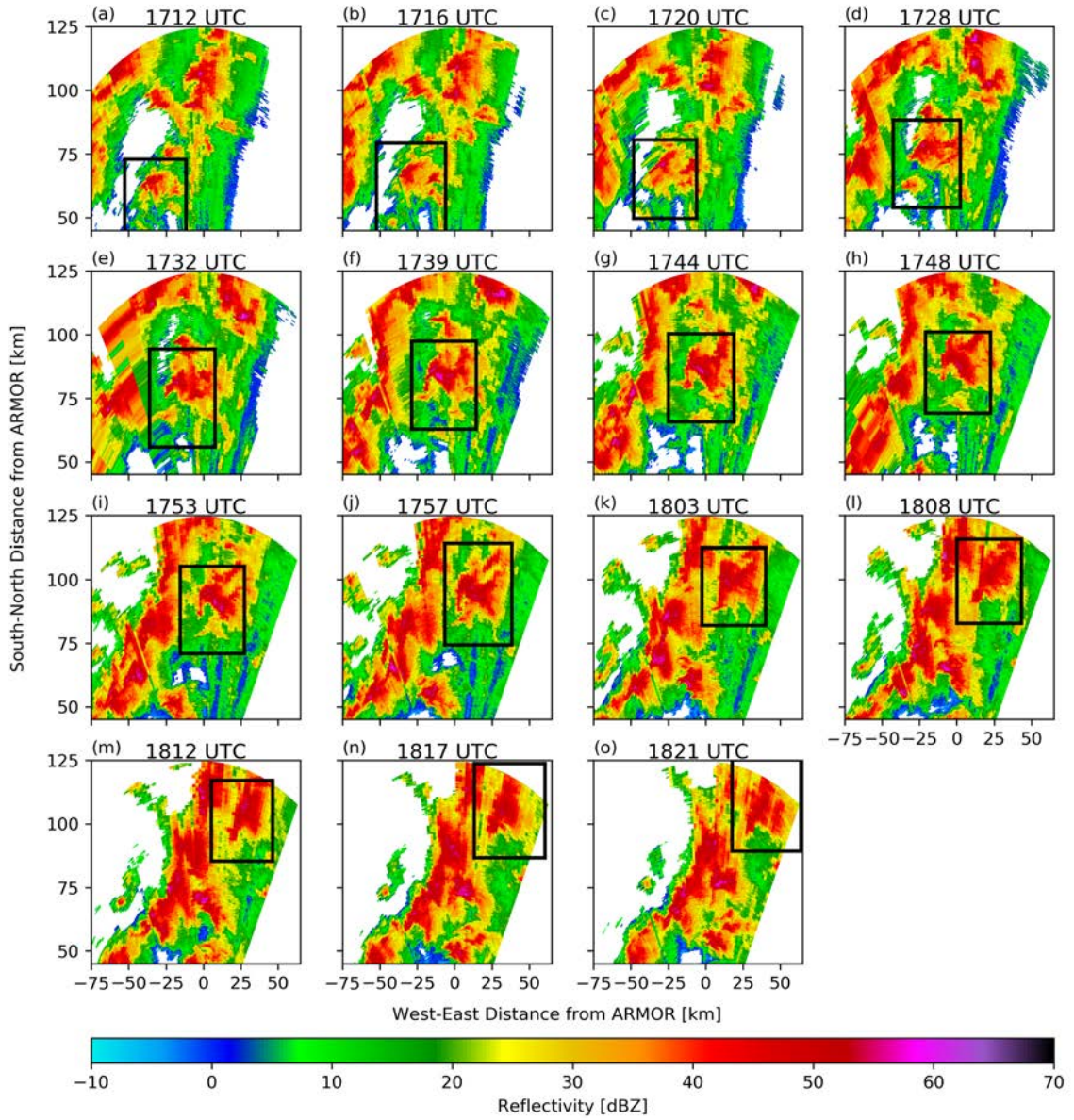


Figure B.5: As in Figure B.1 for the anomalous 10 April 2009 supercell.

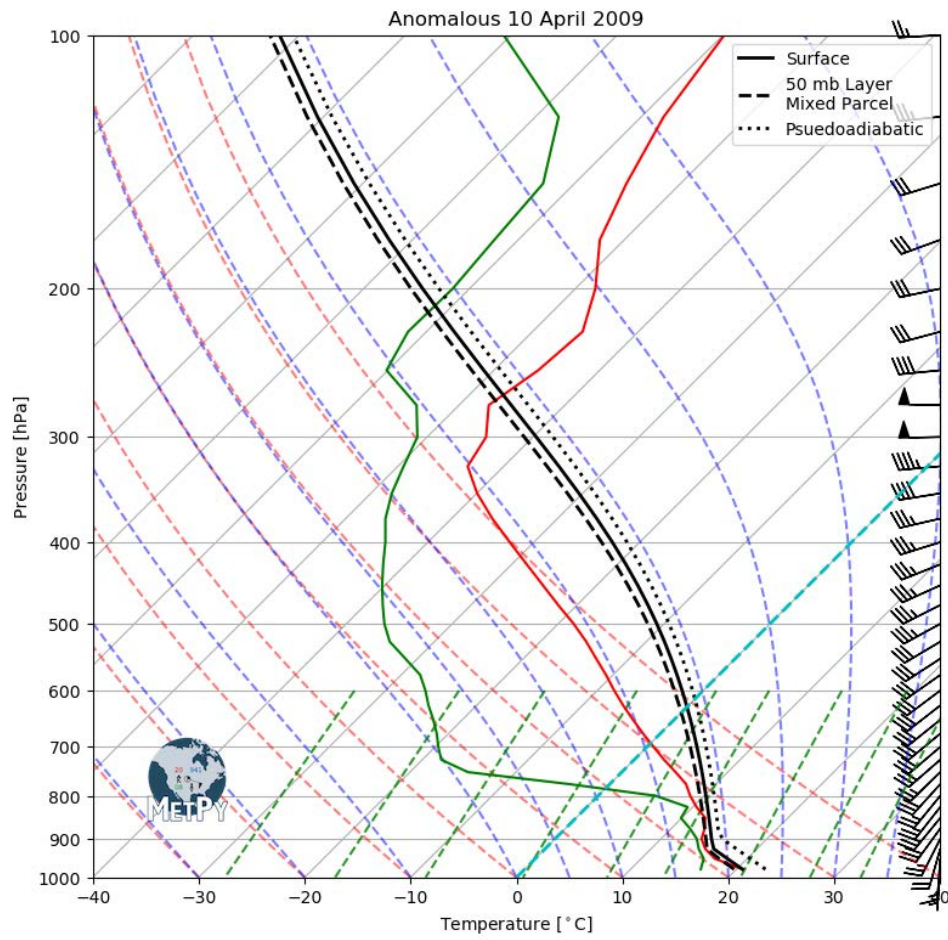


Figure B.6: As in Figure B.2 for the anomalous 10 April 2009 case.

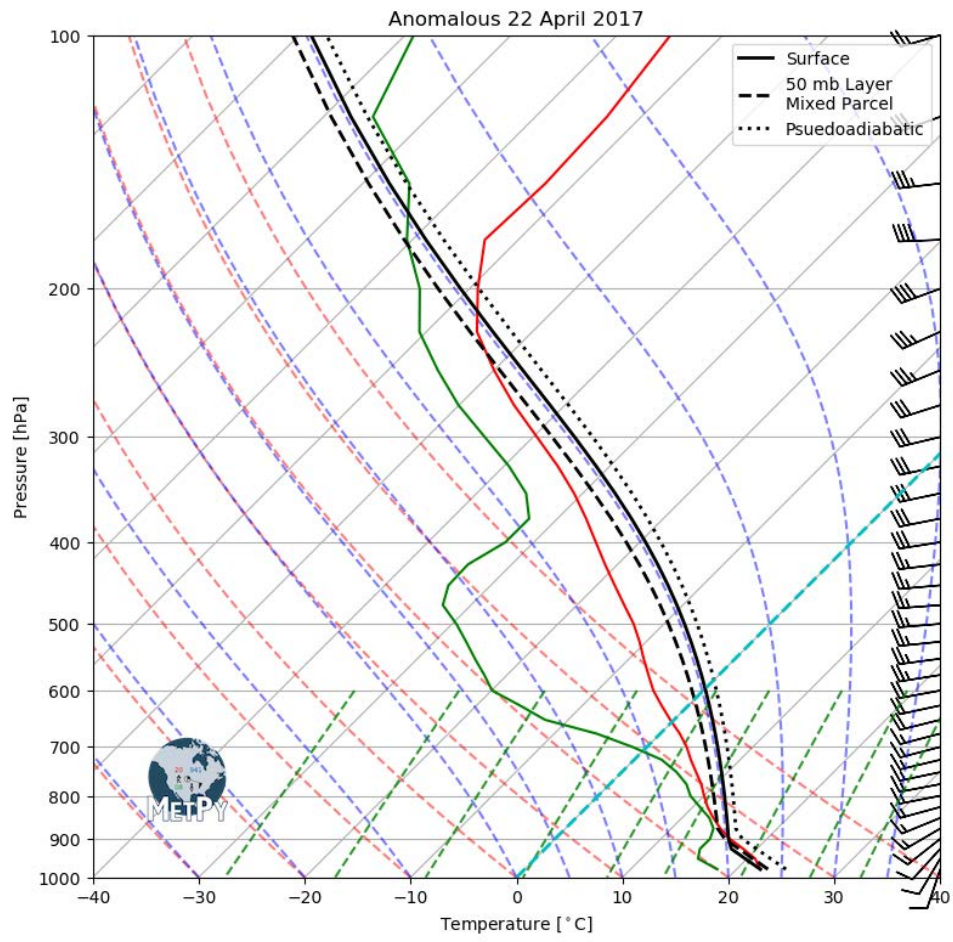


Figure B.7: As in Figure B.2 for the anomalous 22 April 2017 case.

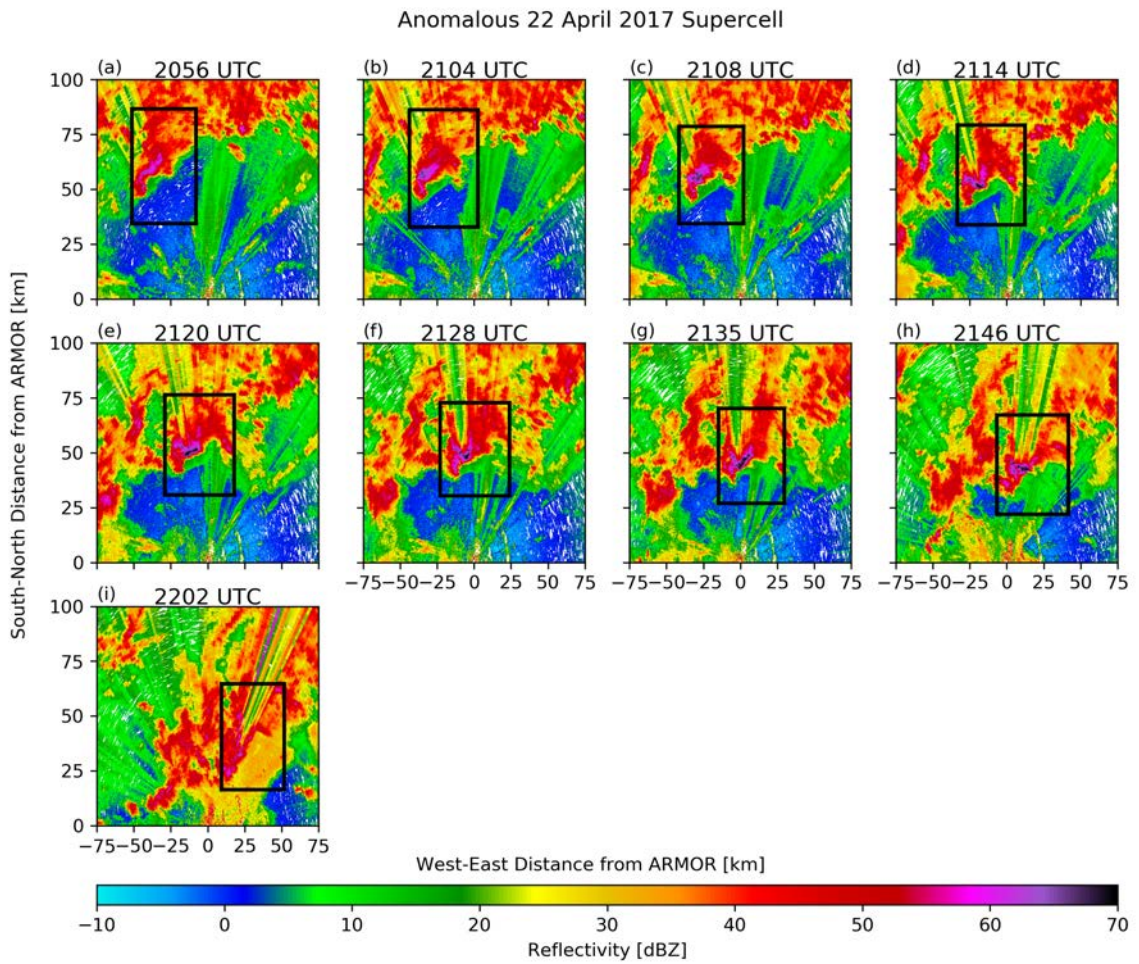


Figure B.8: As in Figure B.1 for the anomalous 22 April 2017 supercell.

REFERENCES

- Avila, E. E., and R. G. Pereyra, 2000: Charge transfer during crystal-graupel collisions for two different cloud droplet size distributions. *Geophysical Research Letters*, **27** (23), 3837–3840, doi: 10.1029/2000GL012302.
- Baker, B., M. B. Baker, E. R. Jayaratne, J. Latham, and C. P. R. Saunders, 1987: The influence of diffusional growth rates on the charge transfer accompanying rebounding collisions between ice crystals and soft hailstones. *Quarterly Journal of the Royal Meteorological Society*, **113** (478), 1193–1215.
- Baker, M. B., and J. G. Dash, 1989: Charge transfer in thunderstorms and the surface melting of ice. *Journal of Crystal Growth*, **97**, 770–776.
- Baker, M. B., and J. G. Dash, 1994: Mechanism of charge transfer between colliding ice particles in thunderstorms. *Journal of Geophysical Research*, **99**.
- Benjamin, S. G., and Coauthors, 2004: An hourly assimilation-forecast cycle: The RUC. *Monthly Weather Review*, **132** (2), 495–518, doi: 10.1175/1520-0493(2004)132<0495:AHACTR>2.0.CO;2.
- Benjamin, S. G., and Coauthors, 2006: From the 13-km RUC to the Rapid Refresh. *Paper presented at 12th Conference on Aviation, Range, and Aerospace Meteorology (ARAM)*, American Meteorological Society, Atlanta, Geor., 27 Jan. - 3 Feb.
- Berdeklis, P., and R. List, 2001: The ice crystal-graupel collision charging mechanism of thunderstorm electrification. *Journal of the Atmospheric Sciences*, **58** (18), 2751–2770, doi: 10.1175/1520-0469(2001)058<2751:TICGCC>2.0.CO;2.
- Biagi, C. J., K. L. Cummins, K. E. Kehoe, and E. P. Krider, 2007: National Lightning Detection Network (NLDN) performance in southern Arizona, Texas, and Oklahoma in 2003-2004. *Journal of Geophysical Research: Atmospheres*, **112** (5), 1–17, doi: 10.1029/2006JD007341.
- Blakeslee, R. J., 2019: GOES-R PLT North Alabama Lightning Mapping Array (LMA) [22 April 2017]. Dataset available online from the NASA Global Hydrology Resource Center DAAC, Huntsville, Alabama, Huntsville, Alabama, U.S.A., doi: <http://dx.doi.org/10.5067/GOESRPLT/LMA/DATA401>.
- Bluestein, H. B., and D. R. MacGorman, 1998: Evolution of cloud-to-ground lightning characteristics and storm structure in the Spearman, Texas, tornadic supercells of 31 May 1990. *Monthly Weather Review*, **126** (6), 1451–1467, doi: 10.1175/1520-0493(1998)126<1451:EOCTGL>2.0.CO;2.
- Boccippio, D. J., S. Heckman, and S. J. Goodman, 2001: A diagnostic analysis of the Kennedy Space Center LDAR Network, 1: Data characteristics. *Journal of Geophysical Research: Atmospheres*, **106**, 4769–4786, doi: 10.1029/2000JD900687.
- Branick, M. L., and C. A. Doswell III, 1992: An observation of the relationship between supercell structure and lightning ground-strike polarity. *Weather and Forecasting*, **7** (1), 143–149, doi: 10.1175/1520-0434(1992)007<0143:AOTRB>2.0.CO;2.

- Bringi, V. N., T. D. Keenan, and V. Chandrasekar, 2001: Correcting C-band radar reflectivity and differential reflectivity data for rain attenuation: A self-consistent method with constraints. *IEEE Transactions on Geoscience and Remote Sensing*, **39** (9), 1906–1915, doi: 10.1109/36.951081.
- Brothers, M. D., E. C. Bruning, and E. R. Mansell, 2018: Investigating the relative contributions of charge deposition and turbulence in organizing charge within a thunderstorm. *Journal of the Atmospheric Sciences*, **75** (9), 3265–3284, doi: 10.1175/JAS-D-18-0007.1.
- Bruning, E. C., and D. R. MacGorman, 2013: Theory and observations of controls on lightning flash size spectra. *Journal of the Atmospheric Sciences*, **70** (12), 4012–4029, doi: 10.1175/JAS-D-12-0289.1.
- Bruning, E. C., W. D. Rust, D. R. MacGorman, M. I. Biggerstaff, and T. J. Schuur, 2010: Formation of charge structures in a supercell. *Monthly Weather Review*, **138** (10), 3740–3761, doi: 10.1175/2010MWR3160.1.
- Bruning, E. C., W. D. Rust, T. J. Schuur, D. R. MacGorman, P. R. Krehbiel, and W. Rison, 2007: Electrical and polarimetric radar observations of a multicell storm in TELEX. *Monthly Weather Review*, **135** (7), 2525–2544, doi: 10.1175/MWR3421.1.
- Bruning, E. C., S. A. Weiss, and K. M. Calhoun, 2014: Continuous variability in thunderstorm primary electrification and an evaluation of inverted-polarity terminology. *Atmospheric Research*, **135–136**, 274–284, doi: 10.1016/j.atmosres.2012.10.009.
- Calhoun, K. M., D. R. MacGorman, C. L. Ziegler, and M. I. Biggerstaff, 2013: Evolution of lightning activity and storm charge relative to dual-Doppler analysis of a high-precipitation supercell storm. *Monthly Weather Review*, **141** (7), 2199–2223, doi: 10.1175/MWR-D-12-00258.1.
- Carey, L. D., and R. J. Blakeslee, 2020a: ARMOR and NALMA data corresponding to 10 April 2009 supercell documented in “Observations of anomalous charge structures in supercell thunderstorms in the southeastern United States”. Zenodo, doi: 10.5281/zenodo.3738553.
- Carey, L. D., and R. J. Blakeslee, 2020b: ARMOR and NALMA data corresponding to 2008 storms analyzed in “Examining conditions supporting the development of anomalous charge structures in supercells in the Southeastern United States”. Zenodo, doi: 10.5281/zenodo.3783694.
- Carey, L. D., and K. M. Buffalo, 2007: Environmental control of cloud-to-ground lightning polarity in severe storms. *Monthly Weather Review*, **135**, 1327–1353, doi: 10.1175/MWR3361.1.
- Carey, L. D., and K. R. Knupp, 2017: UAH ARMOR C-band radar data. UCAR/NCAR - Earth Observing Laboratory, Boulder, Colorado, U.S.A., doi: <https://doi.org/10.5065/D6BG2MQG>.
- Carey, L. D., M. J. Murphy, T. L. McCormick, and N. W. S. Demetriades, 2005: Lightning location relative to storm structure in a leading-line, trailing-stratiform mesoscale convective system. *Journal of Geophysical Research: Atmospheres*, **110** (3), 1–23, doi: 10.1029/2003JD004371.

- Carey, L. D., W. A. Petersen, and S. A. Rutledge, 2003a: Evolution of cloud-to-ground lightning and storm structure in the Spencer, South Dakota, tornadic supercell of 30 May 1998. *Monthly Weather Review*, **131** (8), 1811–1831, doi: 10.1175//2566.1.
- Carey, L. D., and S. A. Rutledge, 1998: Electrical and multiparameter radar observations of a severe hailstorm. *Journal of Geophysical Research*, **103** (D12), 13 979–14 000.
- Carey, L. D., S. A. Rutledge, and W. A. Petersen, 2003b: The relationship between severe storm reports and cloud-to-ground lightning polarity in the contiguous United States from 1989 to 1998. *Monthly Weather Review*, **131** (7), 1211–1228, doi: 10.1175/1520-0493(2003)131(1211:TRBSSR)2.0.CO;2.
- Carey, L. D., E. V. Schultz, C. J. Schultz, W. Deierling, W. A. Petersen, A. L. Bain, and K. E. Pickering, 2019: An evaluation of relationships between radar-inferred kinematic and microphysical parameters and lightning flash rates in Alabama storms. *Atmosphere*, **10** (12), 1–36, doi: 10.3390/ATMOS10120796.
- Centers for Disease Control and Prevention, 2019: National Environmental Public Health Tracking Network. URL www.cdc.gov/ephtracking.
- Chmielewski, V. C., and E. C. Bruning, 2016: Lightning Mapping Array flash detection performance with variable receiver thresholds. *Journal of Geophysical Research: Atmospheres*, **121** (14), 8600–8614, doi: 10.1002/2016JD025159.
- Chmielewski, V. C., E. C. Bruning, and B. C. Ancell, 2018: Variations of thunderstorm charge structures in West Texas on 4 June 2012. *Journal of Geophysical Research: Atmospheres*, **123** (17), 9502–9523, doi: 10.1029/2018JD029006.
- Chmielewski, V. C., D. R. Macgorman, C. L. Ziegler, E. Digangi, D. Betten, and M. Biggerstaff, 2020: Microphysical and transportive contributions to normal and anomalous polarity subregions in the 29–30 May 2012 Kingfisher storm. *Journal of Geophysical Research: Atmospheres*, **126** (16), e2020JD032 384, doi: 10.1029/2020JD032384.
- Coleman, L. M., T. C. Marshall, M. Stolzenburg, T. Hamlin, P. R. Krehbiel, W. Rison, and R. J. Thomas, 2003: Effects of charge and electrostatic potential on lightning propagation. *Journal of Geophysical Research: Atmospheres*, **108** (D9), 12–1 — 12–27, doi: 10.1029/2002JD002718.
- Collis, S., A. Protat, and K.-S. Chung, 2010: The effect of radial velocity gridding artifacts on variationally retrieved vertical velocities. *Journal of Atmospheric and Oceanic Technology*, **27**, 1239–1246, doi: 10.1175/2010JTECHA1402.1.
- Crum, T. D., and R. L. Alberty, 1993: The WSR-88D and the WSR-88D Operational Support Facility. *Bulletin of the American Meteorological Society*, **74** (9), 1669–1687.
- Cummins, K. L., and M. J. Murphy, 2009: An overview of lightning locating systems: History, techniques, and data uses, with an in-depth look at the U.S. NLDN. *IEEE Transactions on Electromagnetic Compatibility*, **51**, 499–518, doi: 10.1109/TEM.2009.2023450.
- Curran, E. B., and W. D. Rust, 1992: Positive ground flashes produced by low-precipitation thunderstorms in Oklahoma on 26 April 1984. *Monthly Weather Review*, **120**, 544–553, doi: 10.1175/1520-0493(1992)120(0544:PGFPBL)2.0.CO;2.

- Davis, T. C., S. A. Rutledge, and B. R. Fuchs, 2019: Lightning location, NO_x production, and transport by anomalous and normal polarity thunderstorms. *Journal of Geophysical Research: Atmospheres*, **124** (15), 8722–8742, doi: 10.1029/2018JD029979.
- Deierling, W., and W. A. Petersen, 2008: Total lightning activity as an indicator of updraft characteristics. *Journal of Geophysical Research: Atmospheres*, **113**, D16 210, doi: 10.1029/2007JD009598.
- Deierling, W., W. A. Petersen, J. Latham, S. Ellis, and H. J. Christian, 2008: The relationship between lightning activity and ice fluxes in thunderstorms. *Journal of Geophysical Research: Atmospheres*, **113**, D15 210, doi: 10.1029/2007JD009700.
- DiGangi, E. A., D. R. MacGorman, C. L. Ziegler, D. Betten, M. Biggerstaff, M. Bowlan, and C. K. Potvin, 2016: An overview of the 29 May 2012 Kingfisher supercell during DC3. *Journal of Geophysical Research*, **121** (24), 14 316–14 343, doi: 10.1002/2016JD025690.
- Dolan, B., and S. A. Rutledge, 2009: A theory-based hydrometeor identification algorithm for X-band polarimetric radars. *Journal of Atmospheric and Oceanic Technology*, **26** (10), 2071–2088, doi: 10.1175/2009JTECHA1208.1.
- Dolan, B., S. A. Rutledge, S. Lim, V. Chandrasekar, and M. Thurai, 2013: A robust C-band hydrometeor identification algorithm and application to a long-term polarimetric radar dataset. *Journal of Applied Meteorology and Climatology*, **52** (9), 2162–2186, doi: 10.1175/JAMC-D-12-0275.1.
- Doviak, R. J., V. Bringi, A. Ryzhkov, A. Zahrai, and D. Zrnić, 2000: Considerations for polarimetric upgrades to operational WSR-88D radars. *Journal of Atmospheric and Oceanic Technology*, **17** (3), 257–278.
- Dye, J. E., and A. Bansemer, 2019: Electrification in mesoscale updrafts of deep stratiform and anvil clouds in Florida. *Journal of Geophysical Research: Atmospheres*, **124** (2), 1021–1049, doi: 10.1029/2018JD029130.
- Dye, J. E., C. A. Knight, V. Tautenhoofd, and T. W. Cannon, 1974: The mechanism of precipitation formation in Northeastern Colorado cumulus III: Coordinated microphysical and radar observations and summary. *Journal of the Atmospheric Sciences*, **31** (8), 2152–2159.
- Dye, J. E., and Coauthors, 1986: Early electrification and precipitation development in a small, isolated Montana cumulonimbus. *Journal of Geophysical Research*, **91** (D1), 1231–1247, doi: 10.1029/JD091iD01p01231.
- Emersic, C., P. L. Heinselman, D. R. MacGorman, and E. C. Bruning, 2011: Lightning activity in a hail-producing storm observed with phased-array radar. *Monthly Weather Review*, **139** (6), 1809–1825, doi: 10.1175/2010MWR3574.1.
- Emersic, C., and C. P. Saunders, 2020: The influence of supersaturation at low rime accretion rates on thunderstorm electrification from field-independent graupel-ice crystal collisions. *Atmospheric Research*, **242**, doi: 10.1016/j.atmosres.2020.104962.
- Emersic, C., and C. P. R. Saunders, 2010: Further laboratory investigations into the Relative Diffusional Growth Rate theory of thunderstorm electrification. *Atmospheric Research*, **98**, 327–340, doi: 10.1016/j.atmosres.2010.07.011.

- Ester, M., H. P. Kriegel, J. Sander, and X. Xu, 1996: A density-based algorithm for discovering clusters in large spatial databases with noise. *KDD*, **96 (34)**, 226–231.
- Fierro, A. O., M. S. Gilmore, E. R. Mansell, L. J. Wicker, and J. M. Straka, 2006: Electrification and lightning in an idealized boundary-crossing supercell simulation of 2 June 1995. *Monthly Weather Review*, **134 (11)**, 3149–3172, doi: 10.1175/MWR3231.1.
- Fleenor, S. A., C. J. Biagi, K. L. Cummins, E. P. Krider, and X. M. Shao, 2009: Characteristics of cloud-to-ground lightning in warm-season thunderstorms in the Central Great Plains. *Atmospheric Research*, **91 (2-4)**, 333–352, doi: 10.1016/j.atmosres.2008.08.011, URL <http://dx.doi.org/10.1016/j.atmosres.2008.08.011>.
- Fuchs, B. R., E. C. Bruning, S. A. Rutledge, L. D. Carey, P. R. Krehbiel, and W. Rison, 2016: Climatological analyses of LMA data with an open-source lightning flash-clustering algorithm. *Journal of Geophysical Research: Atmospheres*, **121**, 8625–8648, doi: 10.1002/2015JD024663. Received.
- Fuchs, B. R., and S. A. Rutledge, 2018: Investigation of lightning flash locations in isolated convection using LMA observations. *Journal of Geophysical Research: Atmospheres*, 1–17, doi: 10.1002/2017JD027569.
- Fuchs, B. R., S. A. Rutledge, B. Dolan, L. D. Carey, and C. Schultz, 2018: Microphysical and kinematic processes associated with anomalous charge structures in isolated convection. *Journal of Geophysical Research: Atmospheres*, **123 (12)**, 6505–6528, doi: 10.1029/2017JD027540.
- Fuchs, B. R., and Coauthors, 2015: Environmental controls on storm intensity and charge structure in multiple regions of the continental United States. *Journal of Geophysical Research: Atmospheres*, **120 (13)**, 6575–6596, doi: 10.1002/2015JD023271.
- Gelaro, R., and Coauthors, 2017: The Modern-Era Retrospective analysis for Research and Applications, version 2 (MERRA-2). *Journal of Climate*, **30 (14)**, 5419–5454, doi: 10.1175/JCLI-D-16-0758.1.
- Gilmore, M. S., and L. J. Wicker, 2002: Influences of the local environment on supercell cloud-to-ground lightning, radar characteristics, and severe weather on 2 June 1995. *Monthly Weather Review*, **130 (10)**, 2349–2372, doi: 10.1175/1520-0493(2002)130<2349:IOTLEO>2.0.CO;2.
- Grant, L. D., and S. C. van den Heever, 2014: Microphysical and dynamical characteristics of low-precipitation and classic supercells. *Journal of the Atmospheric Sciences*, **71**, 2604–2624, doi: 10.1175/JAS-D-13-0261.1.
- Helmus, J. J., and S. M. Collis, 2016: The Python ARM Radar Toolkit (Py-ART), a library for working with weather radar data in the Python programming language. *Journal of Open Research Software*, **4**, 1–6, doi: <http://dx.doi.org/10.5334/jors.119>.
- Helsdon, J. H., S. Gattaleeradapan, R. D. Farley, and C. Christopher Waits, 2002: An examination of the convective charging hypothesis: Charge structure, electric fields, and Maxwell currents. *Journal of Geophysical Research Atmospheres*, **107 (22)**, 9.1 – 9.26, doi: 10.1029/2001JD001495.

- Heymsfield, A. J., and K. M. Miller, 1988: Water vapor and ice mass transported into the anvils of CCOPE thunderstorms: Comparison with storm influx and rainout. *Journal of the Atmospheric Sciences*, **45** (22), 3501–3514, doi: 10.1175/1520-0469(1988)045<3501:WVAIMT>2.0.CO;2.
- Hoffmann, F., 2020: Effects of entrainment and mixing on the Wegener-Bergeron-Findeisen process. *Journal of the Atmospheric Sciences*, **77** (6), 2279–2296, doi: 10.1175/jas-d-19-0289.1.
- Jackson, R., S. Collis, T. Lang, C. Potvin, and T. Munson, 2019: PyDDA: A new Pythonic wind retrieval package. *Paper presented at the 18th Python in Science Conference*, Austin, Texas, 9-15 Jul., Scipy, 111–117, doi: 10.25080/majora-7ddc1dd1-010, [Available online at <https://ntrs.nasa.gov/archive/nasa/casi.ntrs.nasa.gov/20190027316.pdf>].
- James, C. N., and J. Houze, 2001: A real-time four-dimensional Doppler dealiasing scheme. *Journal of Atmospheric and Oceanic Technology*, **18** (10), 1674–1683, doi: 10.1175/1520-0426(2001)018<1674:ARTFDD>2.0.CO;2.
- Jayarathne, E. R., C. P. R. Saunders, and J. Hallett, 1983: Laboratory studies of the charging of soft-hail during ice crystal interactions. *Quarterly Journal of the Royal Meteorological Society*, **109**, 609–630.
- Knapp, M. D. I., 1994: Using cloud-to-ground lightning data to identify tornadic thunderstorm signatures and nowcast severe weather. *National Weather Digest*, **19** (2), 35–42.
- Koshak, W. J., and Coauthors, 2004: North Alabama Lightning Mapping Array (LMA): VHF source retrieval algorithm and error analyses. *Journal of Atmospheric and Oceanic Technology*, **21** (4), 543–558, doi: 10.1175/1520-0426(2004)021<0543:NALMAL>2.0.CO;2.
- Krehbiel, P. R., M. Brook, and R. A. McCrory, 1979: Analysis of the charge structure of lightning discharges to ground. *Journal of Geophysical Research*, **84** (C5), 2432–2456, doi: 10.1029/JC084iC05p02432.
- Krehbiel, P. R., R. J. Thomas, W. Rison, T. Hamlin, J. Harlin, and M. Davis, 2000: GPS-based mapping system reveals lightning inside storms. *Eos, Transactions American Geophysical Union*, **81** (3), 21, doi: 10.1029/00EO00014.
- Kuhlman, K. M., C. L. Ziegler, E. R. Mansell, D. R. MacGorman, and J. M. Straka, 2006: Numerically simulated electrification and lightning of the 29 June 2000 STEPS supercell storm. *Monthly Weather Review*, **134**, 2734–2757, doi: 10.1175/MWR3217.1.
- Lakshmanan, V., T. Smith, G. Stumpf, and K. Hondl, 2007: The Warning Decision Support System-Integrated Information. *Weather and Forecasting*, **22** (3), 596–612, doi: 10.1175/WAF1009.1.
- Lang, T. J., and S. A. Rutledge, 2002: Relationships between convective storm kinematics, precipitation, and lightning. *Monthly Weather Review*, **130** (10), 2492–2506, doi: 10.1175/1520-0493(2002)130<2492:RBCSKP>2.0.CO;2.
- Lang, T. J., and S. A. Rutledge, 2006: Cloud-to-ground lightning downwind of the 2002 Hayman forest fire in Colorado. *Geophysical Research Letters*, **33** (3), 2–5, doi: 10.1029/2005GL024608.

- Lang, T. J., and S. A. Rutledge, 2011: A framework for the statistical analysis of large radar and lightning datasets: Results from STEPS 2000. *Monthly Weather Review*, **139** (8), 2536–2551, doi: 10.1175/MWR-D-10-05000.1.
- Lang, T. J., and Coauthors, 2004: The severe thunderstorm electrification and precipitation study. *Bulletin of the American Meteorological Society*, **85** (8), 1107–1125, doi: 10.1175/BAMS-85-8-1107.
- Lang, T. J., and Coauthors, 2016: Observations of two sprite-producing storms in Colorado. *Journal of Geophysical Research: Atmospheres*, **121**, 9675–9695, doi: 10.1002/2016JD025299.
- Lhermitte, R., and E. Williams, 1985: Thunderstorm electrification: A case study. *Journal of Geophysical Research*, **90** (D4), 6071–6078.
- Logan, T., 2018: Anomalous lightning behavior during the 26-27 August 2007 northern Great Plains severe weather event. *Journal of Geophysical Research: Atmospheres*, **123** (3), 1771–1784, doi: 10.1002/2017JD027750.
- Lyons, W. A., T. E. Nelson, E. R. Williams, J. A. Cramer, and T. R. Turner, 1998: Enhanced positive cloud-to-ground lightning in thunderstorms ingesting smoke from fires. *Science*, **282** (5386), 77–80, doi: 10.1126/science.282.5386.77.
- MacGorman, D. R., I. R. Apostolakopoulos, N. R. Lund, N. W. S. Demetriades, M. J. Murphy, and P. R. Krehbiel, 2011: The timing of cloud-to-ground lightning relative to total lightning activity. *Monthly Weather Review*, **139** (12), 3871–3886, doi: 10.1175/MWR-D-11-00047.1.
- MacGorman, D. R., and D. W. Burgess, 1994: Positive cloud-to-ground lightning in tornadic storms and hailstorms. *Monthly Weather Review*, **122** (8), 1671–1697, doi: 10.1175/1520-0493(1994)122<1671:PCTGLI>2.0.CO;2.
- MacGorman, D. R., D. W. Burgess, V. Mazur, W. D. Rust, W. L. Taylor, and B. C. Johnson, 1989: Lightning rates relative to tornadic storm evolution on 22 May 1981. *Journal of the Atmospheric Sciences*, **46** (2), 221–250, doi: 10.1175/1520-0469(1989)046<0221:LRRTTS>2.0.CO;2.
- MacGorman, D. R., A. A. Few, and T. L. Teer, 1981: Layered lightning activity. *Journal of Geophysical Research*, **86** (C10), 9900–9910, doi: 10.1029/JC086iC10p09900.
- MacGorman, D. R., and K. E. Nielsen, 1991: Cloud-to-ground lightning in a tornadic storm on 8 May 1986. *Monthly Weather Review*, **119**, 1557–1574, doi: 10.1175/1520-0493(1991)119<1557:CTGLIA>2.0.CO;2.
- MacGorman, D. R., W. D. Rust, P. Krehbiel, W. Rison, E. Bruning, and K. Wiens, 2005: The electrical structure of two supercell storms during STEPS. *Monthly Weather Review*, **133**, 2583–2607, doi: 10.1175/MWR2994.1.
- MacGorman, D. R., and Coauthors, 2008: TELEX The Thunderstorm Electrification and Lightning Experiment. *Bulletin of the American Meteorological Society*, **89** (7), 997–1013, doi: 10.1175/2007BAMS2352.1.

- Maggio, C., and Coauthors, 2005: Lightning-initiation locations as a remote sensing tool of large thunderstorm electric field vectors. *Journal of Atmospheric and Oceanic Technology*, **22** (7), 1059–1068, doi: 10.1175/JTECH1750.1.
- Mansell, E. R., D. R. MacGorman, C. L. Ziegler, and J. M. Straka, 2002: Simulated three-dimensional branched lightning in a numerical thunderstorm model. *Journal of Geophysical Research: Atmospheres*, **107** (D9), doi: 10.1029/2000JD000244.
- Mansell, E. R., D. R. MacGorman, C. L. Ziegler, and J. M. Straka, 2005: Charge structure and lightning sensitivity in a simulated multicell thunderstorm. *Journal of Geophysical Research: Atmospheres*, **110** (12), 1–24, doi: 10.1029/2004JD005287.
- Mansell, E. R., and C. L. Ziegler, 2013: Aerosol effects on simulated storm electrification and precipitation in a two-moment bulk microphysics model. *Journal of the Atmospheric Sciences*, **70** (7), 2032–2050, doi: 10.1175/JAS-D-12-0264.1.
- May, R. M., S. C. Arms, P. Marsh, E. Bruning, J. R. Leeman, K. Goebbert, J. E. Thielen, and Z. S. Bruick, 2008 - 2020: MetPy: A Python Package for Meteorological Data. Boulder, Colorado, URL <https://github.com/Unidata/MetPy>, doi: 10.5065/D6WW7G29.
- Mazur, V., and L. H. Ruhnke, 1993: Common physical processes in natural and artificially triggered lightning. *Journal of Geophysical Research*, **98** (No. D7), 12 913–12 930, doi: 10.1111/j.1555-2934.2009.01042.x.
- Mazur, V., L. H. Ruhnke, T. A. Warner, and R. E. Orville, 2013: Recoil leader formation and development. *Journal of Electrostatics*, **71** (4), 763–768, doi: 10.1016/j.elstat.2013.05.001.
- Mecikalski, R. M., A. L. Bain, and L. D. Carey, 2015: Radar and lightning observations of deep moist convection across northern Alabama during DC3: 21 May 2012. *Monthly Weather Review*, **143** (7), 2774–2794, doi: 10.1175/MWR-D-14-00250.1.
- Medici, G., K. L. Cummins, D. J. Cecil, W. J. Koshak, and S. D. Rudlosky, 2017: The intracloud lightning fraction in the contiguous United States. *Monthly Weather Review*, **145** (11), 4481–4499, doi: 10.1175/MWR-D-16-0426.1.
- Mitzeva, R. P., C. Saunders, and B. Tsenova, 2006: Parameterisation of non-inductive charging in thunderstorm regions free of cloud droplets. *Atmospheric Research*, **82**, 102–111, doi: 10.1016/j.atmosres.2005.12.006.
- Mitzeva, R. P., C. P. Saunders, and B. Tsenova, 2005: A modelling study of the effect of cloud saturation and particle growth rates on charge transfer in thunderstorm electrification. *Atmospheric Research*, **76** (1-4), 206–221, doi: 10.1016/j.atmosres.2004.11.019.
- Mroz, K., A. Battaglia, T. J. Lang, D. J. Cecil, S. Tanelli, and F. Tridon, 2017: Hail-detection algorithm for the GPM Core Observatory satellite sensors. *Journal of Applied Meteorology and Climatology*, **56** (7), 1939–1957, doi: 10.1175/JAMC-D-16-0368.1.
- Murphy, M. J., and R. K. Said, 2020: Comparisons of lightning rates and properties from the U.S. National Lightning Detection Network (NLDN) and GLD360 with GOES-16 Geostationary Lightning Mapper and Advanced Baseline Imager data. *Journal of Geophysical Research: Atmospheres*, **125** (5), e2019JD031 172, doi: 10.1029/2019JD031172.

- NOAA National Weather Service (NWS) Radar Operations Center, 1991: NOAA Next Generation Radar (NEXRAD) Level 2 Base Data [KHTX site; 17-19 UTC on 10 April 2009 and 20-23 UTC on 22 April 2017]. NOAA National Centers for Environmental Information [Accessed August 2017], doi: doi:10.7289/V5W9574V.
- North, K. W., M. Oue, P. Kollias, S. E. Giangrande, S. M. Collis, and C. K. Potvin, 2017: Vertical air motion retrievals in deep convective clouds using the ARM scanning radar network in Oklahoma during MC3E. *Atmospheric Measurement Techniques*, **10** (8), 2785–2806, doi: 10.5194/amt-10-2785-2017.
- Nowotarski, C. J., J. M. Peters, and J. P. Mulholland, 2020: Evaluating the effective inflow layer of simulated supercell updrafts. *Monthly Weather Review*, **148** (8), 3507–3532, doi: 10.1175/mwr-d-20-0013.1.
- Oye, R., C. K. Mueller, and S. Smith, 1995: Software for radar translation, visualization, editing, and interpolation. *Paper presented at 27th Conference on Radar Meteorology*, American Meteorological Society, Vail, Col., 9-13 Oct., 359–361.
- Padula, F., S. J. Goodman, A. Pearlman, and C. Cao, 2017: GOES-R Advanced Baseline Imager (ABI) and Geostationary Lightning Mapper (GLM) calibration/validation from a field campaign perspective. *Paper presented at International Geoscience and Remote Sensing Symposium (IGARSS)*, Fort Worth, Tex., 23-28 Jul., 301–304, doi: 10.1109/IGARSS.2017.8126955.
- Pedregosa, F., and Coauthors, 2011: Scikit-learn: Machine learning in Python. *Journal of Machine Learning Research*, **12**, 2825–2830.
- Potvin, C. K., D. Betten, L. J. Wicker, K. L. Elmore, and M. I. Biggerstaff, 2012a: 3DVAR versus traditional dual-Doppler wind retrievals of a simulated supercell thunderstorm. *Mon. Wea. Rev.*, **140** (11), 3487–3494, doi: 10.1175/MWR-D-12-00063.1.
- Potvin, C. K., A. Shapiro, and M. Xue, 2012b: Impact of a vertical vorticity constraint in variational dual-Doppler wind analysis: Tests with real and simulated supercell data. *Journal of Atmospheric and Oceanic Technology*, **29** (1), 32–49, doi: 10.1175/JTECH-D-11-00019.1.
- Potvin, C. K., L. J. Wicker, and A. Shapiro, 2012c: Assessing errors in variational Dual-Doppler wind syntheses of supercell thunderstorms observed by storm-scale mobile radars. *Journal of Atmospheric and Oceanic Technology*, **29** (8), 1009–1025, doi: 10.11075/JTECH-D-11-00177.1.
- Proctor, D. E., 1983: Lightning and precipitation in a small multicellular thunderstorm. *Journal of Geophysical Research*, **88** (C9), 5421–5440.
- Qie, X., T. Zhang, C. Chen, G. Zhang, T. Zhang, and W. Wei, 2005: The lower positive charge center and its effect on lightning discharges on the Tibetan Plateau. *Geophysical Research Letters*, **32** (5), 1–4, doi: 10.1029/2004GL022162.
- Rasmussen, E., 2015: VORTEX-Southeast Program Overview. Tech. rep., National Severe Storms Laboratory Tech. Report, Norman, Oklahoma, 36 pp. URL <ftp://ftp.atdd.noaa.gov/pub/vortexse/ProjectOverview.pdf>.

- Rauber, R. M., and S. W. Nesbitt, 2018: *Radar Meteorology: A First Course*. 1st ed., John Wiley & Sons, Hoboken, New Jersey, 461 pp.
- Reap, R. M., and D. R. MacGorman, 1989: Cloud-to-ground lightning: Climatological characteristics and relationships to model fields, radar observations, and severe local storms. *Monthly Weather Review*, **117** (3), 518–535, doi: 10.1175/1520-0493(1989)117<0518:CTGLCC>2.0.CO;2.
- Reynolds, S. E., M. Brook, and M. F. Gourley, 1957: Thunderstorm charge separation. *Journal of Meteorology*, **14** (5), 426–436, doi: 10.1175/1520-0469(1957)014<0426:TCS>2.0.CO;2.
- Rison, W., R. J. Thomas, P. R. Krehbiel, T. Hamlin, and J. Harlin, 1999: A GPS-based three-dimensional lightning mapping system: Initial observations in Central New Mexico. *Geophysical Research Letters*, **26** (23), 3573–3576.
- Rogers, R. R., and M. K. I. Yau, 1989: *A Short Course in Cloud Physics*. 3rd ed., Butterworth-Heinemann, Burlington, MA, 290 pp.
- Rosenfeld, D., B. Fischman, Y. Zheng, T. Goren, and D. Giguzin, 2014: Combined satellite and radar retrievals of drop concentration and CCN at convective cloud base. *Geophysical Research Letters*, **41**, 3259–3265, doi: 10.1002/2014GL059453.
- Rudlosky, S. D., and H. E. Fuelberg, 2010: Pre- and postupgrade distributions of NLDN reported cloud-to-ground lightning characteristics in the contiguous United States. *Monthly Weather Review*, **138** (9), 3623–3633, doi: 10.1175/2010MWR3283.1.
- Rust, W. D., and D. R. MacGorman, 2002: Possibly inverted-polarity electrical structures in thunderstorms during STEPS. *Geophysical Research Letters*, **29** (12), 10–13, doi: 10.1029/2001GL014303.
- Rust, W. D., and Coauthors, 2005: Inverted-polarity electrical structures in thunderstorms in the Severe Thunderstorm Electrification and Precipitation Study (STEPS). *Atmospheric Research*, **76**, 247–271, doi: 10.1016/j.atmosres.2004.11.029.
- Saunders, C. P. R., H. Bax-norman, C. Emersic, E. E. Avila, and N. E. Castellano, 2006: Laboratory studies of the effect of cloud conditions on graupel/crystal charge transfer in thunderstorm electrification. *Quarterly Journal of the Royal Meteorological Society*, **132** (621), 2653–2673, doi: 10.1256/qj.05.218.
- Saunders, C. P. R., and S. L. Peck, 1998: Laboratory studies of the influence of the rime accretion rate on charge transfer during crystal/graupel collisions. *Journal of Geophysical Research*, **103** (12), 13 949–13 956.
- Saunders, C. P. R., S. L. Peck, G. G. Aguirre Varela, E. E. Avila, and N. E. Castellano, 2001: A laboratory study of the influence of water vapour and mixing on the charge transfer process during collisions between ice crystals and graupel. *Atmospheric Research*, **58**, 187–203.
- Schultz, C. J., L. Carey, E. Schultz, and R. Blakeslee, 2017: Kinematic and microphysical significance of lightning jumps versus non-jump increases in total flash rate. *Weather and Forecasting*, 275–288, doi: 10.1175/WAF-D-15-0175.1.

- Schultz, C. J., L. D. Carey, E. V. Schultz, and R. J. Blakeslee, 2015: Insight into the kinematic and microphysical processes that control lightning jumps. *Weather and Forecasting*, **30**, 1591–1621, doi: 10.1175/WAF-D-14-00147.1.
- Schultz, C. J., W. A. Petersen, and L. D. Carey, 2009: Preliminary development and evaluation of lightning jump algorithms for the real-time detection of severe weather. *Journal of Applied Meteorology and Climatology*, **48** (12), 2543–2563, doi: 10.1175/2009JAMC2237.1.
- Schultz, C. J., W. A. Petersen, and L. D. Carey, 2011: Lightning and severe weather: A comparison between total and cloud-to-ground lightning trends. *Weather and Forecasting*, **26** (5), 744–755, doi: 10.1175/WAF-D-10-05026.1.
- Seimon, A., 1993: Anomalous cloud-to-ground lightning in an F5-tornado-producing supercell thunderstorm on 28 August 1990. *Bulletin of the American Meteorological Society*, **74** (2), 189–203, doi: 10.1175/1520-0477(1993)074<0189:ACTGLI>2.0.CO;2.
- Shao, X. M., and P. R. Krehbiel, 1996: The spatial and temporal development of intracloud lightning. *Journal of Geophysical Research: Atmospheres*, **101** (D21), 26 641–26 668, doi: 10.1029/96JD01803.
- Shapiro, A., C. K. Potvin, and J. Gao, 2009: Use of a vertical vorticity equation in variational dual-doppler wind analysis. *Journal of Atmospheric and Oceanic Technology*, **26** (10), 2089–2106, doi: 10.1175/2009JTECHA1256.1.
- Smith, S. B., J. G. LaDue, and D. R. MacGorman, 2000: The relationship between cloud-to-ground lightning polarity and surface equivalent potential temperature during three tornadic outbreaks. *Monthly Weather Review*, **128** (9), 3320–3328, doi: 10.1175/1520-0493(2000)128<3320:TRBCTG>2.0.CO;2.
- Steiger, S. M., R. E. Orville, and L. D. Carey, 2007: Total lightning signatures of thunderstorm intensity over north Texas. Part I: Supercells. *Monthly Weather Review*, **135** (10), 3281–3302, doi: 10.1175/MWR3483.1.
- Stolzenburg, M., 1994: Observations of high ground flash densities of positive lightning in summertime thunderstorms. *Monthly Weather Review*, **122** (8), 1740–1750, doi: 10.1175/1520-0493(1994)122<1740:OOHGFD>2.0.CO;2.
- Stolzenburg, M., D. W. Rust, and T. C. Marshall, 1998: Electrical structure in thunderstorm convective regions. 3. Synthesis. *Journal of Geophysical Research*, **103** (D12), 14 097–14 108.
- Stough, S. M., L. D. Carey, C. J. Schultz, and P. M. Bitzer, 2017: Investigating the relationship between lightning and mesocyclonic rotation in supercell thunderstorms. *Weather and Forecasting*, **32** (6), 2237–2259, doi: 10.1175/WAF-D-17-0025.1.
- Takahashi, T., 1978: Riming electrification as a charge generation mechanism in thunderstorms. *Journal of the Atmospheric Sciences*, **35** (8), 1536–1548, doi: 10.1175/1520-0469(1978)035<1536:REAACG>2.0.CO;2.
- Tao, W. K., J. P. Chen, Z. Li, C. Wang, and C. Zhang, 2012: Impact of aerosols on convective clouds and precipitation. *Reviews of Geophysics*, **50** (2), doi: 10.1029/2011RG000369.

- Tessendorf, S. A., L. J. Miller, K. C. Wiens, and S. A. Rutledge, 2005: The 29 June 2000 supercell observed during STEPS. Part I: Kinematics and microphysics. *Journal of the Atmospheric Sciences*, **62** (12), 4127–4150, doi: 10.1175/JAS3585.1.
- Tessendorf, S. A., S. A. Rutledge, and K. C. Wiens, 2007a: Radar and lightning observations of normal and inverted polarity multicellular storms from STEPS. *Monthly Weather Review*, **135** (11), 3682–3706, doi: 10.1175/2007mwr1954.1.
- Tessendorf, S. A., K. C. Wiens, and S. A. Rutledge, 2007b: Radar and lightning observations of the 3 June 2000 electrically inverted storm from STEPS. *Monthly Weather Review*, **135** (11), 3665–3681, doi: 10.1175/2006MWR1953.1.
- Thomas, R. J., P. R. Krehbiel, T. Hamlin, J. Harlin, and D. Shown, 2001: Observations of VHF source powers radiated by lightning. *Geophysical Research Letters*, **28** (1), 143–146, doi: 10.1029/2000GL011464.
- Thomas, R. J., P. R. Krehbiel, W. Rison, S. J. Hunyady, W. P. Winn, T. Hamlin, and J. Harlin, 2004: Accuracy of the lightning mapping array. *Journal of Geophysical Research: Atmospheres*, **109** (14), 1–34, doi: 10.1029/2004JD004549.
- Tsenova, B., R. Mitzeva, and C. Saunders, 2010: Parameterization of thunderstorm charging including the cloud saturation effect. *Atmospheric Research*, **96** (2-3), 356–365, doi: 10.1016/j.atmosres.2009.11.010.
- van der Velde, O. A., and J. Montanyà, 2013: Asymmetries in bidirectional leader development of lightning flashes. *Journal of Geophysical Research Atmospheres*, **118** (24), 13,504–13,519, doi: 10.1002/2013JD020257.
- Wiens, K. C., S. A. Rutledge, and S. A. Tessendorf, 2005: The 29 June 2000 supercell observed during STEPS. Part II: Lightning and charge structure. *Journal of the Atmospheric Sciences*, **62** (12), 4151–4177, doi: 10.1175/JAS3615.1.
- Williams, E., and Coauthors, 2002: Contrasting convective regimes over the Amazon: Implications for cloud electrification. *Journal of Geophysical Research: Atmospheres*, **107** (D20), 1–19, doi: 10.1029/2001JD000380.
- Williams, E. R., 1985: Large-scale charge separation in thunderclouds. *Journal of Geophysical Research*, **90** (D4), 6013–6025, doi: 10.1029/JD090iD04p06013.
- Williams, E. R., 1989: The tripole structure of thunderstorms. *Journal of Geophysical Research*, **94**, 13 151–13 167.
- Williams, E. R., 2001: The electrification of severe storms. *Severe Convective Storms*, No. 50, Meteorological Monographs, American Meteorological Society, 527–561.
- Williams, E. R., V. Mushtak, D. Rosenfeld, S. Goodman, and D. Boccippio, 2005: Thermodynamic conditions favorable to superlative thunderstorm updraft, mixed phase microphysics and lightning flash rate. *Atmospheric Research*, **76** (1-4), 288–306, doi: 10.1016/j.atmosres.2004.11.009.
- Williams, E. R., and S. Stanfill, 2002: The physical origin of the land-ocean contrast in lightning activity. *Comptes Rendus Physique*, **3** (10), 1277–1292, doi: 10.1016/S1631-0705(02)01407-X.

- Williams, E. R., and Coauthors, 1999: The behavior of total lightning activity in severe Florida thunderstorms. *Atmospheric Research*, **51** (3), 245–265, doi: 10.1016/S0169-8095(99)00011-3.
- Yue, Z., and Coauthors, 2019: Automated Mapping of Convective Clouds (AMCC) thermodynamical, microphysical, and CCN properties from SNPP/VIIRS satellite data. *Journal of Applied Meteorology and Climatology*, **58** (4), 887–902, doi: 10.1175/JAMC-D-18-0144.1.
- Zhang, D., and K. L. Cummins, 2020: Time evolution of satellite-based optical properties in lightning flashes, and its impact on GLM flash detection. *Journal of Geophysical Research: Atmospheres*, **125** (6), doi: 10.1029/2019JD032024.
- Zhu, Y., V. a. Rakov, M. D. Tran, and A. Nag, 2016: A study of National Lightning Detection Network responses to natural lightning based on ground-truth data acquired at LOG with emphasis on cloud discharge activity. *Journal of Geophysical Research: Atmospheres*, **121**, 14 651–14 660, doi: 10.1002/2016JD025574.